Impact of atmospheric stability conditions on wind farm loading and production

Larsen, Gunner Chr.; Ott, Søren; Troldborg, Niels; Chougule, Abhijit S.; Mann, Jakob; Machefaux, Ewan; Verelst, David Robert; Larsen, Torben J.; Mirzaei, Mahmood; Bertagnolio, Franck

Total number of authors:
13

Publication date:
2016

Document Version
Publisher's PDF, also known as Version of record

Impact of atmospheric stability conditions on wind farm loading and production

Department of Wind Energy E Report 2016

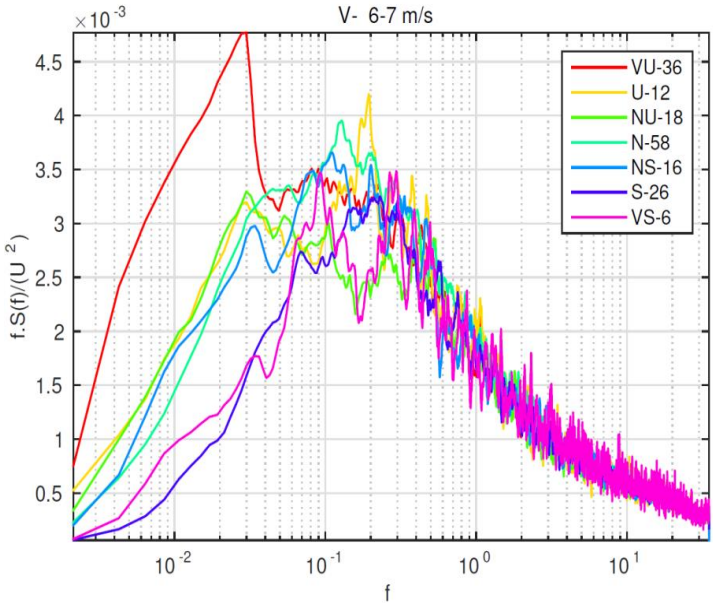

Gunner C. Larsen, Søren Ott, Niels Troldborg, Abhijit S. Chougule, Jakob Mann, Ewan Machefaux, David R. Verelst, Torben J. Larsen, Mahmood Mirzaei, Franck Bertagnolio, Mark C. Kelly, Kurt S. Hansen and Lucas Marion

DTU Wind Energy E-0136(EN)

ISBN: 978-87-93549-03-6
November 2016

DTU Wind Energy
Department of Wind Energy

Authors: Gunner C. Larsen, Søren Ott, Niels Troldborg, Abhijit S. Chougule, Jakob Mann, Ewan Machefaux, David R. Verelst, Torben J. Larsen, Mahmood Mirzaei, Franck Bertagnolio, Mark C. Kelly, Kurt S. Hansen and Lucas Marion

ISBN: 978-87-93549-03-6

November 2016

Title: Impact of atmospheric stability conditions on wind farm loading and production

Department: DTU Wind Energy

Summary:

The project has created a *new basis* for further development and optimization of WT's designed for WF operation. This has been accomplished through developing of more realistic modelling of WF flow fields as well as of such fields interactions with WT's under non-neutral ABL stability conditions. On this basis a *verified model complex* for prediction of structural loads as well as production losses for wind turbines operating in wind farm conditions, which takes into account the effects from ABL stability conditions, is established. Thereby the way to increased reliability and cost efficiency of future wind turbines as well as to more precise prediction of the WF power output is paved.

EUDP-2010 64010-0462

Sponsorship: EUDP

Front page: Inertial subrange power spectra for a variety of ABL stability conditions

Pages: 139

Figures: 101

Tables: 14

References: 106

Technical University of Denmark
Department of Wind Energy
Frederiksborgvej 399
Building 118
4000 Roskilde

Phone 46 77 50 56

gula@dtu.dk

www.vindenergi.dtu.dk

Table of Contents

Overview of project objectives and report structure

The objectives of the present project are:

- To explore and model the influence of buoyancy effects in the atmospheric boundary layer (i.e. atmospheric stability effects) on both *wake losses* and *structural loading* of wind turbines (WT's) operating in wind farms;
- To validate the developed model framework by comparing model predictions with full-scale wind farm (WF) measurements both regarding wake affected production losses and structural loading;
- To demonstrate the capabilities of the developed model framework regarding design of innovative load alleviating wind turbine control systems for WT's operating in wake affected flow conditions; and
- To suggest simplified design procedures that includes atmospheric stability aspects. With the Dynamic Wake Meandering model, on the basis of which the model framework developed in this project is based, being included in the upcoming revised version of the IEC code [8] as a recommended practice, the suggested approach is potentially relevant for future revisions of the IEC code.

This project report is organized as follows: Chapter 1 gives an introduction to the theme of the project. Chapter 2 introduces the concept of ABL stability, including its quantification and classification. Chapter 3 deals with kinematic turbulence modeling for non-neutral stability conditions, including attempts to tweak the classical spectral tensor to such conditions as well as a consistent generalization of the classical Mann spectral tensor model [11],[12],[13] to the non-neutral stability regime. Chapter 4 focuses on the possible influence from the presence of a WF on the big turbulent eddies that dictates the wake meandering. The possible feed-back on the large scale turbulence structures is investigated under various stability conditions using a comprehensive set of full-scale offshore measurements. Chapter 5 demonstrates and validates the impact of ABL stability on wake dynamics, wake losses [14] and turbine fatigue loading [63] for a complete wind farm using the DWM modeling approach. Predictions and full-scale measurements from two offshore WF's are compared for a full wind direction rose with a large range of different wake situations represented. Chapter 6 investigates possibilities for improving WT control for WT's operating under WF conditions. Three possible approaches – individual pitch control, flap based control, and model based control – are discussed, and the capability of one of these approaches is demonstrated using a simplistic generic WF setup combined with a stability climatology derived from a huge set of full-scale data. Finally, Chapter 7 describes a simplified rational WT design approach based on collapsing the probability distribution of a set of stability classes (i.e. the stability climatology) to only two "design stability classes". In Chapter 8 the project achievements are summarized.

1 Introduction

The dependence of WF *production losses* on atmospheric boundary layer (ABL) stability conditions was first investigated by Jensen [1] and Barthelmie [2], who took a phenomenological approach and analysed large sets of full-scale offshore measurements from two Danish wind farms – Horn Rev and Nysted, respectively. For wind directions close to the directions of the WT rows within these farms, their analyses demonstrated a significant impact of ABL stability on WF production.

The first to link this phenomenon to *wake dynamics* was Larsen et al. [3], who conjectured that, in a wake context, ABL stability affects primary wake meandering driven by large (lateral and vertical) turbulent scales, whereas wake expansion in the meandering frame of reference is a second order effect only. Because wake meandering is heavily load generating, the introduction this scientific explanation of the observations in [1],[2] at the same time extended the influence of ABL stability to also incorporate *structural loading* of the individual wind farm turbines.

The goal of the present project is to model the impact caused by ABL stability conditions on both wake losses and structural loading of wind turbines operating in wind farms, to verify the developed models by comparison with full-scale wind farm measurements, and to apply the developed modeling framework for improved design of future MW turbines (incl. their load alleviating control system) operating in wind farms. The investigation is thus limited to WT's operating under WF conditions.

As part of the project, the basic conjecture launched in [3] has been validated by conducting and analyzing detailed full-scale LiDAR based wake measurements [4],[5]. This has enabled establishment of a direct link from ABL stability to the Dynamic Wake Meandering (DWM) model [6],[7], which has recently been included as a recommended practice in the IEC-61400 code [8]. Describing the *un-steady* characteristics of WF flow fields, the DWM model, in combination with an aeroelastic code, facilitates simulation of production as well as loading of WT's operating in wake-affected ABL flow fields.

The core of the DWM model is a *split of scales* in the wake affected flow field, with large turbulence scales being responsible for stochastic *wake meandering*, and small scales being responsible for wake *attenuation* and *expansion* in the meandering frame of reference as caused by turbulent mixing. Thus, essentially the DWM model assumes that the transport of wakes in the ABL can be modeled by considering the wakes to act as passive tracers driven by a combination of large-scale turbulence structures and a mean downstream advection velocity, adopting the Taylor hypotheses.

The large scale turbulence structures used to describe wake dynamics in the DWM model is traditionally provided by a fast Navier-Stokes (NS) consistent kinematic turbulence model [9],[10] which, however, assumes neutral ABL stability and thereby neglect the effects of buoyancy on turbulence production and thus turbulence characteristics. As ABL stability mainly affects the large scale turbulence structures, the effect of buoyancy cannot be neglected.

2 ABL stability and its classification

In the past wind turbines were so relatively small that the rotor could be considered as embedded in the atmospheric surface layer. This allows for a relatively easy extrapolation of wind speeds measured at 10 meter, say, to hub wind speeds at hub height using Monin-Obukhov (M-O) similarity theory [16]. Today, however, turbine hub heights are reaching beyond the surface layer where M-O theory is not valid. Of course M-O theory does not suddenly fail at a precise height; it's validity rather fades away with increasing height in a stability dependent way. In this section we derive new theoretical results that extend M-O theory to cover the whole atmospheric boundary layer. From this a simple, practical model is made that extends wind profiles obtained by traditional M-O theory beyond the surface layer, and thus into the regime where modern WT's are operating. The model was tuned to data from the M2 meteorological mast located near the Horns Reef 1 wind farm [16] and has been validated against meteorological data from several other offshore locations.

2.1 Stability, turbulence and wind turbine wakes

Turbulence is produced in both mechanical and thermal processes. Due to the shear of the mean wind profile, turbulent diffusion will mix air parcels with different velocities, and the mixing process can be regarded as inelastic collisions between eddies. These collisions transform kinetic energy of the mean flow into turbulent kinetic energy (TKE). When relatively large eddies collide and get entangled, they create smaller eddies that in turn collide and create even smaller eddies etc. In this way large scale TKE transforms itself into progressively smaller scales in a process known as the turbulent energy cascade. The cascade eventually stops at very small scales where the TKE is dissipates into heat.

The presence of a vertical heat flux will also affect the turbulence. During unstable atmospheric conditions the air next to the ground is heated. This makes it expand and lifts up the whole atmosphere thus adding potential energy to the atmosphere. This energy is converted to kinetic energy, when buoyancy forces the hot air upwards. This extra kinetic energy input manifests itself both in the form of random TKE but also through the generation of larger and more organized convection rolls or convection cells. In the stable situation the heat flux is negative (downwards), and the thermally induced TKE production is negative, acting as a TKE drain rather than a source. Thus the thermal stratification dampens the turbulence and inhibits the generation of large scale vertical motion. Horizontal motion, on the other hand, is less disturbed because of the low the friction between horizontal layers which leads to increased shear. During strongly stable conditions even very shallow terrain features can generate drainage flows that cause slow, large scale wind fluctuations. The TKE therefore contains a large scale component, which has a site specific rather than a universal character. However, for onshore sites this occurs at rather low wind speeds, where wind turbines are not running, and offshore sites are flat enough to avoid the phenomenon. The nocturnal jet is another feature of stable conditions, which mainly occurs after sunset during the transition from unstable to stable conditions where the turbulence suddenly drops. This causes an imbalance between the pressure gradient, the Coriolis force and the reduced friction that makes the flow accelerate and perform so called inertial oscillations. Low level jets can also result from various kinds of horizontal inhomogeneity such as inhomogeneous heating or roughness (i.e. land/sea) or the passage of a cold front.

The convective heat transfer during unstable conditions is driven by hot air 'bubbles' generated at the ground. The bubbles rise and tend to cluster into larger, elongated structures. At typical hub heights these blobs of slow moving air are similar to turbine wakes both with respect size and velocity deficits. Similar

coherent structures do not form during stable conditions, and fatigue loads caused by turbulence are reduced. On the other hand, turbine wakes decay more slowly in stable conditions thus increasing fatigue loads caused by wakes. Wake losses are also larger**.**

With few exceptions [3],[18] traditionally only shear-generated turbulence (i.e. neutral conditions) has been considered when modeling WT production and WT loading both for WT's operating in WF's and for solitary WT's. However, convection in the atmospheric boundary layer – i.e. buoyancy and its effect on the flow in terms of ABL stability – is prone to play a significant role for WT loading. This was demonstrated in [18] for solitary turbines, where especially tower and rotor loads under diabatic wind conditions are increased compared to the neutral case. For wind turbines operating in WF conditions the influence of ABL stability on loading is further enhanced [20], and in addition comes a significant effect on the production [19]. This is basically due to wake dynamics being highly sensitive to ABL stability conditions [4],[5].

Recognizing the importance of ABL stability the need for a precise definition and thus in turn *quantification* of stability arises preferable as based on easily accessible measured quantities.

2.2 Rough surfaces

The present project is confined to flows over *flat* and *homogeneous terrain*. To be more precise, we are talking about a rough surface with evenly distributed roughness elements (vegetation, buildings, waves etc.) that make the terrain homogeneous in a statistical sense. In the vicinity of the roughness elements, sometimes referred to as the buffer layer, the flow depends on the detailed shape of the surface and therefore does not have a universal character. However, just above the buffer layer a logarithmic layer is always found. In neutral conditions the logarithmic layer extends through the whole surface layer, while the logarithmic wind profile is modified in the upper part of the surface layer in both stable and unstable conditions. In stable conditions the profile tends to become linear with height, while it tends to become constant in unstable conditions, but in any case there will be a logarithmic layer just above the buffer layer. In this region the turbulence is dominated by the large shear production term $\varepsilon = u_*^3/(\kappa z)$, where u_* denotes the friction velocity, κ is the von Kármán constant (~0.41), and z is the altitude. The shear production term diverges for $z \to 0$. Thermally induced TKE production is, on the other hand, evenly distributed over the boundary layer and cannot compete with the mechanical TKE production in the logarithmic layer. The logarithmic layer is therefore essentially neutral. The large shear production must be balanced by large TKE dissipation. The TKE is essentially constant in the surface layer, hence the lifetime of eddies must be very short near the ground ($\cong z/u_*$). It is therefore seems reasonable to assume that eddies created in the buffer zone decay before they have diffused up to the logarithmic layer. Eddies carry momentum, and when they decays, they do not simply die and disappear but must somehow pass their momentum to the flow in order to keep the momentum flux going. Otherwise the conservation law for momentum would be violated. Molecular viscosity is too weak to do the job, so it has to be newborn eddies that carry the momentum on. After the momentum has been passed on to more and more generations of eddies, it seems plausible that the only 'memory' of the ancestors in the buffer layer is the conserved momentum flux. Thus motivated we make the following fundamental conjecture:

The turbulence in the logarithmic layer is of a universal character that does not depend on stability or of the particular mechanism that generates friction at the ground.

One consequence of this is that the statistical properties of the wind field in the logarithmic layer and above do not depend on the friction mechanism. Another consequence is that the influence of a rough

boundary is fully characterized by the behavior in the logarithmic layer. Here the wind profile, decomposed in respectively longitudinal and lateral components, is given by

$$U(z) = \frac{u_*}{\kappa} \log {}^{z}/_{z_0}$$
$$V(z) = 0 \qquad (2.2.1)$$

where, again, $\kappa \cong 0.41$ is the von Karman constant, and u_* is the friction velocity. Thus wind veer and consequently Coriolis force effects are neglected in the logarithmic layer.

This description involves three external parameters: the friction velocity u_* (explicitly defined in equation (2.3.2) below), the roughness length z_0 defined as the height at which the logarithmic profile vanishes (or *seems to vanish* – in case z_0 is located outside the logarithmic layer) and the wind direction. The wind direction is defined as the direction of d$\boldsymbol{U}$/dz for $z=z_0$, with $\boldsymbol{U}$ denoting the mean velocity field.

In practical flow modeling the asymptotic logarithmic form of the mean profile is used as boundary condition, and the buffer layer is not modeled at all. Below we will assume that the flow fields are solutions of this kind without any buffer layer, and the logarithmic layer extending right down to $z=z_0$.

Active devices such as fans and wind turbines may be used to generate friction. Moving roughness elements (e.g. waves on a sea surface) could also be used. These friction mechanisms inject both momentum and TKE, but the conjecture implies that TKE injected at the ground will dissipate in the buffer layer. Ultimately, we could generate friction by setting the whole ground in motion. Imagine that we set the ground in motion with velocity ΔU at time t_0. From the beginning this would change the momentum transfer, but gradually a new steady state would emerge. The situation is different when observed from the Cartesian coordinate system $x'y'z'$ that follows the motion of the ground. Here the fluid experiences a velocity jump $-\Delta U$ at time t_0 and then gradually approach a steady state solution which must be characterized by the same u_* and z_0 as the flow field we started out with in the other system. Now suppose that $\boldsymbol{u}(x', y', z', t)$ is a representative steady state flow field solution in the moving frame. Applying a Galilean transform along the x-axis (note that $\Delta\boldsymbol{U} = (\Delta U,0,0)$) we find that

$$\boldsymbol{u}(x+\Delta U(t-t_0),y,z,t) - \Delta\boldsymbol{U} \qquad (2.2.2)$$

is a representative solution for the final steady state in the original frame. The logarithmic layer mean profile is obtained simply by subtracting ΔU from the original profile, which is equivalent to the replacement

$$z_0 \rightarrow z_0 \exp(\kappa \Delta U/u_*) \qquad (2.2.3)$$

In other words, a change of roughness is equivalent to the transformation:

$$\boldsymbol{u}(\boldsymbol{x}, t) \rightarrow \boldsymbol{u}(\boldsymbol{x} + \Delta\boldsymbol{U}(t - t_0, t) - \Delta\boldsymbol{U} \qquad (2.2.4)$$

Strictly speaking this is a boost transformation that changes the velocity field, not the system of reference, but we will refer to it as a Galilean transformation anyway. The Galilean transformation does not alter the geometry of eddies, it only changes their velocities. Therefore z_0 is not a characteristic length scale of the turbulence; it merely indicates the height where the logarithmic profile vanishes and nothing more.

Suppose we have an ensemble of flow solutions for fixed values of the roughness z_{00}, the angle α between the wind direction and the x-axes and a list $\boldsymbol{q}$ of all the other external parameters, and let $\boldsymbol{U}(z,z_{00},\alpha,\boldsymbol{q})$ denote the corresponding ensemble mean velocity profile. $\boldsymbol{U}=(U,V,0)$ is a horizontal vector, which is conveniently represented as a complex number

$$W(z, z_{00}, \alpha, \boldsymbol{q}) = U(z, z_{00}, \alpha, \boldsymbol{q}) + \imath\, V(z, z_{00}, \alpha, \boldsymbol{q}) \tag{2.2.5}$$

Due to rotational symmetry (a rotated solution is a solution to the rotated problem) we have

$$W(z, z_{00}, \alpha, \boldsymbol{q}) = \exp\{\imath\alpha\}\, W(z, z_{00}, \boldsymbol{q}) \tag{2.2.6}$$

where $W(z; z_{00},\boldsymbol{q})$ is equal to $W(z,z_{00},\alpha,\boldsymbol{q})$ for $\alpha=0$.

Applying a Galilean transformation as above with $\Delta\boldsymbol{U}=\boldsymbol{U}(z_0,z_{00},\alpha,\boldsymbol{q})$ to all flows in the ensemble, we obtain a new ensemble consisting of flows with roughness lengths z_0. Due to possible veer, the angle α may change, while the remaining external parameters in the list $\boldsymbol{q}$ can be chosen so that they are invariant. Therefore

$$W(z;z_0,\boldsymbol{q}) = \exp\{\imath\beta(z_0,z_{00},\boldsymbol{q})\}\ \{\ W(z,z_{00},\boldsymbol{q}) - W(z_0,z_{00},\boldsymbol{q})\ \} \tag{2.2.7}$$

Formally $\beta(z_0,z_{00},\boldsymbol{q})$ is determined so that $\partial W(z,z_{00},\boldsymbol{q})/\partial z = |\partial W(z,z_{00},\boldsymbol{q})/\partial z|$ for $z = z_0$. It represents the veer when going from z_{00} to z_0, which must be an extremely small angle, when both z_{00} and z_0 are in the logarithmic layer. Assuming this is the case we therefore ignore $\beta(z_0,z_{00},\boldsymbol{q})$ and rewrite (2.2.7) as

$$W(z,z_0,\boldsymbol{q}) = W(z,z_{00},\boldsymbol{q}) - W(z_0,z_{00},\boldsymbol{q}) \tag{2.2.8}$$

Differentiation with respect to z gives

$$\partial W(z,z_0,\boldsymbol{q})/\partial z = \partial W(z,z_{00},\boldsymbol{q})/\partial z = \partial F(z,\boldsymbol{q})/\partial z \tag{2.2.9}$$

where the point is that F is a function of z and $\boldsymbol{q}$, and not depending on either z_0 or z_{00}. An integration then yields

$$W(z,z_0,\boldsymbol{q}) = F(z,\boldsymbol{q}) - F(z_0,\boldsymbol{q}) \tag{2.2.10}$$

2.3 Extended Monin-Obukhov theory

Conventional M-O theory describes mean profiles over homogeneous terrain, where the external forcing is also homogeneous, and the flow is statistically stationary in time. The external forcing consists of sensible heat transfer from the ground to the air and a vertical flux of horizontal momentum induced by the ground friction. We postulate that, given enough time, such a steady state would be reached. The Coriolis force is ignored, and the horizontal mean pressure gradient is assumed to be zero. The two should balance each other above the boundary layer, so you can either include both or ignore both. In the extended theory we are about to develop, the Coriolis force is included and a mean pressure gradient is allowed to have a horizontal component, which we assume is constant with height. Such flows are referred to as being barotropic. Baroclinic (non-barotropic) conditions arise in connection to horizontal mean temperature gradients.

A sea surface is almost a perfectly flat and homogeneous terrain, and fairly flat and homogeneous terrain can be found onshore here and there. Uniform, stationary forcing is, on the other hand, somewhat of an

abstraction. The change of insolation during the diurnal cycle makes weather an ever changing phenomenon, and even in the 6 months long polar night the flow shows signs of non-stationarity. Even so theoretical, stationary solutions are of interest if the external forcing changes so slowly, that the turbulent flow can adjust itself to it in a quasi-steady fashion. Near the ground the turbulence consists of relatively small eddies with short lifetimes, and the quasi-steadiness seems to be a decent approximation. Higher above we run into larger eddies with larger time constants, and the steady state assumption becomes less and less feasible. However, the approach to steady state may be either through acceleration or de-acceleration, and chances are that the long term mean of observed, unsteady profiles may still be well represent by the mean steady-state profile. In the same way the effect of baroclinicity changes sign, depending on whether or not the flow goes against the mean temperature gradient, again with a tendency to reduce the net effect in the mean. In any case we must expect a growth with height of the deviations between an actual, ten minutes average profile and the corresponding theoretical, steady state profile.

Having made these reservations we return the derivation of M-O theory. M-O theory (Monin and Obukhov [21], see also Monin and Yaglom [22]) is based on analysis of the following set of model equations

$$\begin{aligned}
\frac{\partial u}{\partial t} + u_j \frac{\partial u}{\partial x_j} &= -\frac{\partial p}{\partial x} + fv + \nu \nabla^2 u \\
\frac{\partial v}{\partial t} + u_j \frac{\partial v}{\partial x_j} &= -\frac{\partial p}{\partial y} - fu + \nu \nabla^2 v \\
\frac{\partial w}{\partial t} + u_j \frac{\partial w}{\partial x_j} &= \frac{g\theta}{T} - \frac{\partial p}{\partial z} + \nu \nabla^2 w \\
\frac{\partial \theta}{\partial t} + u_j \frac{\partial \theta}{\partial x_j} &= 0 \\
\frac{\partial u_i}{\partial x_i} &= 0
\end{aligned} \qquad (2.3.1)$$

Here (u,v,w) is the velocity vector in a standard Cartesian coordinate system *xyz* with vertical *z*-axis and the *x*-axis pointing along the surface wind. The flow is incompressible with *constant density* ρ, but nonetheless with buoyancy governed by the temperature θ. This is called the Boussinesq buoyancy approximation, and it works by assigning a kind of gravitational 'charge' θ/T, which responds to gravity in much the same way as an electric charge responds to an electric field without affecting the inertial mass. We have included the Coriolis force and the Coriolis parameter *f*. Only the vertical component of the Earth rotation vector is retained, so that the flow is effectively being modeled as an incompressible flow on a turn table. The centrifugal force can be written as a gradient, which has been absorbed into the gradient of pressure P and $p=P/\rho$. Molecular viscosity ν has been included, but molecular diffusivity of θ has been omitted. The temperature θ corresponds to the potential temperature of the real world – i.e. the temperature after adiabatic compression to a reference pressure. Finally T is a representative value of the absolute temperature, and g is the acceleration of gravity. Please note these are the Navier-Stokes

equations, without any Reynolds averaging or closure assumptions involved that could potentially compromise the dynamics.

Next step is to introduce M-O scaling. To this end we define three scales[1]

$$u_* = \sqrt{-\overline{u'w'}} \tag{2.3.2}$$

$$\theta_* = -\frac{\overline{\theta' w'}}{u_*} \tag{2.3.3}$$

$$L = \frac{T\, u_*^2}{g\, \theta_*} \tag{2.3.4}$$

The overbars represent ensemble averaging. Both the friction velocity u_* and the temperature scale θ_* are to be evaluated close to the ground. L is the celebrated Monin-Obukhov length scale (actually first introduced by Obukhov). We use these scales to make new non-dimensional variables:

$$\tilde{u} = u/u_*,\ \tilde{\theta} = \theta/\theta_*,\ \tilde{t} = tu_*/L,\ \tilde{z} = z/L \text{ etc.} \tag{2.3.5}$$

There is of course only one way of doing this. Using the scaled variables the governing equations become

$$\begin{aligned}
\frac{\partial \tilde{u}}{\partial \tilde{t}} + \tilde{u}_j \frac{\partial \tilde{u}}{\partial \tilde{x}_j} &= -\frac{\partial \tilde{p}}{\partial \tilde{x}} + \frac{1}{\mu}\tilde{v} + \frac{1}{\mathrm{Re}}\tilde{\nabla}^2 \tilde{u} \\
\frac{\partial \tilde{v}}{\partial \tilde{t}} + \tilde{u}_j \frac{\partial \tilde{v}}{\partial \tilde{x}_j} &= -\frac{\partial \tilde{p}}{\partial \tilde{y}} - \frac{1}{\mu}\tilde{u} + \frac{1}{\mathrm{Re}}\tilde{\nabla}^2 \tilde{v} \\
\frac{\partial \tilde{w}}{\partial \tilde{t}} + \tilde{u}_j \frac{\partial \tilde{w}}{\partial \tilde{x}_j} &= \tilde{\theta} - \frac{\partial \tilde{p}}{\partial \tilde{z}} + \frac{1}{\mathrm{Re}}\tilde{\nabla}^2 \tilde{w} \\
\frac{\partial \tilde{\theta}}{\partial \tilde{t}} + \tilde{u}_j \frac{\partial \tilde{\theta}}{\partial \tilde{x}_j} &= 0 \\
\frac{\partial \tilde{u}_i}{\partial \tilde{x}_i} &= 0
\end{aligned} \tag{2.3.6}$$

Two numbers appear in these equations. The non-dimensional viscosity gives Reynolds number

$$\mathrm{Re} = \frac{L\, u_*}{\nu} \tag{2.3.7}$$

and the non-dimensional Coriolis parameter gives the so called Monin-Kazanski parameter[2]

[1] Usually L is defined with an extra κ in denominator. We drop it to avoid κ from appearing in the scaled equations.

[2] It is common to define it as $\frac{\kappa\, u_*}{f\, L}$, but we have dropped κ.

$$\mu = \frac{u_*}{f\,L} \tag{2.3.8}$$

When the Reynolds number is sufficiently large, as it always is in the ABL, we may assume that flow has reached the high Reynolds number limit, where there is no dependence on Re except at the tiniest, dissipative scales (millimeter size eddies).

We cannot get rid of the second parameter μ. It should be included in the list $\boldsymbol{q}$ of external conditions that determine the shape of mean profiles. Potentially there would be more coming from boundary conditions. If we introduce a closure and solve the RANS equations, the boundary conditions would be characterized by the heat and momentum fluxes at the ground. We are not making any closures here, but it is natural to assume that these two would complete the list of external conditions. However, the non-dimensional values equal to

$$\overline{\tilde{u}'\tilde{w}'} = \frac{\overline{u'w'}}{u_*^2} = -1 \tag{2.3.9}$$

$$\overline{\tilde{\theta}'\tilde{w}'} = \frac{\overline{\theta'w'}}{\theta_* u_*} = -1 \tag{2.3.10}$$

So no additional parameters. One could argue that the mean pressure gradient is also a condition. It is indeed, but it is linked to the surface momentum flux, so we cannot specify both at the same time. The mean value of θ at the surface is also a parameter, but we can add any constant to θ and still have a valid solution; hence we may assume that the value is zero or some other value without loss of generality. The potential temperature difference between top and bottom could also be used as an external condition, but then we cannot specify the surface temperature flux at the same time.

After scaling, μ is therefore the only non-trivial external parameter. Finally, we use the results from the preceding section. This requires a sort of Galilei *invariance* that boosts the flow with a constant velocity. It should be remembered that the coordinate system is rotating, and is therefore not an inertial frame of reference. Transforming to a system that moves with constant velocity seen from a rotating system is therefore a transformation from a rotating system to another rotating system performing a complex spiraling motion. It is therefore not trivial that the Galilei transformation actually works. Thus if $\boldsymbol{u}(\boldsymbol{x},t)$, $\theta(\boldsymbol{x},t)$ and $p(\boldsymbol{x},t)$ solve the equations and $\Delta\boldsymbol{U} = (\Delta U, \Delta V, 0)$ then another solution is given by $\boldsymbol{u}(\boldsymbol{x} + \Delta\boldsymbol{U}(t-t_0),t) - \Delta\boldsymbol{U}, \theta(\boldsymbol{x} + \Delta\boldsymbol{U}(t-t_0,t)$ and $p(\boldsymbol{x} + \Delta\boldsymbol{U}(t-t_0),t) - x\Delta V + y\Delta U$. This can be verified by direct insertion. The mean velocity profile can therefore be written as

$$\widetilde{W}(\tilde{z},\tilde{z}_0,\mu) = \widetilde{F}(\tilde{z},\mu) - \widetilde{F}(\tilde{z}_0,\mu) \tag{2.3.11}$$

If we rewrite $\tilde{F}$ again, now as

$$\widetilde{F}(\tilde{z},\mu) = \frac{1}{\kappa}\left\{\log\tilde{z} - \psi_{\mathrm{m}}(\tilde{z},\mu)\right\} \tag{2.3.12}$$

then we get the familiar looking result

$$W(z) = \frac{1}{\kappa}\left\{\log\left(\frac{z}{z_0}\right) - \psi_{\mathrm{m}}\left(\frac{z}{L},\mu\right) + \psi_{\mathrm{m}}\left(\frac{z_0}{L},\mu\right)\right\} \tag{2.3.13}$$

The difference from the conventional M-O profile is that ψ_{m} now is complex and depends on μ. The corresponding expression for the mean potential temperature profile can be derived along the same lines yielding

$$\theta(z) = \theta_0 + \frac{1}{\kappa}\left\{\log\left(\frac{z}{z_0}\right) - \psi_{\mathrm{h}}\left(\frac{z}{L},\mu\right) + \psi_{\mathrm{h}}\left(\frac{z_0}{L},u\right)\right\} \tag{2.3.14}$$

2.4 The geostrophic drag law

Letting $z\to\infty$ we get the complex geostrophic wind

$$\widetilde{W}_G(\tilde{z}_0,\mu) = \widetilde{F}(\infty,\mu) - \widetilde{F}(\tilde{z}_0,\mu) \tag{2.4.1}$$

We may of course write $\tilde{F}(\infty,\mu)$ as

$$\widetilde{F}(\infty,\mu) = \frac{1}{\kappa}\{\log\mu - A(\mu) - \imath B(\mu)\} \tag{2.4.2}$$

where A and B are real. Using (2.3.12) and (2.3.8) then gives the geostrophic drag law

$$W_G = \frac{u_*}{\kappa}\{\log z_0 f/u_* + \psi_{\mathrm{m}}(z_0/L,\mu) - A(\mu) - \imath B(\mu)\} \tag{2.4.3}$$

Compared to textbooks there is an extra term $\psi_{\mathrm{m}}(\tilde{z}_0,\mu)$. We can always choose to set $\psi_{\mathrm{m}}(0,\mu) = 0$ and, if z_0/L is not too extreme, the extra term will be utterly small. Traditionally, the geostrophic drag law is derived in a different way, which can be found in lots of papers and textbooks. Below we give a short derivation based on J.R. Garratt [23].

The key points are Rossby number similarity, surface layer scaling and asymptotic matching. Rossby number similarity is the idea that there exists an 'upper layer', where the velocity defect $\widetilde{W}_d = \widetilde{W} - \widetilde{W}_G$ only depends on μ and the variable $s = \frac{zf}{u_*}$. The third variable, which $\widetilde{W}_d$ does not depend on, is taken as $t = \frac{z}{z_0}$ (not to be confused with the time variable). It is then suggested that the surface friction Rossby number $\mathrm{Ro} = \frac{u_*}{fz_0}$ is so enormous that $\widetilde{W}_d$ does not depend on it. Then $\widetilde{W}_d$ of course does not depend on $t = s\,\mathrm{Ro}$ either. Furthermore, it is postulated that there exists an 'inner layer', where $\widetilde{W}$ only depends on t and μ. Finally, the asymptotic matching postulates that a 'matched' layer exists where inner-layer and outer-layer scaling are simultaneously valid. It can then be shown, that this is possible only if the profile is logarithmic in the matched layer, and the logarithmic drag law follows – without the $\psi_{\mathrm{m}}(\tilde{z}_0,\mu)$. Note, that in the surface layer $\widetilde{W}$ can be expressed as a function of $\tilde{z} = \mu\, s$ and $\tilde{z}_0 = \frac{\mu\, s}{t}$. The inner layer therefore only extends as far up as the logarithmic layer, and consequently the outer layer must fill the whole boundary layer (except the buffer layer). The matching takes place next to the ground, where $\frac{z}{z_0}$ is not a large number. The argumentation therefore contradicts itself. In the alternative theory we have

presented, an additional assumption like Rossby number similarity is not needed. Note that $\widetilde{W}_d$ can be written as

$$\widetilde{W}_d = \tilde{F}(\tilde{z},\mu) - \tilde{F}(\infty,\mu) = \tilde{F}(\mu s,\mu) - \tilde{F}(\infty,\mu) \tag{2.4.4}$$

and therefore does not depend on z/z_0.

2.5 A practical model

A practical model for 'tall' wind profiles (i.e. extending beyond the surface layer) has been developed and implemented in a Windows application called AMOK. AMOK is freely available from DTU Wind Energy. The model modifies conventional M-O profiles, hence we start describing the particular version of the M-O theory we have used and compare it to some data. For the conventional theory we have used the following profile functions

$$\phi_m(\zeta) = \begin{cases} 1+5\zeta & \text{for } \zeta > 0 \\ (1-19.3\zeta)^{-1/4} & \text{for } \zeta < 0 \end{cases} \tag{2.5.1}$$

$$\phi_h(\zeta) = \begin{cases} 1+7.8\zeta & \text{for } \zeta > 0 \\ (1-12\zeta)^{-1/2} & \text{for } \zeta < 0 \end{cases} \tag{2.5.2}$$

Recall that the ψ functions are obtained as e.g.

$$\psi_m(\zeta) = \int_0^\zeta (1-\phi_m(x))/x\,dx \tag{2.5.3}$$

The integrals can be done analytically, but we skip the expressions, which are fairly long. These profile functions are compatible with those suggested by Högström [24]. They seem to fit data quite well, even if a systematic optimization has not been attempted.

Data for analysis are taken from met mast M2 that operated for many years at Horns Reef (se [16] for a description). In the data analysis the parameters L, u_* and θ_* were first determined from measurements of water temperature T_w measured 2m below the surface, air temperature T_a measured at z_T =13m and wind speed U measured at z_U =15m. It should be safe to use conventional M-O theory for these heights since the measurements are taken in the *surface layer*. In addition we need the Charnock relation [25]

$$z_0 = \frac{A_C u_*^2}{g} + \frac{B_C \nu}{u_*} \tag{2.5.4}$$

where ν is the kinematic viscosity, g = 9.82 m/s^2, A_C = 0.012 and B_C = 0.012. The potential temperature at the surface and at z_T are given by

$$\theta_0 = T_w \tag{2.5.5}$$

$$\theta(z_T) = T_w + z_T g/C_p \tag{2.5.6}$$

This leaves us with four equations (T_a and T_w are absolute temperatures)

$$T_a + \frac{z_T g}{C_P} = T_w + \frac{\theta_*}{\kappa}\left\{\log\left(\frac{z_T}{z_0}\right) - \psi_{\mathrm{h}}\left(\frac{z_T}{L}\right) + \psi_{\mathrm{h}}\left(\frac{z_0}{L}\right)\right\} \tag{2.5.7}$$

$$U = \frac{u_*}{\kappa}\left\{\log\left(\frac{z_U}{z_0}\right) - \psi_{\mathrm{m}}\left(\frac{z_U}{L}\right) + \psi_{\mathrm{m}}\left(\frac{z_0}{L}\right)\right\} \tag{2.5.8}$$

$$z_0 = \frac{A_c u_*^2}{g} + \frac{B_C \upsilon}{u_*} \tag{2.5.9}$$

$$L = \frac{T_w u_*^2}{\kappa\, g\, \theta_*} \tag{2.5.10}$$

and four unknowns[3]: z_0, L, u_* and θ_*. Eliminating z_0 and L we end up with two equations with two unknowns u_* and θ_*, which are solved using Newton-Raphson iteration. Once this is done, the whole profiles can be predicted and compared to what was actually measured. We have chosen to predict the ten minutes average wind speed U_{62} measured by the highest cup anemometer placed at 62m. The prediction is of course

$$U_{62\mathrm{pred}} = \frac{u_*}{\kappa}\left\{\log\left(\frac{62\mathrm{m}}{z_0}\right) - \psi_{\mathrm{m}}\left(\frac{62\mathrm{m}}{L}\right) + \psi_{\mathrm{m}}\left(\frac{z_0}{L}\right)\right\} \tag{2.5.11}$$

This was done for the whole data set yielding more than 170.000 pairs of measured and predicted values. Data with U_{15}<3m/s, where turbines would not be running, were excluded from the analysis. As already mentioned, we cannot hope for a strong case-by-case correlation. However, the distribution of the predicted values may still be accurate if the prediction is unbiased, and if the standard deviation of the prediction error $U_{62\mathrm{pred}}$- U_{62} is small compared to the standard deviation of U_{62}. It therefore makes sense to average over similar cases, where a case is defined by two numbers indicating wind speed and stability. U_{10} and $1/L$ is a popular choice, but it suffers from U_{10} and $1/L$ being strongly correlated, so that the flow cases are concentrated in a quite narrow strip in the (U_{10},$1/L$) plane. This makes it awkward to divide the plane into bins with approximately the same number of flow cases.

We have found that u_* and θ_* is a much better choice, because these variables are fairly independent. The procedure is first to split the data into stable and unstable cases. Each of these are then split into sub-ensembles by cutting the (u_*,θ_*) plane into rectangular bins limited by quantiles of u_* and θ_*. Using quantiles in steps of 10% leaves us with 100 stable bins and 100 unstable bins each containing approximately the same number of cases. Fig. 2 and 3 shows scatter plots (measured vs. predicted) of bin averaged values of U_{62} with separate plots for stable and for unstable conditions. The unstable cases are remarkably well predicted, and there is no need to make any corrections. Most stable cases are also well predicted, but however with some large over predictions. The over predictions occur in the corner where u_* is small, while θ_* is large. The biggest error (7m/s measured – 13.5m/s predicted) corresponds to the u_* between the 0% and the 10% quantiles, and θ_* between the 90% and the 100% quantiles. All the deviating points in fact reflect the positions of the corresponding bins in the (u_*,θ_*) plane. In this region z/L becomes so large, that the prediction is dominated by the term $\psi_{\mathrm{m}}\left(\frac{z}{L}\right) = -5\, z/L$. It is clear that conventional M-O theory fails in these cases.

[3] Note that we now have returned to the conventional definition of L with a κ in the denominator.

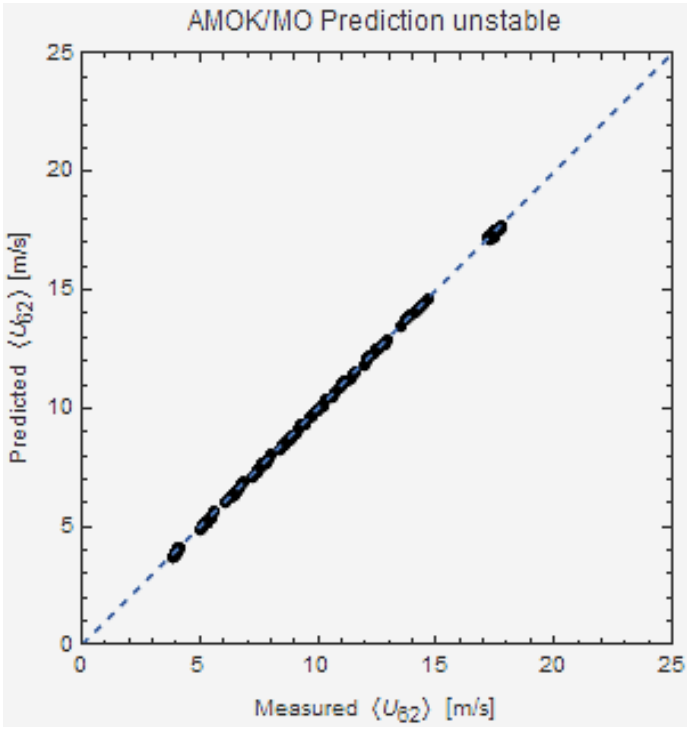

Figure 1: Predicted vs. measured values of bin averaged U_{62}. Horns Reef; unstable cases.

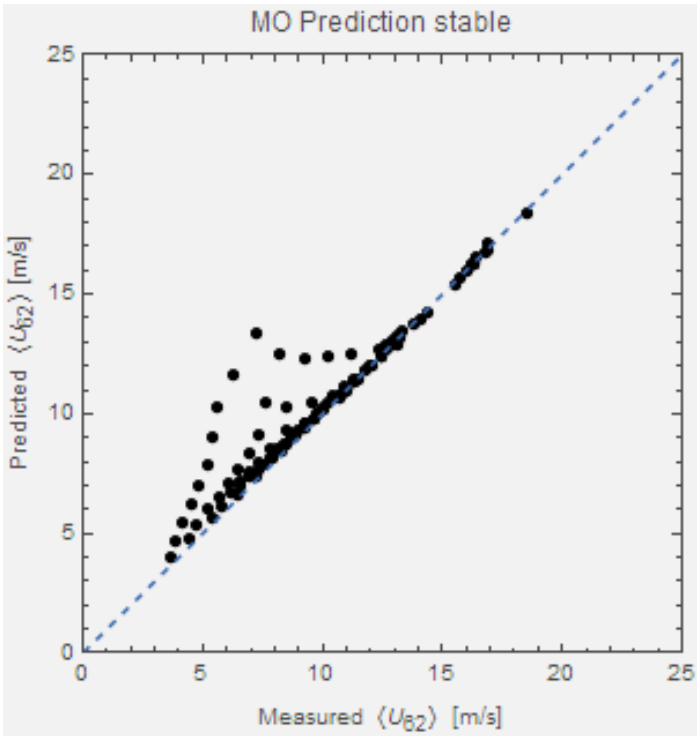

Figure 2: Predicted vs. measured values of bin averaged U_{62}. Horns Reef; stable cases.

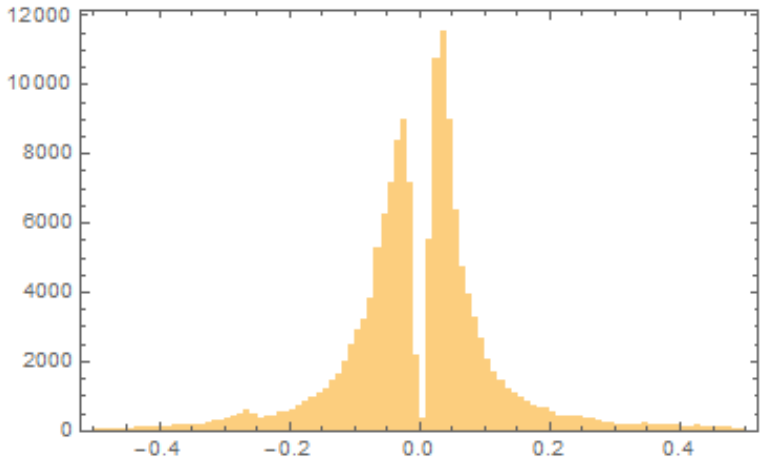

Figure 3: $1/\mu$ histogram obtained from the M2 met mast located at Horns Reef. The dip is caused by dropping wind speeds below 3m/s.

The ambition here is to fit a simple model to data that can be used to extend velocity profiles beyond the surface layer. The theory has been based on the complex mean velocity *W*. This quantity incorporates veer, which, however, is not very important for wind energy applications. We will therefore concentrate on the absolute value $|W|$. It should be noted, that the mean wind speed obtained from a cup anemometer is equal to $\overline{U} = \overline{\sqrt{u^2 + v^2}}$, while $|W| = \sqrt{\overline{u}^2 + \overline{v}^2}$; hence

$$|W| \approx \overline{U}(1 - \frac{1}{2}\mathrm{Ti}^2) \approx \overline{U} \tag{2.5.12}$$

when the turbulence intensity Ti is not too large. The preceding discussions led to the conclusion, that general profiles depend on *z/L*, z_0/L and μ. The latter appears as $1/\mu$ in the scaled equations, where it represents the scaled Coriolis parameter in the Coriolis forcing term. In the surface layer this should somehow be a very small term, and can be neglected if we neglect the mean pressure gradient at the same time. Above the surface layer the two terms gradually become more and more important. Ironically, they tend more and more to cancel each other the higher we go up, but the other terms in the momentum equations decrease even faster with height. In terms of u_* and θ_* we have

$$\frac{1}{\mu} = \frac{fL}{u_*} = \frac{\kappa f T u_*}{\mathrm{g}\,\theta_*} \tag{2.5.13}$$

This is divergent for strictly neutral conditions, and one could a fear that very large values could occur. However, as the histogram in Fig. 3 shows, $1/\mu$ is generally a quite small number. It therefore should make sense to consider a perturbation expansion in terms of powers of $1/\mu$

$$U(\tilde{z}, \tilde{z}_0, \mu) = \frac{u_*}{\kappa}\left|\widetilde{W}(\tilde{z}, \tilde{z}_0, \mu)\right| =$$
$$U_{\mathrm{MO}}(\tilde{z}, \tilde{z}_0)\left(1 + \frac{1}{\mu} f_1(\tilde{z}, \tilde{z}_0) + \frac{1}{\mu^2} f_2(\tilde{z}, \tilde{z}_0) + \cdots\right) \tag{2.5.14}$$

U_{MO} is the conventional M-O profile, which is kept a factor. Keeping only the first term f_1 and assuming that f_1 does not depend $\tilde{z}_0$, some improvements of Fig. 2 was found using $f_1(\tilde{z}, \tilde{z}_0) = -b\,\tilde{z}^2$ with b ranging between 1 and 2. However, the results were much better when written as

$$U(\tilde{z}, \tilde{z}_0, \mu) = \frac{U_{\mathrm{MO}}(\tilde{z}, \tilde{z}_0)}{\sqrt{1 + b\,\tilde{z}^2/\mu}} \tag{2.5.15}$$

This gives the same as the first attempt for small $b\,\tilde{z}^2/\mu$, but behaves much better for large $b\,\tilde{z}^2/\mu$ where U_{MO} is dominated by the linear ψ_{m}, so that U approaches a constant value instead of doing crazy things. Fig. 4 shows results for b=3.6. The improvement compared to Fig.2 is quite obvious.

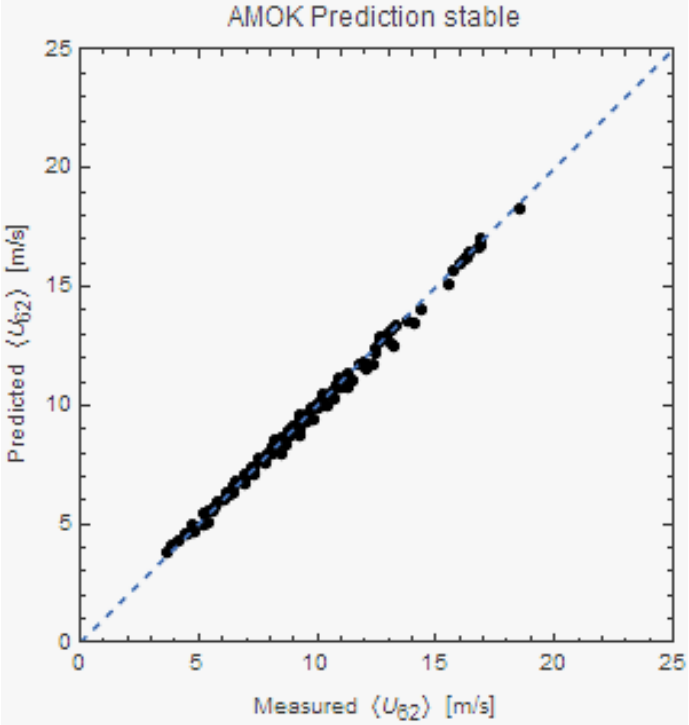

Figure 4: Same as Figure 2 except using correction (2.5.15).

Fig 5. and Fig. 6 show results from the meteorological masts 2 and 3, respectively, located next to the Nysted wind farm [26]. Here water temperature, air temperature at 10m and wind speed at 10m were used to predict the wind speed at 69m. Data from mast 2 are used for westerly wind directions, while data from mast 3 are used for easterly wind directions. The plots are very similar to those from Horns Reef. Conventional M-O theory works perfectly for the unstable cases, while the same pattern of deviations is seen in the stable case. The AMOK prediction is based on value b=3.6 obtained from the Horns Reef data without additional fitting, but even so the AMOK predictions are clearly better than the M-O results.

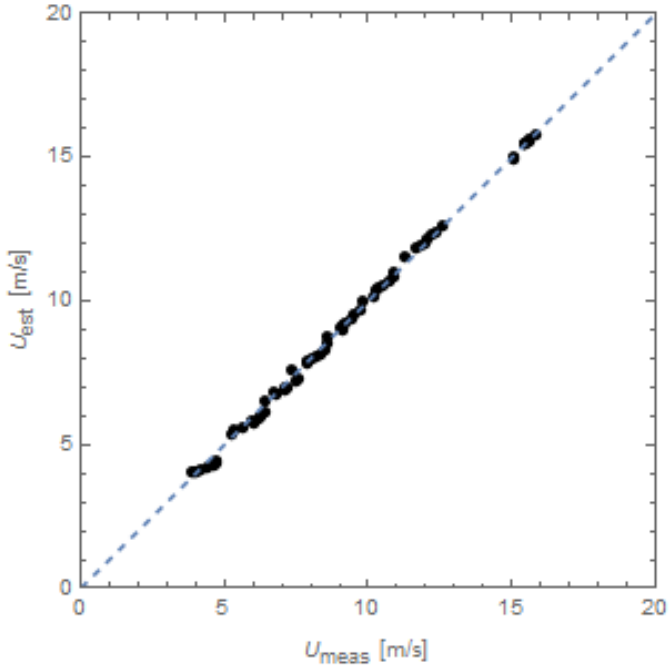

Figure 5: Predicted vs. measured Nysted values of bin averaged U_{69}. Unstable cases.

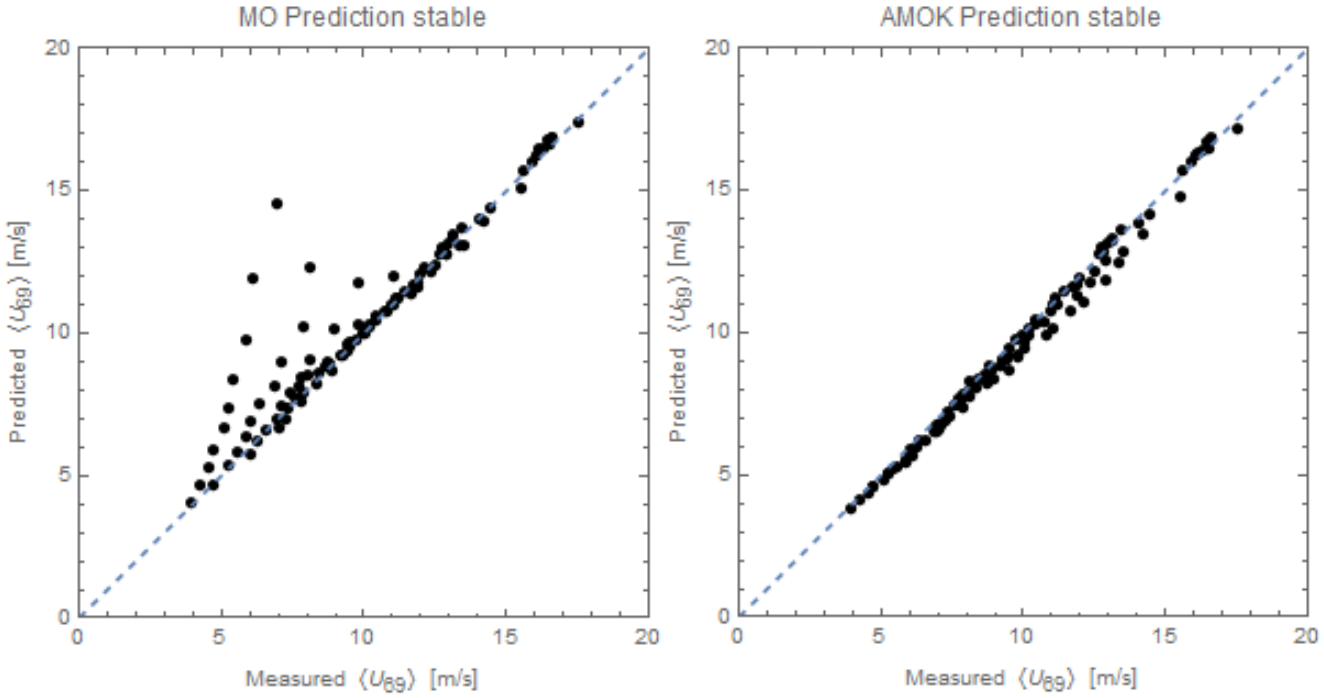

Figure 6: Same as Fig. 2 and Fig.4 but for Nysted U_{69} data.

Fig. 7 and Fig. 8 show results from the meteorological mast at the Læsø offshore site [27], which has a configuration identical to the Horns Reef M2 mast. The exact same pattern as for the Nysted and Horns Reef sites is recognized, which shows that the data analysis yields robust, reproducible results and further that the proposed correction actually works.

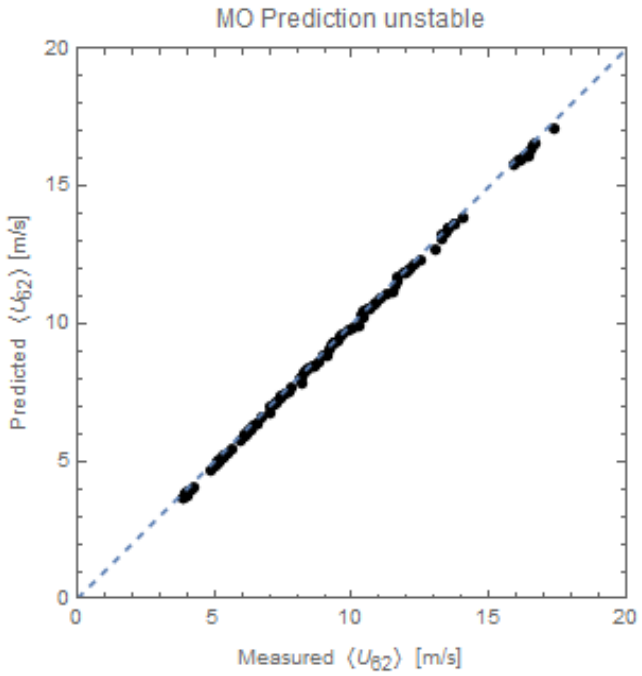

Figure 7: Predicted vs. measured values of bin averaged U_{62}. Læsø; unstable cases.

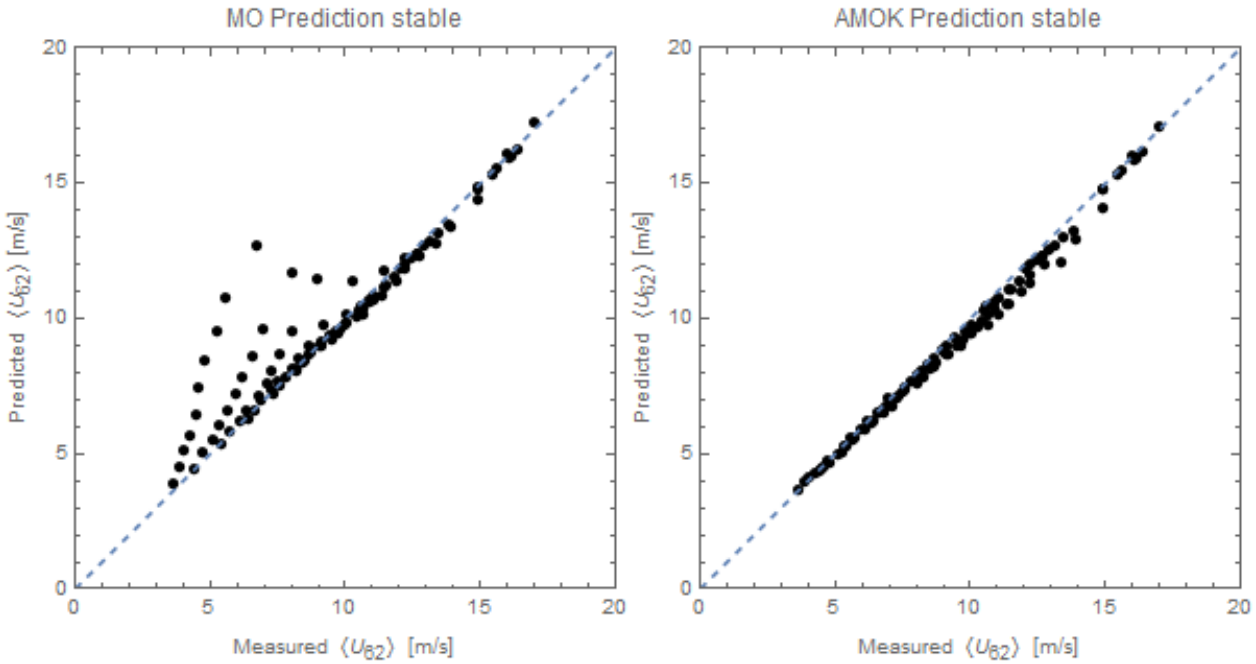

Figure 8: Same as Fig. 2 and Fig.4 but for Læsø U_{62} data.

Fig. 9 shows Weibull distribution fits to the predicted wind speeds at 30m, 45m and 62m for Horns Reef M2 mast. Note, that *separate distributions* were fitted to stable and unstable data. The predictions from conventional M-O theory are also shown. The model performs well and is obviously an improvement over conventional M-O theory. Fig. 10 shows similar results for Nysted using correction parameter b=3.6.

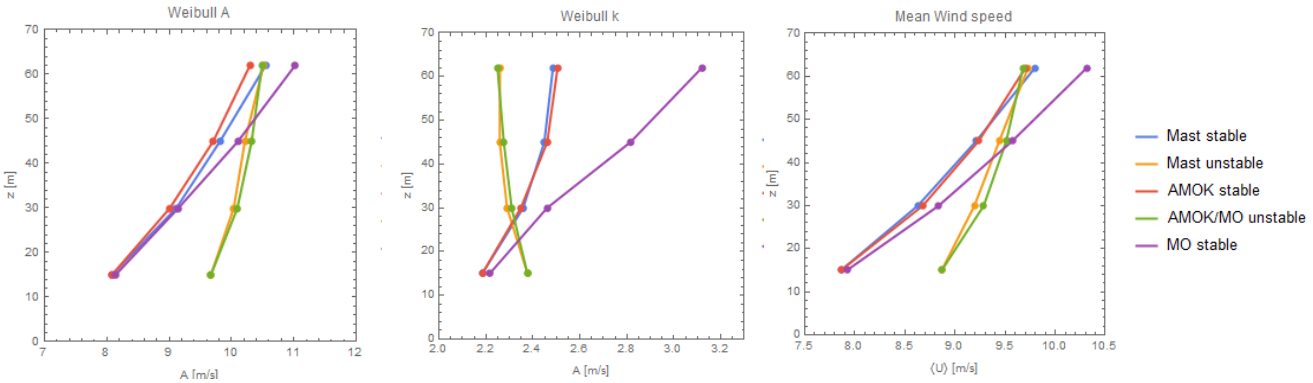

Figure 9: Fitted Weibull distribution parameters for Horns Reef M2. From left to right to left: A, k and mean value.

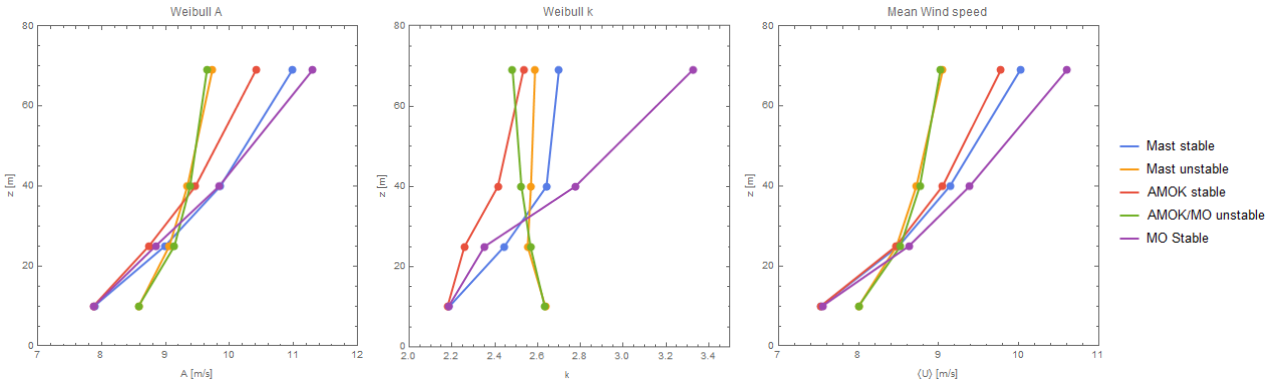

Figure 10: Fitted Weibull distribution parameters for Nysted M2/M3. From left to right to left: A, k and mean value.

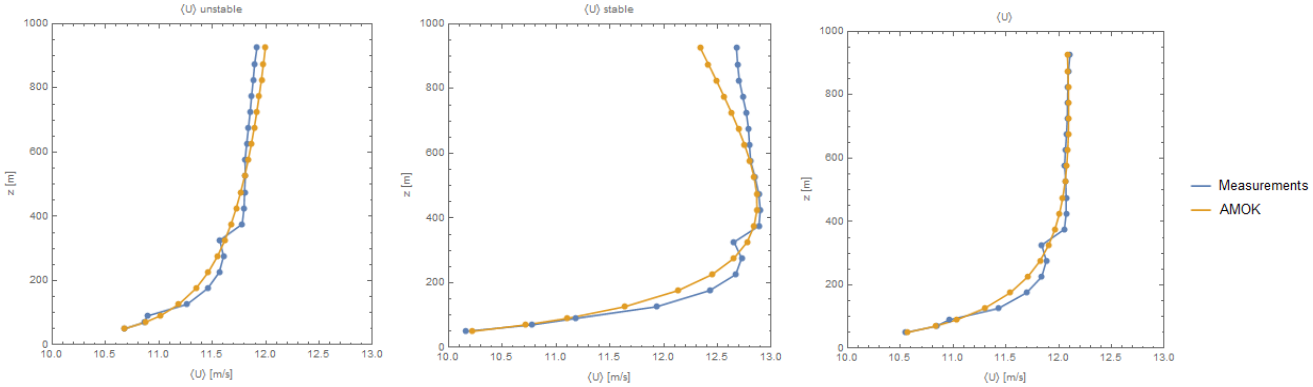

Figure 11: Predicted and measured wind profiles for Fino 3. Left to right: unstable, stable and both.

Fig. 11 shows measured and predicted mean wind speed profiles from the Fino 3 platform. Predictions were made from wind speeds and air temperature measurements at 50m and water temperature. Wind speed measurements were made with a Doppler Lidar and extend up to almost 1km. Again the M-O predictions are almost perfect for unstable conditions. The dip in the measured profiles around z=300m is caused by a reflection in the optical fiber. The stable conditions are also fairly well predicted although with a tendency to under-predict at very large heights. Combining all data we end up with a predicted profile that fits data quite nicely. The fact that it is spot on from 500m and up is of course just a matter of pure luck, but it indicates, that the model is behaving reasonable even for heights elevated high above the surface layer. This is very satisfactory for a relatively simple model, which only requires a single additional adjustable parameter.

2.6 Stability quantification and classification

The main results of this chapter are summarized in equations (2.3.13) and (2.3.14). The complex profile functions $\psi_{\mathrm{m}}(\tilde{z},\mu)$ and $\psi_{\mathrm{h}}(\tilde{z},\mu)$ are universal with an unstable branch for $\tilde{z}<0$ and a stable branch for $\tilde{z}>0$. The profile can be calculated from u_*, θ_*, T, g and f. Both L and μ can be derived from these. For a given site g and f are just constants, and the absolute surface temperature merely serves as an offset on the temperature that does not affect temperature differences. T appears in the definition of L, but it does not matter much if it varies a little. Thus we are left with just two parameters: u_* and θ_*, but other parameter pairs are of course possible.
Above we used u_* and θ_* because they are almost *statistically independent*. A wind climatology can be defined as the joint probability distribution u_* and θ_*, (or whatever variable pair we choose). In section 7 we shall use the wind speed at hub height and 1/L. The use of 1/L was as a stability measure was suggested by Gryning et al. [28], who define stability classes according to the following scheme:

Table 1 Definition of stability classes.

Stability Class iC	Description	Condition
-4	extremely unstable	-50m$< L <$ 0m
-3	very unstable	-100m$< L <$ -50m
-2	unstable	-200m$< L <$-100m
-1	near unstable/neutral	-500m$< L <$-200m
0	neutral	500m$< \|L\|$
1	near stable/neutral	200m$< L <$ 500m
2	stable	50m$< L <$ 200m
3	very stable	10m$< L <$ 50m
4	extremely stable	0m$< L <$ 50m

We adopt this classification here and have supplemented it with two more classes: extremely unstable (iC=-4) and extremely stable (iC=4). For a typical offshore site about 15% of all cases are found in the extreme classes.

3 Kinematic turbulence model for non-neutral stability conditions

The DWM model is, as previously mentioned, an efficient, reliable and popular medium-fidelity approach for dealing with *un-steady* wake affected flow fields. For WF *production* estimation *steady* WF flow field modeling as provided by e.g. full CFD RANS models or fast linearized CFD RANS models [35] may suffice. However, for *load estimation* of WT's exposed to wake affected inflow, an un-steady WF flow field description is inevitable. Insisting on models reflecting the *basic physics* of the problem we are thus left with either a CFD LES actuator disc or line a type of approach or, alternatively, the DWM type of approach. CFD LES models must – like the DWM model – be linked to an aeroelastic model of each and every WT in a WF to provide a complete picture of the load conditions inside a WF for all design load cases. This is extremely CPU demanding and considered unrealistic even with the capacity of nowadays extremely powerful state-of-the-ark super computer clusters. This challenge is further enhanced when including ABL stability as an additional design load case dimension and/or considering optimization of WF layout. CFD LES is, however, very useful in the development and validation of more simplistic model approaches.

Being a medium-fidelity model the DWM model offers significant savings in CPU-demands, and it thereby facilitates detailed WF production/load design simulations to be conducted as will be shown in section 5. The core of the DWM model is a *split of scales* in the wake affected flow field, with large turbulence scales being responsible for stochastic *wake meandering* [6],[7],[29],[30],[31],[32],[33],[34] and small scales being responsible for wake *attenuation* and *expansion* in the meandering frame of reference as caused by turbulent mixing. Thus, essentially the DWM model assumes that the transport of wakes in the ABL can be modeled by considering the wakes to act as passive tracers driven by a combination of large-scale turbulence structures and a mean downstream advection velocity, adopting the Taylor hypotheses[16].

The large scale turbulence structures used to describe wake dynamics in the DWM model is traditionally provided by a fast Navier-Stokes (NS) consistent kinematic turbulence model [9],[10] which, however, assumes neutral ABL stability and thereby neglect the effects of buoyancy on turbulence production and thus turbulence characteristics. As ABL stability mainly affects the large scale turbulence structures, the effect of buoyancy on wake meandering can, however, not be neglected. The research questions to be dealt with in this section are thus how to include the effect of buoyancy on wake dynamics under non-neutral ABL conditions and in addition to investigate the effect of ABL stability on the small turbulent scales, which in the DWM approach is responsible for wake attenuation and expansion in the meandering frame of reference. The research strategy is initially to adopt the following fundamental conjecture [3]:

In a wake context, ABL stability affects primary wake meandering driven by large (lateral and vertical) turbulent scales, whereas wake expansion in the meandering frame of reference is a second order effect only.

With this conjecture as starting point, we will first investigate the possibilities for tweaking the classic Mann tensor model [9] to non-neutral stability conditions by suitable adjustment of the 3 independent input parameters of this model. Secondly, we will introduce a generalization of this spectral tensor, which consistently include buoyancy effects at the cost of additional two input parameters. The last part of this section deals with validation of the above stated conjecture. This part includes validation against detailed full-scale LiDAR and sonic measurements as well as detailed fundamental investigations based on high-fidelity CFD LES computations.

3.1 Classic Mann spectral model

To facilitate inclusion of ABL stability conditions in the DWM wake meandering modeling, we will initially fit the classic Mann spectral tensor model to stable and unstable atmospheric conditions, respectively, although it was developed for *neutral* stratification only. For this purpose we will use the stability classes defined in Table 1.

To adapt the spectral tensor to different atmospheric stability conditions, we need fast response anemometers as e.g. sonic anemometers. As a demonstration example, we will adjust the Mann spectral tensor to the spectra computed from sonic observations performed at 10m, 20m, 40m, 60m, 80m, 100m and 160m above ground level (a.g.l.) at a tall meteorological mast located at Høvsøre, Denmark. To ensure uniform inflow conditions we will limit the investigation to an upwind sector, where the upstream fetch is very flat and homogenous.

Data from the 20 Hz-sonics from 10m and up to 160m were simultaneously available for nearly one year. The time series were analysed based on 10-minute periods and subsequently classified in the above mentioned stability classes. Two different adaptations approaches of the spectral tensor are performed – one based on the full Reynolds stress tensor, and another based on a reduced Reynolds stress tensor.

For the *full Reynolds stress tensor* case, the analysis comprised all non-zero components of the Reynolds stress tensor. Auto-spectra of the *u*, *v* and *w* wind speed turbulence components as well as the *uw* cross-spectrum were normalized with the variance of the longitudinal turbulence component, σ_u^2, and subsequently averaged over all 10-minute runs within each stability interval and at each height. Before averaging the spectra's independent variable was changed from frequency to normalized frequency $n = fz/U$, where f is the frequency in Hz, and U is the mean wind speed at height z. The Mann spectral tensor was then fitted to the spectra by adjusting the three parameters of the model: 1) A length scale describing the size of the energy-containing eddies, L_M; 2) A measure of the energy dissipation, $\alpha\varepsilon^{2/3}$, where α is the spectral Kolmogorov constant, and 3) An eddy lifetime parameter describing the degree of anisotropy, Γ. The fitting was performed as described in [9].

The result of the fit of the Mann spectral model to the average spectra observed at 40m a.g.l. at Høvsøre is shown in Fig. 12.

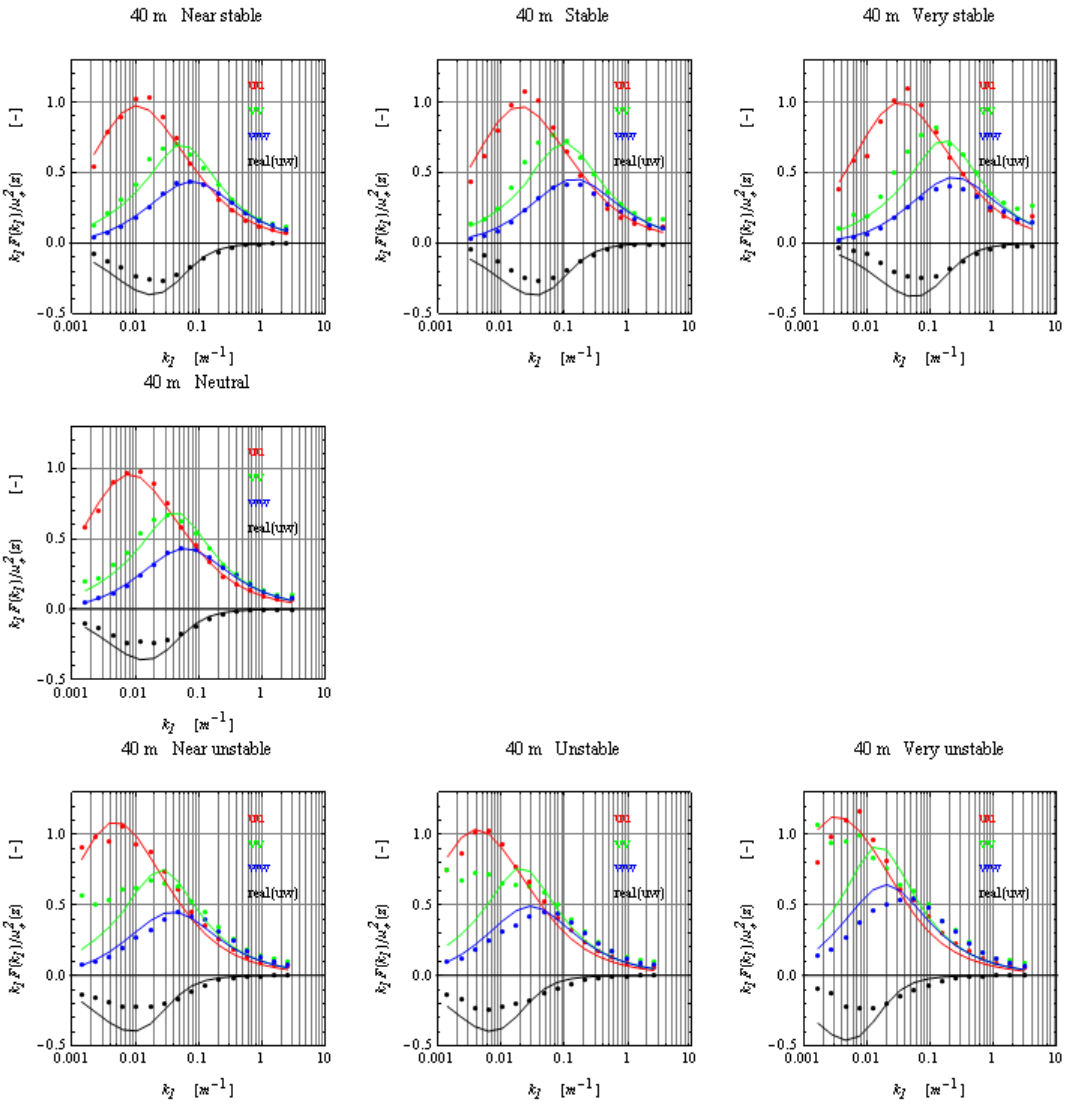

Figure 12: Normalized spectra of the u (red), v (green), w (blue) wind speed components and the real part of the normalized uw-cross spectrum (black) from the sonics at 40m for different stability conditions at Høvsøre, Denmark. The observations are the dots and the Mann spectral model fits are the solid lines.

The Mann spectral tensor adapts well to the observations for stable and neutral stratifications, but underestimates significantly the *v*-spectra in the low frequency regime for unstable and very unstable stratifications. It slightly under-estimates the *uw* co-variance, but fits well the *u*- and *w*-spectra for nearly all stability categories, despite the fact that the model was developed for neutral stratification. The underestimation of the *v*-spectra in the low frequency regime is particularly unfortunate, because the *v* spectrum, in general being more energetic than the *w* spectrum, plays the dominant role in the meandering process in the DWM model.

A heuristic explanation of the lack of match of the *v* spectra is the following: The Mann spectral tensor is basically developed for neutral conditions and consequently not necessary able to adjust perfectly to all stability conditions. As only the *u* and *w* turbulence components are correlated at an arbitrary point in space (e.g. the present observation point), the *v* spectrum is sacrificed in the fitting procedure, because it is significantly less energetic than the *u* spectrum, the *w* spectrum and the *uw* cross-spectrum taken together.

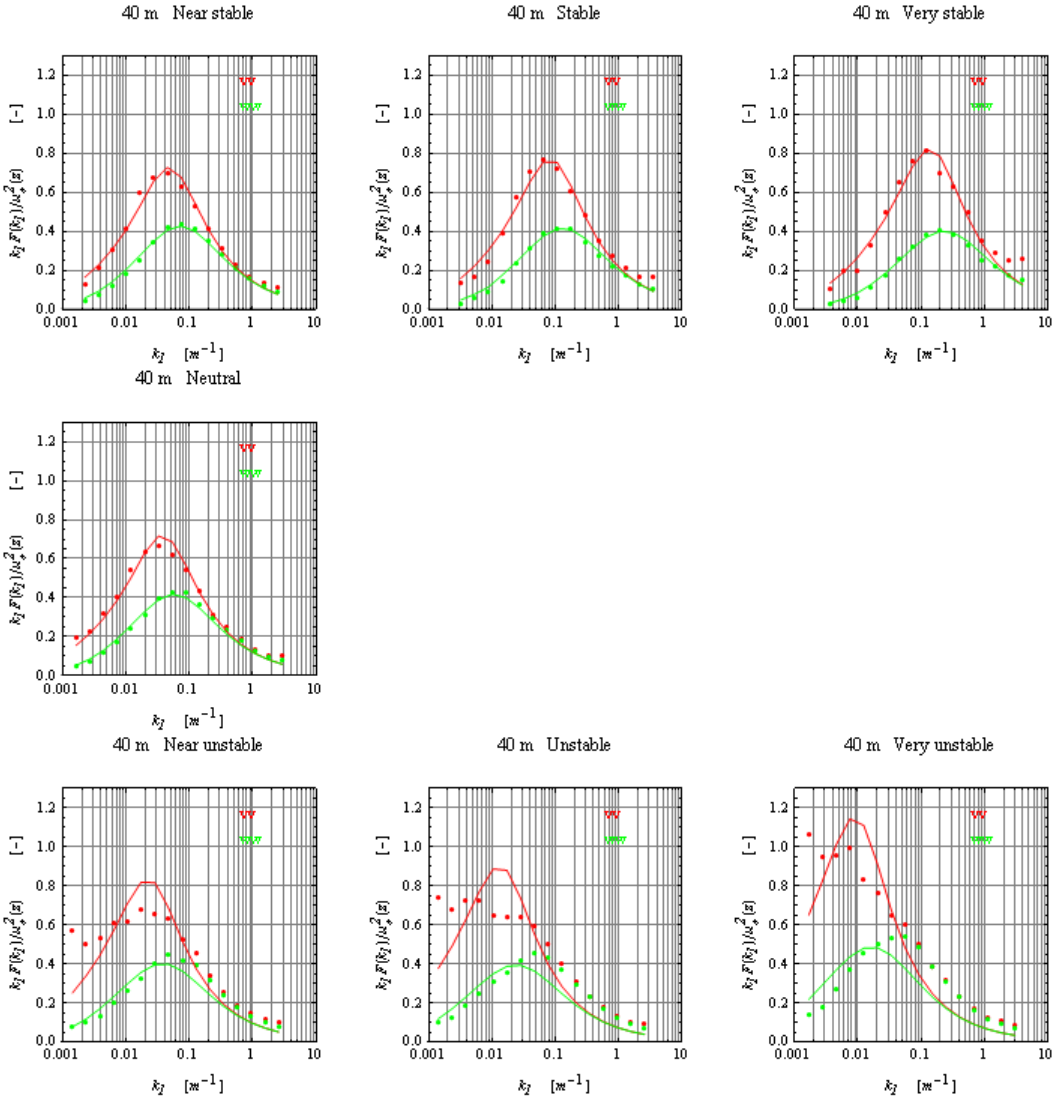

Figure 13: Normalized spectra of the v (red) and w (green) wind speed components from the sonics at 40m for different stability conditions at Høvsøre, Denmark. The observations are the dots and the Mann spectral model fits are the solid lines. The stability goes counter clock-wise from very stable in the top right to very unstable in the bottom right.

The DWM model does not depend on the *u* turbulence component. For the present purpose the above described inexpediency can therefore be mitigated to a certain degree by adapting the Mann spectral

tensor to a reduced Reynolds stress tensor, where only the *v* and *w* turbulence components are taken into account. Following the procedure described for the full Reynolds stress tensor, the Mann spectral tensor is then fitted to the normalized *u* and *v* auto-spectra. Fig. 13 illustrates the result of this fit of the Mann spectral model to the average spectra observed at 40m a.g.l. at Høvsøre.

The Mann model adapts both quantitatively and qualitatively well to the observations for stable and neutral stratifications. For unstable stratifications qualitative deviations can be observed, but the energy in the low frequency spectral regime, which is of primary importance in relation to wake meandering, is much better represented here than in the full Reynolds stress tensor fit (cf. Fig. 12).

With reference to the reduced Reynolds stress tensor fitting Fig. 14 shows the variation with height *z* of the three adjusted input parameters to the Mann spectral tensor for the different stability conditions. The length-scale profile, illustrated in the middle panel, shows that under unstable atmospheric conditions, the size of the turbulent eddies is larger compared to neutral and stable conditions as expected. The plot to the right shows that the anisotropy is strongest closest to the ground and that it only changes appreciable with stability in this region.

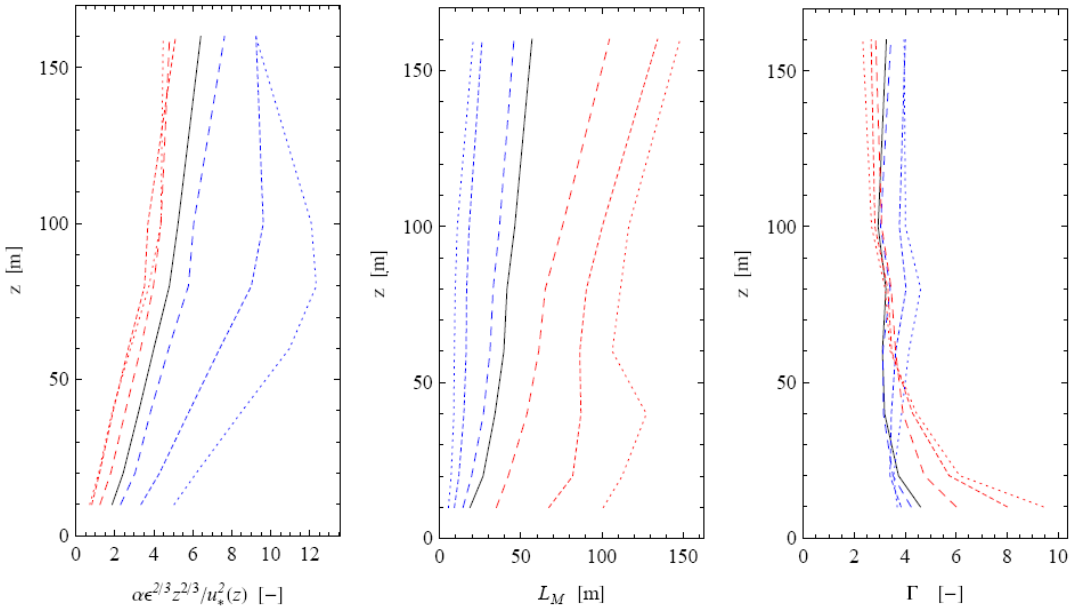

Figure 14: Adjusted parameters of the Mann spectral model to the normalized spectra from the sonic observations at different stability conditions and heights at Høvsøre, Denmark. Neutral stratification is shown in black, stable in blue and unstable in red. The shorter dashed curves are the more extreme stratification. The normalized energy dissipation is shown in the left panel, the length-scale in the middle panel and the degree of anisotropy in the right panel.

3.2 Generalized spectral tensor

Alternatively to tweaking the classic Mann spectral tensor to operate outside the regime it is designed for, a more consistent approach is to use a newly developed generalized spectral tensor, which includes buoyancy effects, for the description of the WF turbulence field. This is in particular true for the description wake meander driving large scale part of this turbulence field. First we will give a summary description of the generalized spectral tensor; then we will describe a rational approach for estimation of

its 5 model parameters; and finally we will briefly focus on validation of its basic features using full-scale data from the HATS field experiment carried out near Kettleman City, California [41].

3.2.1 Buoyancy dependent spectral tensor formulation

The generalized spectral tensor, $\Phi_{ij}(\boldsymbol{k})$, resulting from the governing Rapid Distortion Theory (RDT) equations including buoyancy effects [36],[37],[38], contains two extra parameters, in addition to those of the classicMann spectral tensor model, where $\boldsymbol{k}(t) = (k_1, k_2, k_{30}\text{-}k_1(\mathrm{d}U/\mathrm{d}z)t)$ is a three dimensional wave vector, and t is time. These parameters are: 1) a stability parameter (the Richardson number); and 2) the rate of destruction of temperature variance.

The RDT equations, which include the linearized momentum and the temperature equation in Fourier space, evaluates in time under the influence of a *constant* wind shear ($\mathrm{d}U/\mathrm{d}z$) and a *constant* gradient of potential temperature ($\mathrm{d}\theta/\mathrm{d}z$) from an initial isotropic state of turbulence. In isotropic turbulence, the velocity-spectrum tensor is

$$\Phi_{ij}(\boldsymbol{k}_0) = \frac{E(k)}{4\pi k^2}\left(\delta_{ij} - \frac{k_i k_j}{k^2}\right), \tag{3.2.1}$$

where $\boldsymbol{k}_0 = \boldsymbol{k}(0)$ and k is the length of the wave vector $\boldsymbol{k}$. The energy spectrum, $E(k)$, is given by [39] as

$$E(k) = \alpha\varepsilon^{2/3}L^{5/3}\frac{(kL)^4}{(1+(kL)^2)^{17/6}}, \tag{3.2.2}$$

where $\alpha \approx 1.7$ is the Kolmogorov constant, ε is the rate of viscous dissipation of specific turbulent kinetic energy (TKE), and L is a turbulence length scale.

In order to make the model stationary, the time dependency in the model is removed by incorporating the general concept of an eddy lifetime, $\tau(k)$. The parameterization of $\tau(k)$ is adapted from the classic Mann spectral tensor model. In the inertial sub-range, the lifetime of eddies are proportional to $k^{-2/3}$, and the assumption in the Mann model, for scales larger than the inertial sub-range, is that the eddy lifetime is proportional to k^{-1} divided by their characteristic velocity given by

$$\left(\int_k^\infty E(p)dp\right)^{1/2}, \tag{3.2.3}$$

thus resulting in eddy lifetimes proportional to $k^{-2/3}$ for $k \to \infty$ and to k^{-1} for $k \to 0$.

For the temperature variable, the isotropic three-dimensional spectrum is given as

$$\Phi_{\theta\theta}(\boldsymbol{k}_0) = \frac{S(k)}{4\pi k^2}, \tag{3.2.4}$$

where $S(k)$ is the potential temperature energy spectrum containing the form of the inertial sub-range [16] as

$$S(k) = \beta \varepsilon^{-1/3} \varepsilon_\theta L^{5/3} \frac{(kL)^2}{(1+(kL)^2)^{11/6}}, \tag{3.2.5}$$

Here ε_θ is the dissipation rate for half the temperature variance, and $\beta = 0.8$ is a universal constant [40]. Based on the above formulations of isotropic velocity and temperature spectra combined with the Mann eddy lifetime formulation, RTD results in an anisotropic spectral tensor including buoyancy of the form $\Phi_{ij}(\boldsymbol{k}) = \Phi_{ij}(\boldsymbol{k}; \alpha\varepsilon^{2/3}, L, \Gamma, Ri, \eta_\theta)$, where Ri denotes the Richardson number [16] resulting from the temperature equation, and

$$\eta_\theta \equiv \frac{\varepsilon_\theta}{\varepsilon}\left[\frac{g}{\theta}\left(\frac{dU}{dz}\right)^{-1}\right]^2, \tag{3.2.6}$$

where the potential temperature, θ, as well as dU/dz and dθ/dz are representative of the height of interest.

To summarize, the five adjustable model parameters, which are attainable from *single-point* measurements are: 1) $\varepsilon^{2/3}$; 2) L, which represents a representative size of the energy containing eddies; 3) Γ, which is a measure of the degree of turbulence isotropy; the Richardson number Ri [16]; and 5) η_θ as defined above. Note, that for $Ri = 0$ and $\eta_\theta = 0$, the generalized spectral tensor degenerates to the classic Mann spectral tensor.

Simulation of consistent 3D synthetic turbulence fields requires knowledge of cross-spectra between turbulence components. The spectral tensor model provides the cross-spectrum, χ_{ij}, between any two velocity components, or between any velocity component and temperature, as

$$\begin{aligned}\chi_{ij}&\left(k_1, \Delta y, \Delta y; \alpha\varepsilon^{2/3}, L, \Gamma, Ri, \eta_\theta\right) \\ &\equiv \alpha\varepsilon^{2/3} L^{5/3} \int \Phi_{ij}\left(\boldsymbol{k}; \alpha\varepsilon^{2/3}, L, \Gamma, Ri, \eta_\theta\right) e^{\mathrm{i}(k_2\Delta y + k_3 \Delta z)} dk_2 dk_3 ,\end{aligned} \tag{3.2.7}$$

where Δy and Δz are transverse and vertical separations, respectively. Thus, based on such cross-spectra, the requested turbulence field can be simulated using the approach described in [10], however, presently only implemented for the velocity components.

3.2.2 Fit of model parameters

An automated fit procedure of the 5 model parameters is devised as based on a chi-squared (χ^2) fitting technique similar to the one applied for the classic Mann spectral tensor [9]. The basic idea of the χ^2 fit is to minimize the sum of the squared differences between the theoretical and the estimated spectra and co-spectra. Compared to fitting of model parameters of the classic spectral tensor the χ^2 function, corresponding to the generalized spectral tensor, is expanded by including the θ auto-spectrum as well as the $u\theta$ and $w\theta$ co-spectra and takes the form

$$\begin{aligned}\chi^2(\Gamma, L, \alpha\epsilon^{2/3}, \mathrm{Ri}, \eta_\theta) &= \frac{1}{\mid F_{uw}^{max} \mid}\sum_{n=1}^{N}(F_{uw,t}(k_n) - F_{uw}(k_n))^2 \\ &+ \sum_{l=1}^{4}\frac{1}{\mid F_{l}^{max} \mid}\sum_{n=1}^{N}(F_{l,t}(k_n) - F_{l}(k_n))^2 \\ &+ \sum_{m}^{(1,3)}\frac{1}{\mid F_{m4}^{max} \mid}\sum_{n=1}^{N}(F_{m4,t}(k_n) - F_{m4}(k_n))^2\end{aligned} \tag{3.2.8}$$

where N is the number of wave numbers in the estimated spectra, subscript t corresponds to the model spectra and co-spectra, and $F(*)$ is a spectrum with subscripts referring to type of spectrum – where not explicitly indicated as velocity components u, v, w, component 1 refers to u, component 3 refers to w and component 4 refers to θ normalized [12]. For a given spectrum F^{max} is the corresponding maximum value in the measured spectrum.

In the fitting routine the χ^2 function is called through an interpolation function giving the requested model spectral values as based on a pre-computed look-up table with 4 dimensions representing the parameter set (Γ, Ri, η_θ, kL). The computation of the look-up table is CPU-demanding, and it was consequently carried out on the DTU's super computer facility Gorm for the following parameter ranges: $\Gamma \in [0,5]$; $Ri \in [-0.4,0.2]$; $\eta_\theta \in [0,0.35]$; and $kL \in [0.001,1000]$. The ranges of Ri and η_θ was defined based on inspiration gained from empirical M-O relations [16]. It should be stressed, that these relations are not explicitly incorporated in the model – the sole purpose of using them in the present context is to get an idea of what ranges of these two parameters should be expected.

The fitting routine is initialized by evaluating the χ^2 function (3.2.8) with parameter values of $\alpha\varepsilon^{2/3}$, L and Γ obtained from fitting the classic Mann spectral tensor to respectively the observed velocity auto-spectra and the uw co-spectrum as well as with values of the two additional parameters η_θ and Ri estimated using empirical MO-relations.

An alternative simplistic approach, based on observed fluxes, to drive the buoyant spectral tensor-model is derived in Appendix A.

3.2.3 Model validation

This section deal with a *direct* validation of the generalized spectral tensor against full-scale measurements – further details can be found in [12]. In section 5 we will present a validation of the integrated DWM/HAWC2 platform against full-scale load measurements from the Lillgrunden offshore WF, which may be considered an *indirect* validation of the spectral tensor performance for our particular purpose.

The generalized spectral tensor model is here validated using full-scale data from the HATS field experiment carried out near Kettleman City, California [41]. A number of different setup configurations were explored in the HATS experiment, where basically two horizontal arrays of sonic anemometers, each measuring temperature and three-dimensional wind velocity, were placed at different heights above the ground. The experimental setup is illustrated in Fig. 15, with the horizontal *s-array*, consisting of five sonic anemometers, placed at height z_s above the ground, and the nine sonics in the *d-array* mounted parallel to the s-array at height z_d above ground level. The sonics in the s- and d-arrays were horizontally separated by S_s and S_d, respectively.

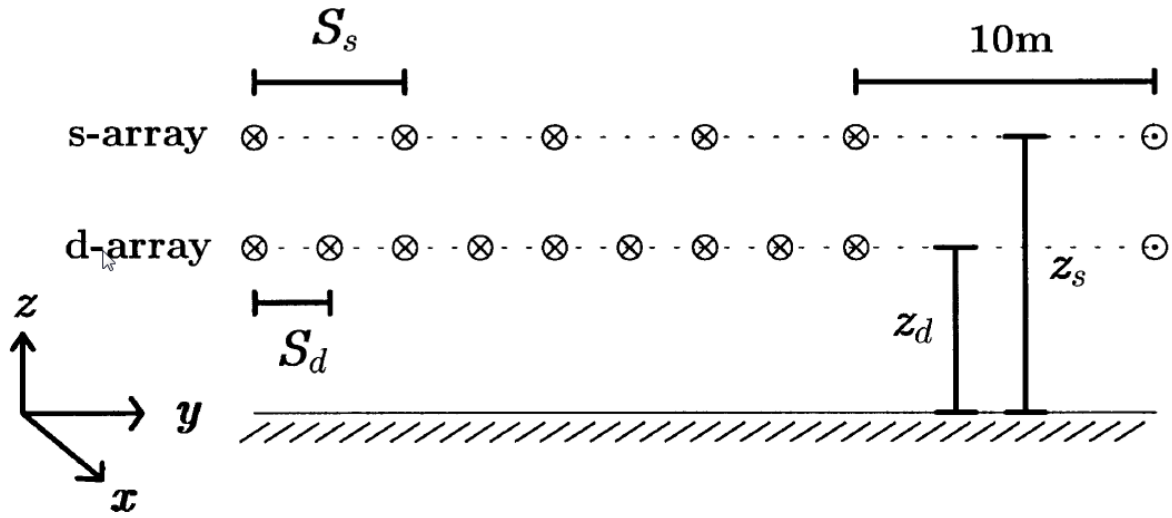

Figure 15: The HATS experimental setup. Sonic anemometers is mounted vertically in the single and double array located respectively at (z_s; z_d) above the ground. Source: Horst et al. (2004).

Both one-point and two-point spectral behavior has been investigated. We estimate velocity auto-spectra and the co-spectrum of *u* and *w* from the measured time-series as

$$F_{ij}(f,z) \equiv \langle \hat{u}_i(f)\hat{u}_j^*(f)\rangle \tag{3.2.9}$$

and the temperature spectrum and the component-wise kinematic heat fluxes, respectively, as

$$\begin{aligned} F_\theta(f,z) &\equiv \langle \hat{\theta}(f)\hat{\theta}^*(f)\rangle, \\ F_{i\theta}(f,z) &\equiv \langle \hat{u}_i(f)\hat{\theta}^*(f)\rangle, \end{aligned} \tag{3.2.10}$$

where f = 20 Hz is the frequency, and $\hat{u}_i(f)$ and $\hat{\theta}(f)$ are the complex-valued Fourier transforms of respectively the ith velocity component and the temperature at height z. The atmospheric stability was measured in terms of the ratio z/L_o, with the Monin-Obukhov length L_o defined in equation (2.3.4). Note, that we have added the subscript *"o"* to the Monin-Obukhov length notation in this context in order to distinct this quantity from the turbulence length scale.

One-point spectra

Two validation examples, representing an unstable and a stable ABL stratification, respectively, are shown in Fig. 16 and in Fig. 17. The fitted model parameters appear from **Table 2** below.

Table 2: Spectral tensor parameters determined from χ^2-fits for given stability identifier z/L_o.

	Model Parameters				
z/L_o	$\alpha\epsilon^{2/3}$ (m$^{4/3}$ s^{-2})	L (m)	Γ	Ri	η_θ
0.08	0.09	2.9	3.7	0.035	0.005
-0.08	0.084	3.57	2.86	-0.04	0.01

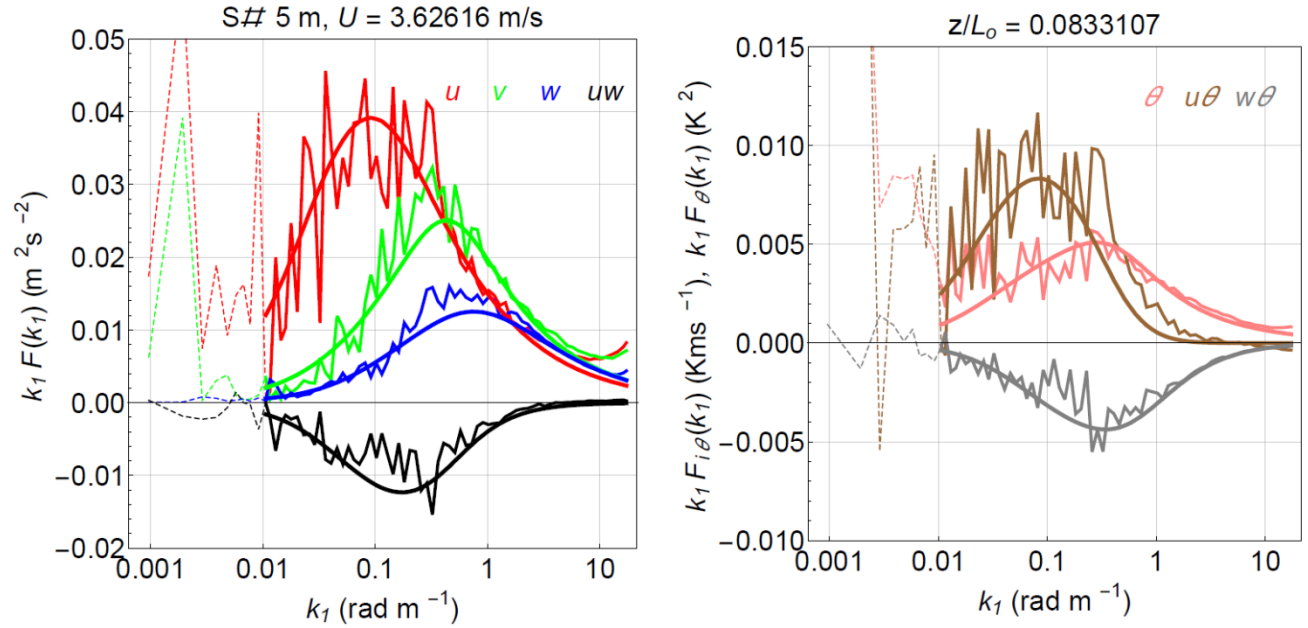

Figure 16: Example of model (co-) spectra fitted with observations at z = 5 m for stable conditions characterized by z/L_o = 0.08. Smooth lines are model predictions and ragged lines are measurements.

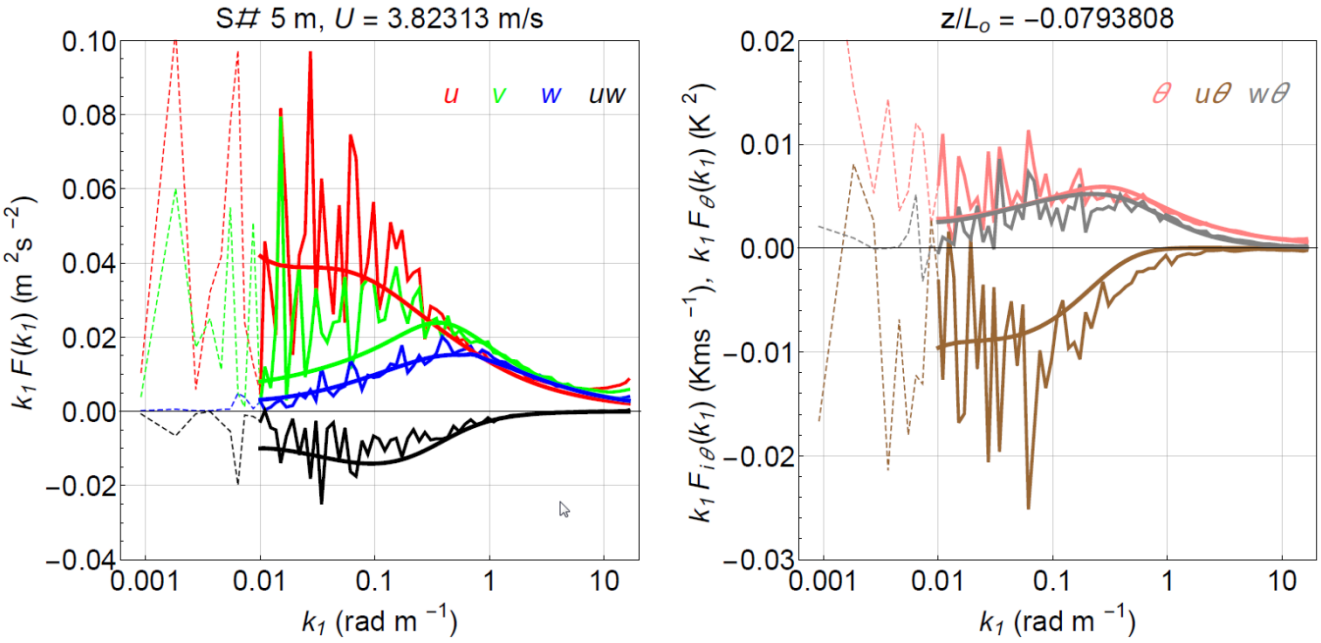

Figure 17: Example of model (co-) spectra fitted with observations at z = 5 m for unstable conditions characterized by z/L_o = -0.08. Smooth lines are model predictions and ragged lines are measurements.

Fig. 16 shows model spectral fits and the corresponding measured spectra for a stable ABL stratification characterized by z/L_o = 0.08. The left hand graph shows velocity spectra as well as the co-spectrum of uw; the right hand graph shows the temperature spectrum as well as the co-spectra of $u\theta$ and $w\theta$. It is observed that the velocity and temperature spectra follow the expected power law in the inertial sub-range, i.e., $F(k_1) \sim k_1^{-5/3}$. This is true both for model spectra and for measured spectra. The uw and $w\theta$ co-spectra follow, as expected, the power law $F(k_1) \sim k_1^{-7/3}$ in the inertial sub-range for both modeled and measured co-spectra. Compared to the $w\theta$ co-spectrum, the observed $u\theta$ co-spectrum decay much faster with wave number, i.e. as $F(k_1) \sim k_1^{-3}$, thus supporting the modeling predictions by Wyngaard and Cot´e [42]

Fig. 17 shows model spectral fits and the corresponding measured spectra for an unstable ABL stratification characterized by z/L_o = -0.08. A significant increase in the energy content of the u-spectrum in the (very) low frequency regime is observed, which in turn causes an increase in the uw and $u\theta$ co-spectra at lower frequencies. This is presumable a meso-scale phenomenon, which is not included in the model framework. We therefore high-pass filtered the data (as shown by dotted lines in Fig. 17) during the spectral fitting, and the five spectral tensor parameters displayer in Table 2 were thereby obtained.

Two-point spectra

Prevailing wind directions close to normal to the plane of sonic arrays are selected for this analysis, and the cross-spectra are further rotated, such that the mean velocity field is (U, 0, 0). The model coherences and cross spectral phases are subsequently calculated. The coherence comparisons are shown in Fig. 18 and in Fig. 19 for vertical and horizontal separations, respectively, for both stable and unstable ABL conditions.

For *vertical* separation, the model spectra are fitted to measurements from the two sonics located in the middle of respectively the s- and d-array to obtain the 5 model parameters. The average of these two sets of parameters are evaluated and subsequently used as inputs to calculate spectral tensor coherences and phases. There was no significant difference in the parameter values obtained from the two single sonics and those obtained from fitting averaged spectra. The *lateral* coherence is calculated between the sonics denoted S#3 and S#4, respectively.

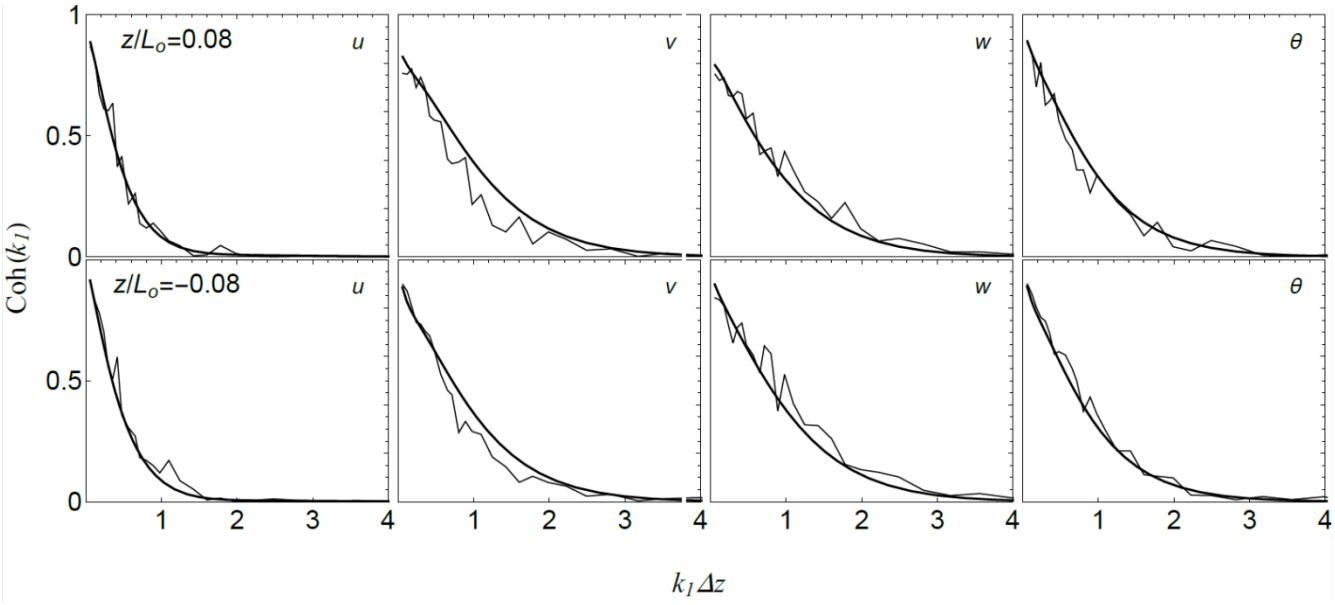

Figure 18: Measured (ragged lines) and model predicted (smooth lines) coherences for stable (z/L_o = 0.08) and unstable (z/L_o = -0.08) stratification for vertical separation Δz = 1 m.

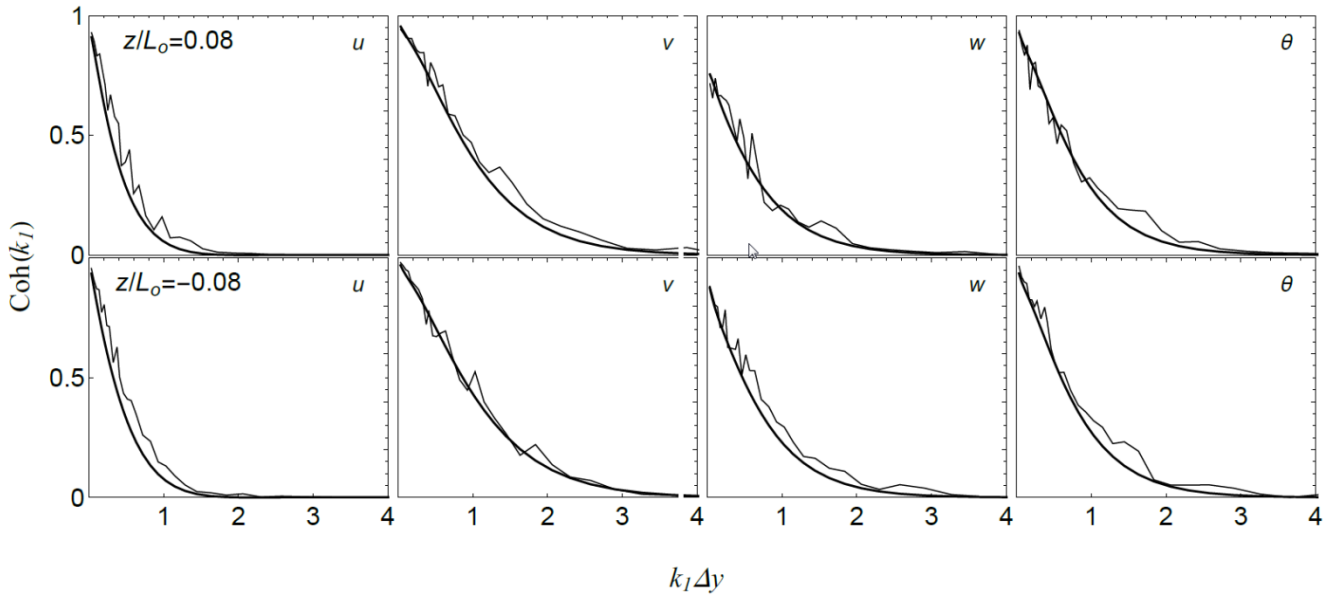

Figure 19: Measured (ragged lines) and model predicted (smooth lines) coherences for stable (z/L_o = 0.08) and unstable (z/L_o = -0.08) stratification for horizontal separation Δy = 0.63 m.

By nature affecting predominantly the low frequency spectral regime, atmospheric stability affects the coherence, which accordingly increases from stable to unstable stratification. ABL stability has the most noticeable effect on the *w*-coherence, while the *u*-coherence is less affected for both vertical and horizontal separations. This was also observed by Chougule et al. [43] (for vertical separation).

Finally, the phases in the modeled cross-spectra are compared with the observed cross spectral phases and shown in Fig. 20 for both stable and unstable ABL stratification and, in both, cases referring to a *vertical* separation of one meter. It can be observed that φ_v (and φ_θ) > φ_u > φ_w (≈ 0), which is consistent with the reportings in Chougule et al. [44]. There is no systematic effect of atmospheric stability on the phases, which is consistent with the reportings in Chougule [11]. Both the model and observed spectral phases for *horizontal* separation were zero.

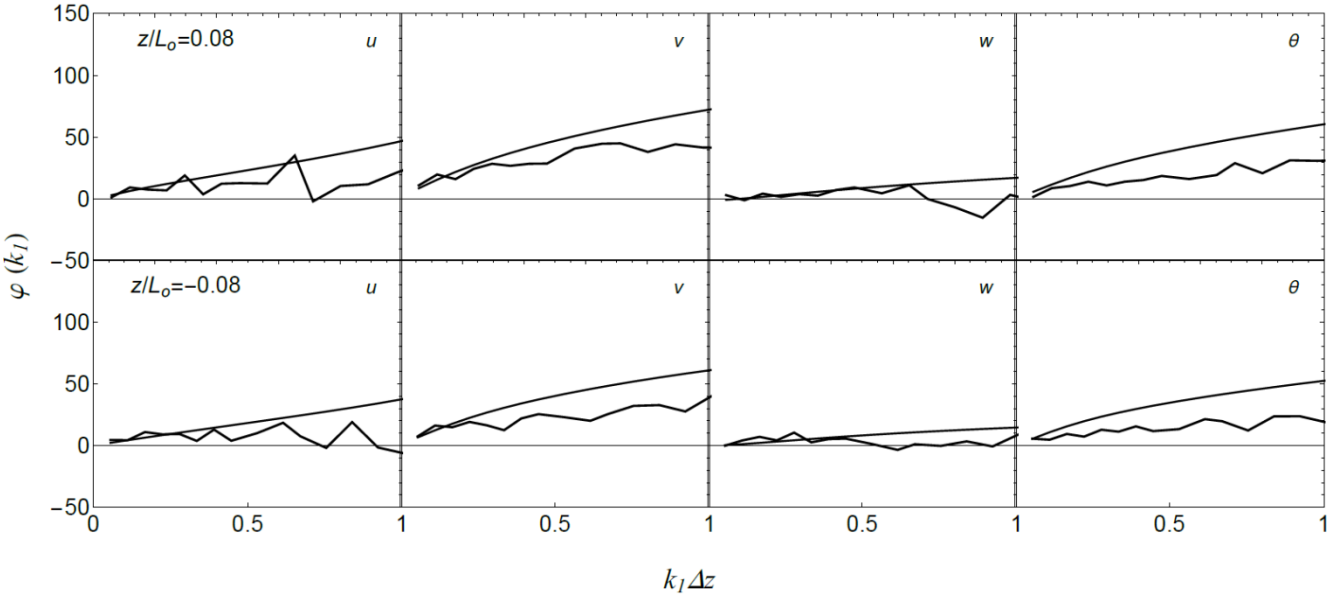

Figure 20: Measured (ragged lines) and model predicted (smooth lines) cross spectral phases for stable (z/L_o = 0.08) and unstable (z/L_o = -0.08) stratification for vertical separation Δz = 1 m.

3.3 Validation wake stability conjecture against full-scale measurements

The fundamental wake stability conjecture launched in [3] has been validated against detailed full-scale LiDAR and sonic wake measurements. This section provides an overview – more details can be found in [4],[5].

As mentioned, the major impact from buoyancy on the ABL turbulence structure is on the large turbulent scales, and being largely based on a convenient split in turbulence scales it may be straight forward to include atmospheric stability aspects into the framework of the DWM model. Crucial in this regard is if the specific scale split applied in the DWM model is such, that ABL stability affects primary the (lateral and vertical) turbulent scales, which drives the wake meandering. This is the essence of the fundamental wake stability conjecture.

For a variety of stability conditions, we will explore this conjecture partly by analyzing full-scale sonic velocity measurements and partly by analyzing both organized wake deficit flow structures and wake dynamics as based on full-scale LiDAR measurements.

We examine this conjecture using a 500kW example turbine. The analysis will focus on lateral turbulence characteristics, since this turbulence component is the most important regarding wake meandering. First a large number of full-scale sonic measurements are analysed with the available data material binned

with respect to both mean wind speed (1m/s bins) and ABS stability (7 stability classes; cf. Table 1). Subsequently dedicated full-scale LiDAR measurements are used to resolve and compare wake characteristics for three different stability conditions with mutually comparable inflow mean wind speeds.

3.3.1 Sonic measurements

The measurement campaign was conducted from June 2011 to early January 2012 at the DTU Risø Campus, and sonic data recorded 16.5m a.g.l. are used for this analysis. To ensure "homogeneous" inflow conditions, only data from the (prevailing) wind direction sector (120° - 150°) is used, resulting in 1122 available 10-minute time series covering the mean wind speed regime ranging from 4-10m/s. The distribution of mean wind speeds conditioned on inflow direction is illustrated in Fig. 21.

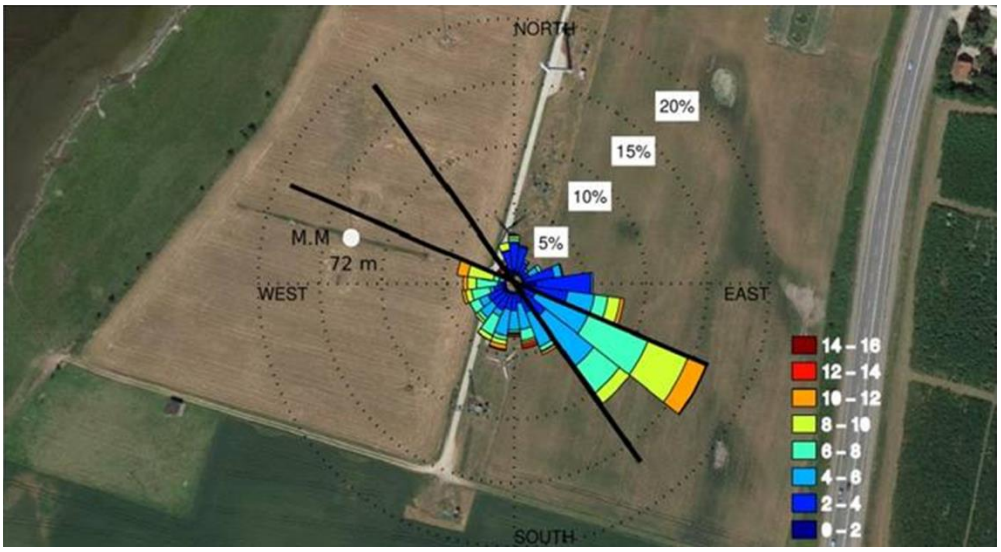

Figure 21: Mean wind speed distribution conditioned on inflow direction.

The selected data population is binned with respect to mean wind speed and ALB stability. The resulting bin matrix is shown in Table 3, where the numbers reflect the number of available 10-minute time series available within each particular bin.

Table 3: Bin matrix specifying number of available 10-minute time series.

Wind speed interval [m/s]	Very unstable	Unstable	Near neutral-unstable	Neutral	Near neutral-stable	Stable	Very stable
4-5	6	2	2	12	12	68	108
5-6	40	20	12	28	28	84	90
6-7	36	12	18	58	16	26	6
7-8	38	56	44	66	12	4	0
8-9	8	12	56	60	6	0	0
9-10	0	2	4	18	0	0	0

For each bin, the power spectrum of the *lateral* turbulence component is evaluated as based on the available 10-minute time series. Prior to the spectral analysis all data have normalized with their respective mean wind speeds and de-trended assuming a linear trend. This is done to assure un-weighted averaging (assuming constant turbulence intensity within stability-wind-speed bins) in the subsequent averaging of spectra belonging to the same bin, which is performed to improve statistical significance of the spectral estimates. Aiming at investigating the spectral characteristics wind speed bin-wise, the described bin-wise normalization of spectra does not provide any restriction for the present data analysis.

Examples of bin-normalized spectra, associated with mean wind speeds in the interval [6; 7]m/s, are shown in Fig. 22.

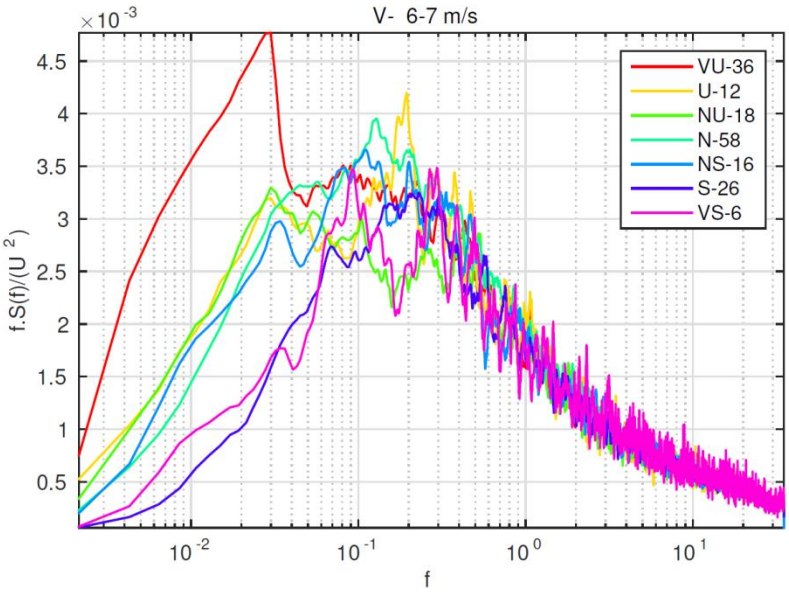

Figure 22: Normalized spectra for various stability conditions and associated with mean wind speeds in the interval [6;7]m/s.

In neutral conditions the turbulence generation is dictated by mechanical friction. For non-neutral ABL conditions buoyancy inters the scene as an additional turbulence source term. The consequence is that *turbulence intensity* as well as *turbulence structure* varies with stability condition. As seen from Fig. 22, ABL stability conditions hardly affect the spectral inertial sub-range regime, but significantly alter the large scale energy-containing spectral regime [16], where the turbulent energy is produced. In the present analysis we will, as already indicated, explore non-neutral stability conditions mean wind speed bin-wise with focus on derived effects on wake meandering dynamics.

For this purpose, we will now focus on the energy balance, quantified in normalized numbers, between "large" and "small" scale turbulence as function of ABL stability condition. Analogues, we will investigate the dependence of the total spectral energy on stability conditions. To relate to the DWM split in scales [6], "large" scale turbulence is in this context defined as turbulence associated with frequencies below a frequency split given by $f_s = U/(2D)$, where U denotes the mean wind speed and D is the diameter of the rotor in question, and "small" scale turbulence in analogy defined as turbulence associated with frequencies above f_s. In the present analysis, U will refer to the *average* of 10-minute mean wind speeds belonging to a particular mean wind speed bin, and D is defined by the previously mentioned Nordtank

500kW example turbine with a rotor diameter of 41m. This turbine was selected as example turbine, because it is the turbine on which the subsequent LiDAR measurement analysis is based.

Table 4 shows the dependence of turbulence variance on ABL stability conditions for the analysed mean wind speed bins, whereas Table 5 and Table 6 show the ABL stability dependence of "large" scale turbulence variance and of "small" scale turbulence variance, respectively.

Table 4: Bin specific variance normalized with variance associated with neutral conditions.

Wind speed interval [m/s]	Very unstable	Unstable	Near neutral-unstable	Neutral	Near neutral-stable	Stable	Very stable
4-5	1,00	0,83	1,20	1,00	1,12	0,77	0,50
5-6	1,51	2,06	1,07	1,00	0,94	0,77	0,54
6-7	1,23	1,00	0,93	1,00	0,95	0,75	0,77
7-8	1,22	1,19	1,04	1,00	0,97	1,28	-
8-9	0,96	0,80	0,88	1,00	0,77	-	-
9-10	-	0,86	0,83	1,00	-	-	-

For all mean wind speed regimes Table 4 reflects, as expected, a clear trend with the turbulent energy increasing relatively for unstable ABL conditions and decreasing relatively for stable ABL conditions. As seen, this difference in energy level is up to a factor between 2 and 3 for low mean wind speeds which, however, is expected to be reduced for higher mean wind speeds, where the mechanically generated turbulence gradually increases relative to the buoyancy generated part. A few "outliers" are observed which is attributed to the limited number of statistical degrees of freedom available for spectral averaging in certain bins (cf. Table 3).

Table 5: Bin specific "large" scale variance normalized with "large" scale variance associated with neutral conditions.

Wind speed interval [m/s]	Very unstable	Unstable	Near neutral-unstable	Neutral	Near neutral-stable	Stable	Very stable
4-5	1,78	1,37	2,93	1,00	0,89	0,76	0,52
5-6	2,23	3,63	1,47	1,00	0,90	0,63	0,37
6-7	1,71	1,07	1,09	1,00	0,96	0,50	0,65
7-8	1,51	1,41	1,16	1,00	0,95	1,33	-
8-9	0,99	0,72	0,88	1,00	0,59	-	-
9-10	-	0,60	0,77	1,00	-	-	-

The results in Table 5 reflects the same clear trend as identified for the total spectral energy, namely that the "large" scale spectral energy increases significantly with increasing buoyancy related turbulence production and vice versa.

Table 6: Bin specific "small" scale variance normalized with "small" scale variance associated with neutral conditions.

Wind speed interval [m/s]	Very unstable	Unstable	Near neutral-unstable	Neutral	Near neutral-stable	Stable	Very stable
4-5	0,78	0,65	0,69	1,00	1,21	0,78	0,51
5-6	1,12	1,26	0,86	1,00	0,96	0,83	0,63
6-7	0,94	0,94	0,83	1,00	0,94	0,90	0,87
7-8	1,04	1,04	0,97	1,00	0,98	1,27	-
8-9	0,92	0,85	0,89	1,00	0,90	-	-
9-10	-	1,11	0,85	1,00	-	-	-

Contrary to the results presented in Table 4 and Table 5, the results in Table 6 show no clear trend with regard to stability dependence of the "small" scale turbulence energy level. Therefore, with the "small" scale turbulence energy level being roughly invariant with respect stability conditions, and the "large" scale turbulence energy level being highly dependent on ABL stability conditions, the present investigation shows that the DWM split in scales roughly "matches" the split in scales between the turbulence energy-containing range and the turbulence inertial sub-range, thus in turn confirming the DWM stability conjecture.

3.3.2 LiDAR measurements

The full-scale LiDAR measurements analysed in this section relate to the same measuring campaign as described above. As a supplement to the sonic recordings, the Nordtank turbine was equipped with a pulsed LiDAR system mounted on a platform at the rear of the turbine nacelle, thus facilitating cross sectional scanning (i.e. cross sections perpendicular to the rotor axis) of the wake affected flow field behind the turbine. A detailed description of the experimental setup can be found in [5], where also the principle of extracting the mean wind speed characteristics from LiDAR measurements recorded outside the wake regime is described. In the present analysis, mean wind speeds associated with the LiDAR recordings are derived using this technique. The experimental setup is shown in Fig. 23.

Figure 23: LiDAR mounted on the rear of the NTK 500kW turbine at the DTU Risø test site.

The wake characteristics in downstream cross sections are resolved as based on a Cartesian scan pattern consisting of 49 measurement points (i.e. 7×7) as illustrated in Fig. 24. For various stability conditions, the basic idea is to resolve and compare the *wake deficit* characteristics in the meandering frame of reference (MFoR) as well as the *wake deficit dynamics*. This is performed for otherwise similar inflow conditions; i.e. mean wind speed and mean wind direction.

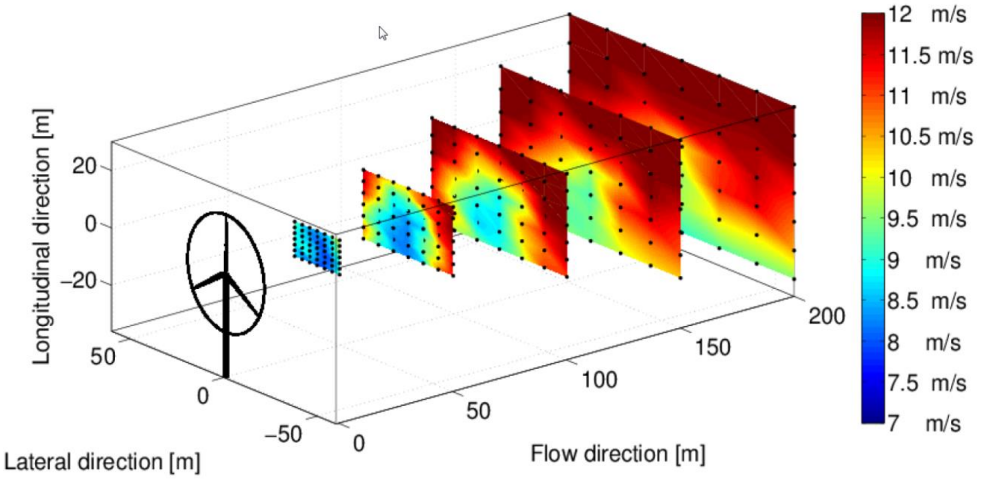

Figure 24: LiDAR scan pattern in 5 downstream flow field cross sections.

The wake deficit dynamics is obtained from "instantaneous" LiDAR cross sectional scans using the wake deficit tracking procedure introduced in [30]. With the wake deficit dynamics determined, it is straight forward to perform a transformation from the fixed frame of reference (FFoR), in which the measured wake affected flow is resolved, to the MFoR.

To obtain robust results, time series with a span ranging between 3 and 5 hours is used in this part of the investigation. To ensure a sufficient amount of data complying with the requirements, this means in turn that it is necessary to merge the former two unstable classes (i.e. "very unstable" and "unstable") into a new stability class denoted "unstable collapsed". Eventually three test cases, associated with low wind conditions and therefore pronounced deficits (i.e. high trust), are selected for this part of the analysis. The characteristics of the selected time series appear from Table 7 below. As expected the ambient turbulence level is increased with ABL stability conditions changing from stable over neutral to unstable.

Table 7: Overall characteristics of test cases.

Stability condition	Mean wind speed at hub height (U_0) [m/s]	Turbulence intensity at hub height [m/s]	Length of time series [hour]
Unstable collapsed	6.82	0.15	3.3
Neutral	7.03	0.14	3.2
Very stable	6.76	0.10	5.5

The results for the wake deficits, as expressed in the MFoR, are shown in Fig. 25 for downstream distances ranging between 1D and 5D, where D denotes the rotor diameter. It is evident that the deficits

expressed in the MFoR are almost invariant to the ABL stability conditions, thus in this respect confirming the conjecture on which the DWM modeling of non-neutral flow fields is based.

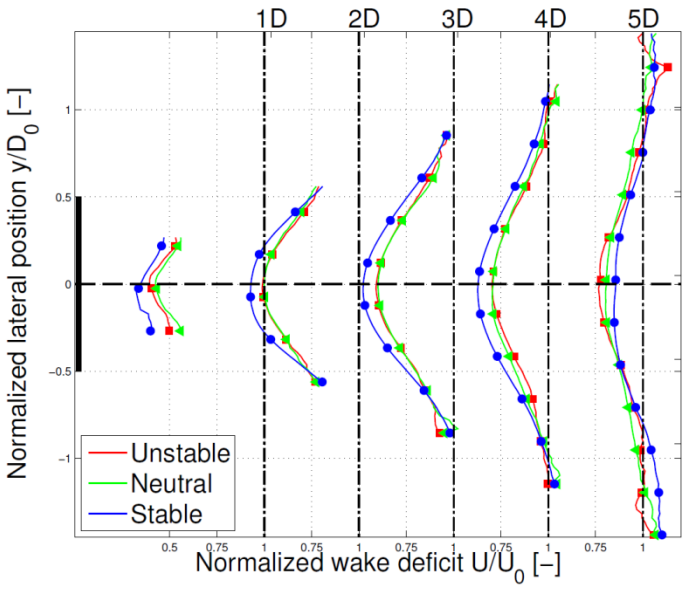

Figure 25: Normalized wake deficits in the MFoR depicted for three different stability conditions.

Turning to wake deficit dynamics, Table 8 shows the variance of the lateral wake center position for the investigated stability conditions. The lateral wake displacements are, in the context of DWM modeling, driven by the large scale lateral turbulent scales, and to facilitate direct comparisons with the inflow results given in Table 5, the results are normalized with respect to displacement variance associated with neutral conditions.

Table 8: Variance of the lateral wake center position normalized with variance of the lateral wake center position associated with neutral conditions.

Downstream distance	Very unstable	Unstable	Near neutral-unstable	Neutral	Near neutral-stable	Stable	Very stable
3D	1,11	1,22	1,26	1,00	0,70	0,81	0,75
4D	1,09	1,36	1,10	1,00	0,59	0,57	0,49
5D	1,04	1,40	1,02	1,00	0,61	0,54	0,40

Qualitatively, also these results confirm the classic DWM conjecture stating that the wake meandering dynamics is driven by large scale turbulence structures, which in turn is highly dependent on ABL stability conditions. Although differences exists among values associated with *specific* stability classes, a quantitative comparison of the results in Table 5 (i.e. mean wind bin 6-7m/s) and Table 8 shows in addition that there is a reasonable agreement between the range of "large" scale *variance* stability dependence and the range of wake center *lateral dynamics variance* stability dependence, respectively, especially considering the fact that these results originate from not identical 10-minute recordings.

In conclusion, we have demonstrated that there is experimental evidence for a significant impact from atmospheric stability on wake affected flow fields in wind farms, and more explicitly justified the fundamental wake stability conjecture stating that, in the context of DWM modeling, ABL stability impacts only the "large" scale turbulence scales within the meandering regime, whereas the "small" scale turbulence regime responsible for wake deficit expansion and attenuation in the MFoR can be assumed invariant with respect to ABL stability conditions.

3.4 LES investigation of the generalized spectral tensor capability

The usual approach when doing LES of the ABL over flat terrain is to use a wall law model in the near ground region and letting the flow be driven by a prescribed forcing (pressure gradient or Coriolis force). Stratification is typically taken into account by prescribing the temperature or heat flux at the ground, while buoyancy effects are accounted for by solving a transport equation for temperature. Normally, periodic boundary conditions are applied to the inlet and outlet of the domain and the simulation is set to run long enough for the generated turbulence to be fully developed and horizontally homogeneous.

This type of LES is generally considered to be the most accurate numerical representation of the ABL over flat terrain that can be achieved today. Its main disadvantage is that it is very computationally demanding, but in connection with simulating stratified ABL also that the degree of stability (which changes in time) is not known a priori. The latter issue makes it difficult to simulate cases with specific stability conditions and thereby to investigate the influence of stability on e.g. wind turbine wakes.

A simpler and less computationally demanding LES approach is to superimpose synthetic turbulence on to a given mean flow [45]. Since this method uses volume forces to prescribe the ABL flow, we will in the following refer to it as the forced boundary layer (FBL) method. The FBL methodology has been used widely in connection with simulating wind turbines operating in the turbulent ABL, and generally good agreement have been documented between measurements and simulations [46],[47]. In all of these works the turbulent fluctuations are generated using the turbulence generator of Mann [9], which can produce turbulence with same spectral characteristics as in the neutrally stratified ABL. Recently, Chougule et al. [11],[13] extended the model of Mann to allow for modeling different stratification. Machefaux et al. [5] used this modified turbulence model together with the FBL methodology to simulate a wind turbine operating in differently stratified ABL. In this work the buoyancy was accounted for by solving a transport equation for temperature and prescribing an initial temperature profile. The advantage of the FBL approach is that inflow characteristics, similar to those observed in measurements, in principle easily can be generated, and thereby a one-to-one comparison can be made between simulations and measurements. In the work of Machefaux et al. [5] a comparison of measured and simulated wake characteristics were made, and an overall fair agreement was found. The main differences were observed in the near wake and in the near ground region due to inaccurate modeling of the nacelle and the influence of the ground. The inadequacy of the near ground treatment is expected to be particularly significant when using the FBL method for modeling a stratified ABL, because the heat flux is not modeled. Thus, while the FBL have shown rather accurate for a neutrally stratified ABL, it still needs validation in non-neutral conditions.

The objective of this section is therefore to further validate the FBL method with standard LES of a *non-neutral* ABL. To do this a standard LES model has been implemented in the in-house Navier Stokes code EllipSys3D [48],[49],[50] as described in the next sections. As part of this work the capability of the method of Chougule et al. [36],[38] in reproducing non-neutral turbulence will also be verified.

3.4.1 Governing equations

The governing equations for the LES are the spatially filtered Navier-Stokes equations

$$\frac{\partial \rho u_j}{\partial x_j} = 0 \tag{3.4.1}$$

$$\frac{\partial \rho u_i}{\partial t} + \frac{\partial \rho u_i u_j}{\partial x_j} - \frac{\partial \tau_{ij}}{\partial x_j} + \frac{\partial p}{\partial x_i} = f_{ext} \tag{3.4.1}$$

where x_i (i={1,2,3}) refers to the longitudinal, lateral and vertical direction, respectively, u_i is the spatially filtered velocity in the i-direction, p is the pressure, f_{ext} represents the external volume forces and the shear stress is given by

$$\tau_{ij} = (\mu + \mu_t)\left(\frac{\partial u_i}{\partial x_j} + \frac{\partial u_j}{\partial x_i}\right) \tag{3.4.2}$$

where μ_t is the turbulent eddy viscosity.

Thermal stratification and Coriolis effects (and other external forces) are included via the source term on the right hand side of the momentum equations:

$$f_{ext} = g_i(\rho - \rho_0) + \epsilon_{i3k} f_c \rho u_k + f_{vol} \tag{3.4.3}$$

Here g_i is the gravitational acceleration, ρ_0 is a reference density, ε is the alternating tensor and $f_c = 2\Omega \sin\lambda$ is the Coriolis parameter, with Ω and λ being the earth's rotation rate and latitude, respectively. The final term, f_{vol}, represent other external forces such as e.g. wind turbine forces.

Buoyancy effects are included by solving an equation for potential temperature:

$$\frac{\partial \rho \theta}{\partial t} + \frac{\partial \rho u_j \theta}{\partial x_j} - \frac{\partial q_j}{\partial x_j} = 0 \tag{3.4.4}$$

Here the heat flux is given by

$$q_j = \left(\mu + \frac{\mu_t}{\sigma_\theta}\right)\frac{\partial \theta}{\partial x_j} \tag{3.4.5}$$

where σ_θ is the turbulent Prandtl number. Density variations due to variations in pressure are assumed small, which means that the flow can be treated as incompressible and that density is not a function of pressure as required in the Boussinesq approximation. The density is linked to the temperature via the ideal gas law:

$$\rho = \frac{P_\infty M}{RT} \tag{3.4.6}$$

where M is the molar mass, P_∞ is the background pressure and R is the universal gas constant.

3.4.2 Sub-filter model

In order to close the governing equations an equation for the turbulent eddy viscosity is need. In the present work we use the Smagorinsky model, which yields:

$$\mu_t = \rho(C_s\Delta)^2\left(2S_{ij}S_{ij}\right)^{1/2} \tag{3.4.7}$$

where C_s=0.1 is a model parameter, $\Delta = (\Delta x \Delta y \Delta z)^{1/3}$ is the filter length scale and

$$S_{ij} = \frac{1}{2}\left(\frac{\partial u_i}{\partial x_j} + \frac{\partial u_j}{\partial x_i}\right) \tag{3.4.8}$$

3.4.3 Boundary conditions

The boundary condition at the ground are defined from wall models using the Monin-Obukhov similarity theory (MOST), which is approximately valid for the atmospheric surface layer over flat terrain. According to MOST we have:

$$\bar{u}(z) = \frac{u_*}{\kappa}\left[\ln\left(\frac{z}{z_0}\right) - \Psi_m\left(\frac{z}{L}\right)\right] \tag{3.4.9}$$

$$\bar{\theta}(z) = \frac{\theta_*}{\kappa}\left[\ln\left(\frac{z}{z_0}\right) - \Psi_h\left(\frac{z}{L}\right)\right] \tag{3.4.10}$$

Here and overbar indicates horizontal averaging, κ is the von Karman constant, u_* is the friction velocity, z_0 is the roughness length, L is the Monin-Obukhov length and

$$\theta_* = \frac{\theta_0 u_*^2}{\kappa g L} \tag{3.4.11}$$

where θ_0 is the temperature at the ground, which is assumed known. The functions ψ_m and ψ_h are empirical functions, which depend on the atmospheric stability. In the present work they are defined as [51]:

$$\Psi_m(\zeta) = \begin{cases} -6.1ln\left(\zeta + \left(1+\zeta^{5/2}\right)^{2/5}\right) & \zeta > 0 \\ ln\left(\frac{1+\Phi_m^{-2}}{8}(1+\Phi_m^{-1})^2\right) - 2tan^{-1}\left(\Phi_m^{-1}\right) + \frac{\pi}{2} & \zeta < 0 \end{cases} \tag{3.4.12}$$

$$\Psi_h(\zeta) = \begin{cases} -5.3ln\left(\zeta + \left(1+\zeta^{11/10}\right)^{10/11}\right) & \zeta > 0 \\ (1+\sigma_\theta)ln\left(\frac{1+\Phi_h^{-1}}{2}\right) + (1-\sigma_\theta)ln\left(\frac{\Phi_h^{-1}-1}{2}\right) & \zeta < 0 \end{cases} \tag{3.4.13}$$

where

$$\Phi_m = (1-16\zeta)^{-0.25} \tag{3.4.14}$$

$$\Phi_h = \sigma_\theta(1-16\zeta)^{-0.5} \tag{3.4.15}$$

In practice the boundary conditions are determined by first determining $\bar{u}$, and $\bar{\theta}$ in the first cell above ground and then use equations (3.4.3.4.9) - (3.4.3.4.11) to determine $u_*$and θ_* and L. Having determined $u_*$and θ_* the wall shear stress and heat flux can be determined as

$$\tau_w = \rho u_*^2 \tag{3.4.16}$$

$$q_h = \rho u_* \theta_* \tag{3.4.17}$$

which then replaces τ_{ij} and q_j in equations (3.4.3.4.1) and (3.4.3.4.4).

3.4.4 Numerical setup

The GABLS [52] inter-comparison setup of a diurnal cycle is used as a basis for the present LES simulation. This simulation assumes a constant geostrophic wind of U_g = -3 m/s and V_g = -9 m/s, a Coriolis parameter of f_c = $8.87 \cdot 10^{-5} s^{-1}$ and a uniform roughness height of z_0 = 0.03m. The temporal variation of the surface temperature is shown in Fig.26 and is a simplified fit to observations. The initial temperature profile is as described by Svensson et al. [52].

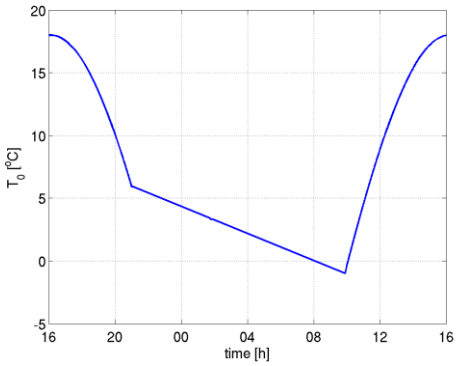

Figure 26: Temporal variation of ground temperature.

The simulations are carried out in a Cartesian grid with a uniform spacing of $\Delta x = \Delta y = \Delta z$ = 12.5m. The dimensions of the grid are $L_x = L_y = 2L_z$ = 4000m. The lower boundary is a wall, where the wall stress and heat flux is determined from Monin-Obukhov theory as described above. Symmetry conditions are applied at the upper boundary, while cyclic conditions are applied on all vertical boundaries. The time step in the simulations is set to Δt = 0.75s. In order to build up turbulence, a full diurnal cycle is simulated before the turbulence characteristics are analysed.

3.4.5 Results

Fig. 27 shows the computed friction velocity (u_*), heat flux (q_h) and inverse Monin-Obukhov length ($1/L$) as a function of time during the day. In day time the ground is warmer than the air above and the ABL is unstable, whereas the opposite is true during night. As a consequence L and q_h are negative during day and positive during night. Furthermore, it is seen that the friction velocity as expected is high during unstable conditions and low in stable conditions. Neutral conditions are seen to occur only as a short transitional phase between stable and unstable conditions.

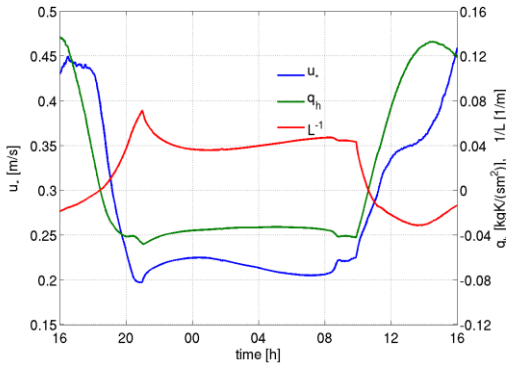

Figure 27: Friction velocity, wall heat flux and inverse Monin-Obukhov length as a function of time of day.

Fig. 28 shows profiles of the velocity and temperature at 17.30 and 00.30, respectively. The corresponding plots of the velocity variance are shown in Fig. 29. The two shown cases represent very unstable and very stable conditions, respectively. In both cases the profiles are computed by averaging horizontally in space and over approximately 10 minutes in time. As expected, the flow is characterized by a strong shear and low turbulence in stable conditions, whereas the opposite is true in unstable conditions. The vertical variation of the variance in the unstable case is qualitatively in agreement with measurements presented in the book of Wyngaard [53]. The variance profiles in the stable case look less convincing, which is most likely due to the poor grid resolution.

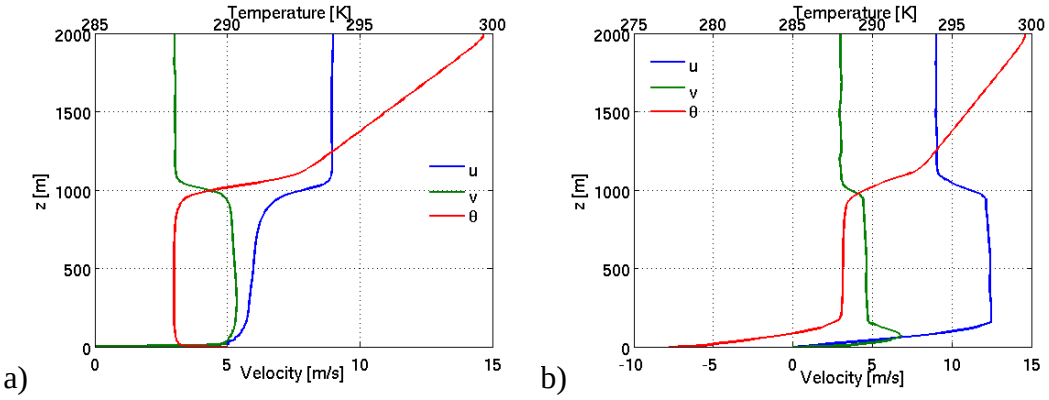

Figure 28: Velocity and temperature profiles at a) 17.30 and b) 00.30.

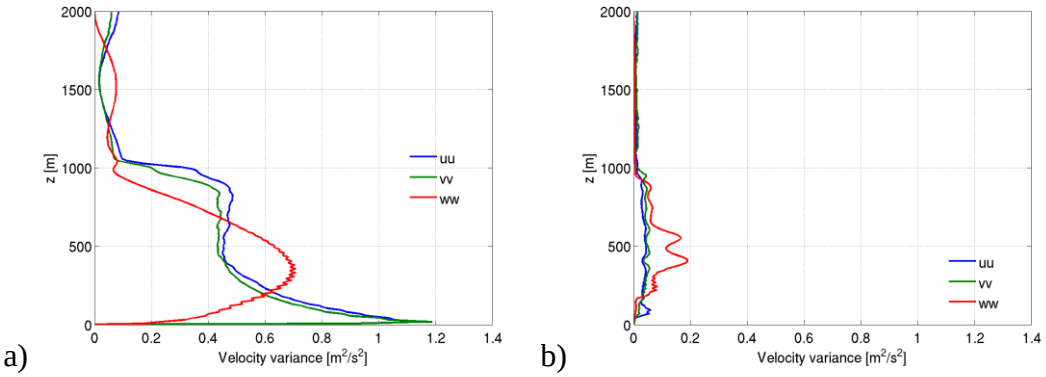

Figure 29: Velocity variance profiles at a) 17.30 and b) 00.30.

Fig. 30 shows the spectral characteristics of each velocity component at approximately 130 m above ground at the same time of day as the profiles shown in Fig. 28 and Fig. 29 were extracted. The -5/3 slope, which is characteristic of the inertial sub-range, is also shown in the plot. The subscript "*h*" indicates that it is the velocity components relative to the mean flow direction at the current height. Hence u_h is in the along the mean flow direction at h = 130 m.

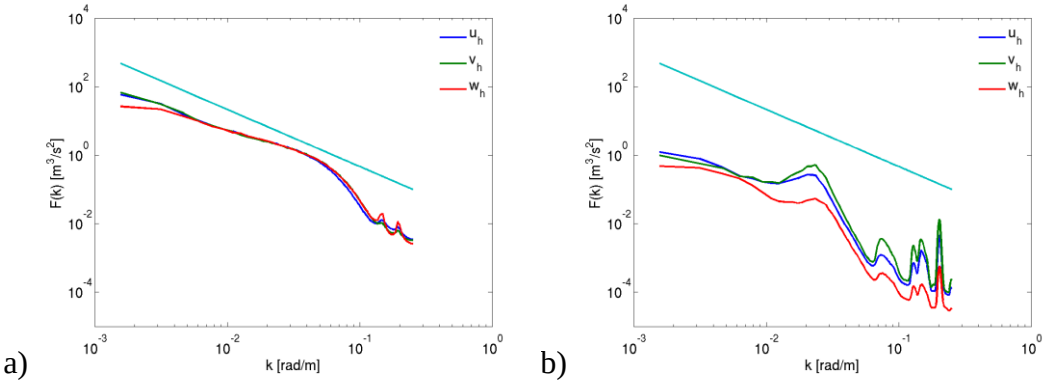

Figure 30: 1D velocity spectra at a) 17.30 and at b) 00.30. The cyan line indicates the inertial sub-range -5/3 slope.

In the unstable case the spectra of each component are very similar indicating that the flow is rather isotropic at the extracted height, which is as expected from Fig. 29. However, this figure also shows that the flow below and above the height at which the spectra are evaluated is far from isotropic. At a first glance the inertial sub-range seems to be rather well resolved in the unstable case, when considering the range of wave numbers from approximately 0.003 to 0.05. However, in the range from 0.008 to 0.02 the slope of the spectra is clearly lower than the expected -5/3. Thus, the spectra only have a slope of -5/3 in the wave number range between 0.02 and 0.05. The rather *limited range of the inertial sub-range* is most likely due to insufficient grid resolution and a too simple sub-grid model, which apparently cannot extract sufficient energy from the resolved flow.

In the stable case the energy is clearly much lower than in the unstable case. It is clear that the inertial sub-range is not well resolved in this case even though it could seem like the spectra have a -5/3 slope at

the lowest wave numbers. The reason for the poor resolution of the inertial sub-range in the stable case is that the turbulence scales are small and therefore the rather coarse grid resolution does not allow for resolving the inertial sub-range well. The "bump" at wave numbers around 0.02-0.03 is unexpected and is probably a result of a too simple sub-grid-scale model.

3.4.6 Kinematic turbulence modeling

In this section we will use the method of Chougule et al. [11],[13] – as described in section 3.2 – to reproduce the turbulence generated by the LES described above. This method is, as previously described, an extension of the spectral tensor model by Mann [9] by allowing for modeling atmospheric stratification. To recap the model is based on 5 parameters: a parameter linking mean wind shear magnitude with eddy lifetime (Γ), the turbulence length scale (L), the viscous dissipation of turbulent kinetic energy ($\alpha\varepsilon^{2/3}$), the gradient Richardson number, Ri, and the rate of destruction of temperature variance (η_θ). The first 3 of these parameters are the same as used in the original work of Mann. The 5 parameters are determined by fitting the model spectra to the spectra computed by the LES. The result of this exercise is shown in Fig. 31 and Fig. 32. As seen the fit is far from perfect, especially in the stable case. This result is contrary to the fitting of the generalized spectral tensor to the full-scale HATS data in section 3.2.3. The poor agreement is partly due to the inability of the spectral tensor model to handle extreme stratification but also due to the limited resolution of the LES, which are incapable of resolving the inertial sub-range properly.

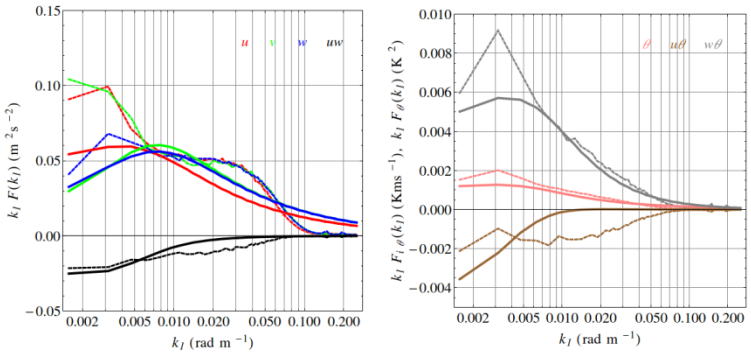

Figure 31: Spectral fit at time 17.30. The dashed lines are LES and full lines the fit.

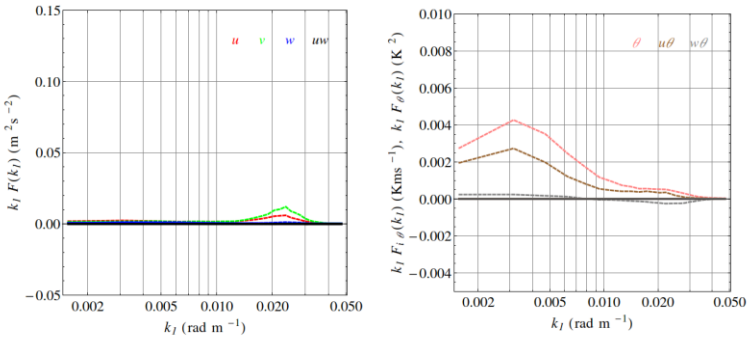

Figure 32: Spectral fit at time 00.30. The dashed lines are LES and full lines the fit.

3.4.7 Simulation of wind turbine wake at different atmospheric stratification

In this section we simulate the wake characteristics of the DTU 10WM wind turbine operating in an unstable and stable ABL, respectively. The simulations are carried out using two different approaches: 1) using precursor generated LES turbulence as described above and 2) using the kinematic approach where turbulence is generated using the spectral model of Chougule et al. and inserting it in a cross section upstream of the turbine. The wind turbine is simulated using an actuator disk method [54].

In the first approach we simply restart the LES simulation described above but with an AD inserted in the center of the domain at a height of 132 m. The AD is aligned with the mean wind direction at hub height and is operating at a constant rotational speed and pitch. The use of periodic boundary conditions is not a problem in this case, because the domain is very large, and because the wind direction is between 30 and 45 degrees, and therefore the wake is completely dissipated before it intersects the turbine again.

In the second approach a new computational domain was generated, which had the same dimensions as in the first approach but used fewer grid points. In the region around and downstream of the turbine the grid cells were cubic with a side length of 12.5m (just as in the grid used in the first approach). This equidistant region extended from 500m upstream to 1500m downstream of the turbine, and its height was 1250m. Outside of the equidistant region, grid points were stretched away towards the outer boundaries. The grid had (160, 160, 128) points in the *x*, *y* and *z*-direction, where *x* is the flow direction at hub height, *y* is the lateral direction and *z* is the vertical direction. The velocity and temperature at the inlet was specified in accordance with the mean profiles from the LES simulation (except above 1000m where a constant temperature was applied). The remaining boundary conditions were symmetry at the wall, periodic on the sides and Neumann at the outlet. The turbine rotor center was located at (1500m, 2000m, 132m), and its axis was aligned with the flow direction (*x*). The synthetically generated turbulent fluctuations are inserted in a cross-section located 500m upstream of the rotor. It turned out that the use of Dirichlet (at the inlet) and Neumann conditions necessitated a change in the scheme of the convective terms. Therefore, instead of using a pure CDS4 scheme, these simulations were carried out using a hybrid scheme that blends CDS4 and QUICK.

Fig. 33 and Fig. 34 show snapshots of the streamwise velocity at hub height using LES and FBL, respectively.

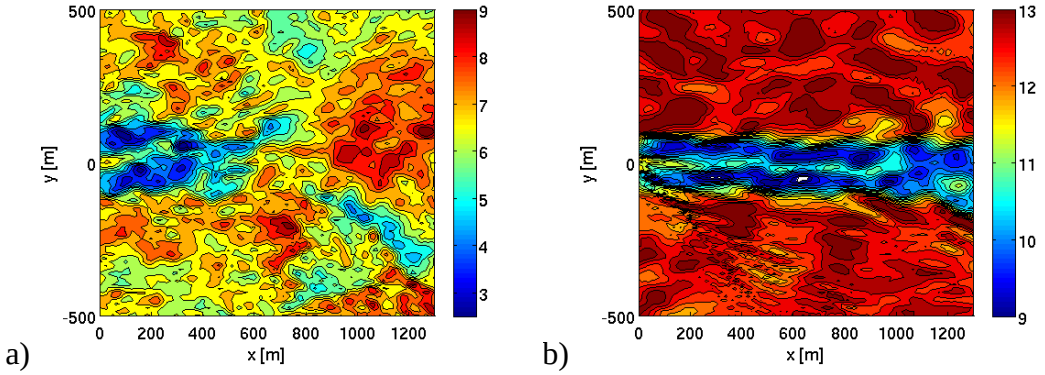

Figure 33: Snapshot of velocity using LES at a) 17.30 and b) 00.30.

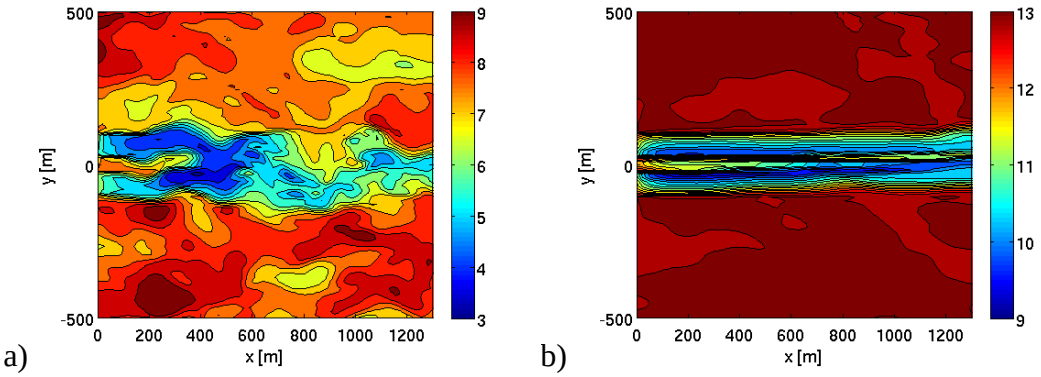

Figure 34: Snapshot of velocity using LES at a) 17.30 and b) 00.30.

The overall level is in good agreement, but it is clear that standard LES resolves smaller scales than when using FBL. The reason for this is due to the shift in convective scheme and the inaccurate spectral fit.

In order to evaluate the level of wake meandering, the dynamics of the wake center is computed. The wake center position at each downstream cross-section is determined from an optimization algorithm where a 1D Gaussian profile is fitted to the unsteady wake at hub height. Fig. 35 shows the standard deviation of the lateral position of the wake center as a function of downstream position computed from the LES and FBL simulations, respectively. The standard deviations are higher in the LES than the FBL, and in the unstable case the slope is also markedly larger. This is as expected from Fig. 31, where it is clear that there is significantly more energy on the large scales in the LES than in the FBL simulations.

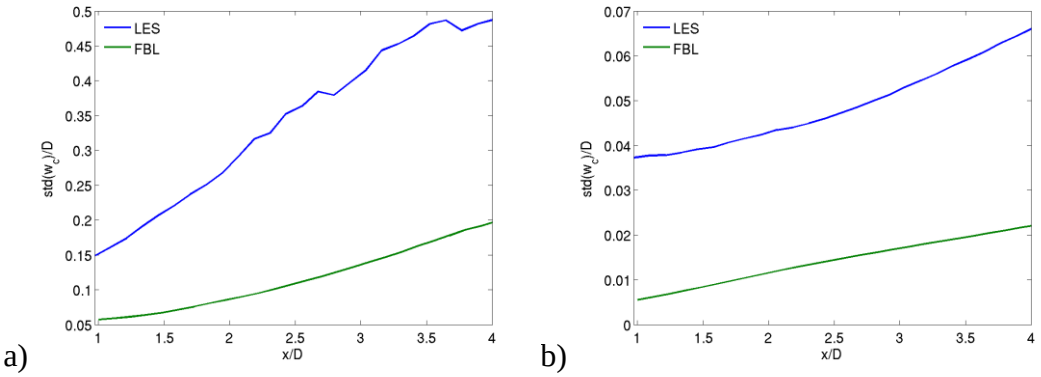

Figure 35: Standard deviation of wake center at a) 17.30 and b) 00.30.

3.4.8 Conclusions

A wind turbine operating in the ABL under different stratifications has been modeled using two different LES approaches. The first is a standard LES, in which the inflow is generated from a precursor simulation, with periodic boundary conditions whereas the second is the FBL method where synthetic turbulence is superimposed on to the mean flow in a cross-section upstream of the rotor. In the latter case the turbulence was generated using the method of Chogule et al. [11],[13]. It was shown this method could not reproduce turbulence with the same spectral characteristics as in the LES. The reason for this was a mix of using a too coarse grid in the LES and the difficulty of the model of Chogule et al. [11],[13]

in handling very unstable conditions. As a consequence of the differences in the turbulence, the dynamics of the wake predicted by the two approaches was also quite different. The differences could however be explained as coming mainly from the differences in energy on the large scales.

4 Wind farm feed-back on large scale turbulence structures

With the wake meandering process in the DWM model being defined by the large scale turbulence structures in the ABL, it is obviously important to determine if the sole presence of a WF in the ABL impacts the characteristics of such large scale structures compared to ambient undisturbed conditions – i.e. in other words to determine if a feed-back process exists between the presence of a WF and the large scale turbulence structure characteristics inside the WF, where the DWM model is to be applied to simulate the un-steady wake affected WF flow field, and further to assess if, in this regard, there is any impact of ABL stability conditions.

To approach this research question, a large data set has been analysed with the purpose of quantifying the impact of atmospheric conditions on turbulence structure and intensity before and after a full-scale offshore wind farm, and, in doing so, turbulence spectra and turbulence intensities have been investigated. As a by-product, it was further decided to use this high frequency data set to validate a study initiated by DONG Energy in the TOPFARM project [55]. It is thus aimed to investigate if the wind farm impacts the large scale turbulence, and if the wake can be regarded as a passive tracer with its transversal movements dictated by the wind's large scale cross-turbulence. The research issue is summarized in Fig. 36.

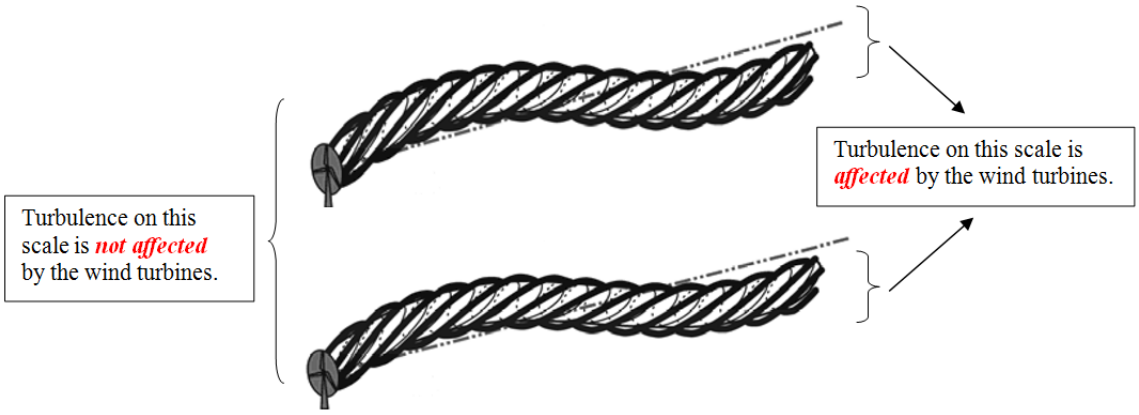

Figure 36: Schematic illustration of the DWM model hypothesis to be investigated.

In the analysis, we will refer to the nomenclature illustrated in Fig. 37, with U being the mean wind speed, and (u,v,w) being turbulence components in the longitudinal, lateral and vertical directions, respectively. Further, we will refer to F_{11} as the auto spectrum of u, F_{22} as the auto spectrum of v and F_{33} as the auto spectrum of w.

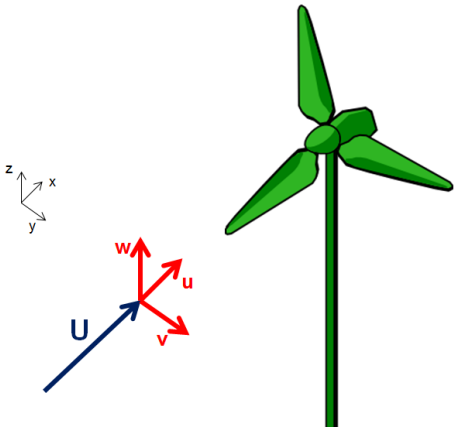

Figure 37: Nomenclature.

4.1 Measurement setup

To investigate the above described task, full-scale experimental data have been compared up- and down-stream of a large offshore wind farm. The experimental data was recorded at Nysted Offshore Windfarm – a park consisting of 72 BONUS 2.3 MW turbines located 10 km from Gedser in southeastern Denmark. The park data, layout and positions of the WT's as well as the meteorology masts are shown in Fig. 38 below.

General data	
Turbine type	Bonus 2,3 MW
Rotor diameter	82.4 m
Hub height	68.8 m
Number of turbines = rows × columns	72 = 9 × 8
Park area	23 km^2
Turbine distance, East - West	867 m = 10.5 D
Turbine distance, North - South	481 m = 5.8 D
Angle of East-West rows	97.6 °
Angle of North-South columns	357.9 °
Distance to coast (Nysted)	9.5 km

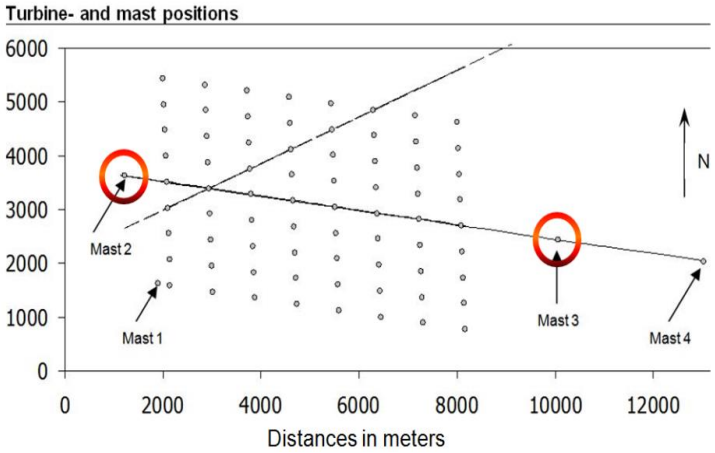

Figure 38: Layout of Nysted Offshore Wind Farm. The two masts used in this work, M2 and M3, are highlighted. Park key data is given in the left hand panel.

The two encircled masts, Mast 2 (M2) and Mast 3 (M3), are the only measurement devices used in the present work; the masts instrumentation and recording systems are identical. The measurement sensors are two sonic anemometers of the type Metek USA-1, both mounted at a height of 63m. These anemometers record all three components of the wind vector with a resolution of 0.1m/s at a sampling rate of 1Hz. A drawing of the mast top as well as a picture of a mast bottom is shown in Fig. 39.

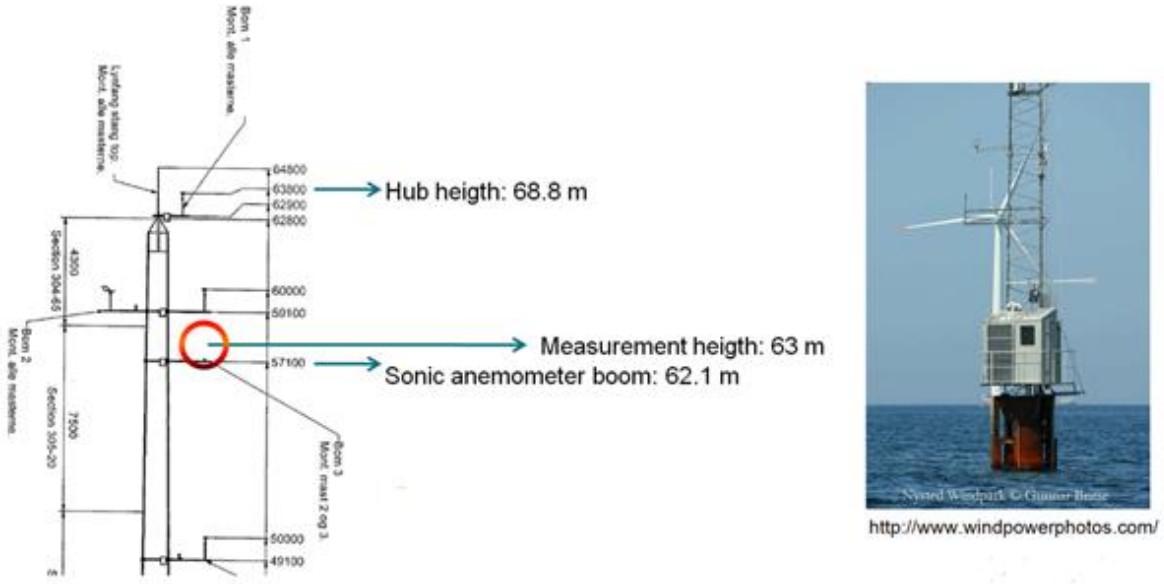

Figure 39: Overview of mast top layout (left) and picture of the mast bottom (right). Boom with the sonic anemometer is indicated with a red circle. The mast booms are pointing toward North.

4.2 Turbulence spectra

Approximately 18 months of experimental data were simultaneously available at M2 and M3. The data was partitioned into segments of 3000 seconds each. This partition has been performed in order to have enough point in the low frequency part and thus to be able to investigate the spectral behavior in this frequency regime. The segments having mean wind directions pointing within ±7° of the direction from M2 to M3 are denoted as "Western Winds", whereas those segments with mean wind directions pointing within ±7° of the direction from M3 to M2 are denoted "Eastern Winds". All data outside these two wind direction bins have been discarded.

4.2.1 Analysis approach

The analysis of the data includes the following four steps:

1. Selection of the 3000s long up-wind segments one by one;
2. Fourier transformation of corresponding segments measured up- and down-stream, where Haning windowing has been applied;
3. The resulting power spectra, *S(f)*, as a function of the frequency, *f*, have been combined in a weighted average; and
4. Finally, log[*S(f)*] has been plotted as a function of *f*.

4.2.2 Spectra of lateral and vertical turbulence components

Only the *v* and *w* turbulence component have been studied, because the DWM wake meandering process are completely defined by these, and in the following each plot will present relevant turbulence spectra both up- and down-stream of the WF in question.

Fig. 40 shows the F_{22} spectra for all wind speeds, which corresponds to 1062 segments for the Western wind direction bin and 342 segments for the Eastern wind direction bin. The difference between up- and downstream spectra for Eastern wind directions is more significant than for Western wind directions, which is in accordance with the location of the downstream meteorological mast (i.e. M2 for western wind directions and M3 for eastern wind directions). The peak around f = 0.5Hz corresponds to the natural frequency of the meteorological mast structure and is consequently disregarded in the analysis.

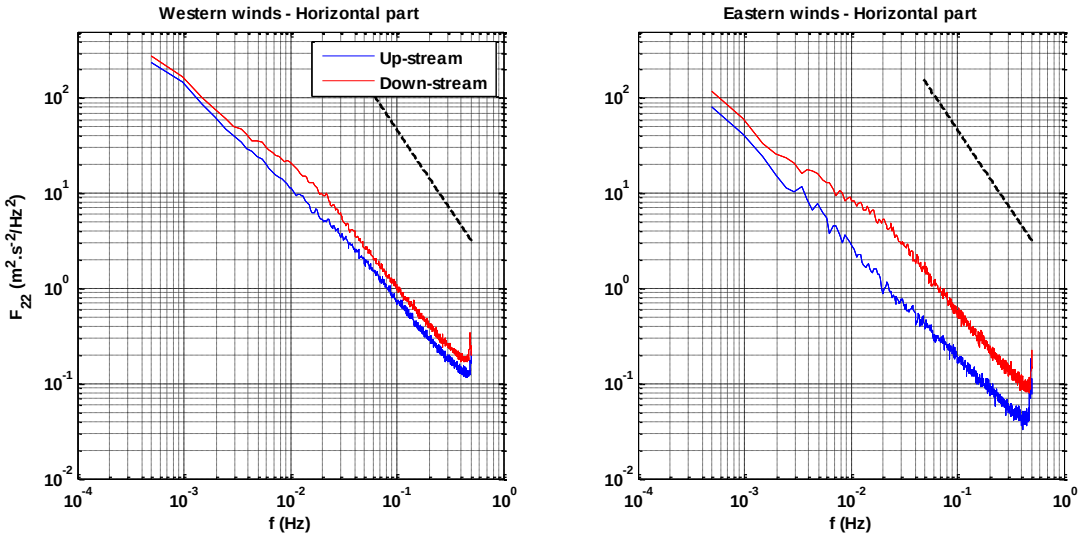

Figure 40: Up- and downstream F_{22} spectra for both Eastern and Western wind directions for all wind speeds.

As for the low frequency part of the spectra, we observe that below a certain frequency the up- and downstream spectra follow the same trends and contain approximately the same amount of energy. This suggests that the wind park does *not* impact the large scale turbulence corresponding to such low frequencies. The same observation is true for the F_{33} spectra, which is shown in Fig. 41.

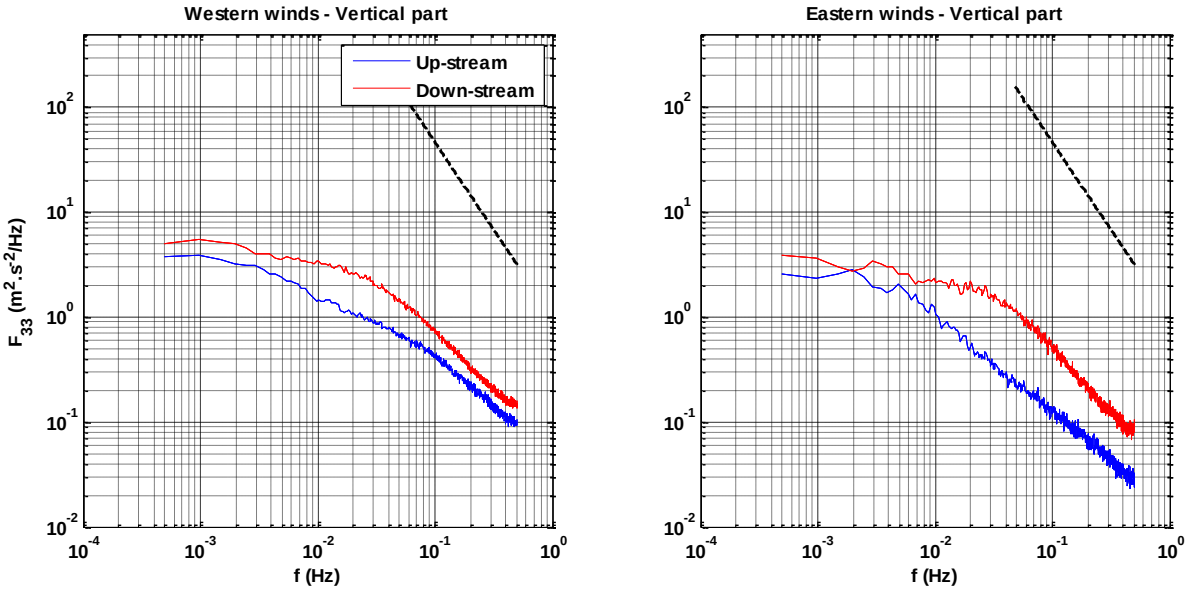

Figure 41: F_{33} spectra up and down stream for all wind speeds.

4.2.3 Wind speed binning and merging frequency

We now look at the impact from the wind speed on the F_{22} and F_{33} spectra, thus investigating if the merging frequency is depending on wind speed. However, the cost is that by binning the wind speed, we reduce the number of available segments for spectral smoothening, which is illustrated in Table 9. This in turn increases the noise on the obtained spectra and consequently increases the uncertainty on the merging frequency determination for some spectra.

Table 9: Available segments for each wind speed bin.

-	Eastern Winds	Western Winds
All Wind Speeds	342	1062
0-5 m/s	61	69
5-7 m/s	64	95
7-9 m/s	81	170
9-11 m/s	88	185
11-13 m/s	26	202
13-15 m/s	21	170
WS>15 m/s	1	171

Fig. 42 shows F_{22} and F_{33} for wind speeds between 13m/s and 15m/s for eastern and western wind directions. These figures illustrate the impact of the number of available segments on the spectral noise level and thereby on the merging frequency determination.

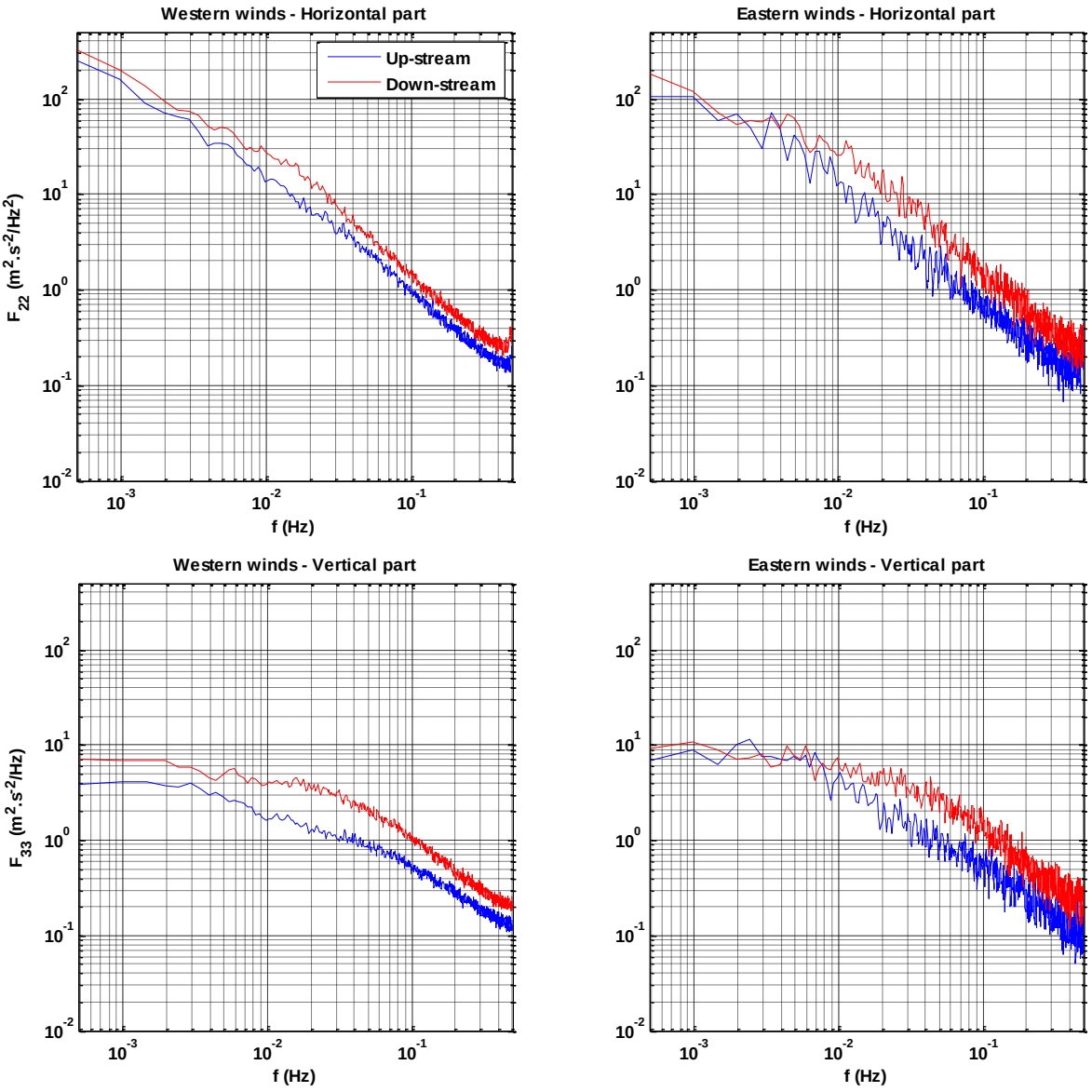

Figure 42: F_{22} and F_{33} for wind speeds between 11 and 13 m/s.

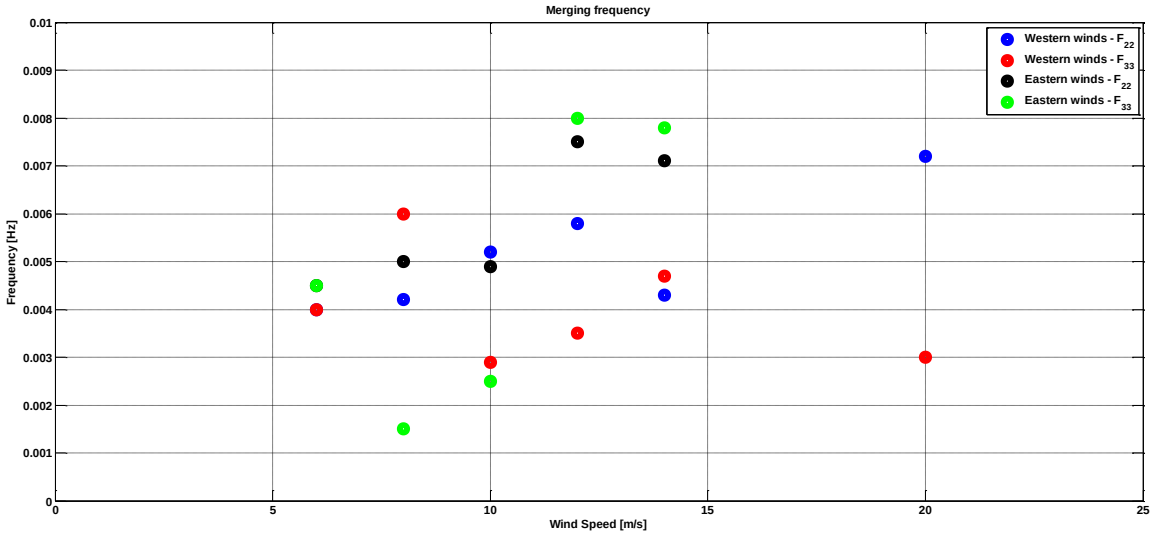

Figure 43: Merging frequency as a function of wind speed for F_{22} and F_{33} for Eastern and Western wind directions.

Fig. 43 shows no clear dependency of the merging frequency on wind speeds, even though F_{33} for western wind directions seems to decrease when the wind speed increases. In summary, we observe that all values remains approximately constant around f = 0.005 Hz, which is in accordance with previous studies on this topic [55],[56]. The large scale turbulence, corresponding to frequencies below approximately 0.005Hz, is therefore not impacted by the presence of the WF.

4.2.4 Longitudinal wind speed fluctuations

To investigate the present recommended practice in the IEC code [8] for simulation of wake affected loads, we finally compare the WF affected turbulence intensity with the analogue undisturbed ambient turbulence intensity. Fig. 44 shows measured F_{11} spectra associated with eastern and western wind directions, respectively, as well the code specified spectrum for WF flows associated with WT class 1 and turbulence class B (dotted line).

Using the effective turbulence intensity approach from the IEC code [8], we conventionally simulate the incoming turbulence field to a WT operating in WF conditions as a turbulence field with an intensity equal to a code specified coefficient times the ambient undisturbed turbulence intensity. Consequently, we here investigate the potential of this approach by analyzing how good this approximation compares with measurements. From Fig. 44 the coefficients 1.4 and 2.4 have been estimated for the western and eastern wind direction bins, respectively.

For the eastern wind direction bin, the simulated spectrum does not capture the peak at low frequencies and starts to fit poorly from f = 0.1Hz and downwards. This is most likely linked to the fact, that not only turbulence intensity but also turbulence structure changes in wake affected flow fields. For the western wind direction bin, both simulated and measured spectra fit well. With mast M3 being located at two row-to-row distances from the WF, the WF affected flow field recorded at this position has recovered to a larger extend than the WF affected flow field recorded at mast M2, which is located only one row-to-row distance from the WF.

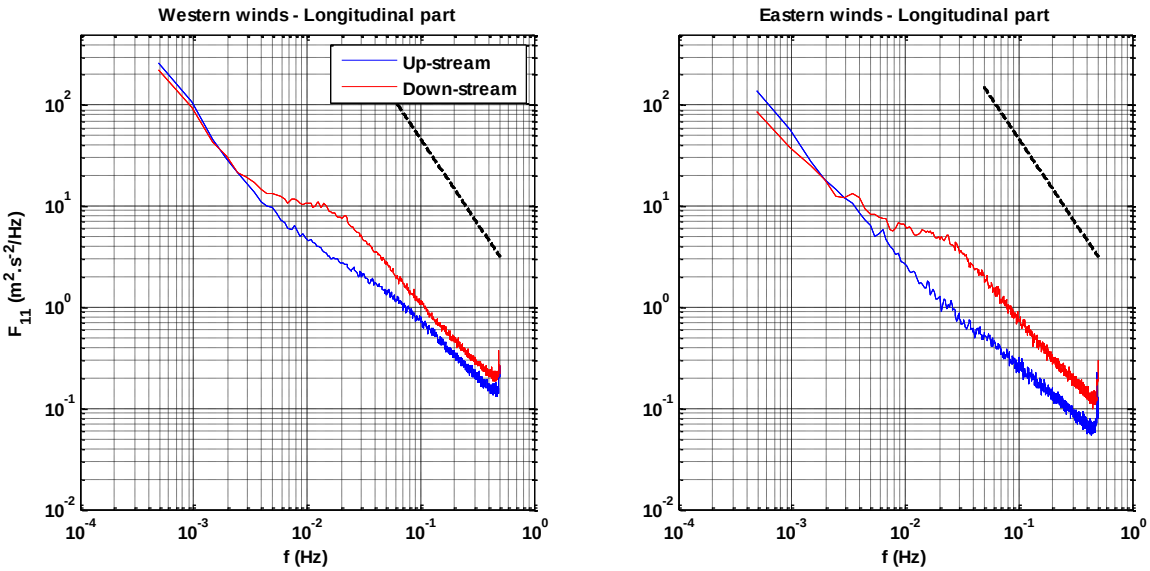

Figure 44: Measured and simulated F_{11} spectra for eastern and western wind directions.

Plotting the spectra shown in Fig. 44 for different stability classes showed that the ABL stability condition does not have any significant impact. It will, however, be of interest to evaluate the non-captured WF affected turbulence intensity, corresponding to the peak below f = 0.1Hz, to assess the consequences for the code specified effective turbulence intensity approach.

4.3 Distribution of ABL stability at the Nysted site

Referring to the ABL stability classification defined in Table 1, Fig. 45 shows the distribution of atmospheric stability conditions at Nysted for both the eastern and western wind direction bin. As these distributions are intended also to support the analysis of the resulting turbulence intensities, the wind direction filtering has been kept to 97±30° for eastern winds (recorded at mast M3) and 277±30° for western winds (recorded at mast M2). However, a filtering corresponding 97±90° and 277±90° would provide a more accurate characterization of the site, but this is accordingly not shown here.

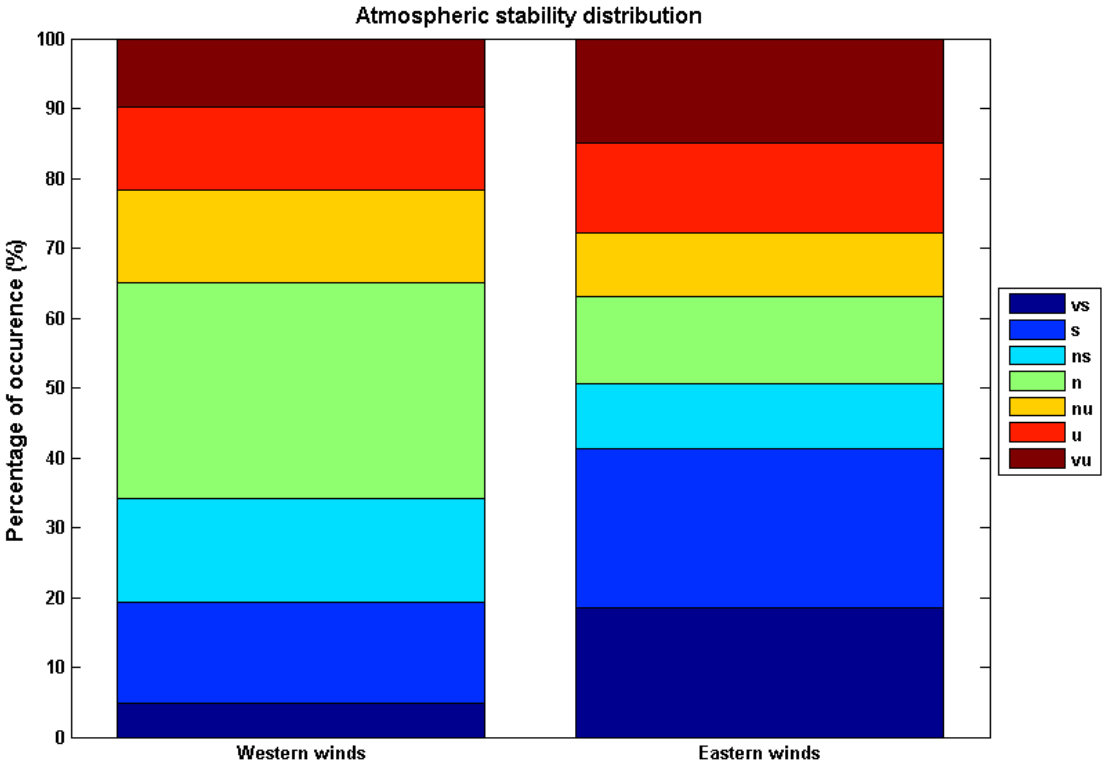

Figure 45: Stability class distribution at Nysted for 2004-2007.

For eastern wind directions a stable atmosphere seems to be more frequent at Nysted. However, no clear trend appears. Strong winds occur most often for westerly wind directions, which explain the increased likelihood of neutral stability conditions in such cases. These results are in accordance with the results obtained by Lange [57].

Fig. 46 shows the dependency of the ABL stability distribution on wind speed.

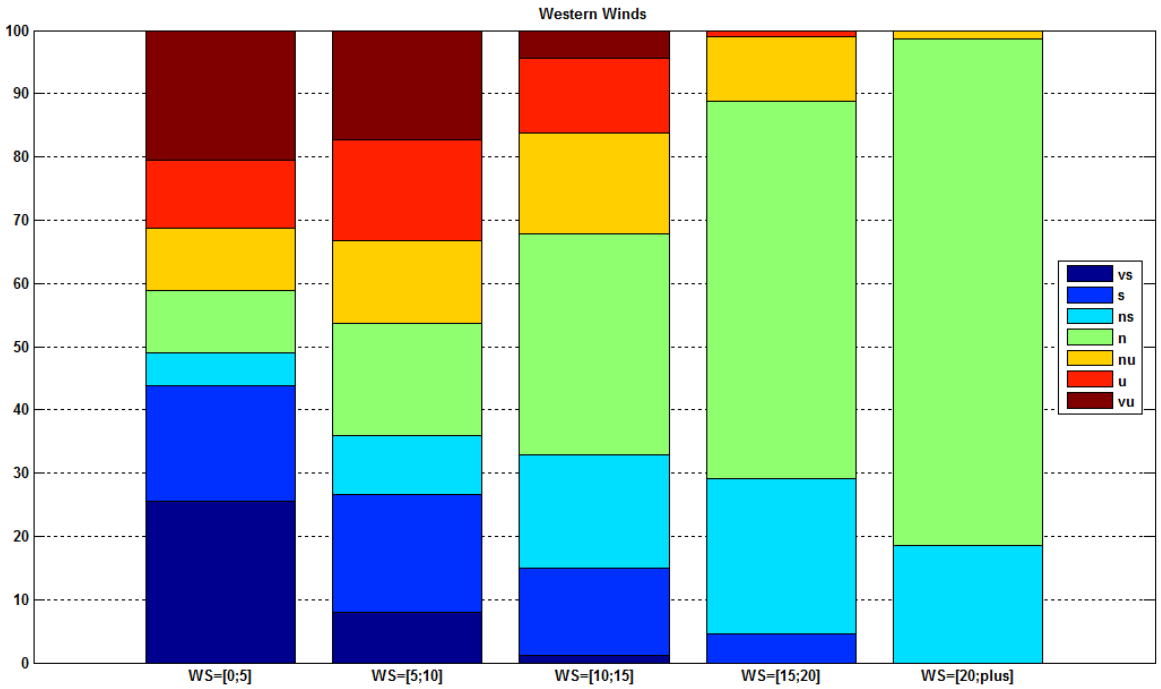

Figure 46: Evolution of stability distribution with wind speeds for western winds.

Neutral conditions become more and more dominant as the wind speed increases, but no clear trend is, however, observed regarding stable and unstable classes.

4.3.1 Turbulence intensity under different ABL stability conditions

As mentioned in the previous section, the eastern wind direction bin is here defined as 97±30 deg and the western wind direction bin as 277±30 deg. This bin size was selected to have enough data to plot curves with sufficient statistical significance. For the same purpose, the stability clases “Nearly Stable”, “Stable” and “Very Stable” have been merged into only one “Stable” class. The same was done for the unstable classes defined in Table 1.

For different stability classes, Fig. 47 and Fig. 48 shows the turbulence intensity plotted against wind speed for the undisturbed ambient situation as well as for the WF influenced situation.

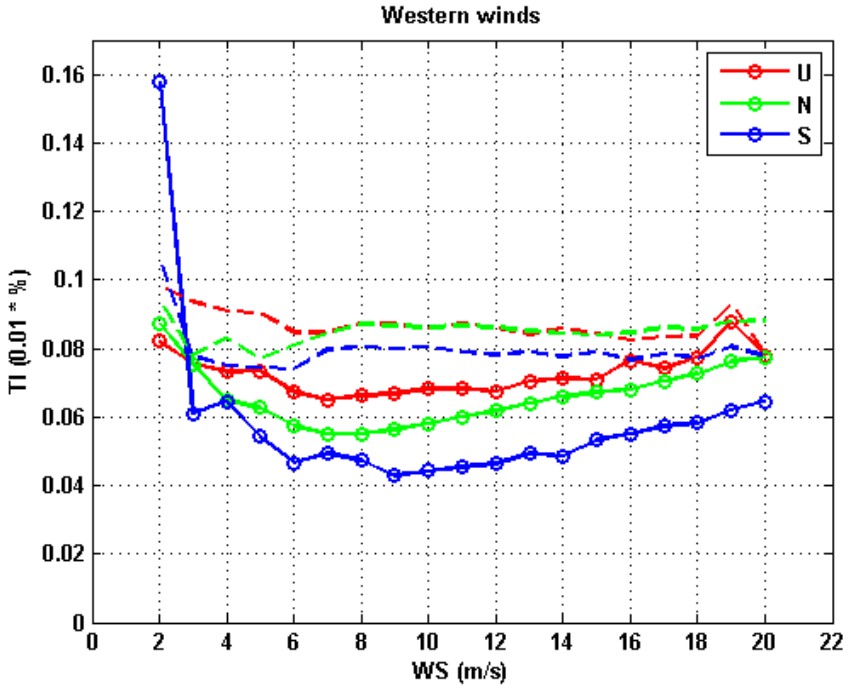

Figure 47: Turbulence intensities upstream (markers) and downstream (dashed lines) the WF for merged unstable; neutral; and merged stable classes for the western wind direction bin.

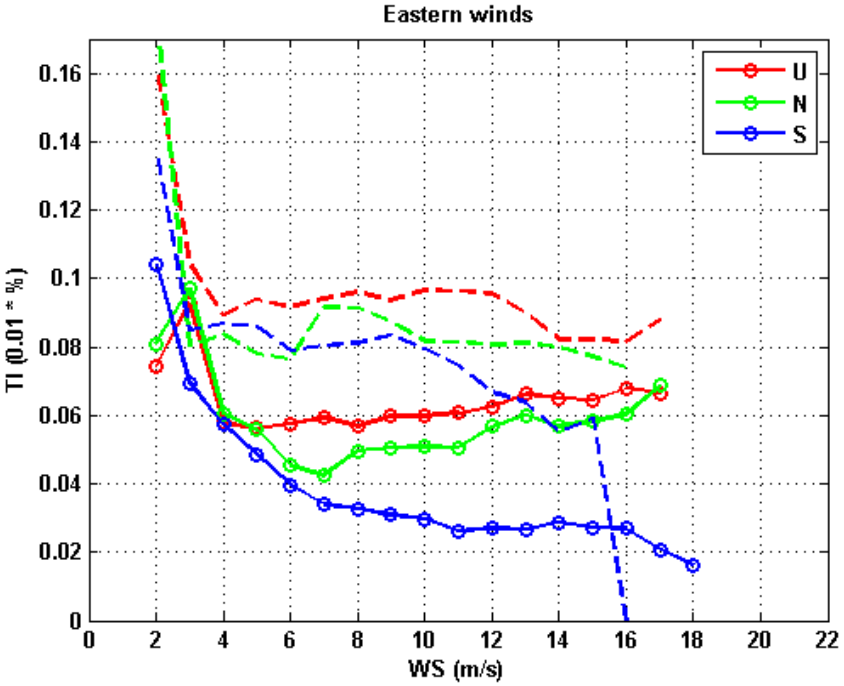

Figure 48: Turbulence intensities upstream (markers) and downstream (dashed lines) the WF for merged unstable; neutral; and merged stable classes for the eastern wind direction bin.

For eastern wind directions there is a clear difference between the three stability classes and in particular between the stable class and the two others. Western wind directions show a less significant difference between the stability classes, even though unstable classes generally correspond to higher turbulence intensity values. It is interesting to notice, that the WF seems to harmonize the turbulence intensity levels through the classes. This is clearly observed for western wind directions. It seems as if the turbulence induced by the WF in stable conditions balanced the increased ambient turbulence corresponding to the unstable case.

In order to understand the limited difference between turbulence intensities associated with specific stability classes (most pronounced for the western wind direction bin), the turbulence intensity level as a function of the stability class has been investigated in analogy with the investigation by Hansen et. al. [17].

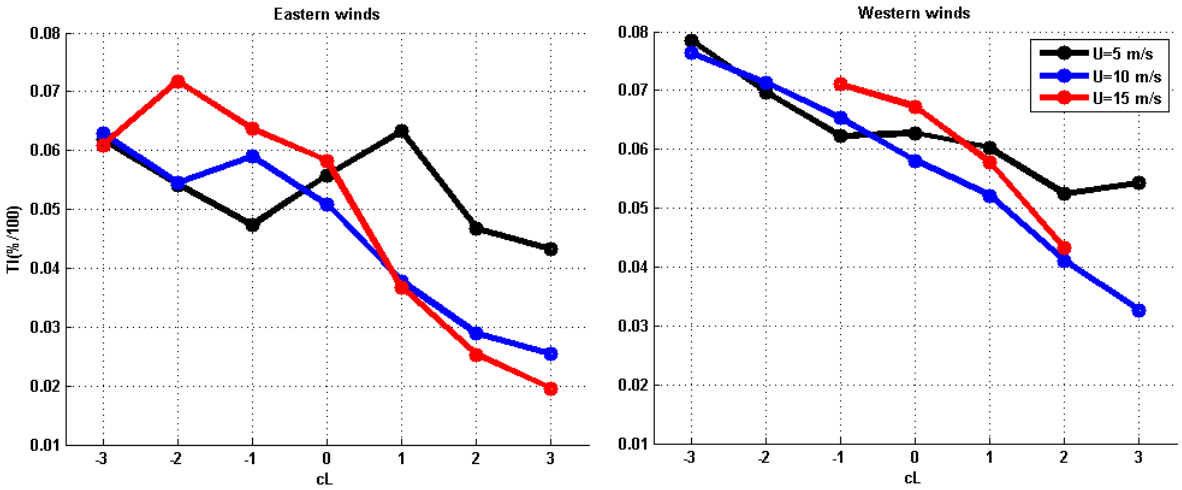

Figure 49: Turbulence intensity as a function of the atmospheric condition at different wind speeds.

Fig. 49 shows the variation of turbulence intensity with the Table 1 stability classes for different wind speeds. The curves associated with the eastern wind direction bin relates to mast M3, whereas the curves associated with the western wind direction bin relates to mast M2. For both direction bins, the turbulence intensity is not particularly wind speed dependant for classes from “very unstable” (i.e. cL = -3) to “nearly stable” (i.e. cL = 1) and more or less follow the same trends with similar intensity values. However for “stable” and “very stable” conditions (i.e. cL = 2 and cL = 3) we see a clear dependence on wind speed with very low turbulence intensity levels for high wind speeds.

This suggests that the classic ABL stability classification in respectively “stable”, “neutral”, and “unstable” conditions may not be appropriated to load related turbulence intensity considerations. Therefore, we take a different perspective and look at the same plot, but now dividing the atmospheric conditions, defined in Table 1, according to the following new classification: cL<1; cL=2; and cL=3. Fig. 50 shows plots corresponding to this new classification.

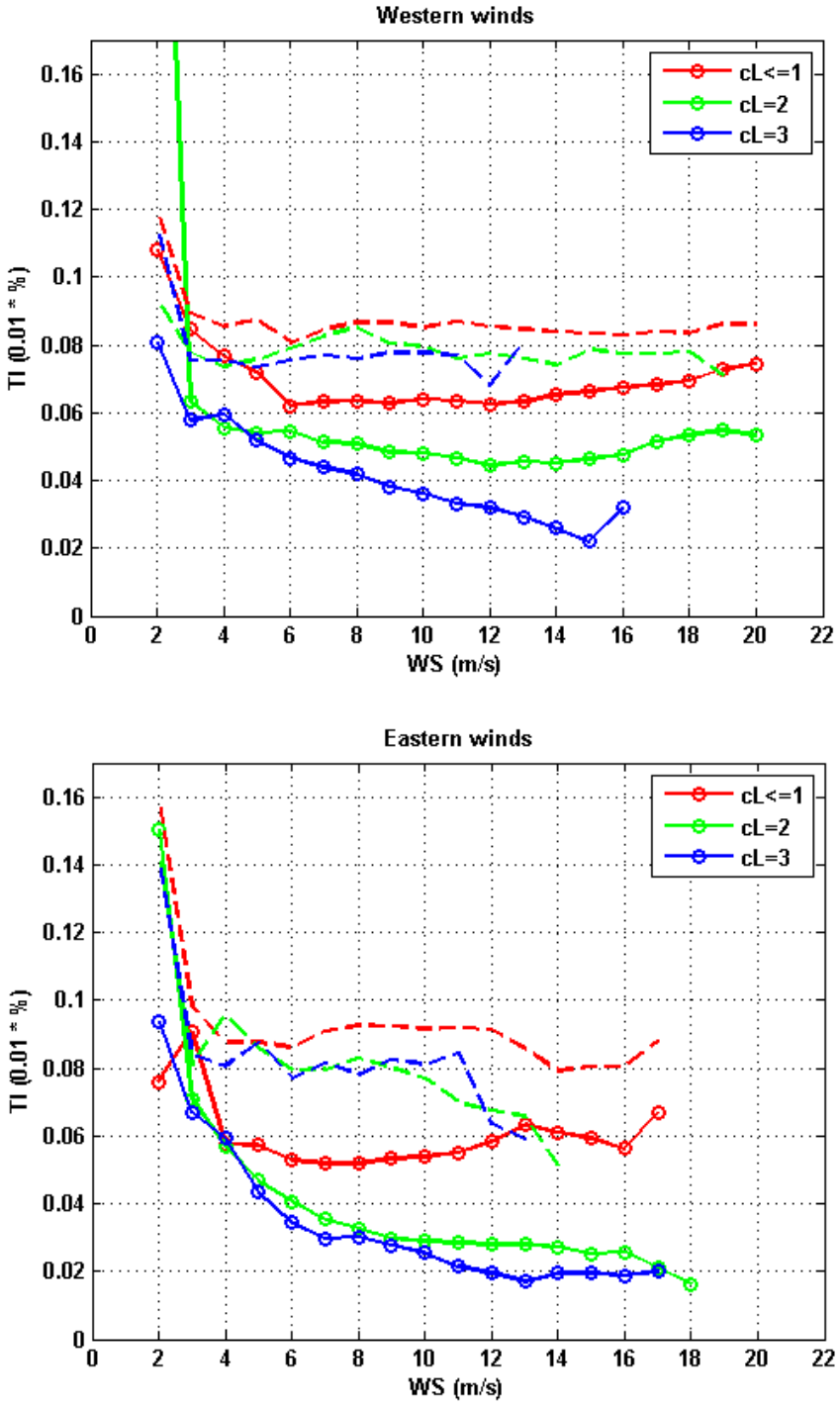

Figure 50: Turbulence intensities upstream (markers) and downstream (dashed lines) the WF for for cL<1, for cL=2, and for cL=3, respectively.

For western wind directions, the turbulence intensity differences between the new classes have significantly increased. The curve for cL<1 displays the same values and trends as the "unstable" curve

obtained for the classic (“unstable”, ”neutral”, ”stable”) classification. We actually overestimated the turbulence intensity in the “very stable” case by treating it the same way as the “stable” and the “nearly “stable” cases.

Again, the WF tends to harmonize the turbulence intensity level for the various atmospheric stability conditions. For eastern wind directions, the cL=2 (“stable”) and cL=3 (“very stable”) classes tend to more or less follow the same trends with similar intensity values. This actually shows that for the eastern winds the "classic" classification is of interest.

Even though the very modest dependence of turbulence intensity with ABL stability condition within the western wind direction bin got a bit clarified thanks to this new classification, it is still unclear, why we do not have the same behavior for eastern and western wind directions. Hansen et. al. [19] showed strongly different behavior for eastern and western wind directions as well. However, their study is based on Horns Rev measurements, where eastern wind directions are obviously influenced by the shore. As for the present study, it is not clear if shore is more east or west of the WF (cf. Fig. 51), and it should be noted that the data have been recorded before Rødsand 2 was established.

Figure 51: Geographic location of the Nysted WF.

Fig. 52 and Fig. 53 show the dependence of turbulence intensity with wind direction at M2 and M3.

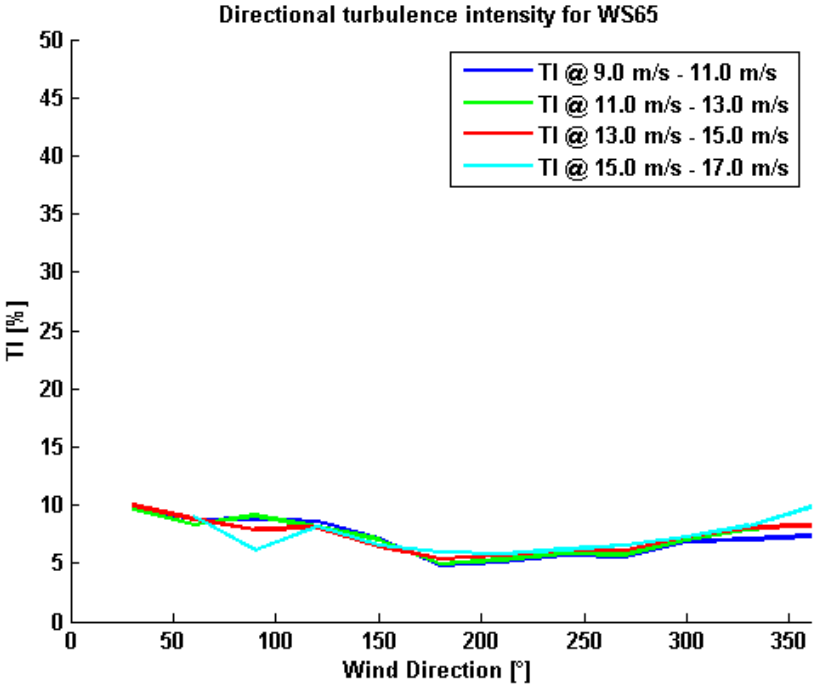

Figure 52: Directional turbulence at M2.

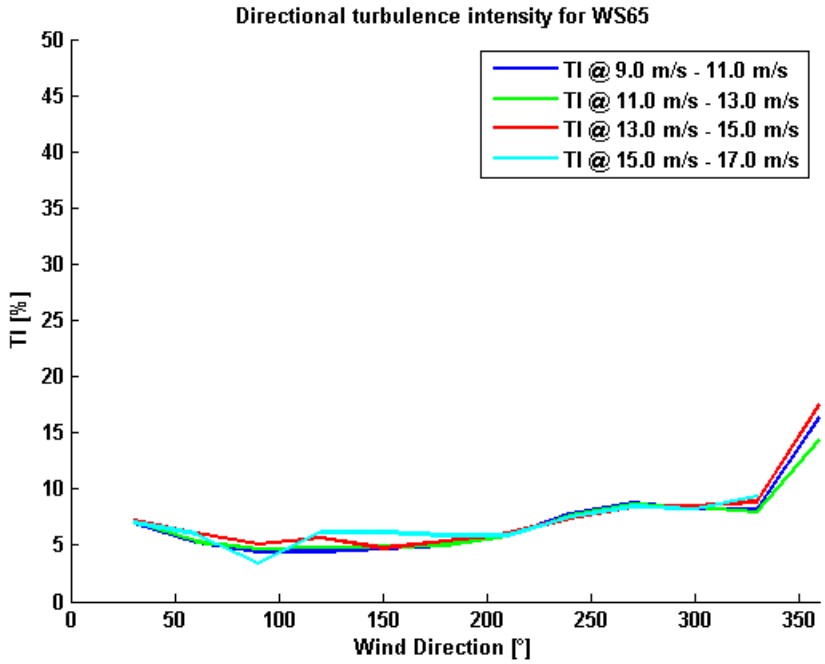

Figure 53: Directional turbulence at M3.

On mast M3 some mast effect on the turbulence measurements are observed for northern directions, but this can obviously not explain effects observed for eastern and western wind directions. Similar mast effects were not observed on M2.

4.4 Summary of findings based on the full-scale Nysted data

In summary, this study has quantified the impact of a WF on undisturbed ambient turbulence spectra. We found that the energy of the lateral and vertical turbulence components on frequency scales less than 0.005 Hz are not influences by the presence of a WF like the Nysted WF. Moreover, an analysis of spectra associated with the longitudinal turbulence component indicates, that the conventional code recommended approach to simulate wake affected turbulence fields might not be accurate. Further studies of WF turbulence intensity levels are, however, needed to fully clarify this issue. Finally, we observed, that the WF tends to harmonize the turbulence intensity levels among the stability classes.

5 Influence from ABL stability on WF production and loading

In this section we will demonstrate and verify the impact of various ABL stability conditions on wake dynamics, wake losses and turbine loading for two complete WF's using the DWM modeling approach, which is recently included in the IEC code as a recommended practice for description of wake affected flow fields. For this purpose we will make use of full-scale data from the Dutch Egmond aan Zee WF [58] as well as from the Swedish Lillgrunden WF. We will moreover investigate the capability of steady flow field modeling for WF production prediction.

5.1 WF production

Obviously, WF production prediction is a topic of utmost importance. WF production predictions are traditionally based on a *steady* description of the WF flow field assuming *neutral* atmospheric stratification, which usually suffices[4]. A large number of models within this model segment have been proposed ranging from simple engineering models to fairly complex CDF based models. Steady CFD models adapt the RANS approach, with the turbulence closure typically based on some variant of the Boussinesq approximation.

To justify the use of steady flow models for WF production prediction, as well as to validate the capability of the un-steady DWM model for such predictions, we will in this section compare model production predictions with full-scale production data from the Egmond aan Zee WF [14]. The un-steady DWM model is considered a medium-fidelity model, and as a representative for the steady modelling approach we will use another medium-fidelity model – the Fuga CFD model [59]. Fuga is a linearized RANS type of CFD model based on a mixed spectral formulation, which makes it approximately one million times faster than a conventional RANS CFD model and at the same time circumvent the problem of numerical diffusion. A dedicated turbulence closure allows buoyancy effects to be approximated in a simple and efficient manner.

Referring to a *steady* flow field description, buoyancy will affect the wake diffusivity such that the wake is more diffusive for *unstable* ABL stratification and less diffusive for *stable* ABL stratification. Buoyancy will for sure affect wake losses for specific wind directions, but whether it is necessary to include ABL stability to get a reliable estimate of *aggregated production* over the WF lifetime remains an open question outside the scope of this report. It will most likely be WF dependent, because both the site ABL stability climatology, the WF layout and the wind direction distribution are influencing factors.

[4] Use of *steady* flow fields are obviously not viable approach for WF load predictions, since WT fatigue loading is the combined result of periodic deterministic loading and un-steady stochastic loading (i.e. turbulence).

5.1.1 Egmond aan Zee WF

The Egmond Aan Zee WF is located outside the coast of the Netherlands, and it consists of 36 Vestas V90 3.0MW wind turbines installed on monopile foundations. The layout of the WF can be seen in Figure 54.

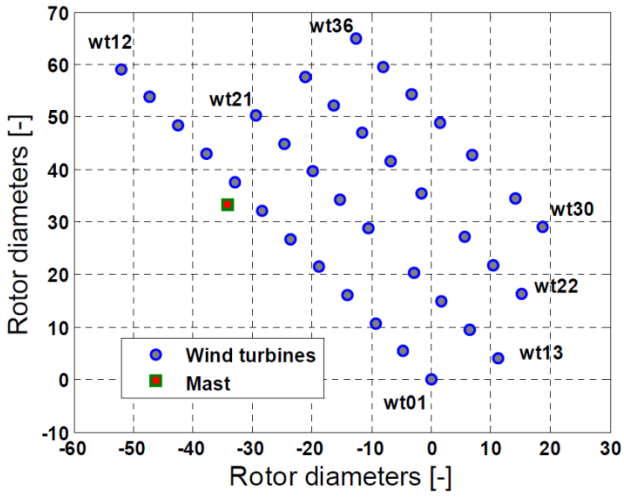

Figure 54: Layout of the Egmond aan Zee WF.

One meteorological mast is located at the site southwest of WT8, see Fig. 54, which is the dominant wind direction at the site. The wind speed and directions are measured at three heights 116m, 70m and 21m, where 70m corresponds to the turbine hub height. The wind direction sensors are calibrated based on power measurements of WT21, where a (local) minimum of the power production is expected at 196 deg. due to the layout of the wind farm. The calibration of the meteorological mast data is explained in details in [60], where an uncertainty level of 1.4 deg. on the final measured wind direction is concluded.

Due to wake disturbances, the recordings from the meteorological mast can unfortunately not be used for all wind directions. In such cases, undisturbed ambient wind directions and wind speeds are derived on the basis of WT SCADA data from WT's operating in free inflow conditions.

5.1.2 Measurements

The available set of measurements consists of approximately 6.000 10-minute average values. Although apparently being a large data set, it is somewhat limited considering that binning has to be performed in three dimensions – mean wind speed, mean wind direction and stability identifier. Therefore, quite crude bins have to be defined in order to secure a reasonable number of observations within each of these.

This has lead to the following binning approach: 1) *Mean wind speeds*, referring to 10-minute means, are projected on three bins – [5;7]m/s, [7;9]m/s and [9;11]m/s; 2) *Mean wind directions* refer to a sliding window averaging procedure, in which the sliding window, extending ± 5 deg. from a particular mean wind direction, is advanced in steps of 1 deg. for the full polar (i.e. from 0 deg. to 360 deg.). In this way we obtain an acceptable wind direction resolution, however, on the cost of multiple re-use of data wind direction wise; and 3) The *stability classes* defined in Tabel 1 are collapsed into only three merged classes, with "unstable" stratification now consisting of the Table 1 set of stability classes {-3,-2},

"neutral" stratification consisting of the Table 1 set of stability classes {-1,0,1}, and "stable" stratification consisting of the Table 1 set of stability classes {2,3}, respectively.

Using the above defined data classification approach the stability distribution, conditioned on wind direction, can be determined mean wind speed wise as shown in Fig. 55, Fig. 56 and in Fig. 57.

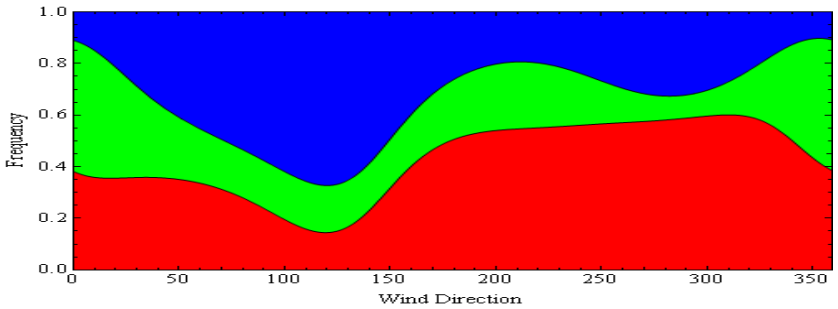

Figure 55: Distribution of stability conditions as function of wind direction for $U \in [5;7]$m/s. Blue refers to "stable", green refers to "neutral", and red refers to unstable".

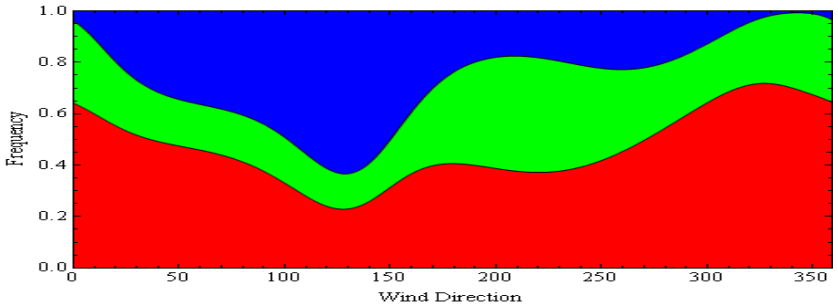

Figure 56: Distribution of stability conditions as function of wind direction for $U \in [7;9]$m/s. Blue refers to "stable", green refers to "neutral", and red refers to unstable".

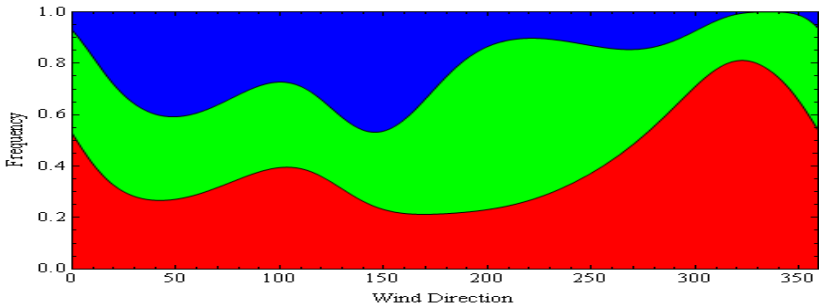

Figure 57: Distribution of stability conditions as function of wind direction for $U \in [9;11]$m/s. Blue refers to "stable", green refers to "neutral", and red refers to unstable".

It is evident that the stability condition, as expected, depends on upstream conditions (i.e. geographical direction and upstream fetch). It is noted that in general neutral stratification become more frequent with increasing wind speeds as also observed in section 4 for the Nysted data. However, for specific wind direction sectors the trend may be different as e.g. the NW sector, where unstable stratification become more frequent with increasing wind speed.

5.1.3 Simulations

For the three mean wind speed bins defined in section 5.1.2, the Egmond aan Zee WF production, covering the full wind direction polar (i.e. 0 deg. – 360 deg.), has been simulated using both the Fuga and the DWM approach. In both cases the median of the respective mean wind speed bins has defined the simulation mean wind speed. In Fuga, non-neutral ABL conditions are accounted for by linking the applied eddy viscosity closure to M-O length and height, whereas such conditions are accounted for in the DWM simulations by using turbulence fields originating from the "classic" Mann spectral tensor approximately adapted to the non-neutral conditions in question.

As for the DWM approach, the simulations were performed with a modified version of HAWC2, in which only the aerodynamics of a rigid rotor was included, in order to reduce the computational time. Thus, the effect of structural dynamics on wake formation and WT production was neglected, but the reduced code still includes a full implementation of the WT controller. Representing rotors by actuator disc's the WT structural dynamics is, of course, also neglected in the Fuga simulations.

The computational loads are significantly different for the two codes. With a direction resolution of 2 deg. the DWM simulations included 19440 10-minute aerodynamic rotor computations for each mean wind speed (i.e. 180×36×3 for 180 directions, 36 turbines and 3 stability classes), which equalize a computational load of approximately 24 hours on 20 processors. With a directional resolution of 1 deg. the Fuga computational setup included 1080 simulations (i.e. 360×3 360 directions and 3 stability classes) corresponding to a computational load less than 20 minutes on a standard PC.

5.1.4 Results

First WF production, aggregated over all wind stability conditions, will be investigated to consolidate the belief that *steady* flow field models suffice for WF production predictions. Simulations covering the full 0 deg. –360 deg. polar for the 8m/s mean wind speed bin have been compared with measurements in Fig. 58.

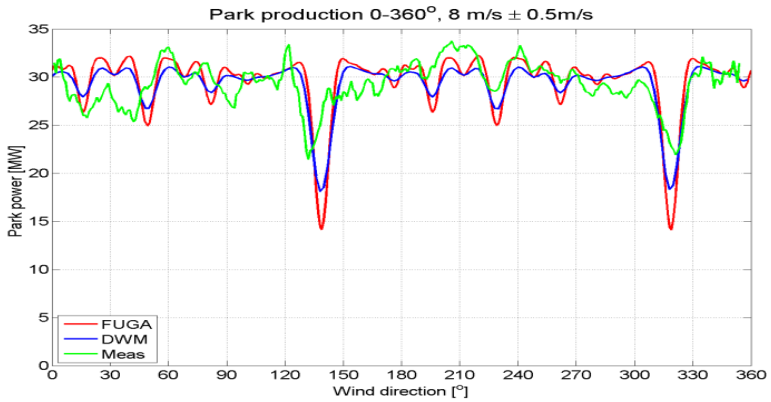

Figure 58: Egmond aan Zee WF production as function of mean wind direction.

Comparing the two model predictions a close agreement is seen. The only notable difference is that the direction variability are slightly smaller for the DWM results than for the Fuga results, which indicates that the directional "smoothening" caused by the "wake meandering" in the DWM model in this case is larger than the directional "smoothening" resulting from the Fuga eddy viscosity closure. However, if we average the WF production over all wind direction, assuming a uniform wind direction probability density function, we obtain a very close agreement between the two model predictions. Fuga and DWM predict a WF production of 29.56MW and 29.26MW, respectively, which equivalence a relative difference of only 1%.

Comparing simulations with measurements we see concordant power drops at wind directions corresponding to WF rows with 7D spacing (i.e. directions 139 deg. and 319 deg.) and WF rows with 11D spacing (i.e. directions 50 deg. and 230 deg.), respectively. However, the simulated drops are more significant than their measured analog. Power drops attributed to WF rows with 13D spacing (i.e. wind direction 16 deg. and 196 deg.) spacing can also be seen in the simulations, where these is more unclear in the measurements. For the simulations we notice, as expected, a π-symmetry for WF row directions. This is only recognized in the measurements for the 7D spacing row, and the measurements are in general more scattered in such aspects than the simulations. The general picture is though largely the same for simulations and measurements. Averaging the measured WF production over all wind directions, again assuming a uniform wind direction, we obtain 29.30MW, which is remarkably close to the predicted values of 29.56MW and 29.26MW, respectively.

The observed differences between simulations and measurements – e.g. differences in magnitudes of the 7D power drops – presumably relates to a multitude of reasons, among which the most important are believed to be:

1) The WF flow field is *not*, as assumed in any of today's micro-scale models, spatial homogeneous on a 10-minute scale, meaning that mean wind speeds and directions measured at one position in the WF differ from wind speeds and directions measured at another position within the WF. This effect is obviously increasing with the spatial scale of the WF, and with an extent of up to 7km the present WF is expected to be subjected to such effects. The impact from these spatial *in-homogeneities* on WF production arises from the fact, that the production of a WT is highly sensitive to the exact type of its wake operation (i.e. full wake or exact degree of partial wake operation). For spatial in-homogeneous WF flow fields no such thing as entire WF rows perfectly aligned in a wind direction context exists, whereby measured WF power drops at WF row directions are expected to be alleviated compared to their simulated analogue;

2) For a given mean wind speed and a given mean wind direction, the simulations assume stationary stochastic turbulence processes, whereas real life turbulence is *non-stationary*. For a given time span (e.g. 10 minutes), the non-stationary part introduces wind speed and direction trends at a given measuring point which, due to the inherent in-homogeneous character of WF flow fields, will vary within the WF; and

3) The turbulence modelling associated with the DWM approach is based on kinematic turbulence models, dedicated to describe the *initial sub-range* of the turbulence, and therefore not a priory expected to be able to account for meso-scale effects on wake meandering. This means that the energy on the large scales dictating the meandering process might be underestimated, which in turn will result in an underestimation of the meandering smoothening effect.

In an attempt to partly compensate for wind speed *trends* within bin's we will in the following present measured production measures relative to a power reference associated with the time span in focus. To further reduce the potential impact of spatial variability, we will define this power reference as a power production *mean* associated with a number of WT's operating in free ambient inflow conditions for a given wind direction.

The WF production, normalized as described above, is shown in Fig. 59 for the 10m/s mean wind speed bin.

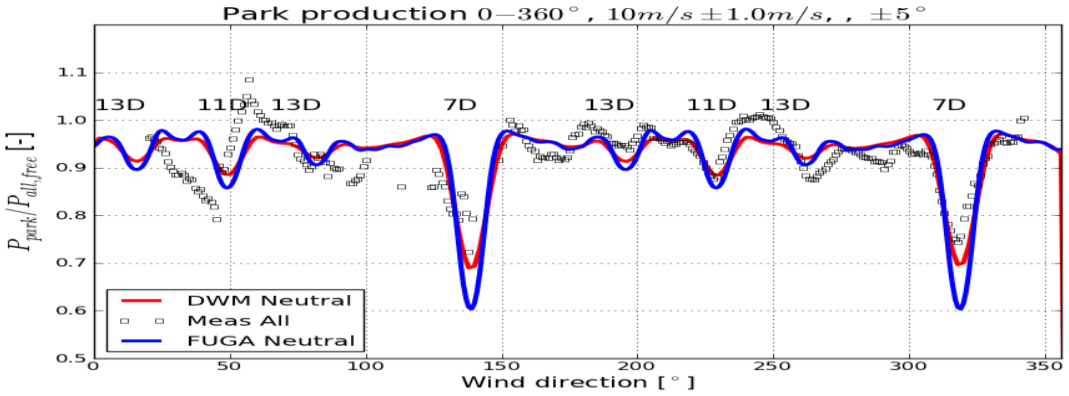

Figure 59: Normalized Egmond aan Zee WF production as function of mean wind direction.

As seen, the directional variability of the measurements seems somewhat reduced, but the power drops in the 7D row case is still more pronounced in the simulations than in the measurements.

We now turn to the impact of ABL stability on WF production. For this purpose, we have compared simulated and measured WF productions for the three collapsed ABL stability classes. For the 10m/s bin, the normalized WF production versus direction is shown in Fig. 60 for "unstable" ABL conditions.

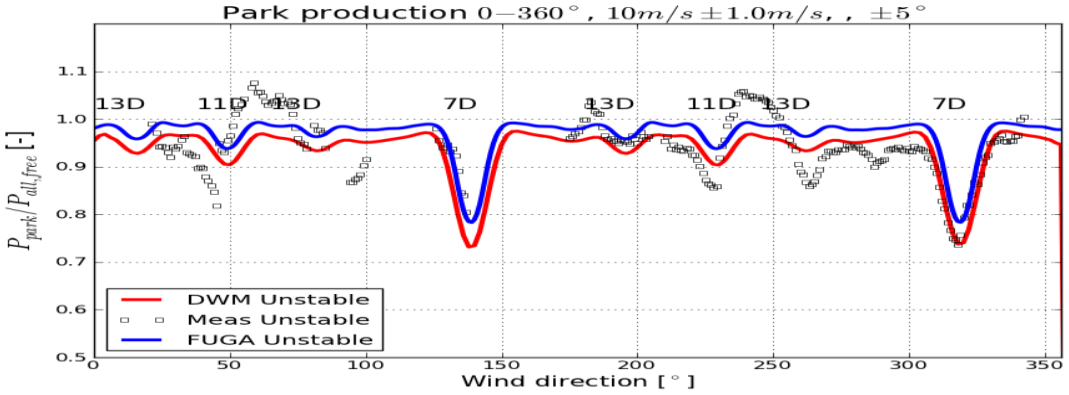

Figure 60: Normalized WF production versus mean wind direction for unstable ABL conditions.

The two model predictions are now slightly offset, with Fuga matching the 7D power drop at 139 deg., and DWM matching the 7D power drop at 319 deg., respectively. Due to limitations in the available data set not all wind directions are represented, and it is difficult to judge which of the two model prediction is the most accurate.

For the “neutral” ABL stability case, the normalized WF production versus direction is illustrated in Fig. 61 for the 10m/s bin.

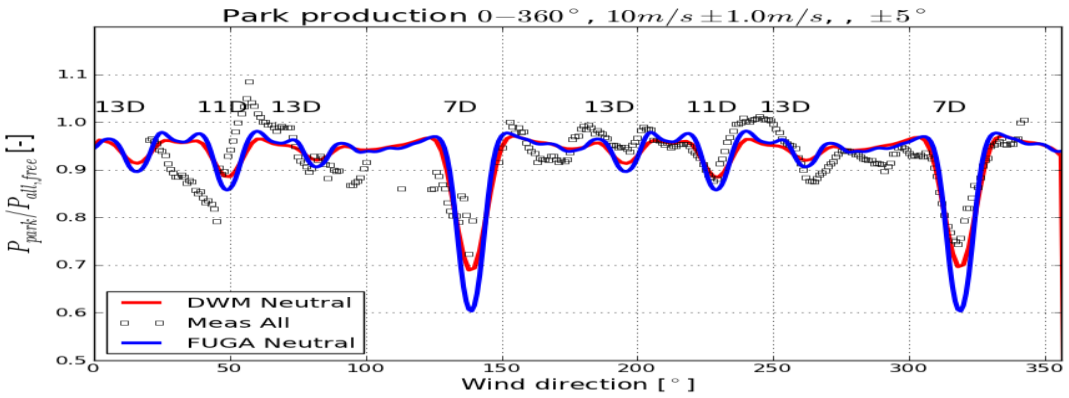

Figure 61: Normalized WF production versus mean wind direction for neutral ABL conditions.

No significant offset between model predictions is observed, but Fuga predicts slightly more directional variability than the DWM model. This is especially pronounced at the 7D power drops, where the DWM model predicts the measured power drops at 139 deg. and at 319 deg. better than the Fuga model. Both models underestimate the production variability in the direction regimes outside the 7D-directions, and again the model predicted π-symmetry is only approximately recovered in the measured data due to the reasons mentioned previously.

Finally, the “stable” ABL stability case is illustrated in Fig. 62, which shows the normalized WF production versus direction for the 10m/s bin.

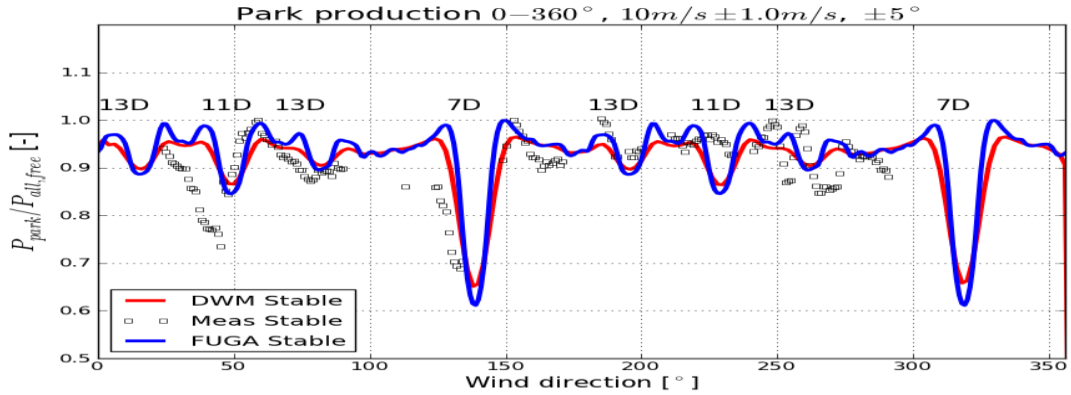

Figure 62: Normalized WF production versus mean wind direction for stable ABL conditions.

The directional variability predicted by Fuga is slightly increased when comparing with the “neutral” case, which is also intuitively expected due to less mixing and thus “sharper” wakes. This is also the case for the DWM predictions, although to a much lesser extent. The power drop at 139 deg. is better predicted by the DWM model, but the production variability in the in the direction regime extending from 150 deg. to 290 deg. is better predicted by Fuga.

In conclusion, a high degree of agreement between two very different simulation approaches is observed, both giving aggregated WF production estimates surprisingly closed to the measured value.

5.2 WF loading

During the project, Siemens Wind Power A/S kindly made a set of high-quality WT load measurement from the Lillgrunden WF available for detailed load analyses. These measurements are probably one of the most comprehensive sets of wake affected wind turbine load measurements ever recorded. The measurement period extends from 2008-06-03 to 2013-03-19 – i.e. over a period of almost 5 years.

5.2.1 Lillgrunden WF

The Lillgrund WF consists of 48 Siemens SWT-2.3-93 WT's, and one of these (C-8) is instrumented with strain gauges resolving blade, main shaft and tower loads, respectively. The layout of the WF is shown in Fig. 63.

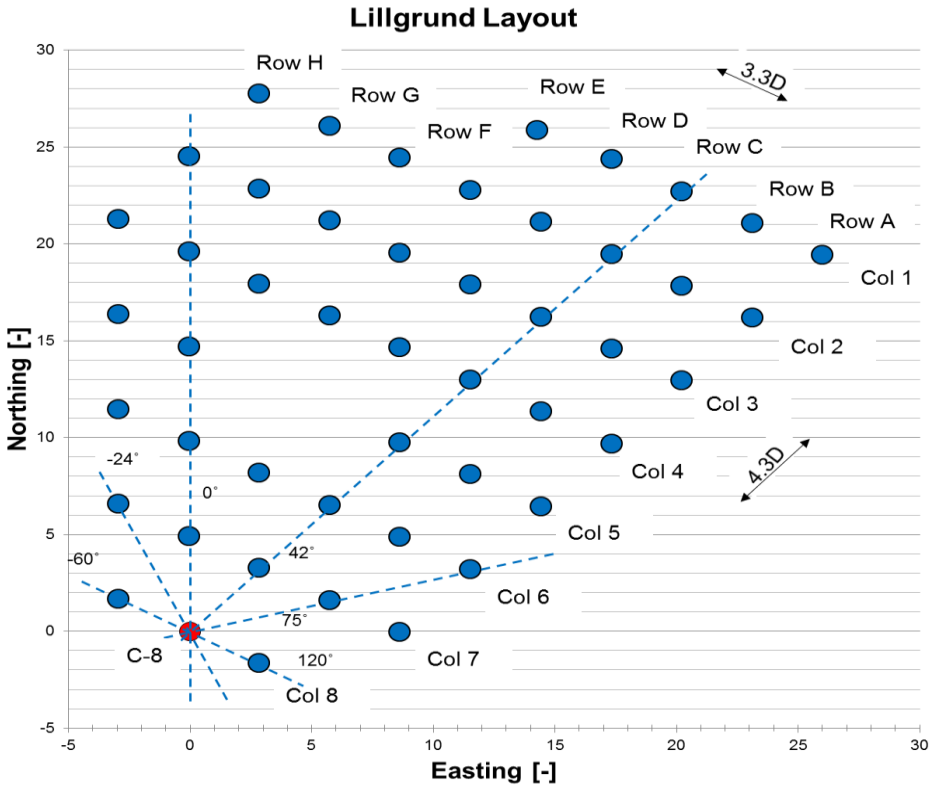

Figure 63: Layout of the Lillgrunden WF with the instrumented WT C-8 marked. Distances are non-dimensioned with the rotor diameter.

Whereas the Egmond aan Zee WF, investigated in section 5.1, is characterized by a "conventional" WT inter spacing, the layout of the Lillgrunden WF is characterized by very small WT inter spacing's – i.e. down to 3.3 D. This makes the Lillgrunden WF especially interesting and challenging as a wake-load validation case, because the close spacing magnifies wake generated load effects compared to more traditional spaced WF's.

5.2.2 Measurements

WT C-8 is instrumented with strain gauges resolving respectively the blade root flap bending moment, the main shaft bending moment and the tower base for-aft bending moment. In addition to these high-frequency data, WT SCADA data (pitch setting, rotational speed and electrical power) were available for the WF WT's during the measuring period. Unfortunately no meteorological mast data was available within the recording period, but as the WT power and pitch angle are directly correlated with the inflow wind speed, the ambient undisturbed wind speed has been determined as based on power and pitch angle recordings for corner placed WT's located in free inflow conditions. A similar philosophy was used for estimating the ambient undisturbed wind direction, which was determined from nacelle orientations of corner placed WT's. These nacelle orientations were initially calibrated against power deficit polar's constrained to directions, where wake losses were dominated by the closest neighboring WT's.

Full polar load cases, associated with normal WT operation, are available for mean wind speeds ranging from 6m/s to 16m/s, and the data have been classified into 2m/s velocity bins. The blade root flap moments and the tower bottom for-aft moments have been post processed to fatigue equivalent moments using the Palmgren-Miner approach and subsequently normalized with the respective fatigue equivalent moments associated with a inflow wind speed of 9m/s – i.e. here represented by mean equivalent moments associated with the velocity bin [8;10]m/s. Wöhler exponents of 5 and 10 were assumed for the tower and blade composite structures, respectively.

5.2.3 Simulations

For the DWM validation study the load response of WT C-8 is simulated for mean wind speeds reflecting the median of the defined velocity bins. Measured wind speed dependent turbulence intensities (TI's) are used, reflecting the offshore wind speed dependent "surface" roughness. However, no attempt is done to resolve TI as function of upstream fetch (i.e. direction). Thus, in the mean wind speed regime 6m/s-14m/s a TI of 5.8% is used – gradually increasing to 6.2% at 16m/s. As previously mentioned, both the deterministic and the stochastic part of the inflow are affected by ABL stability conditions. The deterministic mean wind shear and the stochastic turbulence input are described in the following.

Mean wind shear

The mean wind shear is stability dependent through the buoyancy impact on mixing in the ABL layer – in stable conditions with little mixing the shear profile gradient tend to increase, whereas in unstable conditions with increased mixing the shear profile tend to become more uniform.

In the IEC-61400 code [8] the *neutral* wind shear is specified in terms of a power law approach as

$$U(z) = U_{hub}(z/z_{hub})^{\alpha} \tag{5.2.1}$$

with U being the mean wind speed, z being the height above terrain, and z_{hub} being the hub height. The power exponent α is specified to 0.14 for an offshore site [61]. However, the new (not yet approved) revised version of the IEC code opens alternatively also for use of a log-profile defined as

$$U(z) = U_{hub}\frac{Ln(z/z_0)}{Ln(z_{hub}/z_0)} \tag{5.2.2}$$

with z_0 being the roughness length. The log-profile is physical consistent and used in M-O similarity theory and, as seen, it takes the value 0 at $z = z_0$ and the value U_{hub} at $z = z_{hub}$. However, a recommended

roughness length for offshore sites, consistent with the specifications of the power law exponent in equation (5.2.1), is not yet specified. We will therefore use equation (5.2.2) to introduce the effect of atmospheric stability in the power law description in an approximate manner.

As a first step we rewrite equation (5.2.2) as

$$U(z) = \frac{U_{hub}}{Ln(z_{hub}/z_0)} Ln(z/z_0) = \frac{u_*}{\kappa} Ln(z/z_0) \tag{5.2.3}$$

where the last identity provides the link to the conventional description of the log-profile, with u_* being the friction velocity, and κ being von Karman's constant (= 0.4), viz.

$$\frac{u_*}{\kappa} = \frac{U_{hub}}{Ln(z_{hub}/z_0)} \tag{5.2.4}$$

To establish a connection between the IEC specified power coefficient, α, and the roughness length, z_0, we will require the best possible agreement of respectively the power law profile and log profile over the vertical extent of the rotor, and we will define this best fit in terms of minimum least square deviation. For this purpose we define the functional Π as

$$\Pi(z_0) = {U_{hub}}^2 \int_{z_{hub}-R}^{z_{hub}+R} \left[\frac{Ln(z/z_0)}{Ln(z_{hub}/z_0)} - \left(\frac{z}{z_{hub}}\right)^{\alpha} \right]^2 dz \tag{5.2.5}$$

and define z_0 accordingly as the particular value, $\hat{z}_0$ (cf. Appendix B), that minimize the above functional, viz.

$$\hat{z_0} = \left\{ \hat{z_0} \,\middle|\, \Pi(\hat{z_0}) = \min_{z_0}\{\Pi(z_0)\} \right\} \tag{5.2.6}$$

Adopting M-O similarity theory, the mean wind shear in *stable conditions* is traditionally formulated as [16]

$$\begin{aligned} U(z) &= \frac{u_*}{\kappa}\left[Ln\left(\frac{z}{z_0}\right) - \psi_m^{(s)}\left(\frac{z}{L_M}\right)\left(1 - \frac{z}{2z_i}\right)\right] \\ &\approx \frac{u_*}{\kappa}\left[Ln\left(\frac{z}{z_0}\right) - \psi_m^{(s)}\left(\frac{z}{L_M}\right)\right] \\ &= \frac{u_*}{\kappa}\left[Ln\left(\frac{z}{z_0}\right) + 5\frac{z}{L_M}\right] ; 0 < z/L_M \ \leq 1 \end{aligned} \tag{5.2.7}$$

where L_M is the M-O length, z_i is the height of the atmospheric boundary layer, and $\psi_m^{(s)}$ is the stability function associated with stable stratification. Based on the reflections concerning the neutral shear profile, we will now "transform" relation (5.2.7) into a power law formulation for the stable ABL condition using eq. (5.2.6). The resulting expression is

$$U(z) = U_{hub}(z/z_{hub})^{\alpha} + \frac{5U_{hub}}{Ln(z_{hub}/z_0)}\frac{z}{L_M} ; 0 \leq z/L_M \ \leq 1 \tag{5.2.8}$$

where the value of the roughness length, z_0, will relate to the power law exponent as described in equations (5.2.5) and (5.2.6).

Again adopting M-O similarity theory, the mean wind shear under *unstable conditions* may be formulated as [16], [62]

$$U(z) = \frac{u_*}{\kappa}\left[Ln\left(\frac{z}{z_0}\right) - \psi_m^{(us)}\left(\frac{z}{L_M}\right)\right]$$
$$= \frac{u_*}{\kappa}\left[Ln\left(\frac{z}{z_0}\right) - Ln\left[\frac{1+x^2}{2}\left(\frac{1+x}{2}\right)^2\right] + 2Atan(x) - \frac{\pi}{2}\right]; -2 \le z/L_M < 0; \quad (5.2.9)$$
$$x = \left(1 - 16\frac{z}{L_M}\right)^{1/4}$$

Taking the same approach as for the stable stratification, we arrive at the following approximate expression when taking a power law approach

$$U(z) = U_{hub}\left(\frac{z}{z_{hub}}\right)^{\alpha} + \frac{U_{hub}}{Ln(z_{hub}/z_0)}\left[-Ln\left[\frac{1+x^2}{2}\left(\frac{1+x}{2}\right)^2\right] + 2Atan(x) - \frac{\pi}{2}\right]; \quad -2 \le z/L_M < 0 \quad (5.2.10)$$

where, as in the stable case, the value of the roughness length, z_0, relates to the power law exponent as described in equations (5.2.5) and (5.2.6).

Turbulence

Using the coupled DWM-HAWC2 platform [7] requires simulation of three different turbulence fields – a large scale turbulence field dictating the wake meandering, a traditional turbulence field accounting for conventional WT turbulence loading, and an isotropic and inhomogeneous small scale turbulence field accounting for WT loading caused by wake self generated turbulence. The wake self generated turbulence field is assumed to be invariant with respect to the ABL stability condition and is simulated using the classic Mann turbulence simulator [10]. The two remaining turbulence fields, which are highly dependent on ABL stability conditions, are generated based on the generalized buoyancy dependent spectral tensor [11],[13], which degenerate to the classic spectral tensor for neutral stability conditions. In all cases the turbulence fields are simulated as three dimensional fields resolved in suitable Cartesian grid configurations.

The parameters of the buoyancy dependent spectral tensor are for each stability class defined in Table 1, obtained from fitting model auto- and cross spectra to respective spectra obtained from full-scale sonic measurements from the Høvsøre site in Denmark. Fits are performed based on data recorded at 60m and 40m altitudes, respectively. For both altitudes, data associated with the [8;9]m/s mean wind speed bin were used for the parameter fitting. However, the fits at 40m seem to fit slightly better the full-scale data compared to the 60m data in especially the neutral and the unstable regimes. As 40m altitude moreover is more likely to be within the surface layer, where L_M is defined, than the 60m altitude (especially for stable stratification), it was decided to base input parameters to the generalized spectral tensor on the 40m data fits.

Except for the turbulence intensity (described by the $\alpha\varepsilon^{2/3}$ parameter *when* the remaining parameters have been fixed), it was further decided to adopt the (neutral) turbulence input specifications from the IEC code to [8] mimic the turbulence conditions at the Lillgrunden site, where no high-frequency meteorological measurements, as mentioned, are available. The IEC spectral tensor input parameters were originally obtained by fitting the spectral tensor spectra to a target Kaimal spectra [8].

Since we have decided to base the neutral turbulence generation partly on IEC specifications of turbulence tensor input (i.e. L, Γ – cf. section 3.2), the spectral tensor input parameters for neutral conditions do not match the fitted parameter values from the Høvsøre full-scale data. As a consequence, it was decided to scale (L, Γ) for the non-neutral (i.e. diabatic) conditions accordingly, although this approximation might not be completely true. However, it is believed to be a fair approximation – alternatively the neutral case could defined by the directly fitted values for L and Γ at the Høvsøre site, which is just another approximation to the Lillgrunden conditions. The relevant scaling factors, as well as the fitted values of Ri and η_θ (cf. section 3.2), are for each stability class given in Table 10 below.

Table 10: Scaling factors of ($\alpha\varepsilon^{2/3}$, L, Γ) relative to neutral conditions (indicated with subscript "neu") and specific values of (Ri, η_θ).

Stability Class	$\alpha\varepsilon^{2/3}/\ \alpha\varepsilon^{2/3}{}_{neu}$	L/L_{neu}	$\Gamma/\ \Gamma_{neu}$	Ri	η_θ
-3 (VU)	1,018518519	2,148640625	0,925195542	-0,00349989	0,00093093
-2 (U)	1	1,7584375	1,038538687	-0,0150151	0,000339836
-1 (NNU)	0,925925926	1,439839844	0,993302909	-0,0186692	0,0002
0 (N)	1	1	1	…	…
1 (NNS)	0,990740741	0,8984375	1,068211221	0,04	0,012
2 (S)	0,816648148	0,714277344	1,077575873	0,1	0,000341279
3 (VS)	0,462962963	0,255866406	1,074751047	0,0240355	0,00007

The turbulence input parameters for simulation of the stability dependent turbulence boxes is thus obtained by: 1) Selecting the (L_{neu}, Γ_{neu}) neutral set from the IEC specifications, which equals (33.6m, 3.9) for a large WT; 2) Determine the stability dependent (L, Γ) set using the scale factors defined in Table 10; and 3) Scale the turbulence intensity to match the measured levels using the following property of the generalized spectral tensor [11],[13]

$$\Phi_{ij}\left(\bar{k}, \alpha\varepsilon^{2/3}, L, \Gamma, Ri, \eta_\theta\right) = \alpha\varepsilon^{2/3}\Phi_{ij}\left(\bar{k}, 1, L, \Gamma, Ri, \eta_\theta\right) \qquad (5.2.11)$$

It should be noted, that identical values of the turbulence generation "seed" should be used for all stability classes.

The conventional HAWC2 turbulence scaling procedure is first to generate a turbulence box based on a specified (L, Γ) parameter set and an arbitrary (though positive) value of the variance level quantified by $\alpha\varepsilon^{2/3}$. The turbulence box is subsequently examined in the box center point corresponding to the turbine hub height, and a scaling factor is introduced that multiplied to all turbulence velocity vectors ensures that the prescribed variance level, in the examined point, comply with the requested the variance level. This procedure is a practical approach, which in a straight forward and easy way enables to simulate turbulence for a variety of sites, for which the $\alpha\varepsilon^{2/3}$ parameter are not obtainable from a direct spectral

fits (cf. section 3.2.2). However, it has the drawback that energy from the high frequency part of the spectra, which cannot be included in the turbulence box due to the discretization of the box grid, is transferred to the resolved frequencies, but also – and perhaps more important – that energy is transferred from the low frequency regime to other frequencies due to the limited statistical significance of the simulated low frequency spectral components, that may vary significantly from one realization to another. It is therefore fair to say that with the conventional HAWC2 scaling procedure the resulting turbulence spectrum is somewhat violated. In normal situations these drawbacks seem not to be a major issue, as frequencies up to 0.5Hz are included, and the missing energy on higher frequencies only has marginal influence on the overall load level. Frequency spectra for the turbulence boxes with both conventional and meandering turbulence are shown in Appendix C for the three different stability classes investigated in this study – i.e. stable, neutral and unstable with reference to Table 1. The target turbulence intensity is 6% for neutral conditions, 3.7% for stable conditions and 8% for unstable conditions.

An alternative – and perhaps more consistent – approach is to use a scaling factor based on the theoretical spectral tensor spectrum for neutral conditions. This is approach is used in the studies presented in sections 6 and 7, but not in the present load study. This is because we wanted to make this study a direct extension of a previous study for neutral conditions [63], where the conventional HAWC2 scaling was applied. However, differences between the two scaling approaches are expected to cause only minor changes to the results.

5.2.4 Results

The measured results are presented as scatter plots of fatigue equivalent moments versus ambient undisturbed wind direction. In general a huge scatter is observed in these results, which partly may be attributed to ABL stability effects. However, also other sources is likely to contribute such as air density variations, caused by seasonal variations, which might vary of the order of 10% and thus in turn may account for variations of fatigue equivalent moments of the order of 10%.

The first set of comparison between loads and measurements was reported at the EWEA offshore conference in 2015 [64]. A very fine agreement between simulated and measured blade flapwise bending loads was seen below rated wind speed, cf. Fig. 64. As the measurement database also covered load measurements at wind speeds above rated wind speed, it was possible to compared simulated and measured load in this regime also. To the author's knowledge, this is the first time ever that measured and simulated wake affected wind turbine loads have been compared above rated wind speed. The results, shown in Fig. 64, clearly demonstrate that the original implementation of the DWM model for multi-wake situations, as presented in [64], *under-predicts the load level in multi-wake situations above rated wind speed.*

This issue was further investigated in a paper presented at the EWEA onshore conference in Paris [63], where it was found that the pragmatic assumption of only including wake deficit contributions from the nearest wind turbine is only valid in the wind speed regime below rated wind speed, where a high thrust and turbulent mixing is present. Above rated wind speed the individual upstream emitted WT deficits are significantly reduced, and here it seem to be better to take a linear perturbation approach, which is consistent with limited wake deficit magnitudes. The (relevant) upstream emitted wake deficits is thus directly added, which is also consistent with the approach taken in the linearized CFD

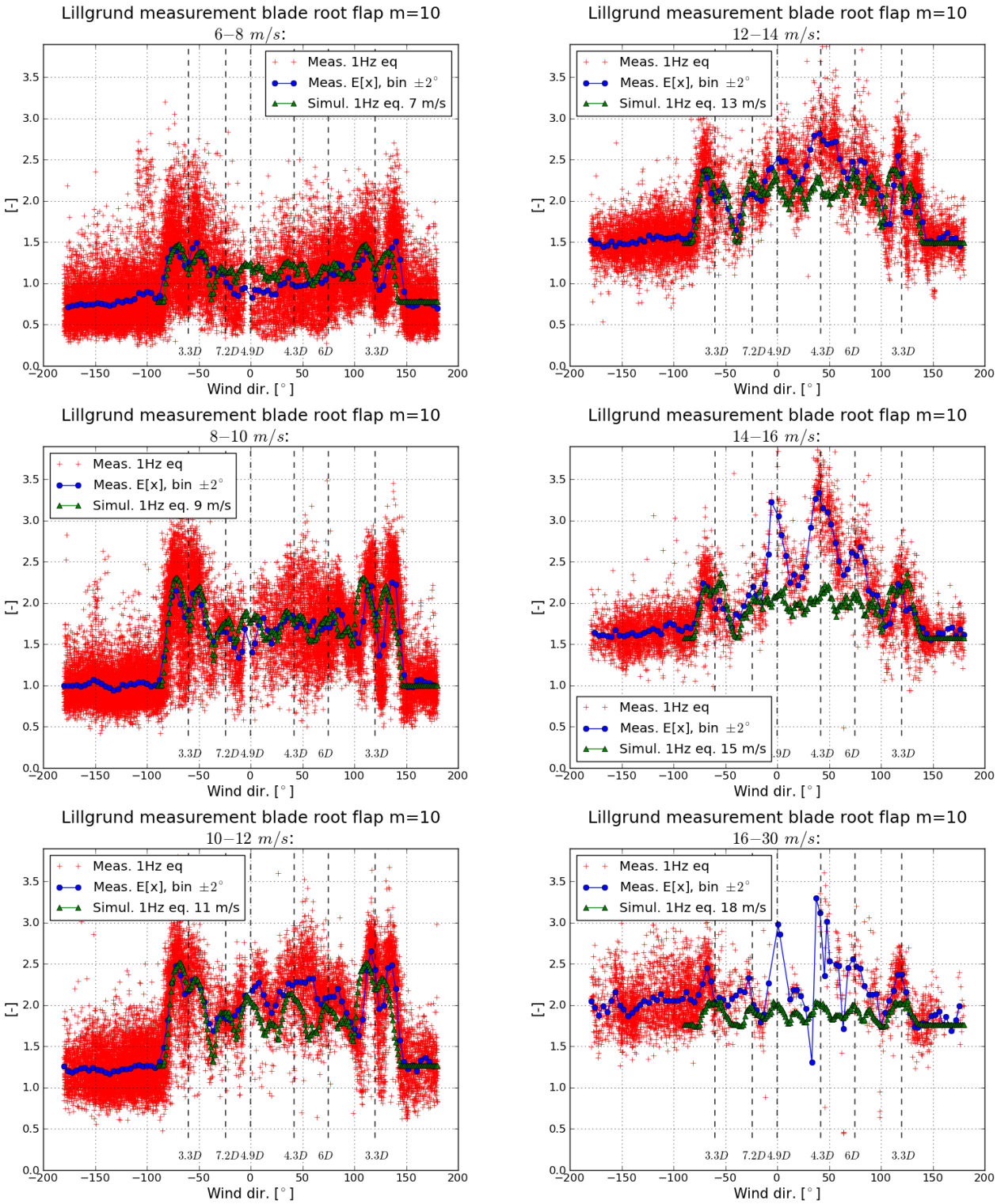

Figure 64: Comparison between measured and simulated flapwise blade root bending moments. A very fine agreement is seen below rated wind speed (left). A significant under-prediction in the multi-wake sector from 0deg. to 100deg. is seen above rated wind speed (right). From [64].

model Fuga [59]. The suggested perturbation approach resulted in a significant improved agreement between measured and simulated load above rated wind speed. This is shown in Fig. 65 for both blade root flapwise moments and tower bottom bending moments.

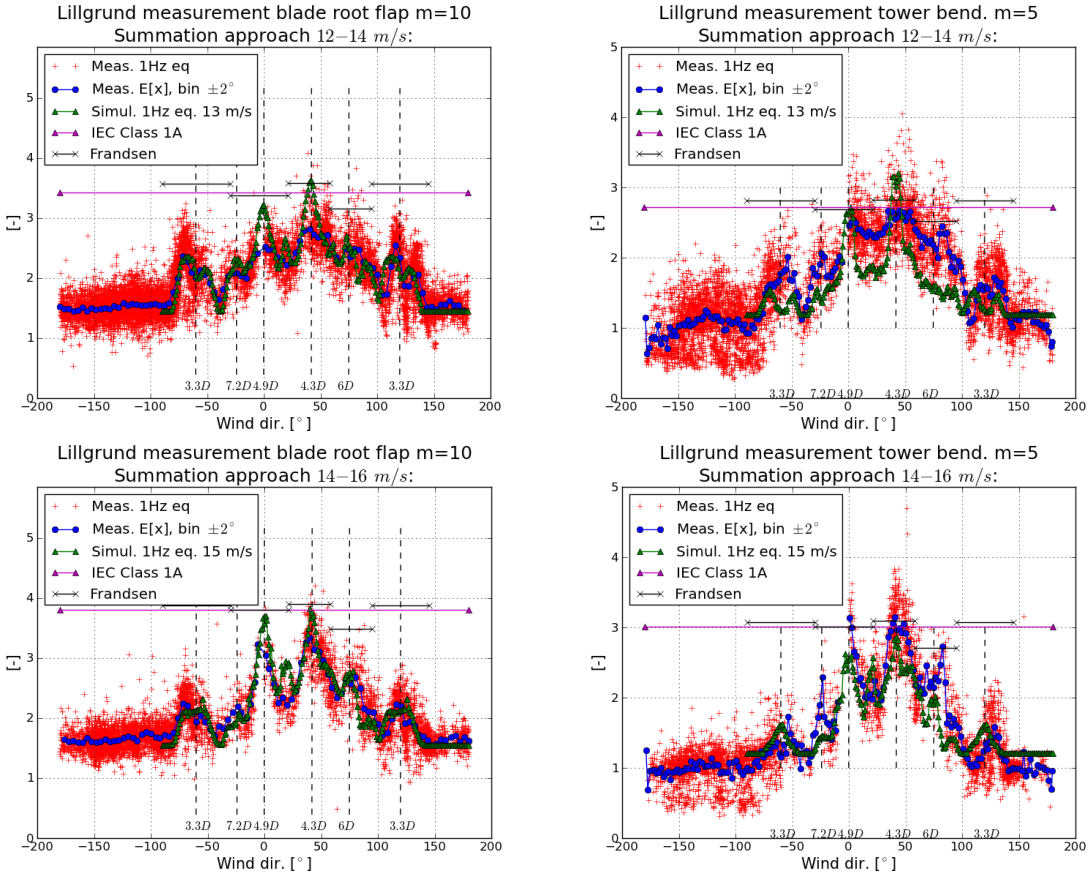

Figure 65: Comparisons of measured and simulated fatigue equivalent moments associated with above rated wind speeds. Using the linear perturbation approach a very fine agreement is obtained for both blade root flapwise moments and tower bottom for-aft moments.

The most recent contribution to the Lillgrunden serial is the inclusion of ABL stability affected turbulence and shear in the load simulations. As described in section 5.2.3 the same simulation procedure as in [63] has been adopted, however, now extended with shear and turbulence created for unstable (-2) and stable (2) conditions – cf. Table 1 for details. Even though temperature recordings covering the measurement period has been obtained from the Drogden lighthouse and corresponding stability levels have been derived, it was for practical reasons not possible to classify the load database according to the ABL stability classes mentioned above before deadline of this report. This work will be done in the future.

However, with the numerical predictions conducted for various ABL stability conditions, it is possible to get insight in how stability affects the load levels, and to what extend stability can explain the rather high scatter level in the measurements. Results are shown in Fig. 66 for below rated wind speed WT operation and in Fig. 67 for above rated wind speed WT operation.

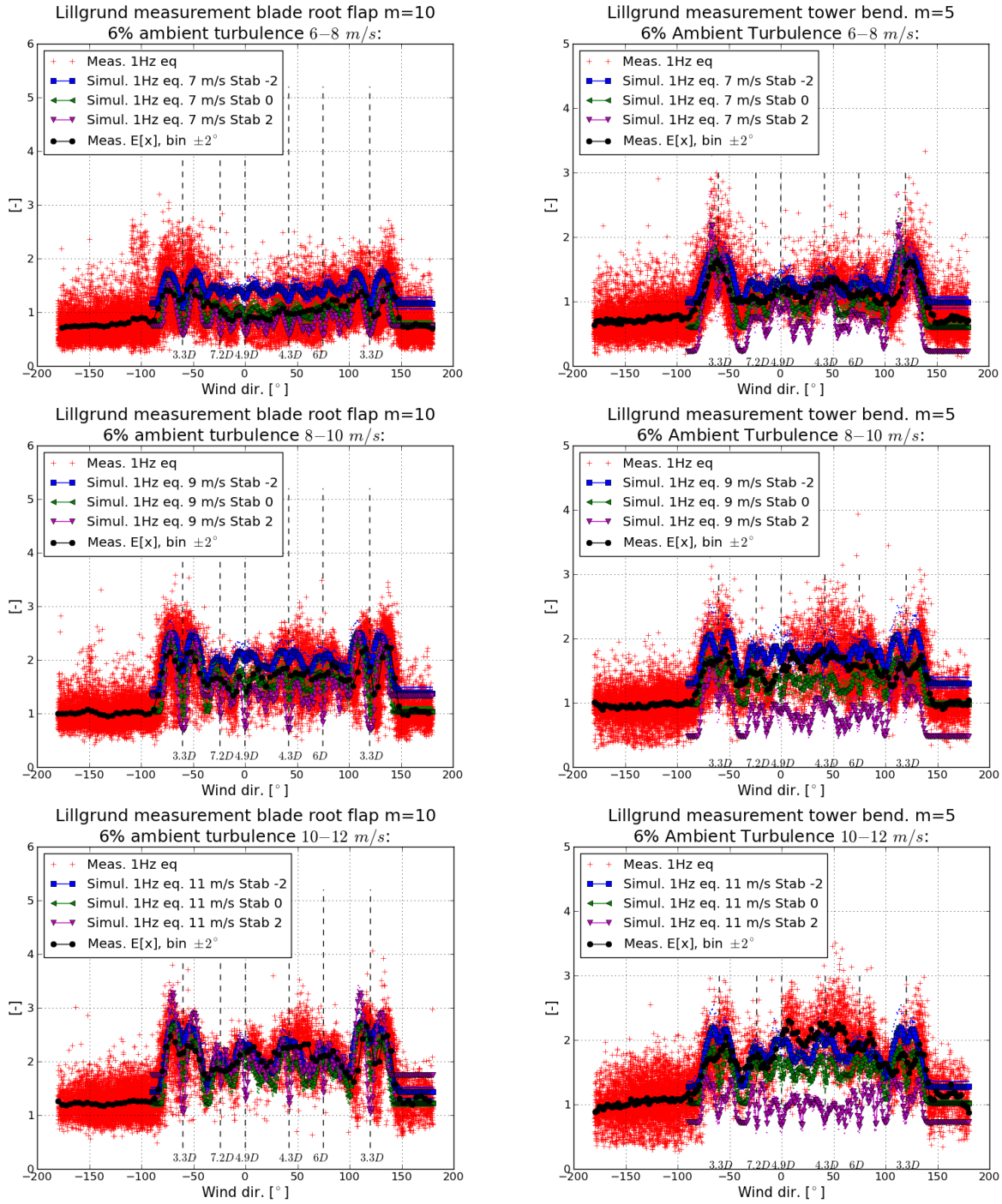

Figure 66: Comparison of measured and simulated fatigue loads for the C-8 turbine below rated wind speed. With reference to Table 1, simulations are conducted for unstable (-2), neutral (0) and stable (2) ABL stability conditions using the maximum deficit wake merging operator.

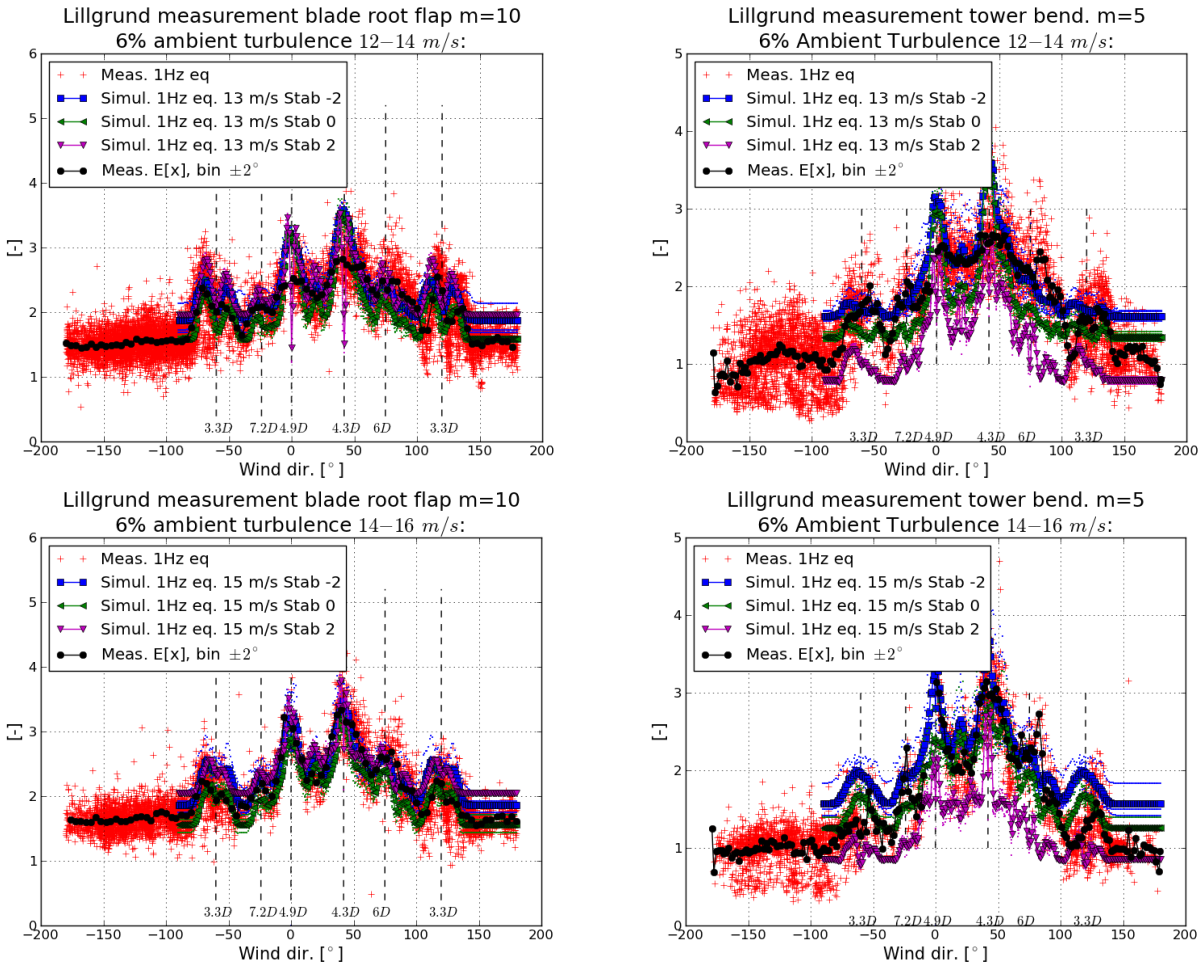

Figure 67: Comparison of measured and simulated fatigue loads above rated wind speed. With reference to Table 1, simulations are conducted for unstable (-2), neutral (0) and stable (2) ABL stability conditions using the linear perturbation deficit wake merging operator.

For all wind speeds it can be seen that the *tower bottom fatigue bending moments* are largest in unstable and smallest in stable ABL conditions. This is easily explained by the difference in turbulence intensity associated with the stability conditions, where unstable conditions causes a turbulence level of 9.8%, neutral conditions corresponds to a turbulence level of 6.0%, and stable conditions corresponds to a turbulence level of 1.99%.

In the inflow sector 150deg.-180deg., the investigated WT is not affected by upstream wakes, and it is thus possible to evaluate the impact from ABL stability on solitary WT loading. When observing the blade *flapwise fatigue loads* in this free sector, the results are significantly different than the tower fatigue loading. Contrary to tower loading, the blade loads are sensitive to both shear and turbulence levels, as both cause varying wind speeds over the rotor area. For rotating WT components these are *counter acting effects*, because stable conditions result in large shear and low turbulence intensity and vice versa for unstable conditions. For most wind speeds, it is seen that both stable and unstable conditions result in a

larger fatigue loads than the neutral case. The only exception is at very low wind speed, where neutral and stable conditions result in approximately identical fatigue load levels, whereas larger fatigue load levels are observed for unstable conditions.

In the wake affected conditions the same trend, with increased tower fatigue loads in unstable conditions and decreased tower fatigue loads in stable conditions, are seen. Also for wake affected inflow conditions the neutral situation seems to cause the smallest blade fatigue loads. However, for *single wake* situations it is interesting to notice, that stable ABL conditions result in both the largest fatigue load level (i.e. in a half-wake situations) and the smallest load level (i.e. in the full wake situation) compared to unstable and neutral ABL conditions. Finally, it is noted that a significant part of the observed measurement scatter potentially can be explained by ABL stability effects, especially remembering that very stable and very unstable stability effects are not included in the present results.

6 Wind turbine control under non-neutral stability conditions

In this chapter different controllers that are used in load simulations are explained. First the basic DTU controller is explained very briefly. This is the *base line* controller for generator torque and collective pitch control. Later, two more advanced controllers for reducing blade loads are explained – namely the individual pitch controller (IPC) and the individual flap controller (IFC). Finally a model based controller is derived and explained. This controller will be used for future research.

In this part, it will be explained how the IPC and IFC (either the classical controllers or the advanced model controllers) reduce the cyclic loads associated with the changes in the blade effective wind speed due to wind shear. The disadvantage of using individual blade controllers is the increased pitch activity (or flap activity). Therefore, an optimization problem can be formulated to assess the blade root bending moment loads and actuator activities and decide when to enable the IPC or IFC controllers. For example in situations where the wind shear is extreme (e.g. for very stable ABL conditions) and the blade effective wind speed thus varies significantly with the azimuth angle, the optimization can decide to enable the IPC or IFC controllers and therefore reduce the blade loads.

6.1 Base line controller

The DTU controller consists of two different controllers for the *partial load* region (i.e. operation below rated wind speed) and the *full load* region (i.e. operation above rated wind speed) as well as a switching mechanism that switches between these two controllers smoothly around the rated wind speed.

6.1.1 The partial load controller

As for the *partial load* controller a simple nonlinear controller based on measurements from the rotational speed of the rotor is used. The control objective in the partial load region is to generate maximum power. This is achieved by keeping the operating point of the WT at the maximum value of the CP curve (the power coefficient of the turbine). In order to do so, two parameters need to be fixed, the collective pitch of the blades and the tip speed ratio (TSR, the ratio between the speed of the tip of the blades and the wind speed). It is easy to keep the collective pitch constants at its optimal value. However, in order to keep the TSR constant, the rotational speed needs to be adjusted with the wind speed. Writing down the equation of TSR and equating it to the optimal value, it is easy to see that the rotational speed become a *linear* function of the wind speed. Therefore, one way of keeping the optimal TSR, is to use wind speed measurements, calculate reference rotational speed and then adjust the rotational speed to follow a reference value. This method is implemented in the DTU controller.

However, another more practical method of keeping the TSR constant is to adjust the generator torque as a nonlinear function of the rotational speed of the rotor. This is achieved by solving a one degree of freedom rigid body equation of motion of the rotor, while keeping TSR and CP values at their optimal values. Using this equation, we can calculate the generator torque as follows

$$Q_g = K\Omega^2 \tag{6.1.1}$$

in which K is calculated as

$$K = \frac{0.5\rho A R^3 C_p(\theta_{opt}, \lambda_{opt})}{\lambda_{opt}^3} \tag{6.1.2}$$

where Ω is the rotational speed of the rotor, ρ is the air density, A is the rotor swept area, R is the rotor radius, C_p is the power coefficient value at optimum pitch θ_{opt} and optimum tip speed ratio λ_{opt}.

6.1.2 The full load controller

As for the *full load* controller the objective is to keep the rotational speed and the generated power constant at their rated values. This is achieved by adjusting the collective pitch of the blades in response to errors in the rotational speed and, in some cases, additionally errors in the generated power. The gains of the PI controller are scheduled based on changes in the pitch angle to compensate for changes in the system due to changes in the operating point of the WT. Full details of the controller are given in [65].

6.2 Individual pitch controller

On a large WT the effective wind speeds on the individual blades can be different, and they change as the azimuth angle of the blades change. This is due to different effects such as wind shear, tower shadow and stochastic spatial distribution of the wind field. Difference in the effective wind speeds result in different loads on the blades, and therefore it is desirable to adjust pitch of the blades individually to mitigate these loads. It is possible to reduce the flapwise bending using individual pitch, and different model based and classical methods have been suggested to control the blades individually. Since individual pitch control (IPC) is inherently a multi-input multi-output (MIMO) problem, it would be natural to use MIMO model based control methods. However classical methods can still be used, and with some transformation of the measurement signals and control actions it is possible to use PI controllers to achieve results as good as the ones using MIMO model based methods. In this work we briefly explain the individual pitch controller used in the succeeding "design load" simulations. Flapwise blade root bending moments are used as the measurement signals, and three azimuth dependent pitch signals are calculated, which are subsequently superimposed with the collective pitch and used as the pitch references of the individual blades.

The three measurements obtained from the blade root bending moment sensors can be transformed into three signals that represent a mean value and two independent differential signals, respectively. This is achieved by transforming the signals from the non-rotating multi-blade coordinate to the rotating multi-blade coordinate. The mean value is controlled by the collective pitch controller and is therefore not considered in this controller. The IPC controller has to mitigate the two independent differential signals, called d-q signals

$$\begin{pmatrix} M_d \\ M_q \end{pmatrix} = \left(\frac{2}{3}\right) \begin{pmatrix} \cos(\theta) & \cos(\theta + \frac{2\pi}{3}) & \cos(\theta + \frac{4\pi}{3}) \\ \sin(\theta) & \sin(\theta + \frac{2\pi}{3}) & \sin(\theta + \frac{4\pi}{3}) \end{pmatrix} \begin{pmatrix} M_1 \\ M_2 \\ M_3 \end{pmatrix} \tag{6.2.1}$$

The signals M_1, M_2 and M_3 are measured by e.g. strain gauges, and the signals M_d and M_q are calculated using the equations above. Two PI controllers are used to mitigate M_d and M_q by calculating corresponding β_d and β_q values. The β_d and β_q values refer to rotating multi-blade coordinates and are subsequently transformed back to non-rotating multi-blade coordinates yielding three individual signals using the following equations

$$\begin{pmatrix}\beta_1\\ \beta_2\\ \beta_3\end{pmatrix} = \begin{pmatrix}\cos(\theta) & \sin(\theta)\\ \cos(\theta+\frac{2\pi}{3}) & \sin(\theta+\frac{2\pi}{3})\\ \cos(\theta+\frac{4\pi}{3}) & \sin(\theta+\frac{4\pi}{3})\end{pmatrix}\begin{pmatrix}\beta_d\\ \beta_q\end{pmatrix} \quad (6.2.2)$$

A block diagram of the controller is shown in Fig. 68.

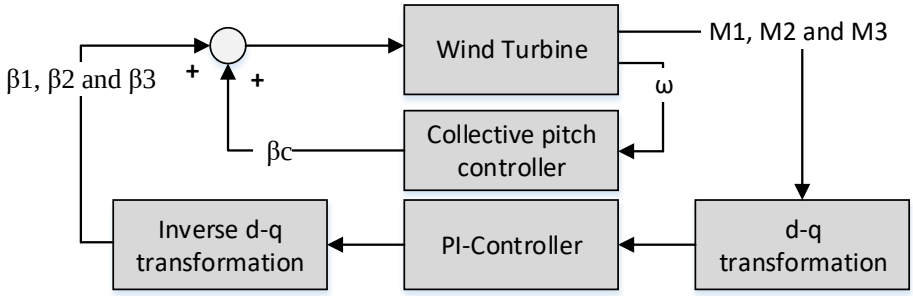

Figure 68: Block diagram of the individual pitch controller.

6.3 Individual flap controller

The individual flap controller (IFC) is another method of alleviating flapwise loads on the blades. The same principle as the IPC is used to transform the blade root bending moments in the non-rotating multi-blade coordinate to the rotating multi-blade coordinates. The same controller configuration as shown in Fig. 68 is used, except that the signals calculated are individual flap signals instead of individual pitch signals. More details on this controller can be found in [66].

6.4 Model predictive individual pitch control

In this section we report preliminary results of using LiDAR assisted model predictive individual pitch control of the DTU-10MW wind turbine. This is a preliminary study and demonstrates the potentials of using advanced model based controllers employing new technologies, such as LiDARs for better control of WT's. Some simplifying assumptions are taken, which will be explained in the upcoming sections.

Model predictive control (MPC) has been an active area of research and has been successfully applied on different applications in the last decades [67]. The reason for its success is its straightforward ability to handle *constraints*. Moreover it can employ *feed-forward* measurements in its formulation, which is a key feature we will employ in this work. This ability helps us to use LiDAR measurements in the controller. Besides, MPC can easily be extended to MIMO systems. WT control is basically a MIMO control problem, although traditionally the different inputs and outputs are paired, and separate control loops are used to overcome the control problem. In this work we treat the problem as a MIMO control problem, so the controller is aware of the interactions between different inputs and outputs and automatically compensate for this where necessary.

The main drawback of MPC is its on-line *computational complexity* which has kept its application to systems with relatively slow dynamics for a while. Fortunately with the rapid progress of fast computations, better optimization algorithms, off-line computations using multi-parametric

programming [68] and dedicated algorithms and hardware, its applications have been extended to even very fast dynamical systems such as DC-DC converters [69].

Basically MPC uses a model of the plant to predict plants future behavior in order to compute appropriate control signals to control outputs/states of the plant. To do so, at each sample time MPC uses the current measurement/estimates of outputs/states and solves an optimization problem. The result of the optimization problem is a sequence of control inputs, of which only the first element is applied to the plant, and the procedure is repeated at the next sample time with new measurements [70]. This approach is called *receding horizon control*. Therefore basic elements of MPC are:

- A model of the plant to predict its future;
- A cost function which reflects control objectives;
- Constraints on inputs and states/outputs;
- An optimization algorithm;
- The receding horizon principle.

Depending on the type of the model, which can be linear, hybrid and nonlinear, the control problem is called linear MPC, hybrid MPC and nonlinear MPC, respectively. Nonlinear MPC is normally computationally very expensive, and generally there is no guarantee that the solution of the optimization problem of MPC is a *global* optimum. In this work we extend the idea of linear MPC using a linear plant, whose parameters vary as a function of a scheduling variable. Besides, the disturbance to the system is known beforehand, and therefore the controller can take appropriate actions before the disturbance affects the outputs. There are some assumptions that restrict our solution to a specific class of problems. The scheduling variable is assumed to be known for the entire prediction horizon, and the operating point of the system mainly depends on the scheduling variable.

6.4.1 WT modeling

In order to design and simulate a closed loop system with a model based controller, we need two types of models. One model is the high fidelity simulation model, which should be as accurate as possible in modeling the overall behavior of the plant. This model includes all the possible nonlinearities and dynamics of the real system.

The second model is called the design model, which should be as simple as possible; yet it should be able to capture the most important dynamics and behavior of the system. Normally the design models are linearized and used locally around a linearization point. In the next two sections both the high fidelity simulation model and the linearized design model will be explained in details.

High fidelity simulation

In order to close the loop and test performance of the controller we need a simulation model. The simulation model behavior should be as close to the behavior of the real system as possible. Normally the simulation models include all degrees of freedom and the nonlinearities that can be modeled mathematically. There is the possibility of using different simulation models, developed by different research institutes, to verify closed loop behavior in different simulation scenarios. In this work FAST (Fatigue, Aerodynamics, Structures, and Turbulence) [71] is used as the simulation model, and the DTU-10MW reference wind turbine [72] is used as the plant. FAST is a publicly available program for simulating wind turbine behaviors. The FAST code is an aero-elastic simulator capable of predicting both the extreme and fatigue loads of two- and three-bladed horizontal-axis WT's. In the simulation model 10 degrees of freedom are enabled, which are: generator, drive train torsion, 1st and 2nd tower

fore-aft, 2nd tower side-side, 1st and 2nd blade flapwise and 1st blade edgewise degrees of freedom. The model structure is illustrated in Fig. 69.

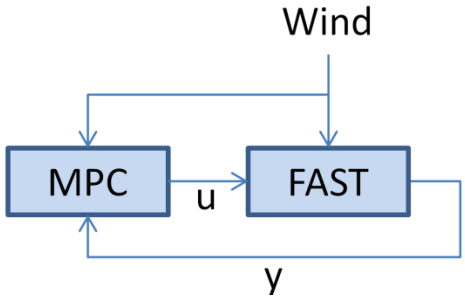

Figure 69: Closed loop system.

Design model

In this section the nonlinear model and important degrees of freedom are explained. Afterwards the linearization procedure is described, and a linear parameter varying model is derived for use in the model predictive controller.

For modeling purposes, the WT can be divided into four sub-systems: Aerodynamics sub-system, mechanical sub-system, electrical sub-system and actuator sub-system. The aerodynamic sub-system converts wind forces into mechanical torque and thrust on the rotor. The mechanical sub-system consists of drive train, tower and blades. The drive train transfers rotor torque to the electrical generator. The tower holds the nacelle and withstands the thrust force. Blades transform wind forces into toque and thrust. The generator sub-system converts mechanical energy to electrical energy, and finally the blade-pitch and generator-torque actuator sub-systems are part of the control system. To model the whole WT, models of these sub-systems are derived, and at the end they are connected together. Fig. 70 below shows the basic sub-systems and their interactions.

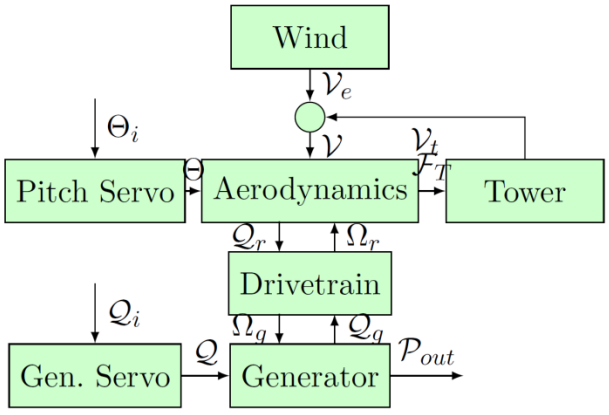

Figure 70: WT sub-systems.

The dominant dynamics of the WT come from its flexible structure. Several degrees of freedom can be considered to model the flexible structure, but for control design, just a few important degrees of freedom are usually considered. In Fig. 71 the basic degrees of freedom, which are normally being considered in

the design model, are shown. In this work we have considered two degrees of freedom – namely the rotational degree of freedom (DOF) and the tower fore-aft motion.

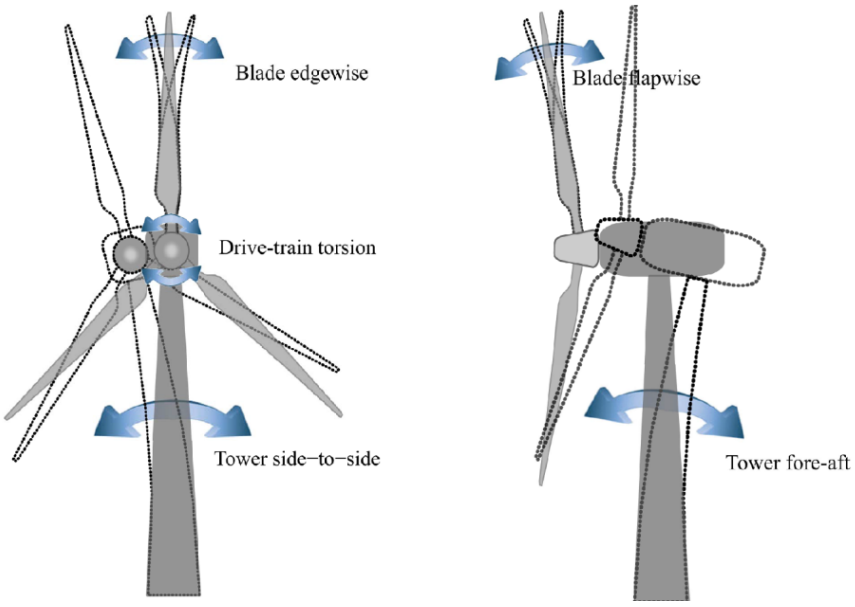

Figure 71: Basic degrees of freedom in a WT.

Nonlinearity of the WT model mostly comes from its aerodynamics. Blade element momentum (BEM) theory is used to numerically calculate aerodynamic torque and thrust on the wind turbine [73]. Having the aerodynamic torque and modeling the tower fore-aft degrees of freedom with simple mass-spring-damper, the whole system of equations with 2 elastic degrees of freedom becomes

$$\begin{aligned} J_r\dot{\Omega}_r &= Q_r - N_g\, Q_g \\ M_t\ddot{X}_t &= Q_t - C_t\,\dot{X}_t - K_t\,X_t \\ P_e &= Q_g\,\Omega_g \end{aligned} \tag{6.4.1}$$

in which Q_r and Q_t are aerodynamic torque and thrust. J_r is the rotor moment of inertia, Q_g is the generator torque, Ω_g is the generator rotational speed, and N_g is the gearbox ratio. The tower mass, damping and stiffness factors are represented by M_t, C_t and K_t, respectively, and P_e and X_t are the generated electrical power and tower displacement. Values of the parameters can be found in [72]. The torque and thrust are nonlinear functions of the rotor rotational speed Ω_r, the effective wind speed V_e and the blade pitch angle Θ.

$$\begin{aligned} Q_r &= \frac{1}{2}\frac{1}{\Omega_r}\rho\pi R^2 V_e^3 C_p(\Theta,\Omega_r,V_e) \\ Q_t &= \frac{1}{2}\rho\pi R^2 V_e^2 C_t(\Theta,\Omega_r,V_e) \end{aligned} \tag{6.4.2}$$

For controller design purposes we need to *linearize the nonlinear model* given in equation (6.4.1). The nonlinear terms are the aerodynamic torque and generated power. As mentioned before the aerodynamic

torque is a nonlinear function of effective wind speed V_e, rotational speed Ω_r and pitch of the blade Θ. This nonlinear function is determined by a look-up table. The look-up table is produced using blade element momentum theory (BEM). The generated power is nonlinear because it is a product of its two inputs, namely rotational speed and generator torque. The linearized state space model becomes

$$\begin{aligned}
\Delta Q_r(\omega,\theta,v_e) &= \underbrace{\frac{\partial Q_r}{\partial \omega}}_{\alpha_1}\Delta\omega + \underbrace{\frac{\partial Q_r}{\partial \theta}}_{\beta_{11}}\Delta\theta + \underbrace{\frac{\partial Q_r}{\partial v_e}}_{\beta_{12}}\Delta v_e \\
\Delta Q_t(\omega,\theta,v_e) &= \underbrace{\frac{\partial Q_t}{\partial \omega}}_{\alpha_2}\Delta\omega + \underbrace{\frac{\partial Q_t}{\partial \theta}}_{\beta_{21}}\Delta\theta + \underbrace{\frac{\partial Q_t}{\partial v_e}}_{\beta_{22}}\Delta v_e \\
\Delta P_e &= \underbrace{\frac{\partial P_e}{\partial \omega_g}}_{Q_{g0}}\Delta\omega_g + \underbrace{\frac{\partial P_e}{\partial Q_g}}_{\omega_{g0}}\Delta Q_g
\end{aligned} \tag{6.4.3}$$

in which the linearization is done as follows

$$\begin{aligned}
\left.\frac{\partial Q_r}{\partial \theta}\right|_{(\theta^*,\omega_r^*,v_e^*)} &= \left.\frac{1}{2}\frac{1}{\omega_r}\rho\pi R^2 v_e^3\frac{\partial C_p}{\partial \theta}\right|_{(\theta^*,\omega_r^*,v_e^*)} \\
\left.\frac{\partial Q_r}{\partial \omega_r}\right|_{(\theta^*,\omega_r^*,v_e^*)} &= \left.\frac{1}{2}\rho\pi R^2 v_e^3(-\frac{1}{\omega_r^2}C_p + \frac{1}{\omega_r}\frac{\partial C_p}{\partial \omega_r})\right|_{(\theta^*,\omega_r^*,v_e^*)} \\
\left.\frac{\partial Q_r}{\partial v_e}\right|_{(\theta^*,\omega_r^*,v_e^*)} &= \left.\frac{1}{2}\frac{1}{\omega_r}\rho\pi R^2(3v_e^2C_p + v_e^3\frac{\partial C_p}{\partial v_e})\right|_{(\theta^*,\omega_r^*,v_e^*)}
\end{aligned} \tag{6.4.4}$$

To get a linear model of the system we need to linearize the nonlinear model explained above around its operating points, which are determined by wind speed averaged over the rotor area. Wind speed changes along the blades and with the azimuth angle (angular position) of the rotor. This is because of wind shear, tower shadow and stochastic spatial distribution of the wind field. Therefore, a single wind speed does not exist to be used and measured in order to find the operating point. We bypass this problem by defining a fictitious variable called effective wind speed (v_e), which characterizes the effect of wind on the rotor disc of the WT. Using the linearized aerodynamic torque and thrust, state space matrices for the 3 DOFs linearized model become

$$\begin{aligned}
\dot{\omega}_r &= \frac{\alpha_1(v_e)}{J_r}\omega_r + \frac{\beta_{11}(v_e)}{J_r}\theta + \frac{\beta_{12}(v_e)}{J_r}(v_e - v_t) - Q_g \\
\dot{x}_t &= v_t \\
\dot{v}_t &= \frac{\alpha_2(v_e)}{M_t}\omega_r + \frac{\beta_{21}(v_e)}{M_t}\theta + \frac{\beta_{22}(v_e)}{M_t}(v_e - v_t) - \frac{C_t}{M_t}v_t - \frac{K_t}{M_t}x_t \\
P_e &= Q_{g0}\omega_g + \omega_{g0}Q_g
\end{aligned} \tag{6.4.5}$$

in which the lower-case variables are deviations away from the steady state of the upper-case variables given in the first three equations. Consequently, the parameters of the linearized model are functions of wind speed, which in our approach acts as a scheduling variable. A detailed description of the model and linearization is given in [74].

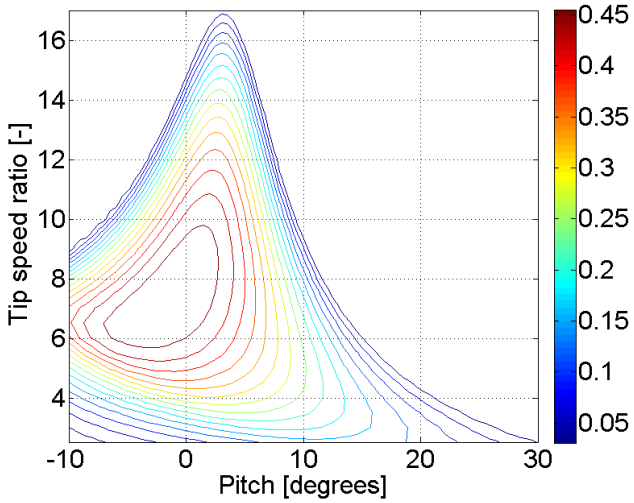

Figure 72: Cp curve of the WT.

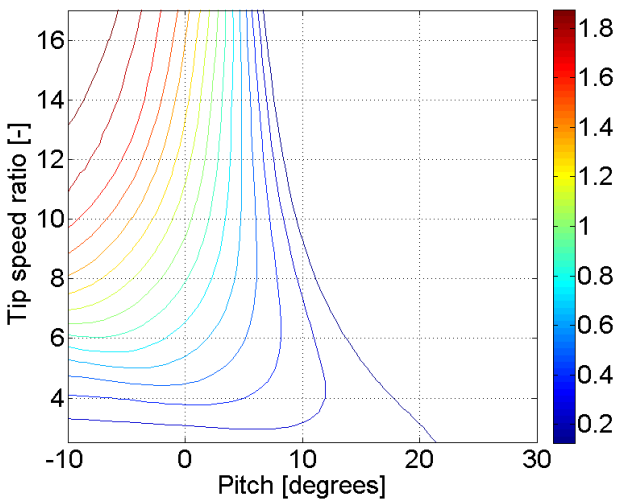

Figure 73: Ct curve of the WT.

According to the model described by the system of equations (6.4.5), the matrices of the state space model become

$$A(\gamma) = \begin{pmatrix} \frac{\alpha_1(v_e)}{J_r} & 0 & \frac{\beta_{12}(v_e)}{J_r} \\ 0 & 0 & 1 \\ \frac{\alpha_2(v_e)}{M_t} & -\frac{K_t}{M_t} & -\frac{C_t}{M_t} \end{pmatrix} \tag{6.4.6}$$

$$B(\gamma) = \begin{pmatrix} \frac{\beta_{11}(v_e)}{J_r} & \frac{\beta_{12}(v_e)}{J_r} \\ 0 & 0 \\ \frac{\beta_{21}(v_e)}{M_t} & \frac{\beta_{22}(v_e)}{M_t} \end{pmatrix} \tag{6.4.7}$$

$$C(\gamma) = \begin{pmatrix} 1 & 0 & 0 \\ Q_{g0} & 0 & 0 \\ \frac{\beta_{22}(v_e)}{M_t} & -\frac{K_t}{M_t} & -\frac{C_t}{M_t} \end{pmatrix} \tag{6.4.8}$$

$$D(\gamma) = \begin{pmatrix} 0 & 0 \\ 0 & \omega_0 \\ \frac{\beta_{21}(v_e)}{M_t} & \frac{\beta_{22}(v_e)}{M_t} \end{pmatrix} \tag{6.4.9}$$

in which $x = (\omega_r \quad x_t \quad \dot{x}_t)$, $u = (\theta \quad Q_g)$, $y = (\omega_r \quad P_e \quad \dot{x}_t)$ are states, inputs and outputs, respectively. Now that we have the *linearized state space model* of the system, we can proceed to use this model in the control design procedure.

6.4.2 Controller design

In this section we begin by explaining model predictive control (MPC) and different components of it in general. Then we will present the linear MPC formulation. After explaining linear model with known disturbance, we will explain how the MPC problem of such system with can be formulated.

Model predictive control

Generally the nonlinear dynamics of a plant can be modeled with the following difference equation

$$x_{k+1} = f(x_k, u_k, d_k) \tag{6.4.10}$$

with x_k, u_k and d_k being states, inputs and disturbances, respectively. Using the nonlinear model, the nonlinear MPC problem can be formulated as

$$\begin{aligned} \min_{u} \quad & \ell(x_N) + \sum_{i=0}^{N-1} \ell(x_{k+i|k}, u_{k+i|k}) \\ \text{Subject to} \quad & x_{k+1} = f(x_k, u_k, d_k) \\ & u_{k+i|k} \in \mathbb{U} \\ & \hat{x}_{k+i|k} \in \mathbb{X} \end{aligned} \tag{6.4.11}$$

where l denotes some arbitrary norm and U and X show the set of acceptable inputs and states. As it was mentioned, this problem is computationally too expensive, because of the nonlinear model. One way to avoid this problem is to linearize around an equilibrium point of the system, and then use the linearized model instead of the nonlinear model. We can also employ the fact that we know the future values of the disturbance to the system, namely the wind speed.

Linear MPC formulation

The problem of linear MPC can be formulated as

$$\begin{aligned} \min_{u_0, u_1, \ldots, u_{N-1}} \quad & \|x_N\|_{Q_f} + \sum_{i=0}^{N-1} \|x_{k+i|k}\|_Q + \|u_{k+i|k}\|_R \\ \text{Subject to} \quad & x_{k+1} = Ax_k + Bu_k \\ & u_{k+i|k} \in U \\ & \hat{x}_{k+i|k} \in X \end{aligned} \tag{6.4.12}$$

Assuming that we use norms 1, 2 and ∞, the optimization problem becomes convex, provided that the sets U and X are convex. Convexity of the optimization problem makes it tractable and guarantees that the solution is the global optimum. The problem above is based on a single linear model of the plant around one operating point. However, for some plants the assumption of a linear model does not hold for long prediction horizons. This is because the plant operating point changes, for example on the basis of disturbances that act as a scheduling variable. An example could be a WT for which wind speed acts as a scheduling variable and changes the operating point of the system.

WT control is a challenging problem as the dynamics of the system changes based on wind speed, which has a stochastic nature. Here we use the wind speed as the scheduling variable. With the advances in the LiDAR technology [75], it is possible to measure wind speed ahead of the turbine, and this enables us to have the scheduling variable of the plant for the entire prediction horizon. As it was mentioned in section

before, wind turbines are nonlinear dynamical systems, and if we use the nonlinear model directly in the MPC formulation, the optimization problem associated with the MPC becomes non-convex. In general, non-convex optimization problems are very complicated to solve, and there is no guarantee that we could achieve a global optimum. One way to avoid complex and non-convex optimization problems is to linearize the system around an equilibrium point, and then use the obtained linearized model as an approximation of the nonlinear model. However, for WT's the assumption of the approximate linear model does not hold for long prediction horizons. This is because the operating point of the system changes as a function of wind speed which, as mentioned, has a stochastic nature. In the next section we formulate the MPC problem using the linearized state space model with varying parameters as a function of wind speed.

Linear LPV formulation with wind speed dependent parameters

The linear parameter varying (LPV) model of the nonlinear system is of the following form

$$\tilde{x}_{k+1} = A\tilde{x}_k + B\tilde{u}_k + B_d\tilde{d}_k \tag{6.4.13}$$

This model is formulated based on deviations from the operating point. However, we need the model to be formulated in absolute values of inputs and states. Because the operating point in our problem changes as a function of the scheduling variable, we need to introduce a variable to capture its behavior. In order to rewrite the state space model in the absolute form we use $\tilde{x}_k = x_k - x_k^0$, $\tilde{u}_k = u_k - u_k^0$ and $\tilde{d}_k = d_k - d_k^0$, where x_k^0, $u_k^0$and d_k^0 are values of states, inputs and disturbance at the operating point. Therefore, the LPV model becomes

$$x_{k+1} = x_{k+1}^0 + A(x_k - x_k^0) + B(u_k - u_k^0) + B_d(d_k - d_k^0) \tag{6.4.14}$$

which can be written as

$$x_{k+1} = Ax_k + Bu_k + B_d d_k + f_k \tag{6.4.15}$$

with

$$f_k = x_{k+1} - (Ax_k^0 + Bu_k^0 + B_d d_k^0) \tag{6.4.16}$$

Now having the linear model (in fact this is an affine model) of the system we can proceed to compute the state predictions as

$$\begin{aligned}
x_{k+1} &= Ax_k + Bu_k + f_k \\
x_{k+2} &= Ax_{k+1} + Bu_{k+1} + f_{k+1} \\
&= A(Ax_k + Bu_k + f_k) + Bu_{k+1} + f_{k+1} \\
&= A^2x_k + ABu_k + Af_k + Bu_{k+1} + f_{k+1} \\
x_{k+3} &= Ax_{k+2} + Bu_{k+2} + f_{k+2} \\
&= A(A^2x_k + ABu_k + Af_k + Bu_{k+1} + f_{k+1}) + Bu_{k+2} + f_{k+2} \\
&= A^3x_k + A^2Bu_k + A^2f_k + ABu_{k+1} + Af_{k+1} + Bu_{k+1} + f_{k+1} \\
y_k &= Cx_k + Du_k + g_k \\
y_{k+1} &= Cx_{k+1} + Du_{k+1} + g_{k+1}
\end{aligned} \tag{6.4.17}$$

Now that we know how to calculate the state and output predictions we can stack the predictions in one vector as below

$$
\begin{aligned}
X &= \begin{pmatrix} x_{k+1} & x_{k+2} & \dots & x_{k+N} \end{pmatrix}^T \\
U &= \begin{pmatrix} u_k & u_{k+1} & \dots & u_{k+N-1} \end{pmatrix}^T \\
Y &= \begin{pmatrix} y_k & y_{k+1} & \dots & y_{k+N-1} \end{pmatrix}^T \\
D &= \begin{pmatrix} d_k & d_{k+1} & \dots & d_{k+N-1} \end{pmatrix}^T \\
F &= \begin{pmatrix} f_k & f_{k+1} & \dots & f_{k+N-1} \end{pmatrix}^T \\
G &= \begin{pmatrix} g_k & g_{k+1} & \dots & g_{k+N-1} \end{pmatrix}^T
\end{aligned}
\tag{6.4.18}
$$

Using the stacked notation the state and output predictions can be written as functions of the current state, the input sequence (stack of it), and the disturbance

$$
\begin{aligned}
&X = \Phi_x x_k + \Gamma_u U + \Gamma_d D + \Gamma_f F \\
&Y = CX + DU + \Phi_g G \\
&\quad \Longrightarrow \\
&Y = C\Phi_x x_k + C\Gamma_u U + C\Gamma_d D \\
&\quad + C\Gamma_f F + DU + \Phi_g G
\end{aligned}
\tag{6.4.19}
$$

in which the matrices are defined as

$$Y = \begin{pmatrix} y_k \\ y_{k+1} \\ \vdots \\ y_{k+N-1} \end{pmatrix} \qquad U = \begin{pmatrix} u_k \\ u_{k+1} \\ \vdots \\ u_{k+N-1} \end{pmatrix} \qquad D = \begin{pmatrix} d_k \\ d_{k+1} \\ \vdots \\ d_{k+N-1} \end{pmatrix}$$
$$F = \begin{pmatrix} f_k \\ f_{k+1} \\ \vdots \\ f_{k+N-1} \end{pmatrix} \qquad G = \begin{pmatrix} g_k \\ g_{k+1} \\ \vdots \\ g_{k+N-1} \end{pmatrix} \tag{6.4.20}$$

$$\Phi_x = \begin{pmatrix} I \\ A \\ A^2 \\ \vdots \\ A^{N-1} \end{pmatrix} \qquad \Phi_g = \begin{pmatrix} I \\ I \\ I \\ \vdots \\ I \end{pmatrix} \tag{6.4.21}$$

$$\Gamma_u = \begin{pmatrix} B & 0 & \dots & 0 \\ AB & B & \dots & 0 \\ \vdots & \vdots & \ddots & \vdots \\ A^{N-2}B & A^{N-3}B & \dots & B \end{pmatrix} \quad \Gamma_f = \begin{pmatrix} I & 0 & \dots & 0 \\ A & I & \dots & 0 \\ \vdots & \vdots & \ddots & \vdots \\ A^{N-2} & A^{N-3} & \dots & I \end{pmatrix}$$
$$\Gamma_d = \begin{pmatrix} B_d & 0 & \dots & 0 \\ AB_d & B_d & \dots & 0 \\ \vdots & \vdots & \ddots & \vdots \\ A^{N-2}B_d & A^{N-3}B_d & \dots & B_d \end{pmatrix} \tag{6.4.22}$$

After computing the state predictions as functions of control inputs, we can write down the optimization problem similar to a linear MPC problem as a quadratic program – more details can be found in [76]. The problem of linear MPC can be formulated as

$$\begin{array}{rl} \min\limits_{U} & Y^T Q Y + U^T R U \\ \text{Subject to:} & U \in \mathbb{U} \\ & X \in \mathbb{X} \end{array} \tag{6.4.23}$$

6.4.3 Controller objectives

The most basic control objective of a WT is to maximize captured power during the lifetime of the WT, which is equivalent with maximizing captured power when wind speed is below its rated value. This is also called maximum power point tracking (MPPT). However, when wind speed is above rated, control objective becomes regulation of the outputs around their rated values while trying to minimize dynamic loads on the structure. These objectives should be achieved against fluctuations in wind speed, which acts as a disturbance to the system. In this work we have considered operation of the WT in the above

rated (full load) regime. Therefore, we try to regulate rotational speed and generated power around their rated values and alleviate the effect of wind speed fluctuations.

Collective pitch controller

The first controller uses the linearized model, which was explained in the previous sections, augmented with a second order system modeling actuator dynamics. Measured outputs that are fed to this controller are

$$\begin{pmatrix} \omega_r \\ P_e \\ a_t \\ \theta_c \\ V_{hh} \end{pmatrix} \begin{matrix} \text{Rotor rotational speed} \\ \text{Generated power} \\ \text{Tower top acceleration} \\ \text{Measured collective pitch} \\ \text{Hub height wind speed vector} \end{matrix}$$

For the collective pitch controller we have used a dual mode horizon MPC approach. In this approach the infinite horizon of the cost function is divided into a finite horizon cost function as shown in the optimization problem (6.4.23) and a terminal cost equivalent to the rest of the horizon to infinity. The matrix Q_f of the terminal cost in formula (6.4.12) is found by solving an Algebraic Riccati Equation (ARE). In order to solve the ARE, we need dynamics of the system. We use the wind speed of the last sample of LiDAR measurement as the best estimate of the wind speed for $k \geq N$, and therefore we assume dynamics of the system to be constant and determined by this wind speed. Solving ARE's online might be time consuming, and therefore we bypass this problem by making a grid of wind speeds and finding a Q_f for each wind speed offline. During the simulation we use a look-up table of Q_f matrices and find the appropriate matrix. Of course, this approach holds only if the constraints are not active at the end of horizon. In the WT case we make sure that the constraints are not active by taking the prediction horizon long enough.

Individual pitch controller

The objective of this controller is to reduce fluctuations of blade root bending moments by adjusting the pitch angle based on calculated effective wind speeds and blade root bending moment measurements for each blade individually. The controller will reduce 1P fluctuations of blade root bending moments. The fluctuations in the blade root bending moments are considered to originate from the bending moment produced by the hub height wind speed. Measurements that are fed to the individual pitch controller are out-of-plane blade root bending moments and calculated effective wind speeds

$$\begin{pmatrix} M_1 \\ M_2 \\ M_3 \\ V_1 \\ V_2 \\ V_3 \end{pmatrix} \begin{matrix} \text{Flapwise blade root bending moment of blade 1} \\ \text{Flapwise blade root bending moment of blade 2} \\ \text{Flapwise blade root bending moment of blade 3} \\ \text{Wind speed vector for blade 1} \\ \text{Wind speed vector for blade 2} \\ \text{Wind speed vector for blade 3} \end{matrix}$$

6.4.4 Simulations

In this section simulation results for the obtained controllers, which are denoted as MPC IPC (the proposed approach) and PI IPC (the benchmark controller), are presented. The controllers are implemented in MATLAB and are tested on a full complexity FAST [71] model of the reference wind

turbine [77]. The tuning matrices are taken to be Q = diag(1105, 0.51, 5.5, 0.002, 0.155) and R = diag(100,1), respectively. Simulation results are shown for two scenarios – one stochastic hub height wind speed with wind shear, and one with extreme wind shear. Both scenarios are taken from the IEC standard [8].

Extreme wind shear

In this section simulation results for a vertical extreme wind shear (EWS) event are presented. A power law wind profile is used to demonstrate wind shear. In the vertical EWS event, the shear power law exponent ramps up from a normal value of 0.2 to an extreme value of 0.3 in 2 seconds and after 10 seconds ramps down to the normal situation. Controller performance for the MPC IPC and PI IPC are compared for this event. A comparison of blade pitch is given in figures below.

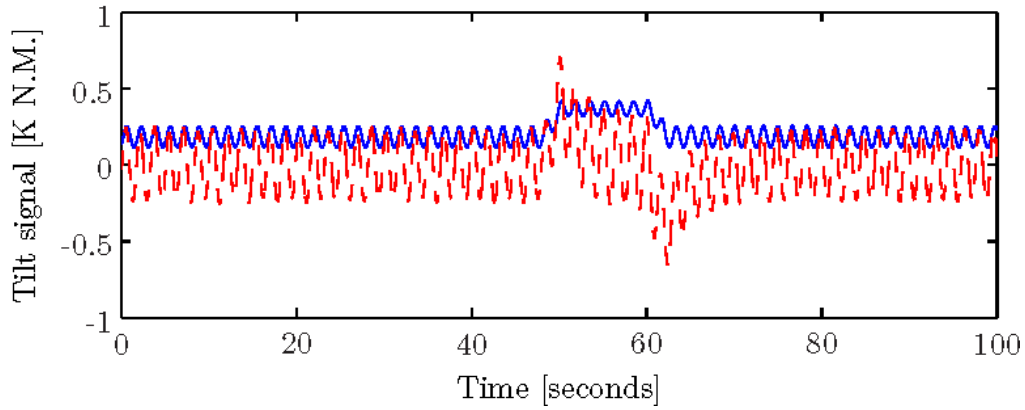

Figure 74: Tilt signal; MPC IPC is solid-blue, and PI IPC is red-dashed.

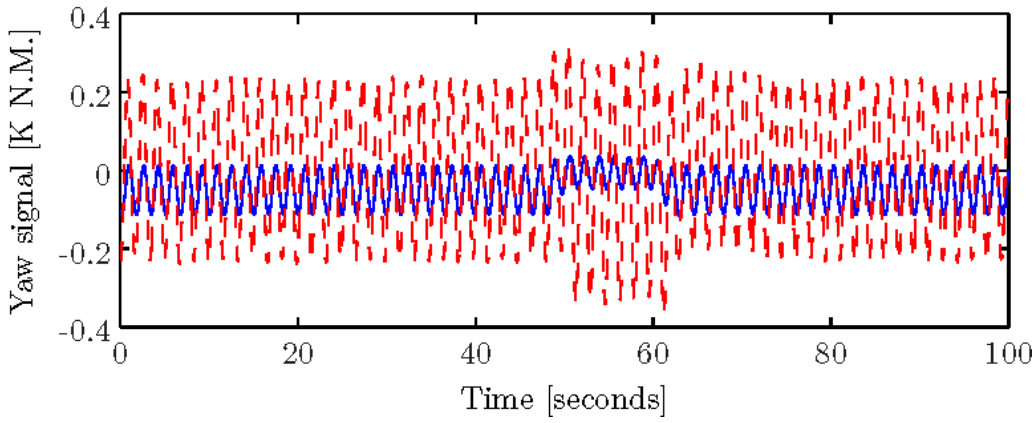

Figure 75: Yaw signal; MPC IPC is solid-blue, and PI IPC is red-dashed.

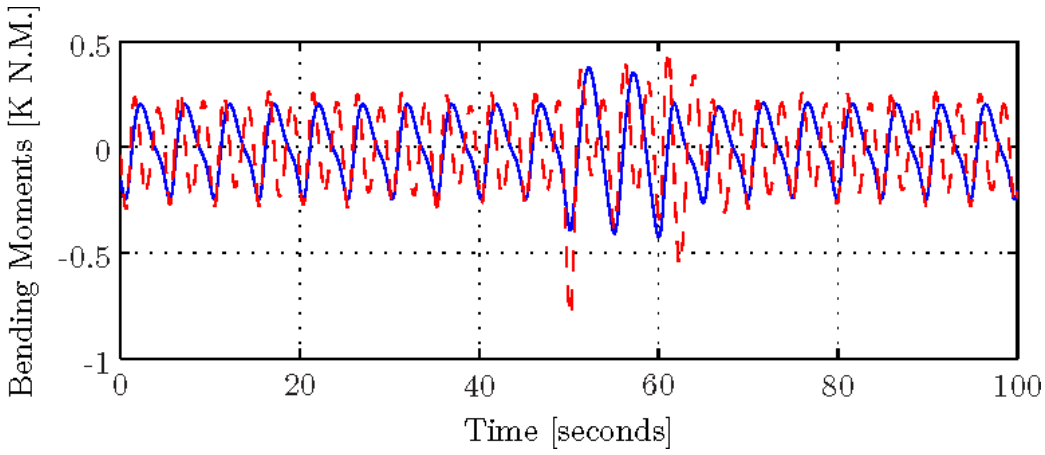

Figure 76: Blade bending moments; MPC IPC is solid-blue, and PI IPC is red-dashed.

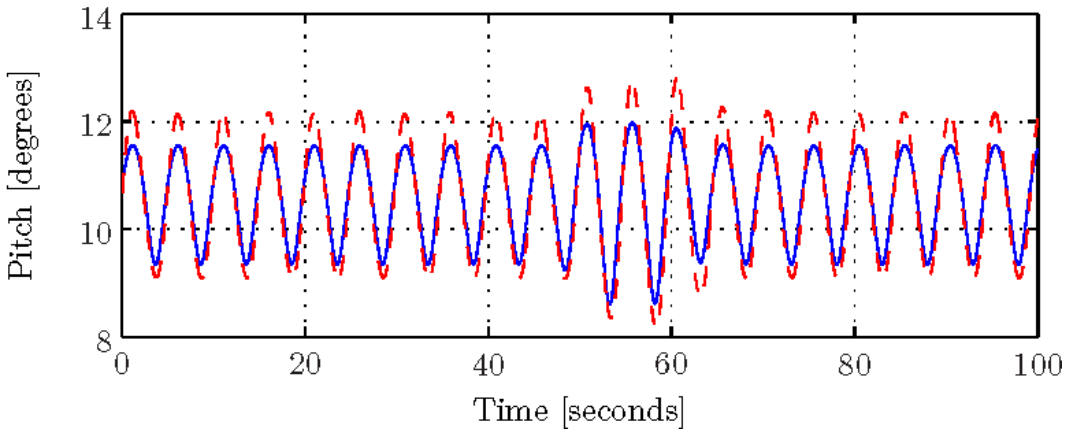

Figure 77: Pitch of one blade; MPC IPC is solid-blue, and PI IPC is red-dashed.

As it can be seen, the MPC IPC gives a smoother increase in blade pitch while PI IPC has an overshoot. Out-of-plane blade root bending moments of one of the blades are given in Fig. 76. Clearly the MPC IPC gives better performance in reducing both steady state and transient fluctuations. In order to simplify comparison of the signals, Coleman transformation of the three out-of-plane blade root bending moments are calculated, and the results, namely yaw and tilt signals, for both controllers are given in Fig. 74 and Fig. 75, respectively.

Stochastic wind

In this scenario, simulations are done with hub height turbulent wind. The Kaimal model [8] is chosen as the turbulence model, and TurbSim [78] is used to generate the wind profile. Mean wind shear is included with 0.2 as the value for the power-law exponent. In order to stay in the full load regime, a realization of a turbulent wind field is based on category C of the IEC 61400-1turbulence categories [8] with 18m/s as the mean wind speed. The results are given in the following figures.

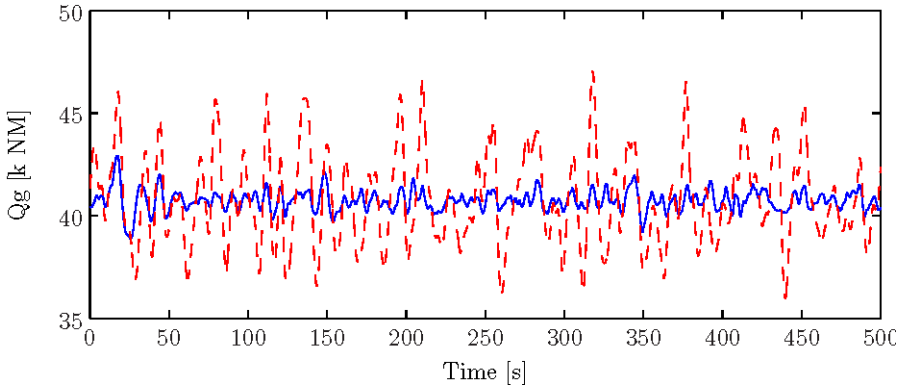

Figure 78: Generator-torque reference; MPC IPC is blue-solid, and PI IPC is red-dashed.

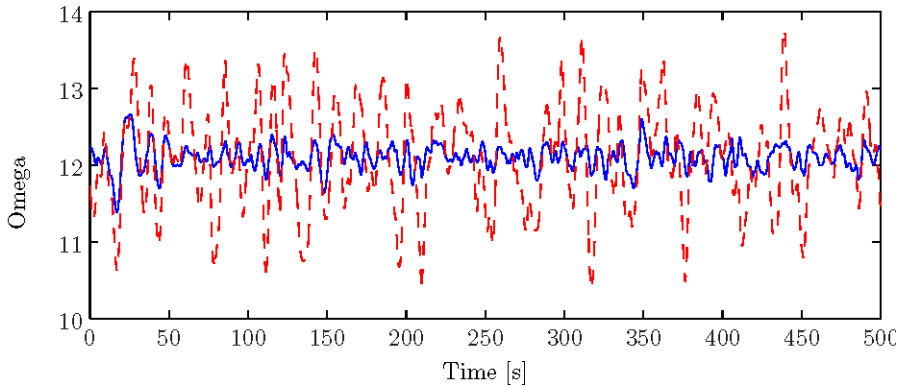

Figure 79: Rotor rotational speed (ωr); MPC IPC is blue-solid, and PI IPC is red-dashed.

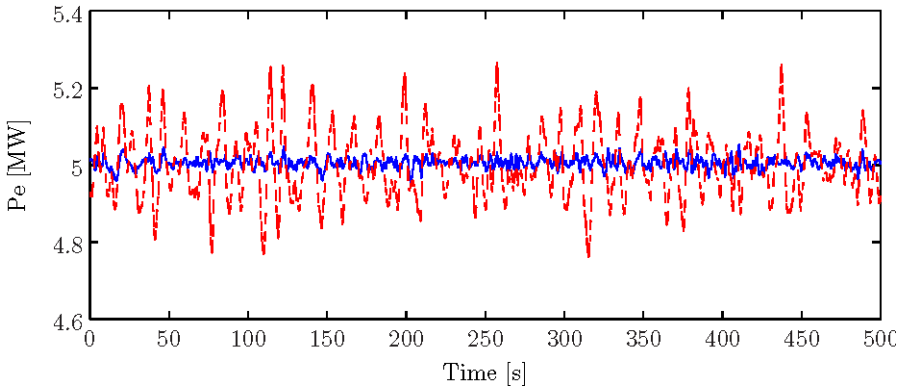

Figure 80: Electrical power; MPC IPC is blue-solid, and PI IPC is red-dashed.

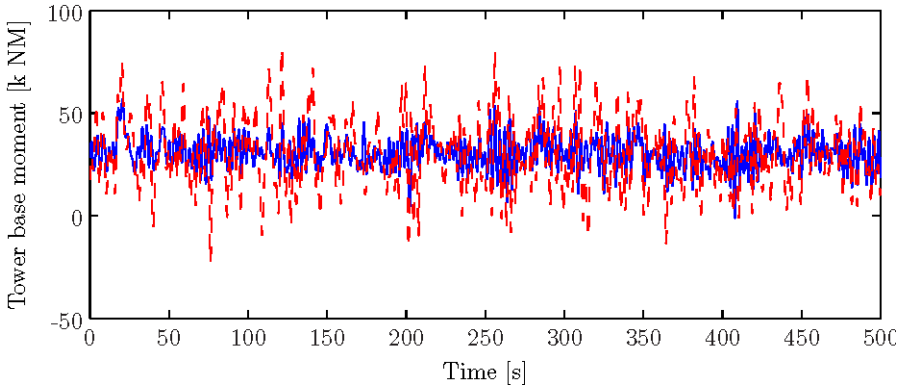

Figure 81: Tower base pitching (or fore-aft); MPC IPC is blue-solid, and PI IPC is red-dashed.

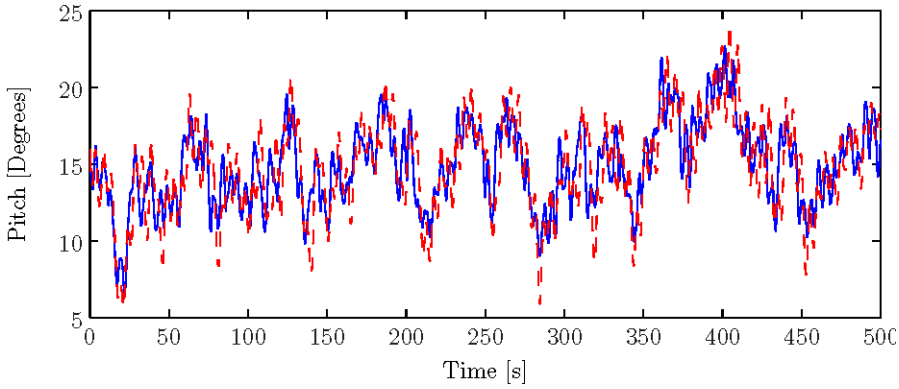

Figure 82: Pitch of one of the blades; MPC IPC is solid-blue, and PI IPC is red-dashed.

As seen the MPC IPC controller is superior in all investigated aspects compared to the PI IPC controller.

6.5 Simplistic controller test case

In this section we will investigate the load alleviating potential of controllers, more advanced that the base line controller described in section 6.1, for WT's operating in WF's. Obviously, real WF's represent a broad range of topological variations, which in turn will affect the loading of the individual WF WTs. To proceed we therefore need to define a suitable representative test case.

6.5.1 Generic WF

Considering the closest upstream WT as the most load influencing, we will define the simplest possible generic WF topology – namely a WF consisting of only two WT's. This simple WF is investigated for three different distances between the WT's representing respectively small (3D), medium (5D) and large (8D) WT inter-spacings**.**

In an attempt to include impact from various inflow conditions on the wake loading the following wake cases are considered for each of the WT inter-spacings:

- Partial wake inflow cases with inflow angles relative to the imaginary line connecting the two turbines defined as: $\{\pm i \times [\text{Arctan}(D/jD)+\text{Arctan}(TI)]/5\}$; $i = 0, 1, \ldots, 5$; where j takes the values 3, 5 or 8 according to the turbine spacing in question.

Each of the partial wake inflow cases are assumed to have *identical probability* for occurrence – i.e. uniform probability density function (pdf) of the individual inflow cases. This imaginary WF layout along with its set of inflow conditions is illustrated in Fig. 83.

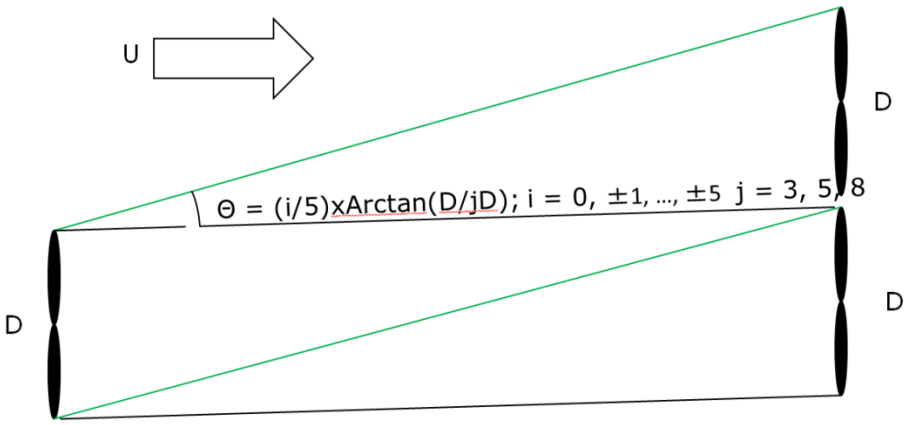

Figure 83: Generic WF layout and the defined set of inflow cases.

6.5.2 Computational setup - wind fields

We will assume onshore wind conditions and define the ambient wind climate – i.e. the deterministic mean wind field and the turbulence – conditioned on the ABL stability condition according to the description given in section 5.2. Only exception is – as mentioned in section 5.2.4 – scaling of the turbulence. Here, we will use a scaling factor based on the theoretical spectral tensor spectrum for neutral conditions.

Referring to the turbulence description in section 5.2, $\alpha\varepsilon^{2/3}_{\text{neu}}$ is a scaling parameter, which for a *fixed* parameter set (L_{neu}, Γ_{neu}) determines the *variance* intensity of the generated *neutral* turbulence field. For a given target intensity value we determine the particular $\alpha\varepsilon^{2/3}_{\text{neu}}$ value, which corresponds to the requested theoretical target value. This $\alpha\varepsilon^{2/3}_{\text{neu}}$ value is determined from the following relation [9]

$$\sigma_{iso}^2 = \frac{9\sqrt{\pi}\,\Gamma(1/3)}{55\,\Gamma(5/6)}\,\alpha\varepsilon_{neu}^{2/3}\,L_{neu}^{2/3} \approx 0.688\,\alpha\varepsilon_{neu}^{2/3}\,L_{neu}^{2/3} \tag{6.5.1}$$

in which $\Gamma(*)$ is the gamma function, σ_{iso}^2 denotes the variance of an analogue isotropic turbulence field, and other nomenclature is explained in section 5.2. Isolating $\alpha\varepsilon^{2/3}_{\text{neu}}$ from (6.5.1) we obtain

$$\begin{aligned}\alpha\varepsilon_{neu}^{2/3} \approx 1.453\,L_{neu}^{2/3}\,\sigma_{iso}^2 &= 1.453\,L_{neu}^{2/3}\,\frac{\sigma_{\text{target}}^2}{\frac{\sigma_{\text{target}}^2}{\sigma_{iso}^2}\left(\Gamma_{neu}\right)} \\ &\approx 1.453\,L_{neu}^{2/3}\,\frac{(TI\times U)^2}{3.25}\end{aligned} \tag{6.5.2}$$

where the relationship between σ_{iso}^2 and σ_{11}^2 (i.e. variance of the longitudinal turbulence component), for neutral conditions (i.e. classic Mann spectral tensor), is given in Fig. 84 below.

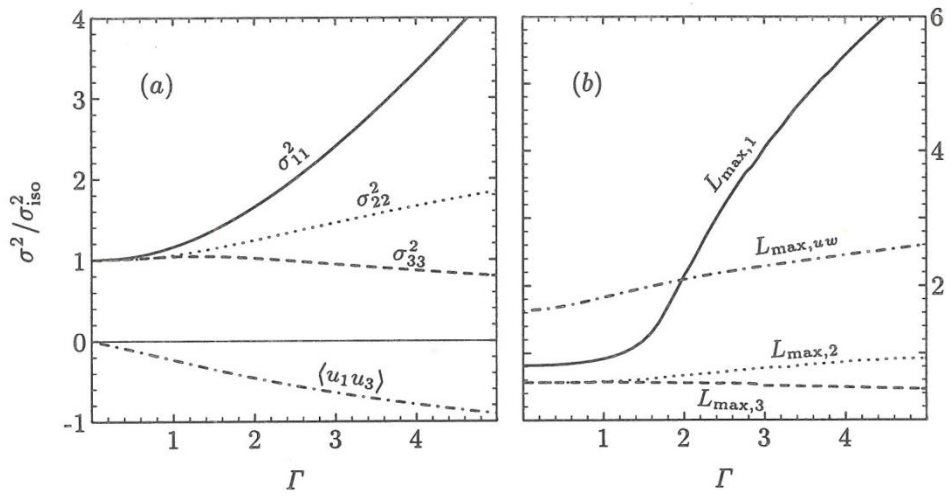

Figure 84: Dependence of turbulence component variances and component length scales with spectral tensor parameter Γ.

Thus, the scaling factor to be applied on turbulence boxes generated according to the specifications in Table 10 is therefore $\sqrt{\alpha\varepsilon_{neu}^{2/3}} = \alpha^{1/2}\varepsilon_{neu}^{1/3}$. To summarize, the following procedure is applied to obtain the requested neutral and non-neutral turbulence fields:

1) For each stability class turbulence boxes are simulated using relevant (Ri_g, η_θ) parameters and the turbulence length scale determined as $L = L_{\text{IEC code}} \times (L/L_{\text{neu}})$, the turbulence eddy lifetime parameter given by $\Gamma = \Gamma_{\text{IEC code}} \times (\Gamma/\Gamma_{\text{neu}})$, and $\alpha\varepsilon^{2/3} = 1 \times (\alpha\varepsilon^{2/3}/\alpha\varepsilon^{2/3}_{\text{neu}})$. The respective scaling values (L/L_{neu}), ($\Gamma/\Gamma_{\text{neu}}$) and ($\alpha\varepsilon^{2/3}/\alpha\varepsilon^{2/3}_{\text{neu}}$) as well at the ($Ri_g$, η_θ) sets are obtained from Table 10, and, as mentioned, based on analysis of full-scale data from the Danish Høvsøre site;
2) For a specified mean wind speed, the turbulence fields resulting from 1) are subsequently scaled to the requested intensity at the site of interest by multiplying with a *common* factor for all stability classes, $\alpha^{1/2}\varepsilon_{neu}^{1/3}$, where $\alpha\varepsilon_{neu}^{2/3}$ is obtained from equation (6.5.2). This scaling is justified by the property of the generalized spectral tensor stated in equation (5.2.11).

We will assume *onshore* wind conditions, and to mimic such wind conditions the undisturbed ambient wind climate are defined in accordance with IEC class 2A For each mean wind speed and for each stability class, 6 realisations (i.e. 6 different turbulence seeds) of each type of turbulence boxes are conducted to improve statistical significance of the results.

6.5.3 Computational setup – WT fatigue loads

Load simulations are performed using the state-of-the-art aeroelastic code HAWC2 [79] coupled with the DWM model [7] together with the NREL 5MW turbine [77] with a rotor diameter of 126m and a hub height equal to 90m. The structural part of HAWC2 is based on a multi-body formulation using the floating frame of reference method. Each body includes its own coordinate system with calculation of internal inertia loads, when this coordinate system is moved in space, and hence large rotation and translation of the body motion are accounted for.

The WT sensors defined for the analysis are: blade flap bending moment; rotor yaw moment; and tower bottom for-aft moment. These three sensors are selected because they reflect the most significantly wake driven loading of turbine main components. The focus of the study is on turbine *fatigue loads*, and consequently all sensor signals are post processed to give fatigue equivalent moments as based on the traditional Palmgren-Miner linear damage accumulation rule [80]. A Wöhler exponent of 4 was used for tower and rotor loading, whereas a Wöhler exponent of 12 was used for blade loading.

Simulated mean wind speeds in the range [5;25]m/s with steps of 2m/s, each with yaw errors as specified in the IEC code (-10^o; 0 ^{o}; 10^o) with probabilities of occurrence of respectively (25%, 50%, 25%), are considered for the WF turbine design envelope. This leads to a total of 49.896 aeroelastic computations for the onshore case for *each* of the two investigated controllers.

6.5.4 Climatology

A representative onshore ABL stability climatology – i.e. the pdf of a given stability condition conditioned on the mean wind speed – is obtained by analysing 51.935 10-minute data series from a meteorological tower at the Dutch Cabauw site. This site is characterized by flat and (relative) homogeneous upstream conditions. The stability classification is performed using the AMOK approach described in section 2.5. The resulting conditional stability pdf's were subsequently "transformed" to be conditioned on the mean wind speed at hub height level – i.e. 90m asl. The data set covered the mean wind speed range [4;16]m/s with an acceptable data coverage. The resulting stability climatology is illustrated in Fig. 85. As expected, the neutral stability condition prevails in the high wind regime, where mechanical friction dominates buoyancy effects.

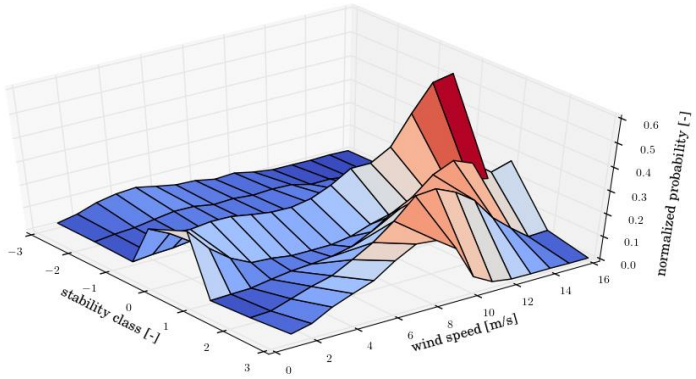

Figure 85: Stability climatology obtained from Cabauw measurements.

6.5.5 Results

Based on the described setup, we will compare the WF performance of the *base line controller* and the *individual pitch controller*, respectively. The considered WT design cycle is limited to IEC DCL 1.2 (i.e. normal operation), and, in accordance with the IEC code, the mean wind speed is assumed to be Rayleigh distributed. In terms of probability of occurrence, a simulated mean wind speed is to be considered as the median of a 2m/s bin, such that e.g. a simulated 5m/s represents the mean wind speed bin [4;6]m/s. Given the fact that the climatology is available for up to 16m/s only, we replace the Rayleigh distribution by a variant – namely the Rayleigh distribution constrained to the mean wind regime, where the climatology is available and the WT is operation; i.e. [4;16]m/s.

The *metric* for the controller inter comparison is the WT DCL 1.2 fatigue loading aggregated over all stability classes, all yaw errors and all mean wind speeds represented in the available climatology. Prior to convoluting the computed fatigue loads with the respective pdf's, these are, for each of the investigated sensors, averaged over the computed stochastic realizations – i.e. for each individual load case determined as the arithmetic mean of the 6 fatigue equivalent moments associated with the applied 6 turbulence seeds.

The results are, for the three different investigated WF spacings, summarized in the tables below.

Table 11: Aggregated WT design cycle fatigue equivalent moments for the 3D spacing case.

	Base line [kNm]	***Individual pitch*** [kNm]
Blade root flap	5636.46	4987.76
Tower bottom for-aft	7852.56	7887.63
Tower top torsion	1911.23	1867.21

Table 12: Aggregated WT design cycle fatigue equivalent moments for the 5D spacing case.

	Base line [kNm]	***Individual pitch*** [kNm]
Blade root flap	5544.87	4719.94
Tower bottom for-aft	6756.54	6811.76
Tower top torsion	1877.19	1826.92

Table 13: Aggregated WT design cycle fatigue equivalent moments for the 8D spacing case.

	Base line [kNm]	***Individual pitch*** [kNm]
Blade root flap	5504.96	4579.14
Tower bottom for-aft	6424.63	6489.45
Tower top torsion	1865.56	1813.26

In conclusion, it is obvious from the results presented in Table 11, Table 12, and Table 13, that the individual pitch controller is superior to the traditional base line controller for WT's operating in WF's – at least for this simple case study. This is true for all investigated WT component cross sectional moments except the tower bottom for-aft moment, which is marginally increased with the individual pitch controller. Similar results have previously been obtained for solitary WT's [83], and given the fact that *all* the present load cases origin from wake affected inflow cases; that the closest wake generating WT are the most load influencing; and the load margins between the base line and the individual pitch controller are significant, is believed that the above conclusion is also valid for most other WF layouts.

7 Design procedures including ABL stability effects

The IEC standard [8] for wind turbine loads describes the load envelope, which a turbine design has to comply with. However, the present version of this code does not consider the ABL stability effects, which is especially important for wake affected inflow conditions, because ABL stability impacts load generating wake dynamics in *addition* to its general influence on turbulence and the wind shear profile. At this point it should be noted that the present project, and therefore also this particular analysis, is restricted to wake affected WT inflow conditions. The present section deals with possibilities for including ABL stability in recommended practices for WT design.

7.1 Including an additional stability dimension

A straight forward inclusion of the ABL stability load aspect in the IEC code would be to add a new dimension – the ABL stability – to the recommended design basis. Depending on the characteristics of upstream fetch it could be argued to also condition the stability statistics on direction, but in a code context this is, however, mush too detailed. A code consistent implementation would be to quantify stability by defining a number of *stability classes* with each their probability of occurrence *conditioned* on the mean wind speed. This type of implementation requires definition of characteristics climatologies for at least an *offshore* and an *onshore* case, respectively.

The drawback of an additional design cycle dimension is the considerable amount of additional computational load resulting. This motivates an investigation of whether or not it is possible to collapse an ABL stability probability distribution into a few *design stability classes*, whereby the computational load will be significantly reduced compared to adding the full stability dimension. This investigation is treated in section 7.2.

7.2 Collapse of the stability dimension into a few design stability classes

We will investigate the potential of *design stability classes* by analysing a very simple generic WF populated with only two 5MW turbines, and we will operate these WT's under a stability climatology representing an *offshore* site. Moreover, we will limit the study to a simplified design envelope consisting of *normal operation* fatigue driven load cases only – i.e. IEC DCL 1.2 in analogy with the analysis presented in section 6.5.

7.2.1 Approach

The basic idea is to base the investigation on a mapping of the ABL stability pdf on selected pdf's associated with predefined load sensors on turbine main components (i.e. tower, main shaft and blades); and moreover to be able to consistently track back arbitrary load sensor quantiles to quantiles of the driving stochastic forcing under consideration (i.e. ABL stability), thus facilitating the definition of a representative design stability class on a rational basis for a *pre-specified confidence level*.

The treatment of the resulting single-input multiple-output system is based on a classical theorem for transformation of stochastic variables. Let a stochastic variable, ξ, characterize some type of external inflow conditions (e.g. ABL stability), and l be a stochastic variable characterizing some resulting wind turbine load response (e.g. aggregated fatigue equivalent moment corresponding to a mean wind speed specific member of the selected *simplified design envelope*, DCL 1.2, and associated with a specific main component cross section).

Thus

$$l = L(\xi) \tag{7.2.1}$$

where $L(\bullet)$ is a (load) transformation function, which relates the external wake and stability affected wind loading with the structural response signal in question. The relationship between the pdf of ξ, f_ξ, and the requested pdf of l, f_l, is given as [81]

$$f_l(l) = \sum_{i=1}^{N} \frac{f_\xi(\xi_i)}{|L'(\xi_i)|} \tag{7.2.2}$$

where $(\bullet)'$ denotes differentiation with respect to ξ, and N is the number of ξ_i-roots satisfying the equation

$$l = L(\xi_i) \tag{7.2.3}$$

for *specific choices* of l.

Once the load transformation (7.2.1) is defined, the "inverse tracking", relating an arbitrarily selected design envelope load quantile to quantiles of the driving stochastic forcing in a rational manner, is straight forward and established by evaluating the inverse transformation. The inverse transformation is, however, *only unique* if the number of roots, N, in the above equation equals one. In this case, the inverse tracking is given by

$$\xi = L^{-1}(l) \tag{7.2.4}$$

The suggested approach is illustrated in Fig. 86, where it is also indicated that the complicated load transformation function $L(\bullet)$ is numerically determined using the aeroelastic code HAWC2 coupled with the DWM model.

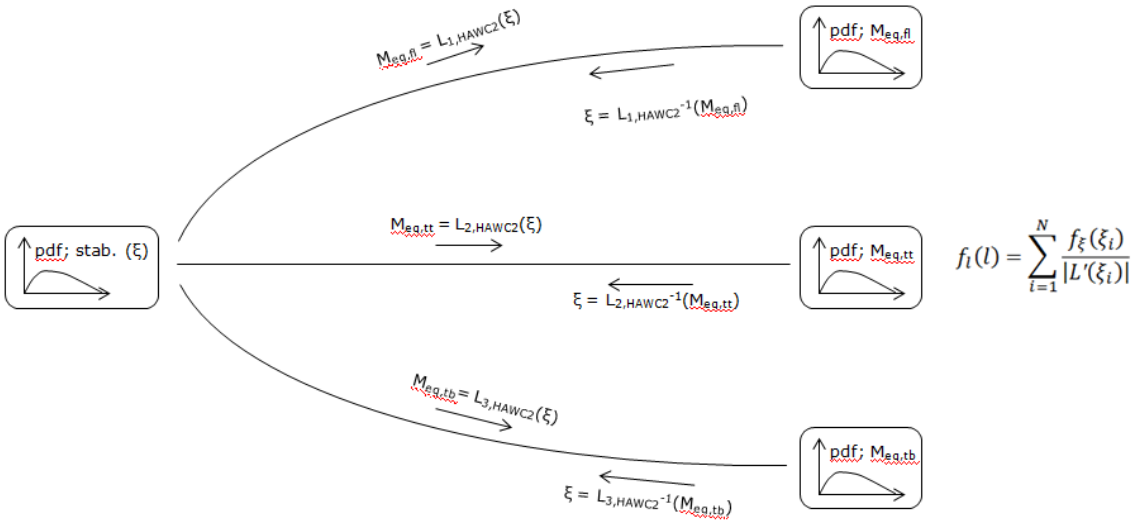

Figure 86: Transformation(s) between stochastic input (ABL stability) and stochastic output (component fatigue load response).

The case where N is larger than one thus poses a "selection problem", which in the end will rely on a motivated definition. A logical choice among the countable number of possible candidates, ξ_i, are the particular ξ_i contributing the most to the load quantile in question, ξ_m, i.e.

$$\xi_m = \left\{ \xi_m \left| \frac{f_\xi(\xi_m)}{|L'(\xi_m)|} = \max_i \frac{f_\xi(\xi_i)}{|L'(\xi_i)|} \right. \right\} \tag{7.2.5}$$

The present study will be based on a 98% confidence level.

7.2.2 Case study

As mentioned, real WF's obviously in general represent a broad range of topological variations, which in turn will affect the particular loading of the individual WT. For the present study we will use the simplistic WF defined in section 6.5.1, and we will argue that because the closest wake generating WT in general are the most load influencing, and because we only assess the *relative* importance of various ABL stability conditions, the results of the present investigation reach beyond this particular case study. Also in analogy with the investigation in section 6.5.1 we will analyse *design stability classes* associated with three different distances between the WT's representing respectively small (3D), medium (5D) and large (8D) WT inter-spacings.

7.2.3 Climatology

A representative offshore ABL stability climatology is obtained by analysing 167.762 10-minute series from a meteorological tower at the Danish Horns Rev site. The stability classification is performed using the AMOK approach described in section 2.5 with temperature input from a sensor located well within the surface layer (i.e. at 13m above sea level (asl)), and wind speed input from a top-mounted cup anemometer at 62m asl. The resulting conditional stability pdf's were subsequently "transformed" to be conditioned on the mean wind speed at hub height level – i.e. 90m asl. The data set covered the mean wind speed range [4;25]m/s with an acceptable data coverage. The resulting stability climatology is illustrated in Fig. 85.

At low mean wind speeds the mechanical friction is low both because the water surface is "smooth" and because the friction, for a given surface "roughness", scales with the mean flow velocity. The buoyancy impact on the stability condition, on the other hand, is *not* wind speed dependent, and therefore the balance between the friction and buoyancy created turbulence depends on the mean wind speed. An artefact of this is clearly seen in Fig. 87, where buoyancy dominates in the low speed regime resulting in an overrepresentation of non-neutral stability conditions contrary to the situation in the high speed regime, where friction based neutral conditions prevails.

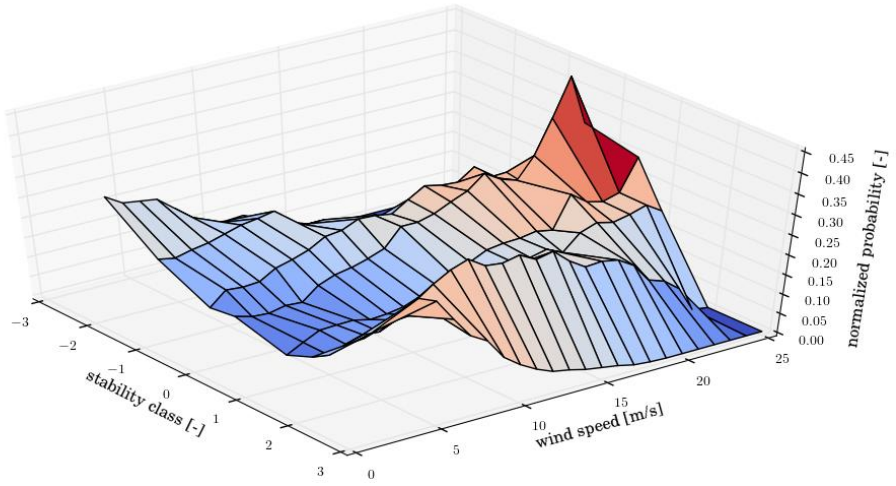

Figure 87: Stability climatology obtained from Horns Rev measurements.

7.2.4 Transformation functions

The transformation *L* defined in section 7.2.1 is determined *numerically* using the state-of-the-art aeroelastic code HAWC2 [79] coupled with the DWM model [7] and applied with the NREL 5MW turbine [77]. As focus is on IEC DCL 1.2, the post processing of sensor results (i.e. transformation to fatigue equivalent moments) also align with the investigation performed in section 6.5. Thus, the transformation *L* includes the entire numerical processing leading from *ABL stability inflow condition* to specific main component fatigue moments (including averaging of processed equivalent moments over performed stochastic realizations (i.e. over the range of the 6 turbulence seeds applied). The setup has required a total of 49.896 aeroelastic computations.

7.2.5 Results

Contrary to the investigation performed in section 6.5, we aim for results (i.e. *design stability classes*) *conditioned* on the mean wind speed. This is because the stability pdf depends on the mean wind speed, because arbitrary mean wind speed pdf's can be consistently treated, and because the computational requirements is largely identical with the computational load that would result, in case the *design stability classes* were based on the full IEC DCL 1.2 design cycle resulting from convoluting the mean wind specific loads with a specified mean wind distribution. In terms of computational load, the only difference is generation of more turbulence fields in case the *design stability classes* turn out to be mean wind speed dependent – the number of aeroelastic computations is identical.

Because of the discrete character of the derived response pdf's, we must adopt a suitable interpolation scheme in order to resolve relevant quantiles with sufficient accuracy. For this purpose we use a dedicated spline-like approach developed in [82], which assures that the probability mass, associated with a particular stability bin, is preserved using a suitable interpolation function of differentiability class C^3.

For the medium size WT spacing (i.e. 5D) examples of (seed-averaged) fatigue equivalent flap root moment response curves and their derivatives as well as the resulting load pdf's and cumulative distribution functions (cdf's) are shown in Fig. 88 and Fig. 89 for the mean wind speeds 8m/s and 14m/s,

respectively. The derivatives are determined using a second order central difference scheme except for the “end points”, where second order forward and backward approaches are used.

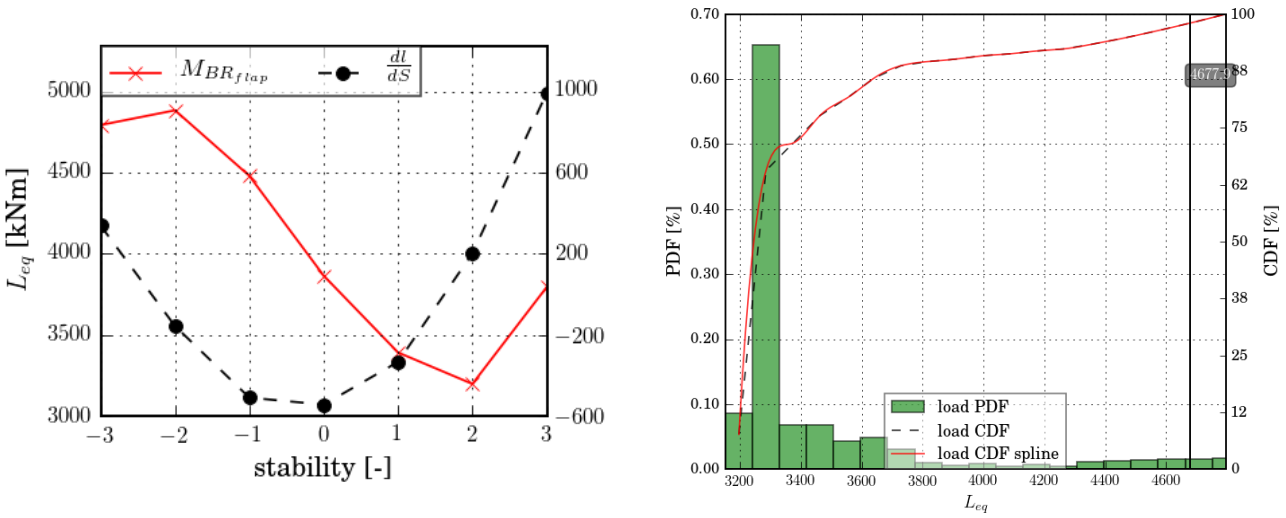

Figure 88: The 5D 8m/s case. (left) Load response function, *M_{BRflap}* (red), and its derivative, dl/dS (black), for the blade root flap moment as function of the stability identifier; (right) Load response pdf and cdf for the blade root flap moment.

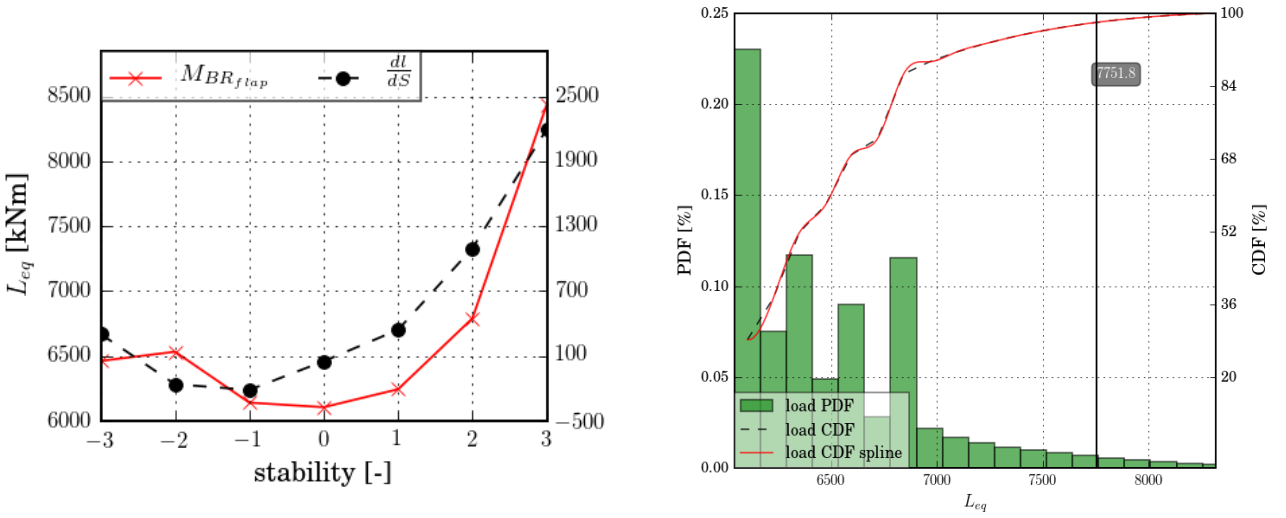

Figure 89: The 5D 14m/s case. (left) Load response function, *M_{BRflap}* (red), and its derivative, dl/dS (black), for the blade root flap moment as function of the stability identifier; (right) Load response pdf and cdf for the blade root flap moment.

The same results, but for the tower top torsion fatigue moments, are shown in Fig. 90 and Fig. 91 for the mean wind speeds 8m/s and 14m/s, respectively.

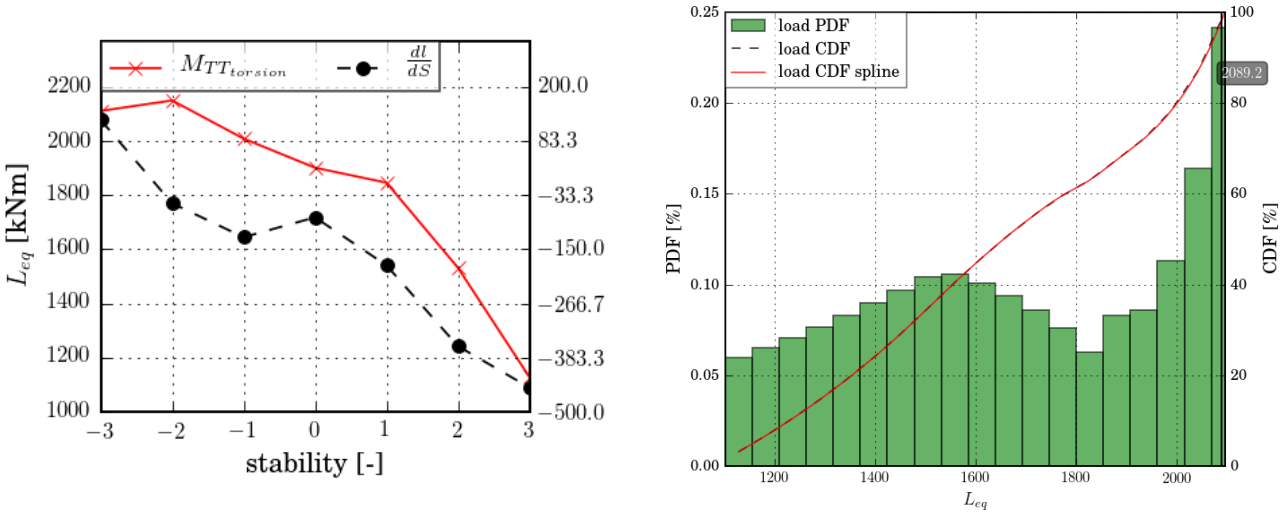

Figure 90: The 5D 8m/s case. (left) Load response function, $M_{TTtorsion}$ (red), and its derivative, dl/dS (black), for the tower top torsion moment as function of the stability identifier; (right) Load response pdf and cdf for the blade root flap moment.

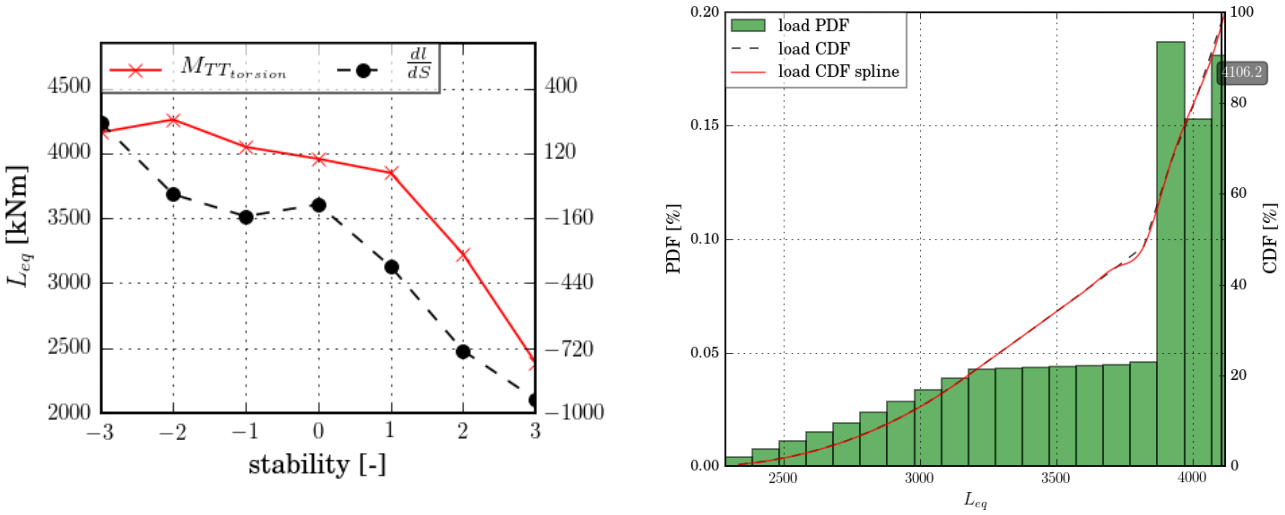

Figure 91: The 5D 14m/s case. (left) Load response function, $M_{TTtorsion}$ (red), and its derivative, dl/dS (black), for the tower top torsion moment as function of the stability identifier; (right) Load response pdf and cdf for the blade root flap moment.

Finally analogue results, but now for the tower bottom for-aft fatigue moments, are shown in Fig. 92 and Fig. 93 for the mean wind speeds 8m/s and 14m/s, respectively.

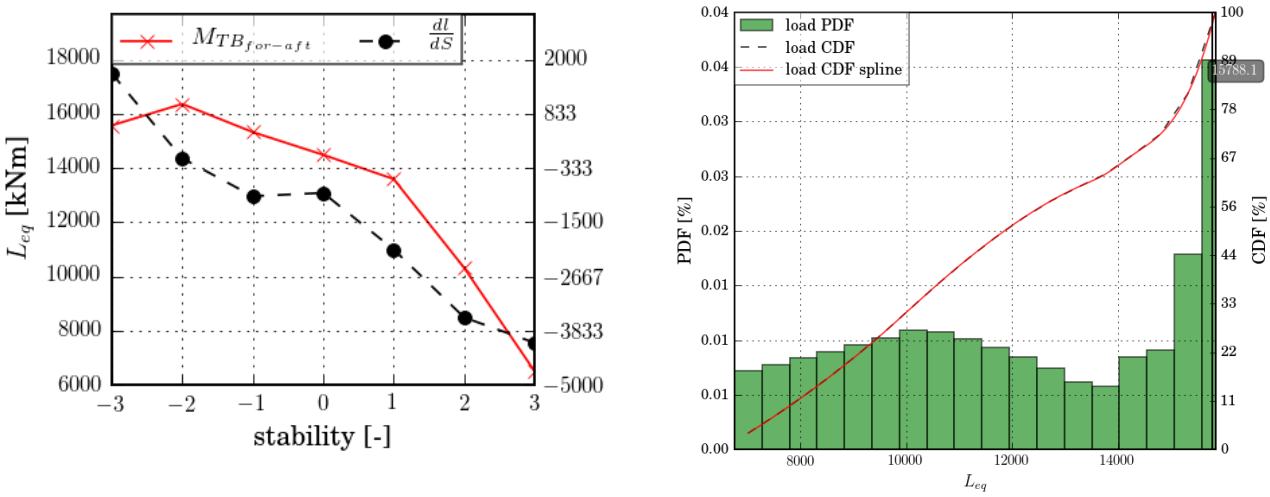

Figure 92: The 5D 8m/s case. (left) Load response function, $M_{TBfor-aft}$ (red), and its derivative, dl/dS (black), for the tower bottom for-aft moment as function of the stability identifier; (right) Load response pdf and cdf for the blade root flap moment.

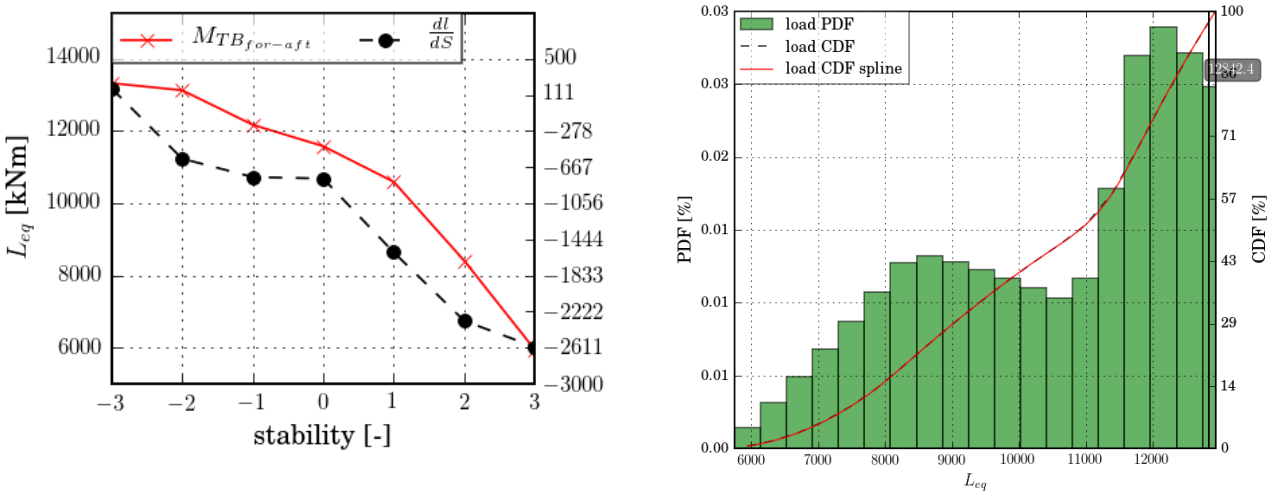

Figure 93: The 5D 14m/s case. (left) Load response function, $M_{TBfor-aft}$ (red), and its derivative, dl/dS (black), for the tower bottom for-aft moment as function of the stability identifier; (right) Load response pdf and cdf for the blade root flap moment.

7.2.6 Discussion

We see that response curves are (roughly) *monotonic* in the ABL stability measure, making the selection problem mentioned in section 7.1 an easy task. For the *tower* loading the gradients with respect to the stability measure are (predominantly) negative for all mean wind situations, indicating that the fatigue loading decreases for increasing degree of stable ABL stratification. This is expected. For the *blade* loading, however, the sign of gradients with respect to the stability measure depends on the mean wind speed. In the low wind regime these gradients are predominantly negative (cf. Fig. 88), whereas they are positive in the high wind regime (i.e. increasing fatigue loading for degree of stable ABL stratification), which at a first glance might seem surprising. This behaviour is an artefact of this component *rotating* through a shear layer, which is significantly affected by ABL stability conditions (cf. section 5.2). The wind shear variability with stability class (cf. Table 1) is illustrated in Fig. 94.

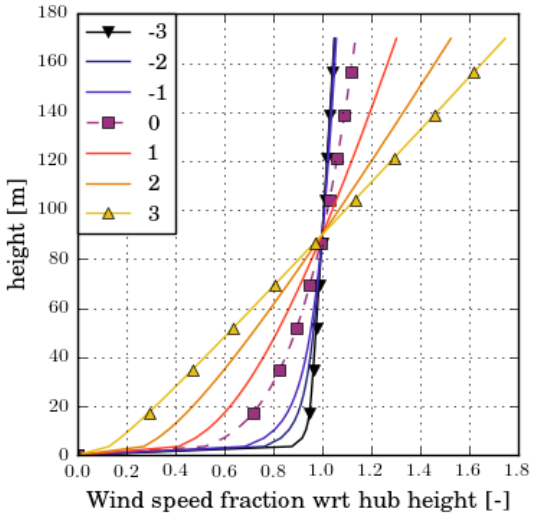

Figure 94: Wind shear profiles as function of stability class (cf. Table 1).

For increasing degree of stable stratification, a rotating WT component will thus experience two counteracting effects: 1) Decreasing turbulence loading as well as degreasing load exposure from wake dynamics; and 2) Increasing periodic fluctuating loading from wind shear. The balance between these two effects dictates the sign of the fatigue load gradients with respect to the stability measure. The tower, however, is not sensitive to the wind shear, which explains the strictly monotonic behaviour of tower fatigue loading with the stability measure.

As a consequence of this observation it is clear, that a *universal* design stability class, covering all turbine components, is not obtainable. We therefore aim at one design stability class for the rotating components of a WT and another design stability class covering the non-rotating WT components. This means that the computational burden will be considerable reduced compared to straight forward inclusion ABL stability as an additional design dimension as described in section 7.1 but, however, increased by a factor of two compared to present practice, where ABL stability effects are not considered.

7.2.7 Synthesis

It follows from the previous discussion, that the sought *design stability class*, c_d, is a function of the mean wind speed U, the component load response l_i and the requested confidence level cl: $c_d = c_d(U, l_i, cl)$. Adopting a 98% confidence level, the design stability class is thus described by the hyper-plane defined by $cl = 0.98$.

For the blade loading, it is straight forward to use the approach derived in section 7.2.1 to derive the sought design stability class. Since the tower loading is represented by two sensors, derivation of a design stability class is slightly more involved. For an unambiguous derivation, a complete consistence among the involver load sensors is required. This is seldom the case. To the degree that sensor-dependent design stability classes result, one option is to take a *conservative approach* ensuring that all design driving sensors adapt *at least* to the required confidence level. For this to be meaningful the relevant component design loads must respond in a reasonable coherent manner on the ABL stability measure, meaning that these are predominantly monotonic in the stability measure and furthermore with identical sign of the load gradient with respect to this stability measure. This is the case for the investigated tower sensors, and taking this approach for the tower loading our findings can be summarized into the recommendations given in Table 14.

Table 14: Design stability class conditional on mean wind speed, spacing and turbine component.

Wind speed [m/s]	3D		5D		8D	
	Blade (c_d)	Tower (c_d)	Blade (c_d)	Tower (c_d)	Blade (c_d)	Tower (c_d)
4	-2	-2	-2	-2	-2	-1
6	-2	-2	-2	-2	-2	-2
8	-2	-2	-1	-2	-2	-2
10	3	-2	3	-2	3	-2
12	3	-2	3	-2	3	-2
14	3	-2	3	-2	3	-2
16	2	-2	2	-2	2	-2
18	2	-2	2	-2	3	-2
20	2	-2	2	-2	2	-2
22	2	-2	2	-2	2	-2
24	1	-1	1	-1	1	-1

In conclusion we conjecture, as already mentioned in section 7.2.2, there is no reason to believe, that the relative impact of stability should vary significantly with topology. This conjecture is supported by the derived design stability classes in Table 14 being (almost) spacing independent. It is finally notable that none of the derived design stability classes are the neutral case, although this stability conditions is approached for very large wind speeds.

8 Summary of project achievements

The project has created a *new basis* for further development and optimization of WT's designed for WF operation. This has been accomplished through developing of more realistic modelling of WF flow fields as well as of such fields interactions with WT's under non-neutral ABL stability conditions. On this basis a *verified model complex* for prediction of structural loads as well as production losses for WT's operating in WF conditions, which takes into account the effects from ABL stability conditions, is established. Thereby the way to increased reliability and cost efficiency of future WT's as well as to more precise prediction of the WF power output is paved.

To detail the above mentioned we list below a selection of specific achievements:

- The classic M-O theory is extended to altitudes relevant for modern WT's. Besides impacting stability classification this may also have a significant influence on simulated fatigue loading of rotating WT components, where the periodic deterministic loading caused by wind shear often is the dominating factor. For details we refer to section 2 as well as to section 7;
- Initial studies using the DWM approach under non-neutral ABL conditions was limited by the lack of a consistent kinematic model for turbulence modeling under such stability conditions, and the Mann spectral tensor, although developed for neutral conditions, was used in an approximate manner to cover also non-neutral conditions. This shortcoming has been overcome by the development of buoyancy dependent spectral tensor, whereby ABL stability effects can be consistently accounted for within the framework of the DWM model. For details we refer to section 3 as well as to section 5;
- Using high-fidelity LES computations, two approaches for non-neutral turbulence modeling – the precursor and the forced boundary layer method – have been explored and compared. More work is needed to obtain mutually consistent results. For details we refer to section 3;
- Validation of a *fundamental wake stability conjecture*, which links the DWM approach with non-neutral ABL stability conditions. For details we refer to section 3;
- Investigation and quantification of the influence from the presence of a WF on the large turbulent eddies that dictates the wake meandering. For details we refer to section 4;
- Demonstrated that *steady* flow field models suffice for WF production predictions. For details we refer to section 5;
- A new and more accurate DWM wake superposition algorithm has been devised for above rated wind speeds. For details we refer to section 5;
- Demonstrated that ABL stability effects can explain a significant part of the large measurement scatter observed in full-scale data from the Lillgrunden WF. For details we refer to section 5;
- Demonstrated that an individual pitch controller is superior to the traditional base line controller for WT's operating in WF's. For details we refer to section 6;
- Demonstrated that wind shear is the dominating fatigue load generating factor for rotating components of WT operating under stable ABL conditions in WF's. For details we refer to section 7;
- Devised a simplified IEC consistent design procedure including ABL stability aspects. For details we refer to section 7.

9 List of publications, presentations and reports

[1] G.C. Larsen, T.J. Larsen, S. Ott, K.S. Hansen, H.Aa. Madsen (2012). Full scale verification of wind farm production predictions. XXIII ICTAM, 19-24 August, Beijing, China.

[2] K.S. Hansen, R. Barthelmie, S. Ott and G.C. Larsen (2012). Park power deficit due to atmospheric stability. The Science of Making Torque from Wind 2012, October 9-11, Oldenburg, Germany.

[3] G.C. Larsen, T.J. Larsen, K.S. Hansen, A. Chougule, J. Mann, H.Aa. Madsen (2013). The impact of atmospheric stability on wake losses. ICOWES2013 Conference 7-19 June, Lyngby, Denmark.

[4] T.J. Larsen, H. Aa. Madsen, G.C. Larsen, K. S. Hansen (2013). Validation of the dynamic wake meander model for loads and power production in the Egmond aan Zee wind farm. Wind Energy, **16**, pp. 605-624.

[5] T.J. Larsen, G.C. Larsen, H. Aa. Madsen and K. S. Hansen (2012). Wind farm production estimates. In: Proceedings of EWEA 2012 - European Wind Energy Conference & Exhibition. EWEA - The European Wind Energy Association.

[6] K.S. Hansen, G.C. Larsen and S. Ott (2014). Dependence of offshore wind turbine fatigue loads on atmospheric stratification. Journal of Physics: Conference Series (Online), **524**, 012165.

[7] M. Kelly, G.C. Larsen, N.K. Dimitrov, and A. Natarajan (2014). Probabilistic Meteorological Characterization for Turbine Loads. Journal of Physics: Conference Series (Online), **524**, 012076.

[8] R.-E. Keck, M. de Maré, M.J. Churchfield, S. Lee, G.C. Larsen and H.Aa. Madsen, (2014). On atmospheric stability in the dynamic wake meandering model. Wind Energy, **17**, pp. 1689–1710.

[9] R.-E. Keck, M. de Mare, M.J. Churchfield, S. Lee, G.C. Larsen and H.Aa. Madsen (2015).Two improvements to the dynamic wake meandering model: including the effects of atmospheric shear on wake turbulence and incorporating turbulence build-up in a row of wind turbines. Wind Energy, **18**, pp. 111–132.

[10] G.C. Larsen (2013). Challenges in wind farm optimization. International Conference on Future Technologies for Wind Energy, University of Wyoming, Laramie, U.S.A, October 7-9. Invited presentation.

[11] G.C. Larsen, E. Machefaux E and A. Chougule (2015). Wake meandering under non-neutral atmospheric stability conditions – theory and facts. Journal of Physics: Conference Series (Online), **625**, 012036.

[12] E. Machefaux, G.C. Larsen, K. Tilman, N. Troldborg, M.C. Kelly, A. Chougule, K.S. Hansen and J.S. Rodrigo (2016). An experimental and numerical study of the atmospheric stability impact on wind turbine wakes. Wind Energy, **19**, pp. 1785–1805.

[13] E. Machefaux, G.C. Larsen, N. Troldborg, K.S. Hansen, N. Angelou, T. Mikkelsen and J. Mann (2016). Investigation of wake interaction using full-scale LiDAR measurements and large eddy simulation, Wind Energy, **19**, pp. 1535-1551**.**

[14] E. Machefaux, G.C. Larsen and J.P. Murcia Leon (2015). Engineering models for merging wakes in wind farm optimization applications. Journal of Physics: Conference Series (Online), **625**, 012037.

[15] E. Machefaux, G.C. Larsen, N. Troldborg and A. Rettenmeier (2013). Single Wake Meandering, Advection and Expansion - An analysis using an adapted Pulsed LiDAR and CFD LES-ACL simulations. EWEC 2013, Copenhagen.

[16] E. Machefaux, G.C. Larsen, N. Troldborg, M. Gaunaa and A. Rettenmeier (2015). Empirical modeling of single-wake advection and expansion using full-scale pulsed LiDAR-based measurements. Wind Energy, **18**, pp. 2085–2103.

[17] T.J. Larsen, G.C. Larsen, H.Aa. Madsen, K. Thomsen and S.M. Pedersen (2015). Comparison of measured and simulated loads for the Siemens SWT2.3 operating in wake conditions at the Lillgrund Wind Farm using HAWC2 and the dynamic wake meander model**.** EWEA Offshore Conference, 10-12 March, Copenhagen, Denmark.

[18] T.J. Larsen, G.C. Larsen, H.Aa. Madsen and S.M. Pedersen (2015). Wake effects above rated wind speed - An overlooked contributor to high loads in wind farms. EWEA Annual Conference and Exhibition 2015, 17-20 November, Paris, France.

[19] G.C. Larsen, D. R. Verelst, F. Bertagnolio, S. Ott and A. Chougule (2016). In search for a canonical design ABL stability class for wind farm turbines. Journal of Physics: Conference Series (Online), **753**,032015.

[20] A. Chougule, J. Mann, M. Kelly and G.C. Larsen (2016). Validation of buoyancy driven spectral tensor model using HATS data. Journal of Physics: Conference Series (Online), **753**,032038.

[21] A. Chougule, J. Mann, M. Kelly and G.C. Larsen (2016). Modeling atmospheric turbulence via rapid-distortion theory: spectral tensor of velocity and buoyancy. Accepted for publication in Journal of the Atmospheric Sciences.

[22] G.C. Larsen (2016). Medium fidelity modeling of non-stationary wake affected flow fields under non-neutral ABL stability conditions. Shanghai Workshop 1st Symposium on Offshore Wind Energy Research (SOWER), Shanghai, China.

[23] E.L. Petersen, C.B. Hasager, M. Courtney, A. Natarajan, T.J. Larsen, H. Bredmose, G.C. Larsen, P.E. Sørensen, N.A. Cutululis and N.-E. Clausen (2015). Offshore Wind Farms. Handbook of Clean Energy Systems. Ed. J. Yan. Wiley.

References

[1] L. Jensen (2007). Analysis of array efficiency at Horns Rev and the effect of atmospheric stability. 2007 European Wind Energy Conference and Exhibition, Milan, 7-10 May.

[2] R.J. Barthelmie et al. (2007). Analysis of atmospheric impacts on the development of wind turbine wakes at the Nysted wind farm. European Offshore Wind 2007, Berlin.

[3] G.C Larsen, T.J. Larsen, J. Mann, A. Peña, K.S. Hansen and H.Aa. Madsen, (2009). The dependence of wake losses on atmospheric stability characteristics. EUROMECH Colloquium 508 on Wind Turbine Wakes 2009; pp. 35–37.

[4] G.C. Larsen, E. Machefaux E and A. Chougule (2015). Wake meandering under non-neutral atmospheric stability conditions – theory and facts. Journal of Physics: Conference Series (Online), **625**, 012036.

[5] E. Machefaux, G.C. Larsen, K. Tilman, N. Troldborg, M.C. Kelly, A. Chougule, K.S. Hansen and J.S. Rodrigo (2016). An experimental and numerical study of the atmospheric stability impact on wind turbine wakes. Wind Energy, **19**, pp. 1785–1805.

[6] G.C. Larsen, H.Aa. Madsen, K. Thomsen and T.J. Larsen (2008). Wake meandering - a pragmatic approach. Wind Energy, **11**, pp. 377–395.

[7] H.Aa. Madsen, G.C. Larsen, T.J. Larsen and N. Troldborg (2010). Calibration and Validation of the Dynamic Wake Meandering Model for Implementation in an Aeroelastic Code. J. Sol. Energy Eng., **132**(4).

[8] IEC 61400-1. Wind turbines—part 1: Design requirements, 2005.

[9] J. Mann (1994). The Spatial Structure of Neutral Atmospheric Surface-Layer Turbulence. J. of Fluid Mech., **273**, pp. 141-168.

[10] J. Mann (1998). Wind field simulation. Probabilistic Engineering Mechanics, **13**, pp. 269-282.

[11] A. Chougule (2013). Influence of atmospheric stability on the spatial structure of turbulence. DTU Ph.D. Thesis, 109p.

[12] A. Chougule, J. Mann, M. Kelly and G.C. Larsen (2016). Validation of buoyancy driven spectral tensor model using HATS data. Journal of Physics: Conference Series (Online), **753**,032038.

[13] A. Chougule, J. Mann, M. Kelly and G.C. Larsen (2016). Modeling atmospheric turbulence via rapid-distortion theory: spectral tensor of velocity and buoyancy. Accepted for publication in Journal of the Atmospheric Sciences.

[14] G.C. Larsen, T.J. Larsen, S. Ott, K.S. Hansen, H.Aa. Madsen (2012). Full scale verification of wind farm production predictions. XXIII ICTAM, 19-24 August, Beijing, China.

[15] G.C. Larsen, D. R. Verelst, F. Bertagnolio, S. Ott and A. Chougule (2016). In search for a canonical design ABL stability class for wind farm turbines. Journal of Physics: Conference Series (Online), **753**,032015.

[16] J.C. Kaimal and J.J. Finnigan (1994). Atmospheric Boundary layer Flows – Their structure and Measurement. Oxford University Press.

[17] K.S. Hansen, R.J. Barthelmie, L.E. Jensen and A. Sommer (2012). The impact of turbulence intensity and atmospheric stability on power deficits due to wind turbine wakes at Horns Rev wind farm. Wind Energy, **15**, pp. 183–196.

[18] A. Sathe, J. Mann, T. Barlas, W. A. A. M. Bierbooms and G. J. W. van Bussel (2013). Influence of atmospheric stability on wind turbine loads. Wind Energy, **16**, pp. 1013–1032.

[19] K.S. Hansen, R. Barthelmie, S. Ott and G.C. Larsen (2012). Park power deficit due to atmospheric stability. The Science of Making Torque from Wind 2012, October 9-11, Oldenburg, Germany.

[20] K.S. Hansen, G.C. Larsen and S. Ott (2014). Dependence of offshore wind turbine fatigue loads on atmospheric stratification. Journal of Physics: Conference Series (Online), **524**, 012165.

[21] A.S. Monin and A.M. Obukhov (1954). Osnovnye zakonomernosti turbulentnogo peremeshivanija v prizemnom sloe atmosfery (Basic Laws of Turbulent Mixing in the Atmosphere Near the Ground)', *Trudy geofiz. inst. AN SSSR* **24**(151), 163–187.

[22] A.S. Monin and A. M. Yaglom (1971). *Statistical Fluid Mechanics: Mechanics of Turbulence*, Vol. 1, MIT Press, Cambridge, London, 769 pp.

[23] J.R. Garratt, *The atmospheric boundary layer*. Cambridge University Press 1992. ISBN 0 521 38052 9

[24] U. Högström (1988). Non-dimensional wind and temperature profiles in the atmospheric surface layer: A re-evaluation, Boundary-Layer Meteorology **42**, pp. 55-78.

[25] H. Charnock (1955). Wind stress on water surface. Quarterly Journal of the Royal Meteorological Society, **81**, pp. 639–642.

[26] R.J. Barthelmie and L.E. Jensen (2010).Evaluation of wind farm effi ciency and wind turbine wakes at the Nysted offshore wind farm. Wind Energy, **13**, pp. 573–586.

[27] Wind Resources at Laesoe Syd (2002). Project report, Eltra PSO-2000 Proj. nr. EG-05 3248, Programme for measuring wind, wave and current at Laesoe Syd (in Danish).

[28] S.-E. Gryning, E. Batchvarova, B. Brümmer, H. Jørgensen and S. Larsen (2007) On the extension of the wind profile over homogeneous terrain beyond the surface layer. Boundary-Layer Meteorology **124**:251–268

[29] F. Bingöl, J. Mann and G.C. Larsen (2010). Light detection and ranging measurements of wake dynamics. Part I: one-dimensional scanning. Wind Energy, **13**(1), pp. 51–61.

[30] J.-J. Trujillo, F. Bingöl, G.C. Larsen and J. Mann, (2011). Light detection and ranging measurements of wake dynamics. Part II: two-dimensional scanning. Wind Energy, **14**, pp. 61–75.

[31] G. España, S. Aubrun, S. Loyer and P. Devinant (2011). Spatial study of the wake meandering using modeled wind turbines in a wind tunnel. Wind Energy, **14,** pp. 923–937.

[32] G. España, S. Aubrun, S. Loyer and P. Devinant (2012). Wind tunnel study of the wake meandering downstream of a modeled wind turbine as an effect of large scale turbulent eddies. Journal of Wind Engineering and Industrial Aerodynamics, **101**, pp. 24–33.

[33] E. Machefaux, G.C. Larsen, N. Troldborg and A. Rettenmeier (2013). Single Wake Meandering, Advection and Expansion - An analysis using an adapted Pulsed LiDAR and CFD LES-ACL simulations. EWEC 2013, Copenhagen.

[34] E. Machefaux, G.C. Larsen, N. Troldborg, M. Gaunaa and A. Rettenmeier (2015). Empirical modeling of single-wake advection and expansion using full-scale pulsed LiDAR-based measurements. Wind Energy, **18**, pp. 2085–2103.

[35] Ott, S.; Berg, J. and Nielsen, M. (2011). Linearised CFD Models for Wakes, Risoe-R-1772(EN).

[36] A. Chougule (2013). Influence of atmospheric stability on the spatial structure of turbulence. DTU Ph.D. thesis, 109p.

[37] A. Chougule, J. Mann, M. Kelly and G.C. Larsen (2016). Validation of buoyancy driven spectral tensor model using HATS data. Journal of Physics: Conference Series (Online), **753**,032038.

[38] A. Chougule, J. Mann, M. Kelly and G.C. Larsen (2016). Modeling atmospheric turbulence via rapid-distortion theory: spectral tensor of velocity and buoyancy. Accepted for publication in Journal of the Atmospheric Sciences.

[39] T. von Kármán (1948). Progress in the statistical theory of turbulence. Proc. Nat. Acad. Sci., **34**, pp.530–539.

[40] J.C. Kaimal, J.C. Wyngaard, Y. Izumi and O.R. Coté (1972). Spectral characteristics of surface-layer turbulence. Q. J. R. Meteorol. Soc., 98(417), pp.563–589.

[41] T.W. Horst, J. Kleissl, D.H. Lenschow, C. Meneveau, C.H. Moeng, M.B. Parlange, P.P. Sullivan and J.C. Weil (2004). HATS field observations to obtain spatially-filtered turbulence fields from transverse arrays of sonic anemometers in the atmospheric surface layer. J Atmos. Sci., **61**, pp. 1566-1581.

[42] J. C. Wyngaard and O. R. Cot´e. Cospectral similarity in the atmospheric surface layer (1972). Quart. J. R. Met. Soc., **98**, pp.590–603.

[43] A. Chougule, J. Mann, A. Segalini and E. Dellwik (2014). Spectral tensor parameters for wind turbine load modeling from forested and agricultural landscapes. Wind Energy, **18**, pp.469–481.

[44] A. Chougule, J. Mann, M. Kelly, J. Sun, D. H. Lenschow and E. G. Patton (2012). Vertical cross-spectral phases in neutral atmospheric flow. J. Turbul., **13**, pp.1–13.

[45] N. Troldborg, J.N. Sørensen, R. Mikkelsen and N.N. Sørensen (2013). A simple atmospheric boundary layer model applied to large eddy simulations of wind turbine wakes, Wind Energy, **17**, pp. 657–669.

[46] N. Troldborg, G.C. Larsen, H.Aa. Madsen, K.S. Hansen, J.N. Sørensen and R. Mikkelsen (2011). Numerical simulations of wake interaction between two wind turbines at various inflow conditions. Wind Energy, **14**, pp. 859-876.

[47] S.S.A. Ivanell (2010). Numerical Computations of Wind Turbine Wakes. Ph.D. Thesis, Royal Institute of Technology, Linné Flow Centre, Department of Mechanics, Stockholm, Sweden.

[48] J.A. Michelsen (1992). Basis3D - A Platform for Development of Multiblock PDE Solvers. AFM 92-05.

[49] J.A. Michelsen (1994). Block structured multigrid solution of 2D and 3D elliptic PDEs. AFM 94-06.

[50] NN. Sørensen (1995). General purpose flow solver applied to flow over hills. PhD thesis, Risø National Laboratory.

[51] Y. Cheng and W. Brutsaert (2005). Flux-profile relationships for wind speed and temperature in the stable atmospheric boundary layer. Bound.-Layer Meteor., **114**, pp. 519–538.

[52] G. Svensson et al. (2011). Evaluation of the Diurnal Cycle in the Atmospheric Boundary Layer Over Land as Represented by a Variety of Single-Column Models: The Second GABLS Experiment. Boundary-Layer Meteorol, **140**, pp.177–206.

[53] J.C. Wyngaard (2010). *Turbulence in the Atmosphere*. Cambridge University Press.

[54] P.-E. Réthoré (2013). Verification and validation of an actuator disc model.

[55] G.C. Larsen et al. (2011). TOPFARM – next generation design tool for optimization of wind farm topology and operation. Risø-R-1805(EN).

[56] T.A. Ighil (2007). Analysis of Taylor´s "frozen turbulence" hypothesis and the possible feed-back of wind turbines on large scale lateral turbulence components. Risø-R-1234.

[57] B. Lange, S. Larsen, J. Høstrup and R. Barthelmie (2004). The influence of thermal effects on the wind speed profile of the coastal marine boundary layer. *Boundary-Layer Meteorology*¸ **112**, pp. 587–617.

[58] OWEZ (2008). www.norzeewind.nl, "Off shore Windfarm Egmond aan Zee, General report," Tech. Rep. OWEZ R 141 20080215, NordzeeWind.

[59] S. Ott, J. Berg and M. Nielsen (2011). Linearised CFD Models for Wakes, Risø-R-1772(EN).

[60] N. Johansen (2009). Verification of simulated fatigue loads on wind turbines operating in wakes. Tech. Rep., MEK-FM-EP 2009-10, DTU MEK, master thesis.

[61] IEC 61400-3. Wind turbines – part 1: Design requirements for offshore wind turbines, 2009.

[62] C.A. Paulson (1970). The mathematical representation of wind speed and temperature profiles in the unstable surface layer. J. Appl. Meteor., 9, 857-861.

[63] T.J. Larsen, G.C. Larsen, H.Aa. Madsen and S.M. Pedersen (2015). Wake effects above rated wind speed - An overlooked contributor to high loads in wind farms. EWEA Annual Conference and Exhibition 2015, 17-20 November, Paris, France.

[64] T.J. Larsen, G.C. Larsen, H.Aa. Madsen, K. Thomsen and S.M. Pedersen (2015). Comparison of measured and simulated loads for the Siemens SWT2.3 operating in wake conditions at the Lillgrund Wind Farm using HAWC2 and the dynamic wake meander model**.** EWEA Offshore Conference, 10-12 March, Copenhagen, Denmark.

[65] M.H. Hansen and L.C. Henriksen (2013). Basic DTU Wind Energy controller. DTU Wind Energy.

[66] L. Bergami and M.H. Hansen (2016). High-fidelity linear time-invariant model of a smart rotor with adaptive trailing edge flaps. Wind Energy, DOI: 10.1002/we.2014.

[67] S.J. Qin and T.A. Badgwell (1996). An Overview Of Industrial Model Predictive Control Technology. AIChE Symposium Series **93** (316), pp. 232-256.

[68] M. Baotic (2005). Optimal Control of Piecewise Affine Systems – a Multi-parametric Approach. Ph.D. dissertation.

[69] T. Geyer (2005). Low Complexity Model Predictive Control in Power Electronics and Power Systems. Ph.D. dissertation.

[70] J. Maciejowski (2002). Predictive control with constraints. Essex: Pearson Education Lim.

[71] J. M. Jonkman and M.L. Buhl Jr. (2005). FAST User's Guide. Tech. rep., National Renewable Energy Laboratory, Golden, CO.

[72] C. Bak and F. Zahle (2013). Description of the DTU 10 MW Reference Wind Turbine. DTU Wind Energy Report-I-0092.

[73] M.O. Hansen (2008). Aerodynamics of Wind Turbines. Earthscan.

[74] M. Mirzaei, H.H. Niemann and N.K. Poulsen (2011). A mu-Synthesis Approach to Robust Control of a Wind Turbine. The 50th IEEE Conference on Decision and Control and European Control

Conference, Orlando, Florida, pp. 645-650.

[75] M. Harris, M. Hand and A. Wright (2006). LiDAR for Turbine Control. Tech. rep., National Renewable Energy Laboratory.

[76] M. Mirzaei, N.K. Poulsen and H.H. Niemann (2012). Model Predictive Control of a Nonlinear System with Known Scheduling Variable. Proceedings of the 17th Nordic Process Control Workshop, pp.163-168.

[77] J. Jonkman, S. Butterfield, W. Musial and G. Scott (2009). Definition of a 5MW Reference Wind Turbine for Offshore System Development. Tech. rep., National Renewable Energy Laboratory, 1617 Cole Boulevard, Golden, Colorado 80401-3393 303-275-3000.

[78] B.J. Jonkman (2009). TurbSim User's Guide: Version 1.50. Tech. rep., National Renewable Energy Laboratory, 1617 Cole Boulevard, Golden, Colorado 80401-3393 303-275-3000.

[79] T.J. Larsen and A.M. Hansen (2007). How to HAWC2, the Users Manual, Risø-R-1597(EN), Risø National Laboratory - Technical University of Denmark.

[80] M.A. Miner (1945). Cumulative damage in fatigue. Journal of Applied Mechanics, Vol. 12, pp. 159–164.

[81] A. Papoulis (1965). Probability, Random Variables, and Stochastic Processes. McGraw-Hill Kogakusha, Ltd.

[82] G.C. Larsen and K.S. Hansen (2014). De-trending of wind speed variance based on first-order and second-order statistical moments only. Wind Energy, Vol. 17, No. 12, p. 1905-1924.

[83] T.J. Larsen, H.Aa. Madsen and K. Thomsen (2005). Active Load Reduction Using Individual Pitch, Based on Local Blade Flow Measurements. Wind Energy, Vol. 8, No. 1, p. 67-80.

Appendix A

Use of observed fluxes to drive the buoyant spectral tensor-model

Because many wind projects lack high-frequency turbulence measurements – or if there are sonic anemometers onsite, only 10- or 30-minute mean values are stored – it is not possible in these cases to calculate observed spectra of turbulent velocity components or fluxes. Thus, the wind engineer cannot fit the buoyant spectral-tensor model parameters to spectra by the method shown above and in [13]. As an alternative, we exploit the analytically prescribed behaviour of the eddy lifetime within the spectral-tensor model [9], along with classic spectral scaling of turbulent heat flux, to derive[5] an approximation for the two buoyancy-related model parameters (Ri and η_θ).

The Mann-model's eddy lifetime basis

$$\tau(k) \propto \Gamma(kL)^{-2/3}(dU/dz)^{-1} \tag{A.1}$$

and its related integral energy relation [9] can be used to relate the prescribed model parameters $\{\Gamma, L, \alpha\varepsilon^{2/3}\}$ to the model-implied shear dU/dz.[1]

Then, with the spectral scaling $\langle w\theta \rangle \propto \varepsilon\Gamma\sqrt{\eta_\theta}\,\theta/g$, an expression for the model's dimensionless destruction rate of temperature variance emerges:

$$\eta_\theta \propto \left[\frac{g}{\theta}\frac{\langle w\theta\rangle}{\epsilon\Gamma}\right]^2. \tag{A.2}$$

An analogous estimate can also be derived in terms of the variance of temperature $\langle\theta^2\rangle$, but this is more difficult to use and calibrate, because sonic anemometers often have significant amounts of noise in the inertial range towards the highest frequencies; therefore we employ the expression above.

Further, using the definition of gradient Richardson number with the model-implied shear, one arrives at an expression for the model's Richardson number,

$$\mathrm{Ri} \approx \frac{-g}{\theta_0}\frac{\langle w\theta\rangle}{c_h K_h}\frac{2L^{4/3}}{3\alpha\epsilon^{2/3}\Gamma}\ ; \tag{A.3}$$

Here the implied eddy-diffusivity for heat flux was obtained via the mean flux-gradient relation $\langle w\theta\rangle = -K_h\,(\mathrm{d}T/\mathrm{d}z)$ and the definition of temperature-variance destruction rate, expressible as

$$K_h = \frac{4}{9}\eta_\theta\left(\frac{g/\theta_0}{\mathrm{Ri}}\frac{L^{4/3}}{\alpha\epsilon^{2/3}\Gamma^4}\right)^2. \tag{A.4}$$

In order to check these relations, we utilize data from the Horizontal Array Turbulence ('HATS') experiment [41], which consisted of five sonic anemometers mounted at one height and spaced evenly in the cross-wind direction, and another row of nine sonic anemometers mounted at a different height and evenly spaced, such that the row endpoints were at the same position (*y*) for both rows. There were 4 different configurations of the anemometers, whereby each row was at a height between 3m and 8m above ground. The HATS site was flat and relatively uniform [41], thus allowing for a good surface-layer test of our model; more importantly, the dataset facilitates checking the 'translation' of measured stability parameters to model parameters, in somewhat *ideal conditions*.

[5] The fully-detailed derivation is in preparation for publication, so only the basic (useful) derivation/results are reported here, and thus the exact expression is pending.

First, from the HATS data we check the stability-influenced behaviour of measured fluxes, to gauge both how the measured gradients can be 'converted' to fluxes and also how well surface-layer (Monin-Obukhov) theory characterizes the data. This is shown in Fig. A1, where the ratio of heat flux predicted by M-O theory

$$K_h(dT/dz) = \kappa u_* z[\phi_h(z/L)]^{-1}(dT/dz) = (\kappa z)^2(dT/dz)(dU/dz)[\phi_h(z/L)\phi_m(z/L)]^{-1} \quad \text{(A.5)}$$

to measured flux is plotted versus temperature gradient. Figure A1also shows the dimensionless MOST diffusivity (normalized by neutral/ASL theory diffusivity) versus stability $(-z/L)$. The figure shows that the flux-gradient relation implied by MOST holds relatively well for stable conditions and most unstable cases, but for near-neutral and some unstable conditions there is more non-ideal behavior which is not handled well by surface-layer theory.

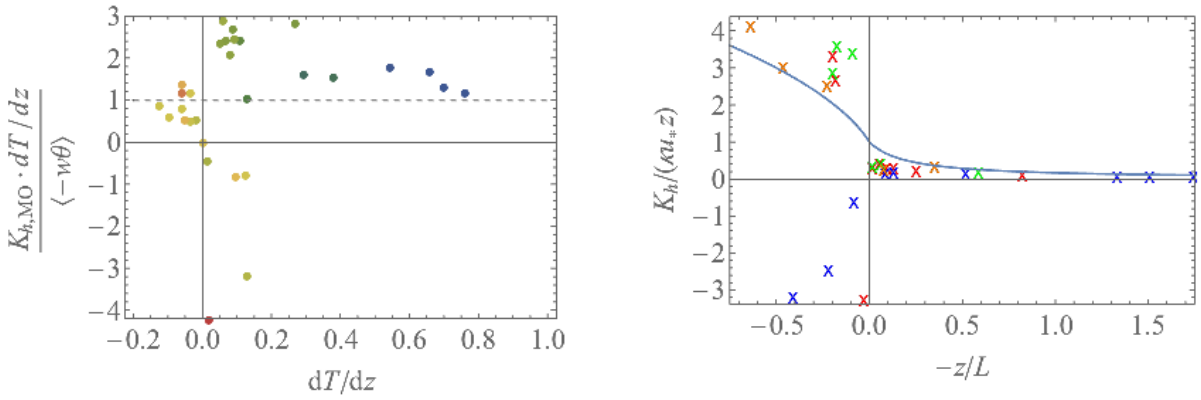

Figure A.1: Left: Ratio of M-O estimated heat flux via flux-gradient relation versus dT/dz; dashed line is M-O theory. Right: diffusivity normalized by surface-layer (ideal neutral) diffusivity scale ($\kappa u_* z$), versus stability ($-z/L$); solid line is M-O theory.

The HATS data do indicate for stable conditions, however, that a reasonable flux-gradient relation exists, not far from similarity theory (MOST). Thus it is possible to estimate η_θ and Ri, based on (A.2) and (A.3) along with the measured heat flux and the parameters $\{L, \varepsilon, \Gamma\}$ obtained from spectral fitting. Assuming a 'perfect fit' for the latter parameters, then one can compare the $\{\eta_\theta, \mathrm{Ri}\}$ obtained from spectral-fitting to that predicted via (A.2–3); this is shown in Fig. A.1. The plots show an approximately linear relationship, roughly 1:1, which supports the use of equations (A.2–3).

Appendix B

Closed form solution of roughness length matching shear power exponent

In this appendix a closed form solution to equation (5.2.6) is provided. Starting point is the functional expressed in equation (5.2.5). Stationary values of this functional is obtained by solving the equation

$$\frac{\partial \Pi(z_0)}{\partial z_0} = 0 \tag{B.1}$$

However, this equation is somewhat easier to solve analytically when using the following reformulation

$$\frac{\partial \Pi(z_0)}{\partial z_0} = \frac{\partial \Pi(z_0)}{\partial (Ln\, z_0)} \frac{\partial \Pi(Ln\, z_0)}{\partial (z_0)} = \frac{\partial \Pi(z_0)}{\partial (Ln\, z_0)} \frac{1}{z_0} = 0 \tag{B.2}$$

As the roughness length in practice is always larger than zero, eq. (B.2) may be simplified as

$$\frac{\partial \Pi(z_0)}{\partial (Ln\, z_0)} = 0 \tag{B.3}$$

The left hand side of this equation is given by

$$\begin{aligned}
\frac{\partial \Pi(z_0)}{\partial (Ln\, z_0)} &= 2V_{hub}^2 \int_{z_{hub}-R}^{z_{hub}+R} \left[\frac{Ln(z) - Ln(z_0)}{Ln(z_{hub}) - Ln(z_0)} - \left(\frac{z}{z_{hub}} \right)^{\alpha} \right] \frac{Ln(z) - Ln(z_{hub})}{(Ln(z_{hub}) - Ln(z_0))^2} dz \\
&= \frac{2V_{hub}^2}{(Ln(z_{hub}) - Ln(z_0))^3} \int_{z_{hub}-R}^{z_{hub}+R} \left[(Ln(z))^2 - (Ln(z_0) + Ln(z_{hub}))Ln(z) + Ln(z_0)Ln(z_{hub}) \right] dz \\
&\quad - \frac{2V_{hub}^2}{(Ln(z_{hub}) - Ln(z_0))^2} \int_{z_{hub}-R}^{z_{hub}+R} \left[z_{hub}^{-\alpha} z^{\alpha} Ln(z) - z_{hub}^{-\alpha} Ln(z_{hub}) z^{\alpha} \right] dz \\
&= A(z_0) \left[z(Ln(z))^2 - 2(zLn(z) - z) - (Ln(z_0) + Ln(z_{hub}))(zLn(z) - z) + zLn(z_0)Ln(z_{hub}) \right]_{z_{hub}-R}^{z_{hub}+R} \\
&\quad - B(z_0) \left[z_{hub}^{-\alpha} \left(\frac{z^{\alpha+1}}{\alpha+1} Ln(z) - \frac{z^{\alpha+1}}{(\alpha+1)^2} \right) - z_{hub}^{-\alpha} Ln(z_{hub}) \frac{z^{\alpha+1}}{\alpha+1} \right]_{z_{hub}-R}^{z_{hub}+R} \\
&= A(z_0) \left[z(Ln(z))^2 - 2(zLn(z) - z) - Ln(z_{hub})(zLn(z) - z) \right]_{z_{hub}-R}^{z_{hub}+R} \\
&\quad + A(z_0) Ln(z_0) \left[-(zLn(z) - z) + zLn(z_{hub}) \right]_{z_{hub}-R}^{z_{hub}+R} \\
&\quad - B(z_0) \left[z_{hub}^{-\alpha} \left(\frac{z^{\alpha+1}}{\alpha+1} Ln(z) - \frac{z^{\alpha+1}}{(\alpha+1)^2} \right) - z_{hub}^{-\alpha} Ln(z_{hub}) \frac{z^{\alpha+1}}{\alpha+1} \right]_{z_{hub}-R}^{z_{hub}+R} \\
&= A(z_0) C_1 + A(z_0) Ln(z_0) C_2 - B(z_0) C_3
\end{aligned} \tag{B.4}$$

with

$$A(z_0) \equiv \frac{2V_{hub}^2}{\left(Ln\left(z_{hub}\right) - Ln\left(z_0\right)\right)^3} = \frac{2V_{hub}^2}{\left(Ln\left(z_{hub} / z_0\right)\right)^3},$$

$$B(z_0) \equiv \frac{2V_{hub}^2}{\left(Ln\left(z_{hub}\right) - Ln\left(z_0\right)\right)^2} = \frac{2V_{hub}^2}{\left(Ln\left(z_{hub} / z_0\right)\right)^2},$$

$$C_1 \equiv \left[z\left(Ln(z)\right)^2 - 2\left(zLn(z) - z\right) - Ln\left(z_{hub}\right)\left(zLn(z) - z\right)\right]_{z_{hub}-R}^{z_{hub}+R},$$

$$C_2 \equiv \left[-\left(zLn(z) - z\right) + zLn\left(z_{hub}\right)\right]_{z_{hub}-R}^{z_{hub}+R}$$

$$C_3 \equiv \left[z_{hub}^{-\alpha}\left(\frac{z^{\alpha+1}}{\alpha+1} Ln(z) - \frac{z^{\alpha+1}}{(\alpha+1)^2} \right) - z_{hub}^{-\alpha} Ln\left(z_{hub}\right) \frac{z^{\alpha+1}}{\alpha+1} \right]_{z_{hub}-R}^{z_{hub}+R} =$$

$$= \left[z_{hub}^{-\alpha}\left(\frac{z^{\alpha+1}}{\alpha+1} Ln\left(z / z_{hub}\right) - \frac{z^{\alpha+1}}{(\alpha+1)^2} \right) \right]_{z_{hub}-R}^{z_{hub}+R}.$$

The solution to eq. (B.3) may thus be found as

$$A(z_0)C_1 + A(z_0)Ln(z_0)C_2 - B(z_0)C_3 = 0 \tag{B.5}$$

or

$$Ln(z_0) = \frac{C_3 Ln\left(z_{hub}\right) - C_1}{C_2 + C_3} \tag{B.6}$$

whereby

$$z_0 = e^{\frac{C_3 Ln\left(z_{hub}\right) - C_1}{C_2 + C_3}} \tag{B.7}$$

Appendix C

Turbulence spectra

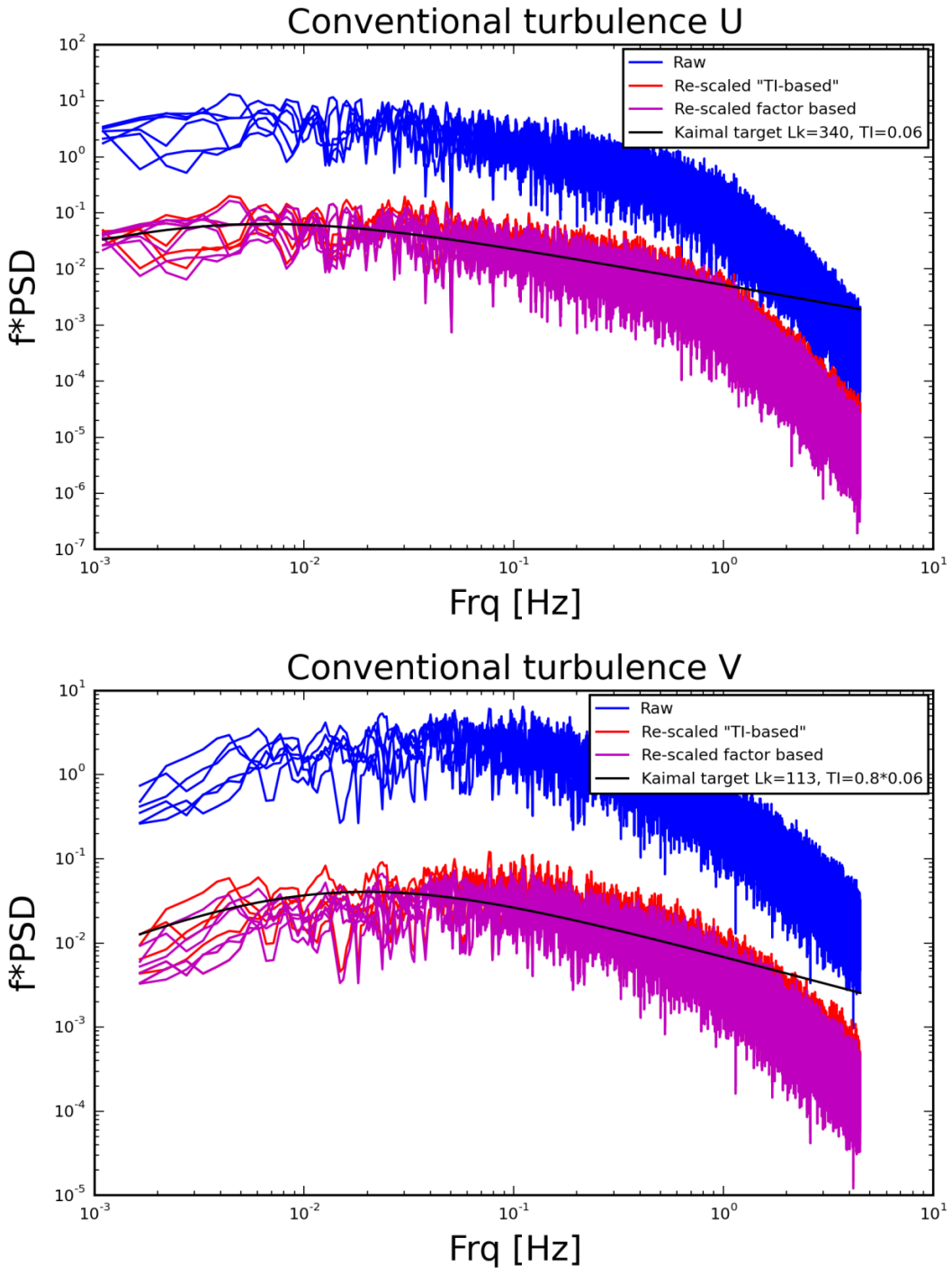

Figure C.1: Comparison of the used conventional turbulence spectra with the Kaimal reference spectrum (ti=6%). The "raw" box spectrum is plotted together with rescaled turbulence using respectively 1) turbulence intensity based and 2) "factor" based scaling.
Top: u-component; Bottom: v-component.

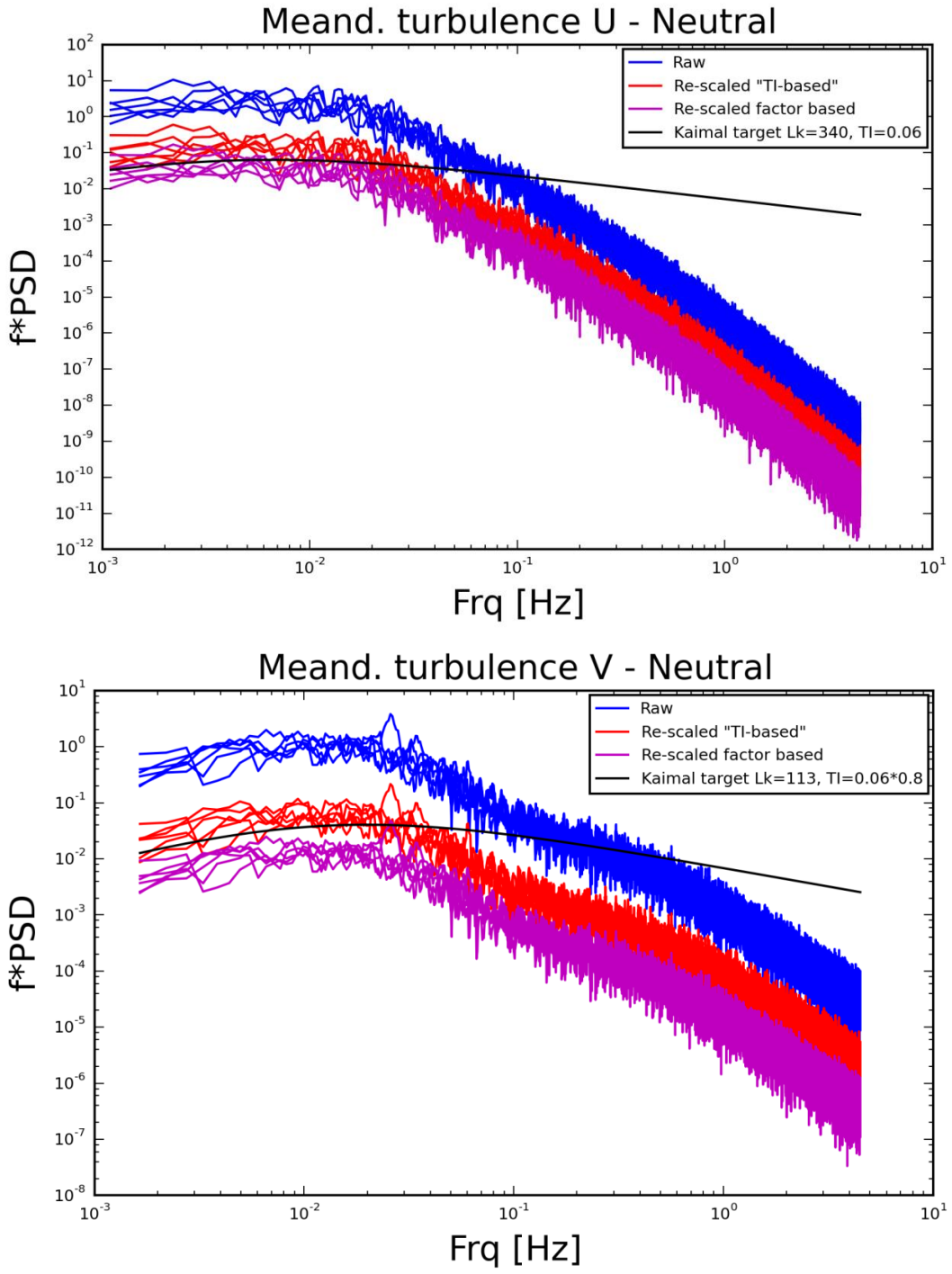

Figure C.2: Comparison of the used *neutral* conventional turbulence spectra with the Kaimal ref. spectrum (ti=6%). The "raw" box spectrum is plotted together with rescaled turbulence using respectively 1) turbulence intensity based and 2) "factor" based scaling. Top: u-component; Bottom: v-component.

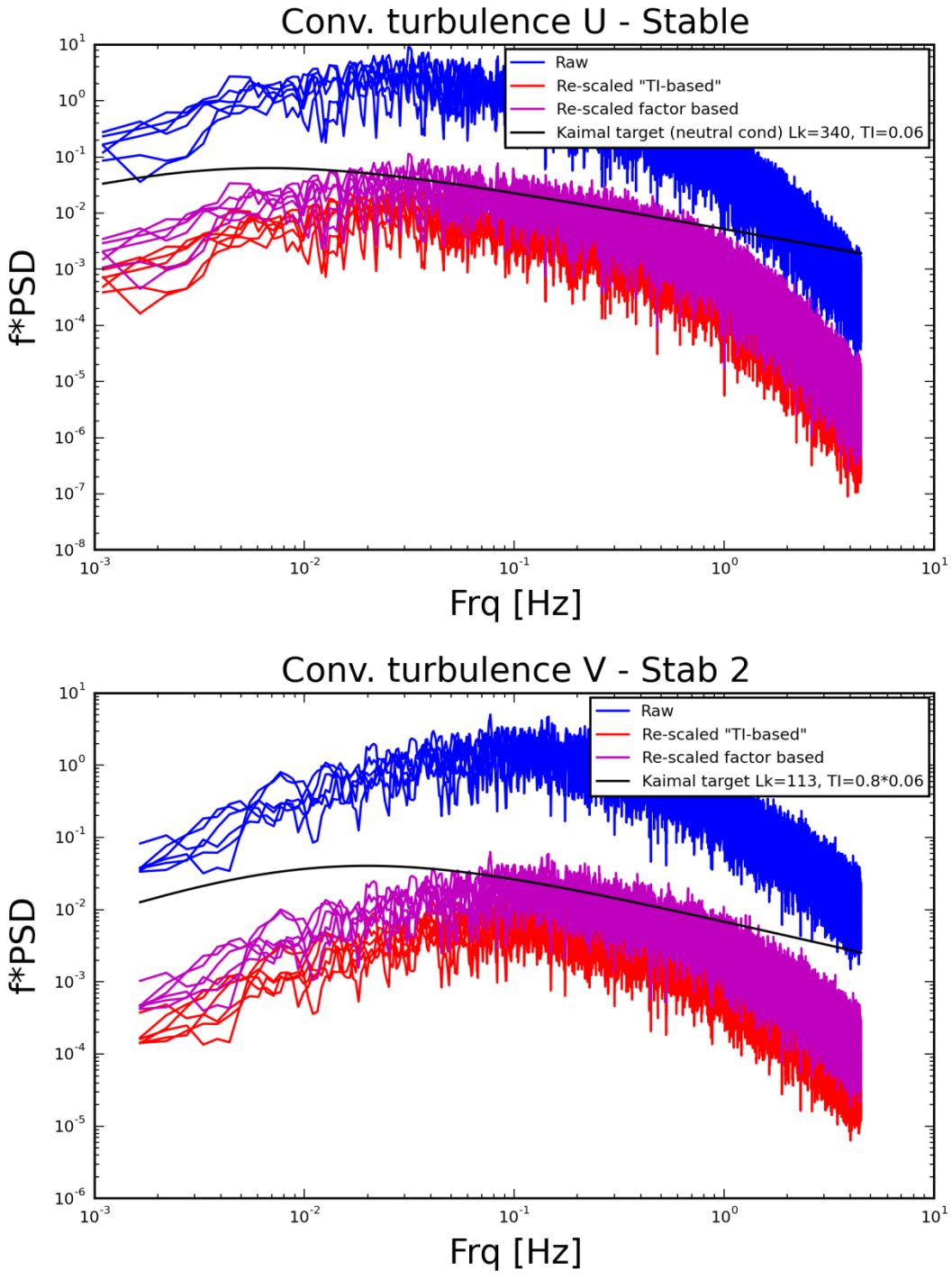

Figure C.3: Comparison of the used *stable* conventional turbulence spectra with the neutral Kaimal reference spectrum (ti=6%). The "raw" box spectrum is plotted together with rescaled turbulence using respectively 1) turbulence intensity based and 2) "factor" based scaling. Top: u-component; Bottom: v-component.

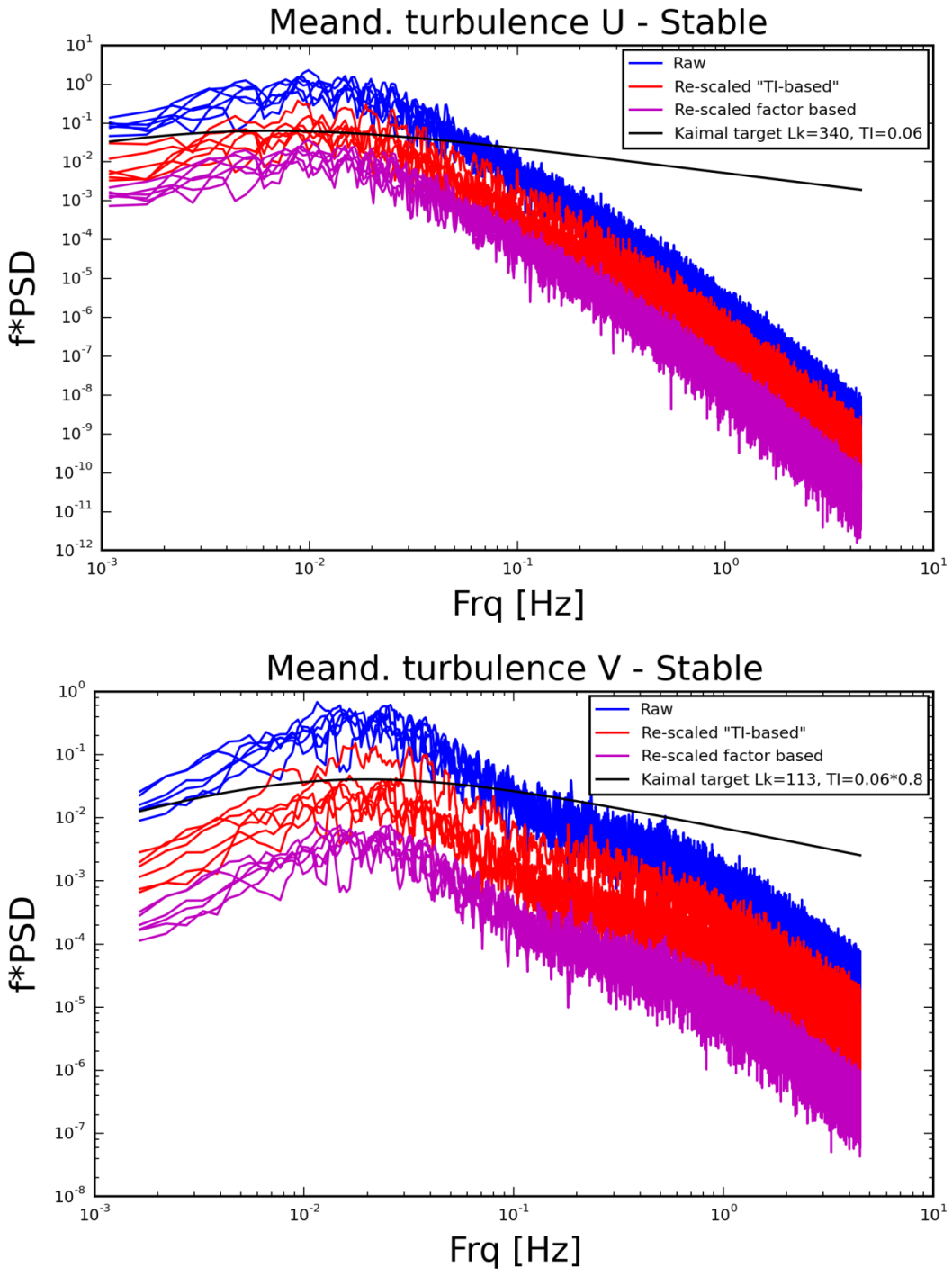

Figure C.4: Comparison of the used *stable* meandering turbulence spectra with the neutral Kaimal reference spectrum (ti=6%). The "raw" box spectrum is plotted together with rescaled turbulence using respectively 1) turbulence intensity based and 2) "factor" based scaling. Top: u-component; Bottom: v-component.

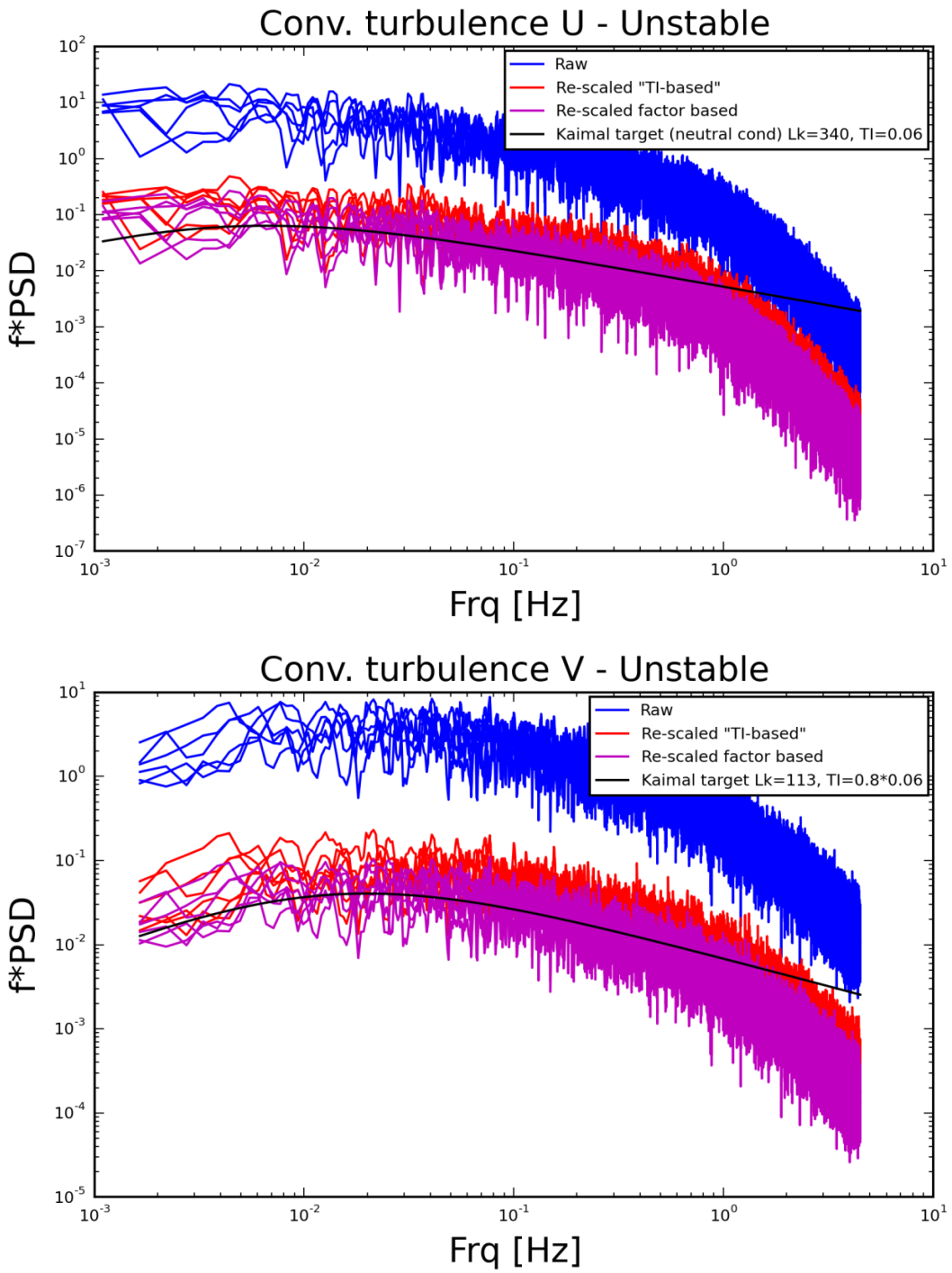

Figure C.5: Comparison of the used *unstable* conventional turbulence spectra with the neutral Kaimal reference spectrum (ti=6%). The "raw" box spectrum is plotted together with rescaled turbulence using respectively 1) turbulence intensity based and 2) "factor" based scaling. Top: u-component; Bottom: v-component.

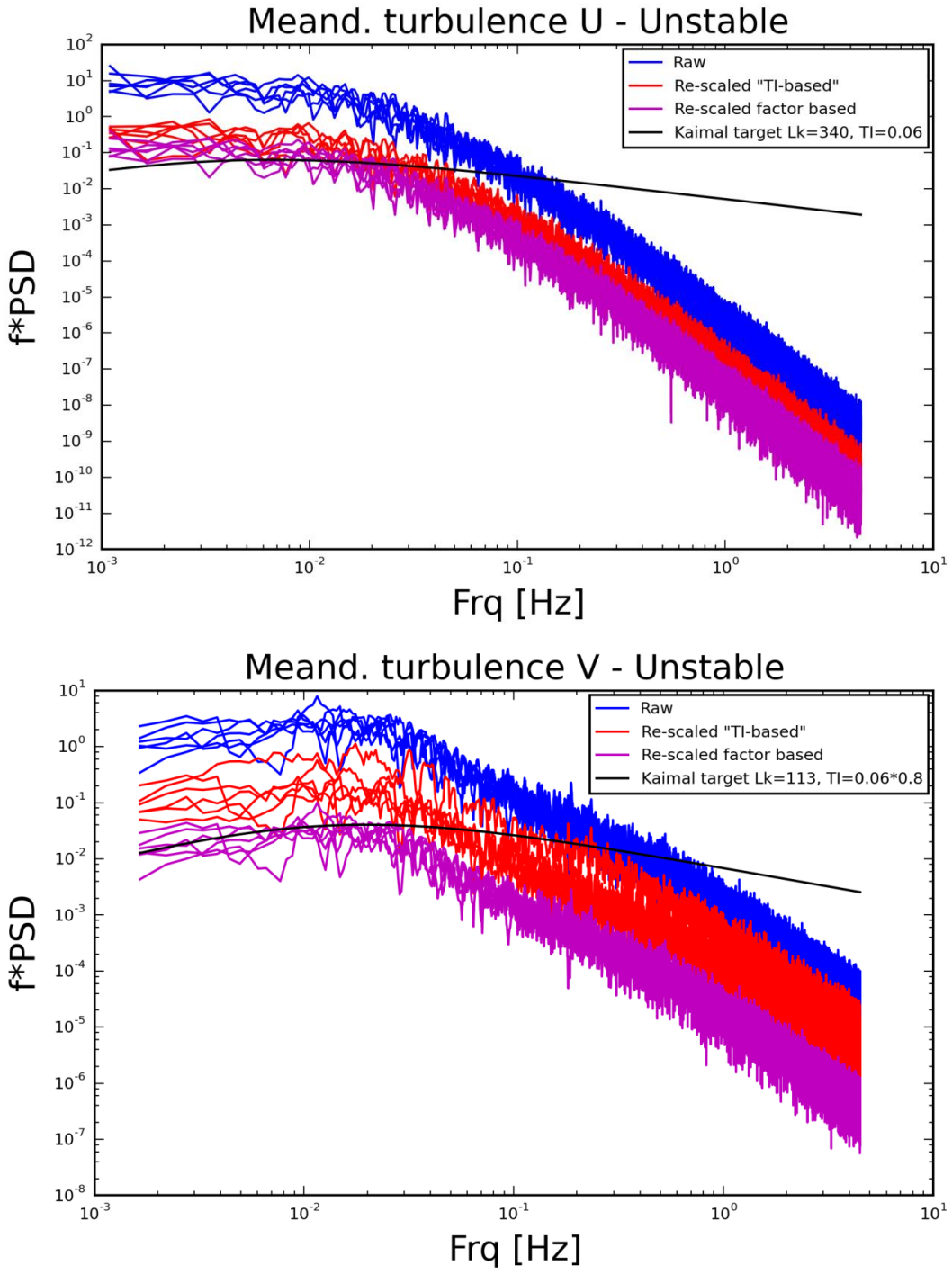

Figure C.6: Comparison of the used *unstable* meandering turbulence spectra with the neutral Kaimal reference spectrum (ti=6%). The "raw" box spectrum is plotted together with rescaled turbulence using respectively 1) turbulence intensity based and 2) "factor" based scaling. Top: u-component; Bottom: v-component.

DTU Wind Energy is a department of the Technical University of Denmark with a unique integration of research, education, innovation and public/private sector consulting in the field of wind energy. Our activities develop new opportunities and technology for the global and Danish exploitation of wind energy. Research focuses on key technical-scientific fields, which are central for the development, innovation and use of wind energy and provides the basis for advanced education at the education.

We have more than 240 staff members of which approximately 60 are PhD students. Research is conducted within nine research programmes organized into three main topics: Wind energy systems, Wind turbine technology and Basics for wind energy.

Technical University of Denmark
Department of Wind Energy
Frederiksborgvej 399
Building 118
4000 Roskilde
Phone 46 77 50 85

info@vindenergi.dtu.dk
www.vindenergi.dtu.dk